Processing and Properties of Advanced Ceramics and Glasses

CONFERENCE PROCEEDINGS

Joint Annual Meeting of the Slovak Silicate Scientific-Technological Society,

KIMS Korea-SAS Slovakia Workshop on Advanced Ceramics,

FunGLASS Conference on Functional Materials.

Stará Lesná - High Tatras, Slovakia
October 29 - 31, 2018

ORGANIZING INSTITUTIONS:

Institute of **M**aterials **R**esearch of the **S**lovak **A**cademy of **S**ciences
« »
Slovak **S**ilicate **S**cientific - **T**echnological **S**ociety
« »
Korea **I**nstitute of **M**aterials **S**cience
« »
Centre for **F**unctional and **S**urface **F**unctionalized **G**lass

Scientific Board:

Prof. Pavol Šajgalík, SAS, Slovakia
Pavol Hvizdoš, PhD., IMR SAS, Slovakia
Prof. Jongman Lee, KIMS, Korea
Prof. Dušan Galusek, FunGlass, Slovakia

Organizing Committee:

Prof. Ján Dusza, IMR SAS, Slovakia
Alexandra Kovalčíková, PhD., IMR SAS, Slovakia
Erika Múdra, PhD., IMR SAS, Slovakia
Assoc. Prof. Miroslav Hnatko, IICH SAS, Slovakia
Andrea Stropková, MBA. Fun Glass, Slovakia
Anna Jurová, IICH SAS, Slovakia

Published by:

Institute of Materials Research, Slovak Academy of Sciences, Košice, Slovak Republic

Phone: +421 55 792 2402
Fax: +421 55 792 2408
http: www.imr.saske.sk

Editors: Erika Múdra, Alexandra Kovalčíková
ISBN: 978-80-89782-10-9
EAN: 9788089782109
Cover photo: Erika Múdra, IMR SAS (nanograins of SnO_2 - fiber)

This conference was realized within the frame of the project „Research Centre of Advanced Materials and Technologies for Recent and Future Applications “PROMATECH” ITMS: 26220220186, which was supported by the Operational Program “Research and Development” financed through European Regional Development Fund.

This conference is part of a project that has received funding from the European Union's Horizon 2020 research and innovation programme under grant agreement N°739566.

CONTENTS

KOMPOZITNÉ MATERIÁLY SiC-GRAFÉN S VYSOKOU ELEKTRICKOU A TEPELNOU VODIVOSŤOU
SiC-GRAPHENE COMPOSITES WITH HIGH ELECTRICAL AND THERMAL CONDUCTIVITY
O. Hanzel, Z. Lenčéš, Y.W. Kim , P. Šajgalík..7

Ce^{3+} DOPED YTTRIA NANOPOWDERS FOR TRANSPARENT YTTRIA CERAMICS PREPARED BY PRECIPITATION METHOD
N. P. Govindan, M. Michálková, D. Galusek..12

LUMINISCENCIA Er^{3+}/Yb^{3+} DOPOVANEJ ZIRKONIČITANOVEJ KERAMIKY INDUKOVANÁ UP-KONVERZIOU ŽIARENIA
UP-CONVERSION INDUCED LUMINESCENCE IN Er^{3+}/Yb^{3+} CO-DOPED ZIRCONATE CERAMICS
E. Trusova, R. Klement, Ľ. Bača, K. Podbolotov, P. Veteška, A.Gatial, Y. Halahovets,
M. Janek……………………………………………………………………………18

PREPARATION AND STUDY OF MICROSTRUCTURE OF YTTRIA AND CERIA STABILIZED TETRAGONAL ZIRCONIA POLYCRYSTALS FOR DENTAL APPLICATIONS
A. Nowicka, H. F. El-Maghraby, D. Galusková, D. Galusek..23

ADHESION AND IMPACT WEAR RESISTANCE OF TiC-BASED COATINGS PREPARED BY DCMS AND HIMIPS
J. Daniel, J. Grossman, T. Fořt, J. Sobota, L. Zábranský, P. Souček, K. Bernátová, V. Buršíková, P. Vašina……………………………………………………………………27

$TiO_2 – SiO_2 – Al_2O_3$ FILMS FOR HUMIDITY SENSORS
VRSTVY $TiO_2 – SiO_2 – Al_2O_3$ PRE SENZORY VLHKOSTI
K. Faturíková, A. Plško, M. Liška...34

PRÍPRAVA, CHARAKTERIZÁCIA A OXIDAČNÉ SPRÁVANIE KERAMICKÝCH POVLAKOV PRIPRAVENÝCH Z ORGANOKREMIČITÝCH PREKURZOROV S PASÍVNYMI PLNIVAMI
PREPARATION, CHARACTERIZATION AND OXIDATION BEHAVIOR OF POLYMER DERIVED CERAMIC COATINGS WITH PASSIVE FILLERS
I. Petríková, M. Parchovianský, P. Švančárek, G. Motz, D. Galusková, D. Galusek………...39

NOVEL ALKALI-ACTIVATION BASED PROCESS FOR THE MANUFACTURING OF SODA-LIME GLASS FOAMED PANELS AND GRANULES
A. Rincón, E. Bernardo…………………………………………………………………44

NANOSTRUCTURED CATALYTIC THIN FILMS PREPARED BY SOLUTION COMBUSTION SYNTHESIS ON MULLITE-CORDIERITE CERAMICS
H. Shymanskaya, R. Papou, N. Sdobnyakov, D. Sokolov, V. Myasnichenko.........................49

VPLYV PRÍDAVKU Al_2O_3 NA SPEKANIE A UPCONVERSION VLASTNOSTI $CaZrO_3$
INFLUENCE OF Al_2O_3 ADDITION ON SINTERING BEHAVIOUR AND UPCONVERSION OF $CaZrO_3$
P. Veteška, K. Tomanová, Z. Hajdúchová, Ľ. Bača, M. Janek……………………………….54

ODLIEVANIE A BEZTLAKOVÉ SPEKANIE Al_2O_3 KERAMIKY AKO MODELU PRE PRÍPRAVU 3D OBJEKTOV
CASTED ALUMINA CERAMICS AS A MODEL FOR SINTERING OF 3D PRINTED OBJECTS PREPARED BY FFF
M. Orlovská, K. Tomanová, V. Kovár, M. Kitzmantel, E. Neubauer, Ľ. Bača………………59

POVRCHOVÁ MODIFIKÁCIA Si_3N_4 KYSLÍK-ACETYLÉNOVÝM PLAMEŇOM – VPLYV ZLOŽENIA NA HRANICI ZŔN
SURFACE MODIFICATION OF Si_3N_4 BY OXYACETYLENE TORCH – INFLUENCE OF GRAIN BOUNDARY COMPOSITION
M. Hičák, M. Hnatko, M. Labudová, D. Galusková, J. Sedláček, P. Šajgalík........................64

ÚLOHA FYZISORBOVANÝCH ČASTÍC PRI ELEKTROFORETICKEJ DEPOZÍCII PRÁŠKOV Al_2O_3 A YSZ
THE ROLE OF PHYSISORBED SPECIES ON ELECTROPHORETIC DEPOSITION OF Al_2O_3 AND YSZ POWDERS
J. Ráheľ, M. Ilčíková, J. Dugáček, D. Pavliňák, D. Drdlík…………………………………...72

CHARAKTERISTIKY THz ODOZVY Er^{3+}/Yb^{3+} DOPOVANEJ $La_2Zr_2O_7$ KERAMIKY
CHARACTERSTICS OF THz RESPONSE FOR Er^{3+}/Yb^{3+} DOPED $La_2Zr_2O_7$ CERAMICS
M. Janek, E. Trusova, Ľ. Bača, P. Veteška, R. Klement, M. Naftaly………………………...76

MIKROŠTRUKTÚRA A VLASTNOSTI TI-B_4C KOMPOZITOV PRIPRAVENÝCH PROCESOM ADITÍVNEJ VÝROBY
MICROSTRUCTURE AND PROPERTIES OF Ti-B_4C COMPOSITES PREPARED BY ADDITIVE MANUFACTURING
Ľ. Bača , N.Stelzer , L. Vály , D.Grech, E. Neubauer , M. Kitzmantel………………………82

SYNTÉZA, SPEKANIE A OPTICKÉ VLASTNOSTI SPINELOV MgAlON A $MgAl_2O_4$
SYNTHESIS, SINTERING AND OPTICAL PROPERTIES OF MgAlON AND $MgAl_2O_4$ SPINEL CERAMICS
M. Radwan, Z. Lenčéš, P. Šajgalík...87

PREPARATION OF YB_4 CERAMICS BY REACTION SINTERING FROM ELEMENTS
Z. Kováčová, L. Bača, E. Neubauer……………………………………………………..93

PRÍPRAVA A CHARAKTERIZÁCIA VYSOKOTEPLOTNEJ KERAMIKY NA BÁZE ZrB_2-SiC
PREPARATION AND CHARACTERIZATION OF ZrB_2-SiC BASED ULTRA HIGH TEMPERATURE CERAMICS
Z. Fürdősová, I. Dlouhý, P. Tatarko……………………………………………………´98

VPLYV MORFOLÓGIE PRÁŠKOV NA BEZTLAKOVÉ SPEKANIE KERAMIKY Z B_4C: POTENCIÁL PRE APLIKÁCIU V 3D-TLAČI
EFFECT OF POWDERS MORPHOLOGY ON THE PRESSURELESS SINTERING OF B_4C CERAMICS: POTENTIAL FOR 3D-PRINTING APPLICATION
M. Vozárová, Zuzana Kováčová, E. Neubauer, M. Kitzmantel, L. Bača, Ľ. Orovčík, V. Trembošová, M. Janek...104

3D TLAČ OXIDOVEJ KERAMIKY Z POLYMÉRNYCH KOMPOZITOV POUŽITÍM FDM TECHNOLÓGIE
3D PRINTING OF OXIDE CERAMICS FROM POLYMER COMPOSITES USING FDM TECHNOLOGY
K. Randová, P. Veteška, Z. Hajdúchová, J. Feranc, K. Tomanová, R. Plavec, Ľ. Bača, M. Janek……………………………………………………………………………………110

PRÍPRAVA FEROSILICIDOV SPRACOVANÍM DRUHOTNÝCH SUROVÍN Z PRIEMYSLU
PREPARATION OF FERROSILICIDES BY UTILIZATION OF WASTE MATERIAL OF INDUSTRY
R. Bystrický, M. Hnatko, J. Sedláček..114

ELEKTROSTATICKÉ ZVLÁKŇOVANIE – JEDINEČNÁ TECHNOLÓGIA PRÍPRAVY MIKROVLÁKIEN NA BÁZE TITÁNU
ELECTROSPINNING - A UNIQUE TECHNOLOGY FOR PRODUCTION Ti - BASED MICROFIBERS
I. Shepa, E. Mudra, A. Kovalcikova, J. Dusza……………………………………………119

PRÍPRAVA KOMPAKTNÝCH A NANORÚRKOVÝCH TiO_2 VRSTIEV NA FLEXIBILNEJ KAPTONOVEJ FÓLIÍ A ŠTUDOVANIE ICH FOTOKATALYTICKÝCH VLASTNOSTÍ
PREPARATION OF COMPACT AND NANOTUBE TiO_2 LAYERS ON FLEXIBLE KAPTON TAPE AND STUDY OF THEIR PHOTOCATALYTIC PERFORMANCE
P. Petrisková, M. Motola, O. Monfort, G.Plesch...124

SYNTÉZA A VLASTNOSTI BÓROM DOPOVANÝCH NANOČASTÍC ZnO V THz OBLASTI
SYNTHESIS AND PROPERTIES OF BORON DOPED ZnO NANOPARTICLES IN THz REGION
D. Furka, S. Furka, M. Naftaly, A. Czímerová, M. Čaplovičová, M. Janek………………..129

KIMS Korea-SAS Slovakia Workshop on Advanced Ceramics

HIPIMS VS. DC SPUTTERED HYDROGENATED W-C:H COATINGS: STRUCTURE AND MECHANICAL PROPERTIES
F. Lofaj, M. Kabátová, A. Kovalčíková, V. Girman, J. Dobrovodský, D.Vaňa, M. Beňo.....134

FACILE SURFACE MODIFICATION TECHNIQUES OF CERAMIC MEMBRANES FOR THE APPLICATION TOWARDS WATER PURIFICATION
J. Lee, J.-H. Ha, I.-H. Song...135

HIGH ENTROPY CARBIDES: NOVEL MATERIALS FOR EXTREME ENVIRONMENTS
T. Csanádi, E. Castle, M. Reece, J. Dusza..136

IMPROVED THERMAL CONDUCTIVITY OF SILICON NITRIDE BY INTENTIONAL OXYGEN REMOVAL
H.-N. Kim, Y. Li, Y.-J. Park, J.-W. Ko, H.-D. Kim...137

A STUDY ON POROUS CERAMIC MEMBRANES PREPARED BY LOW-COST RAW MATERIALS FOR POTENTIAL MICROFILTRATION APPLICATIONS
J.-H. Ha, J. Lee, I.-H. Song...138

ELECTRIC FIELD ASSISTED JOINING OF ADVANCED SiC-BASED CERAMICS
P. Tatarko, X. Zhou, S. Grasso, I. Dlouhý, M. Ferraris...138

POROUS THERMAL INSULATION COATINGS FOR INTERNAL COMBUSTION AUTOMOBILE ENGINES
J.-J. Choi, S.-J. Yoon, Ch.-W. Ahn, B.-D. Hahn..140

EFFECT OF DIFFERENT PROCESSING TECHNOLOGIES ON DEVELOPMENT OF BORON CARBIDE/GRAPHENE PLATELETS CERAMICS
R. Sedlák,A. Kovalčíková, P. Rutkowski, A. Dubiel, S. Grasso, H. Porwal, V. Girman, M. Fides, E. Múdra, J. Balko, M. J Reece, J. Dusza……………………………………………141

RESEARCH ACTIVITIES ON THE TRANSPARENT POLYCRYSTALLINE CERAMICS AT KIMS
Y.-J. Park, H.-N.Kim, J.-W. Ko, H.-D. Kim……………………………………….……………..142

SiC-GRAPHENE COMPOSITES WITH HIGH ELECTRICAL AND THERMAL CONDUCTIVITY
O. Hanzel, Z. Lenčéš, Y.-W. Kim, P. Šajgalík...143

KOMPOZITNÉ MATERIÁLY SiC-GRAFÉN S VYSOKOU ELEKTRICKOU A TEPELNOU VODIVOSŤOU

SiC-GRAPHENE COMPOSITES WITH HIGH ELECTRICAL AND THERMAL CONDUCTIVITY

O. Hanzel[1], Z. Lenčéš[1], Y.W. Kim [2], P. Šajgalík[1]

[1]*Institute of Inorganic Chemistry, Slovak Academy of Sciences, Dúbravska cesta 9, 845 36 Bratislava, Slovak Republic*

[2] *Functional Ceramics Laboratory, Department of Materials Science and Engineering, University of Seoul, Seoul 02504, Republic of Korea*

ABSTRACT

Dense silicon carbide/graphene nanoplatelets (GNPs) and silicon carbide/graphene oxide (GO) with yttrium oxide and scandium oxide as sintering additives were prepared by rapid hot pressing (RHP). Sintering of composites was performed in nitrogen atmosphere at 2000°C for 30 min under uniaxial pressure of 50 MPa. After sintering samples were annealed in gas pressure sintering (GPS) furnace at 1800°C for 6 h under 30 MPa of pressure in a nitrogen atmosphere. The aim of the present contribution was to investigate the influence of the GNPs and GO additions, orientations of the graphene layers and effect of annealing on electrical and thermal properties of such prepared composites. Electrical conductivity as well as thermal diffusivity measured in parallel direction to graphene layers were significantly increased after addition of graphene and after post-sintering annealing of samples.

Keywords: silicon carbide, graphene, rapid hot press, annealing, functional properties

INTRODUCTION

Silicon carbide (SiC) is an important structural material due to its excellent thermal conductivity, wear resistance, oxidation resistance, and high-temperature mechanical properties [1–7]. Tailoring of electrical and thermal conductivity of structural ceramics is important for many applications, for example, static charge dissipation devices, manufacturing components by electro-discharge machining, heat exchangers and electronic substrates. From this point of view incorporation of graphene into ceramic matrix is very promising due to its extraordinary electrical and thermal conductivity [8-11]. Polycrystalline SiC ceramics exhibits a wide range of thermal conductivity values from 30 W/m.K to 270 W/m.K. It depends on many factors like specific chemistry of sintering additives, microstructure and post-heat treatment conditions. For example, hot-pressed SiC sintered with

BeO yielded a thermal conductivity of 270 W/m.K [12]. A SiC ceramic sintered with Al_2O_3–Y_2O_3 had a conductivity of 55–90 W/m.K [13,14]. There are several strategies for improvement of thermal conductivity of SiC ceramics: (1) decrease in lattice oxygen from SiC grains by using Y_2O_3 and Sc_2O_3 as a sintering additives, (2) the use of sintering additives comprising cations insoluble in SiC such as the replacement of the Al compound by sintering additives with no or low solubility in SiC, (3) a decrease in grain boundary segregation, which induces grain boundary scattering [15], (4) annealing of sintered sample in order to increase grain size and also to anneal defects in structure of graphene incorporated in ceramic matrix. The aim of the present contribution was to investigate the influence of the GNPs and GO additions, orientations of the graphene layers and effect of annealing on functional properties (electrical conductivity and thermal diffusivity) of such prepared composites.

EXPERIMENTAL

For preparation of composite powders we used either commercially available GNPs (thickness < 4 nm, Cheap Tubes Inc., USA) or we synthesized GO in lab. Composite powders with different amount of graphene nanoplatelets from 1 to 10 wt. % or 1 wt. % of graphene oxide were prepared. Firstly, the appropriate amounts of GNPs/GO were dispersed in distilled water by intense ultrasonication (Sonopuls HD 3200, 20 kHz, Bandelin electronic GmbH, Germany) through a titanium probe (Ø 13 mm) for a duration of 60 min with a sonication power of 80 W. After that, silicon carbide powder with 1 vol.% Y_2O_3–Sc_2O_3 additives were added into the suspensions and homogenized on magnetic stirrer for 3 h. Every hour suspension was ultrasonicated for 5 min. The prepared suspensions were then immediately sprayed into a liquid nitrogen in order to prevent separation of any phases and water was removed from the frozen powders by a freeze dryer for 24-48 h. Finally, the resultant composite powders were dried at 80 °C overnight and sieved through a 71 μm micro-sieve. In case of reference powder, without any addition of graphene, all components were ball milled together in isopropanol with SiC balls for 24 h. Isopropanol was removed from suspension by vacuum rotary evaporator. Resulting reference powder were dried at 80°C over night and then sieved through 71 μm microscreen. Composite and reference powders were placed in graphite die and surrounded by graphite paper (foil) in order to prevent direct contact between powder compact and graphite die and sintered in rapid hot press (DSP 507, Dr. Fritsch GmbH., Germany) at 2000°C with holding time of 30 min, uniaxial pressure 50 MPa under nitrogen atmosphere and with heating rates 100°C/min. From each composition three samples were made in order to get materials for testing of electrical and thermal conductivity and studying influence of graphene layers orientations and effect of annealing on properties of such prepared materials. Final dimensions of prepared samples were 20 mm in diameter and thickness approximately 3-4 mm and approximately 10 mm in case of thick samples.

After sintering some samples were annealed in gas pressure sintering (GPS) furnace at 1800°C for 6 h under 30 MPa of pressure in a nitrogen atmosphere.Densities of prepared composites were measured by Archimedes method using mercury as the immersion medium.

Thermal diffusivity measurements were done using Laser flash analyser Linseis LFA 1000 in direction parallel and perpendicular to pressing axis and also before and after annealing. To evaluate thermal diffusivity sample 10 x 10 mm and thickness approximately 2 - 3 mm were cut and plane parallel grinded. Data were averaged for each measuring temperature over at least three measurements.

Electrical conductivity was measured by four point probe method either by mechanical contacts or with indium solder contacts in direction parallel and perpendicular to pressing axis and also before and after annealing.

RESULTS

Relative density of prepared composites slightly decrease with increasing content of graphene. However, almost fully dense composites were prepared by RHP even at high loading of graphene, in case of sample with 10 wt. % relative density was around 97 %. Electrical conductivity was investigated as a function of amount of graphene, its orientation in SiC matrix and effect of annealing. With increasing amount of graphene electrical conductivity increases in both measuring directions. Electrical conductivity measured in direction parallel to graphene layers was higher than in perpendicular direction due to the preferential orientation of graphene in composites. Arrangement of graphene layers in parallel direction creates more conductive paths and also intrinsic anisotropy of electrical conductivity of graphene itself resulted in higher values of electrical conductivity of composites than in perpendicular direction. The highest value 12496 S/m was obtained in parallel direction for sample with 10 wt. % of GNPs after annealing. Post-sintering annealing has no significant influence on electrical conductivity of samples.

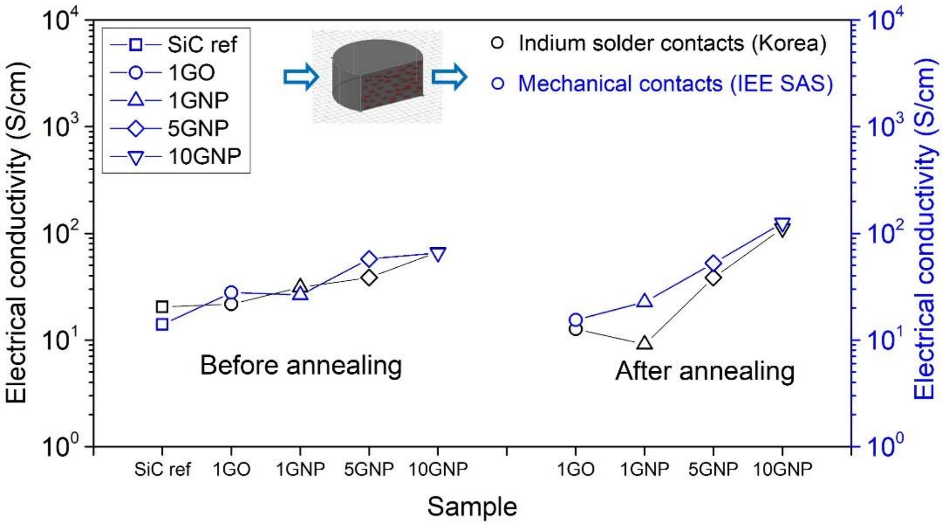

Fig. 1. Electrical conductivity of SiC-graphene composites in parallel direction to graphene layers before and after annealing.

Thermal diffusivity of SiC-graphene composites was investigated as a function of amount of graphene, its orientation in matrix and effect of annealing. After addition of graphene thermal diffusivity measured in direction perpendicular to graphene layers decreased up to 33.4 mm^2/s (for sample with 10 wt. % of GNPs without annealing). There are several reasons for this behaviour like higher porosity (around 3 %), preferential orientation of graphene – more boundaries between matrix and graphene in this measurement direction, smaller grain size – higher amount of graphene (10 wt. %) effectively hinders grain growth even during annealing. The resulting decrease in thermal diffusivity of SiC-graphene samples measured in perpendicular direction to graphene layers indicates that phonon-pores, phonon-defects and phonon-bondaries scattering as well as intrinsic thermal conductivity of graphene layers in perpendicular direction play a dominant role in influencing of thermal diffusivity of composites. After addition of graphene thermal diffusivity measured in direction parallel to graphene layers increases significantly up to 104.4 mm^2/s for sample with 5 wt. % of graphene after annealing. This indicates that graphene layers in parallel direction could be effective in formation of conductive phonon channels, moreover annealing of sample leads to increasing of grain size, decreasing of lattice oxygen, healing defects in graphene layers. Beneficial influence of post sintering annealing in all cases was confirmed.

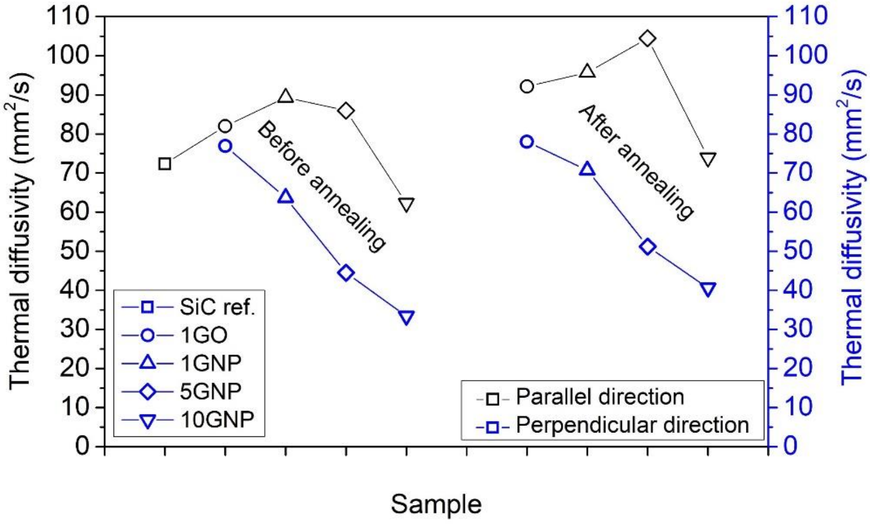

Fig. 2. Comparison of thermal diffusivity at RT in parallel and perpendicular direction

CONCLUSION

$SiC-Y_2O_3-Sc_2O_3$ composites with addition of either GNPs or GO were succesfully prepared. Almost fully dense composites were prepared by RHP even at high loading of GNPs (RD were higher than 97 %). The thermal diffusivity of sample with 5 wt.% of GNPs in parallel direction to graphene layers remarkably increased after annealing to 104.4 mm^2/s from value 72.3 mm^2/s measured for the reference sample (without addition of graphene and annealing). At the same time the electrical conductivity increased from 1400 S/m (for reference sample) to 9402 S/m for composite with 5 wt. % of GNPs.

ACKNOWLEDGMENT

This work was supported by the Slovak Research and Development Agency project no. APVV-15-0540 (Assessment of secondary raw materials for the preparation of materials used in extreme conditions) and project CERANEA (Multifunctional Ceramic/Graphene Coatings for New Emerging Applications).

REFERENCES

[1] Kleebe, H. J. SiC and Si3N4 materials with improved fracture resistance, J. Eur.Ceram. Soc., 10 (1992) 151–159.

[2] Sciti, D., Bellosi, A. Effects of additives on densification, microstructure andproperties of liquid-phase sintered silicon carbide, J. Mater. Sci., 35 (2000) 3849–3855.

[3] Biswas, K., Rixecker, G., Aldinger, F. Improved high temperature properties of SiC-ceramics sintered with Lu2O3-containing additives, J. Eur. Ceram. Soc., 23 (2003) 1099–1104.

[4] Strecker, K., Hoffmann, M. J. Effect of AlN-content on the microstructure and fracture toughness of hot-pressed and heat-treated LPS-SiC ceramics, J. Eur.Ceram. Soc., 25 (2005) 801–807.

[5] Balog, M., Šajgalík, P., Hnatko, M., Lenčéš, Z., Monteverde, F., Keckes, J., Huang, J.L. Nano-versus macro-hardness of liquid phase sintered SiC, J. Eur. Ceram. Soc., 25 (2005) 529–534.

[6] Kaur, S., Riedel, R., Ionescu, E. Pressureless fabrication of dense monolithic SiC ceramics from a polycarbosilane, J. Eur. Ceram. Soc., 34 (2014) 3571–3578.

[7] Kim, K. J., Lim, K. Y., Kim, Y. W. Electrical and thermal properties of SiC ceramics sintered with yttria and nitrides, J. Am. Ceram. Soc., 97 (2014) 2943–2949.

[8] Prasher, R. Graphene spreads the heat. Materials Science, 328 (2010) 185-186.

[9] Balandin, A. A. Thermal properties of graphene and nanostructured carbon materials. Nature materials, 10 (2011) 569-581.

[10] Ghosh, S., Calizo, I., Teweldebrhan, D., Pokatilov, E. P., Nika, D. L., Balandin, A. A., Bao, W., Miao, F., Lau, C. N. Extremely high thermal conductivity of graphene: Prospects for thermal management applications in nanoelectronic circuits. Applied Physics Letters, 92 (2008) 151911-1-3.

[11] Chen, J., Jang, C., Xiao, S., Ishigami, M., Fuhre, M. S. Electronic properties and devices: intrinsic and extrinsic performance limits of graphene devices on SiO2.
Nature Nanotechnology, 3 (2008) 206–209.

[12] Ogihara, S., Maeda, K., Yakeda, Y., Nakamura, K. Effect of impurity and carrier concentrations on electrical resistivity and thermal conductivity of SiC ceramics containing BeO, J. Am. Ceram. Soc., 68 (1985) C16–C18.

[13] Liu, D. M., Lin, B. W. Thermal conductivity in hot-pressed silicon carbide, Ceram. Int., 22 (1996) 407–414.

[14] Volz, E., Roosen, A., Hartung, W., Winnacker, A. Electrical and thermal conductivity of liquid phase sintered SiC, J. Eur. Ceram. Soc., 21 (2001) 2089–2093.

[15] Kim, Y. W., Lim, K. Y., Seo, W. S. Microstructure and thermal conductivity of silicon carbide with Yttria and Scandia. J. Am. Ceram. Soc., 97 (2014) 923-928.

Ce^{3+} DOPED YTTRIA NANOPOWDERS FOR TRANSPARENT YTTRIA CERAMICS PREPARED BY PRECIPITATION METHOD

Nibu Putenpurayil Govindan, Monika Michálková, Dušan Galusek

Centre for functional and surface functionalized glass, Alexander Dubcek University of Trencin, Studentska 2, 91150 Trencin, Slovak Republic

ABSTRACT

In optics, transparency is the physical property of materials allowing light pass through it without being scattered. Transparent polycrystalline ceramic (TPC) materials have attracted a significant attention as candidates for various applications, including laser gain media in solid state lasers, electro-optical devices and scintillators. Yttria (Y_2O_3) is widely known as a promising optical material owing to its broad range transparency, high melting temperature (2430 ^oC), outstanding refractoriness and excellent chemical stability. Therefore, polycrystalline transparent yttria ceramics have been exploited as perfect candidate to replace single crystals in various applications, including transparent windows, missile domes, bulb envelopes and laser host. Our results report on preparation of Ce^{3+} doped Y_2O_3 nanopowders by precipitation method using ammonium hydroxide as precipitation agent. The influence of precipitation agent and concentration of reactants, morphology, particle size and degree of agglomeration was evaluated. Partly agglomerated powders with the primary size of Y_2O_3 nanoparticles ~200 nm with cubic crystal structure were prepared. The optimum concentration of ammonia precipitation agent was found to be 0.5 M. Ultrasonic de-agglomeration of the powder was most efficient if the pH value was adjusted to 11 through addition of NH_4OH water. Stabilisation of the suspension was reached by the addition of Dolapix CE64 or Darvan CN. The green compact prepared by vacuum-pressure filtration method has the relative density about 43 %.

Keywords: Y_2O_3, Transparent ceramics, Zeta potential

INTRODUCTION

Transparent ceramics are attractive optical materials that offer many advantages over single crystals, including greater shape control, higher homogeneity of the dopant, and faster and lower cost fabrication methods. The field of transparent ceramics starts in1960'swiththe development of translucent Al_2O_3 for lighting applications [1–3], and slowly expanded into other areas including transparent arm [4], lasers [5,6], and scintillators [7]. To date, various transparent ceramics with high purity and high density have been produced, including simple oxides such as MgO, Y_2O_3, and ZnO, composite or complex oxides such as ZrO_2–Y_2O_3, $Y_3Al_5O_{12}$, spinel ($MgAl_2O_4$), and AlN, for applications in solid-state lasers, electro-optical devices, X-ray scintillators, and thermally conductive components [8–10]. Among transparent ceramic materials yttria ceramics has been developed for applications in e.g. solid state lasers. Y_2O_3 transparent ceramics are also very efficient NIR-visible up-converters, and can be used as materials for X-ray scintillator applications [11]. Our results report on preparation of $Y_{1.99}Ce_{0.01}O_3$ nanopowders by precipitation method using ammonium hydroxide as precipitation agent. The concentration of reactants, morphology, particle size and degree of agglomeration was evaluated.

EXPERIMENTAL PART

The aqueous nitrate solution of Y^{3+} was prepared by dissolving yttria powders (99.99 %,) in diluted nitric acid (HNO_3) and deionized water under stirring and heating, then diluted into 0.1 M with deionized water. The solution of Ce^{3+} was prepared by dissolving cerium nitrate (99.99 %,) in deionized water then diluted into 0.1M with deionized water. The mixed metal nitrate solution was dripped into a 0.5 M ammonium solution, under continuous rapid stirring, ensuring there was sufficiently high excess of ammonia to eliminate any pH fluctuations throughout the process. The mixed metal nitrate solution was added with the use of peristaltic pump at 5.0 ml/min, completing the reaction in 24 h. The mixed solution turned to opaque white slurry. After 12 h aging the slurry was vacuum filtered through filter paper and the resulting white precipitate washed with distilled water. The washed precipitate was dried overnight in air at 100°C. The dried precipitate was crushed and ground in an agate mortar and pestle, and calcined in air for 3 h at 700 °C (heating rate 10°C/min). Ultrasonication (20 kHz) was then used to de-agglomerate the nanopowder, using calculated amounts of Y_2O_3 powder and ammonium solution to adjust the pH value of the suspension, and using Commercial dispersants Dolapix CE 64 (Zauba, Austria) or Darvan CN (Vanderbilt Minerals, Germany). Ultrasonication was applied in order to de-agglomerate the suspension. After sonication particle size, distribution and Zeta potatioal were determined as a function of pH and sonication time using particle size analyser (Brookhaven 90Plus BI-Zeta). Green compacts were prepared by pressure filtration of the ultrasonically de-agglomerated stabilized yttria suspension. The pressure filtration was performed in special die with the diameter of 15 mm. The suspension (20 wt. % solid loading) was poured into the die and after closing the mould, pressure 20 bar was applied through a hydraulic press. The water from the suspension was drained through massive perforated metal bottom with polymeric membrane (pore size 0.2 μm).

CHARACTERIZATION OF POWDERS

Crystallization temperatures of the pre-calcined powders were determined by differential scanning calorimetry combined with and thermogravimetry (Netzsch STA 449 F1 Jupiter TG / DTA / DSC). Powder X-ray diffraction (XRD) patterns were acquired using powder X-ray diffractometer (Panalytical Empyrean DY1098). The Scherrer equation was used to the size of coherently diffracting domains, which in ideal case can be identified as the primary size of individual particles. The Scherrer equation can be written as:

$$D = \frac{K\lambda}{\beta cos\theta}$$

Particle size distributions and particle morphologies were determined through scanning electron microscope (JEOL JSM-7600 F / EDS / WDS / EBSD)

RESULTS AND DISCUSSION

Thermal behaviour of yttria precipitate

Figure 1 presents results of DTA and related TG analysis of prepared [$Y_2(NO_3)_3 \cdot xY(OH)_3 \cdot yH_2O$] precipitate. First broad endothermic peak up to 200 °C is related to dehydration of free and physically absorbed molecular water. Similarly as it is in [12, 13] dehydration of chemisorbed and combined water from $Y(OH)_3$ and α-$Y(OH)_3$ represents the endothermic peak at 350°C. The dehydration of structural water from YOOH phase occurs at around 450°C which confirms DTA data – at this temperature weak endothermic peak can be found [13, 14]. Because of HNO_3 presence during dissolving of yttria the basic yttrium hydroxy-nitrate complex [$Y_2(NO_3)_3 \cdot xY(OH)_3 \cdot yH_2O$] is formed. Decomposition of such a complexes takes place about 530 °C and this temperature is also related to the beginning of the yttrium oxide crystallization [12,15].Consequently, according to TG/ DTA decomposition of prepared yttria precursor is completed at 600 °C and with further increasing of the temperature no exo- nor endothermic effect can be detected.

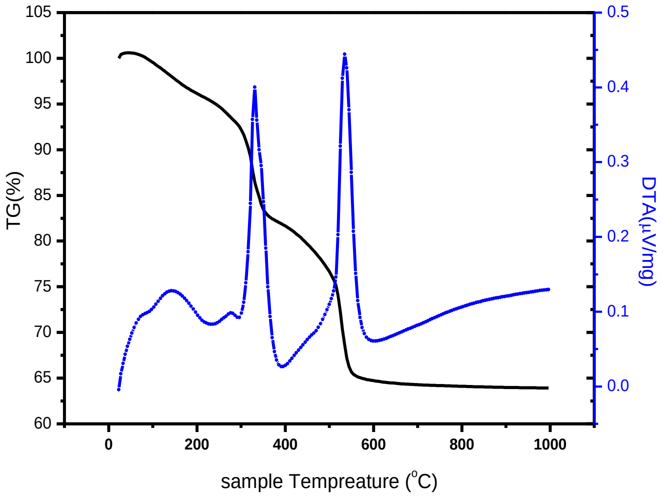

Fig.1. DTA/TGA data for the precipitated hydroxide precursor

XRD analysis: determination of phase composition.

Figure 2. shows the XRD patterns of Y_2O_3 powder calcined at 700°C. As shown in the figure, the pure cubic Y_2O_3 phase was obtained with good crystallinity and the primary particle size of approximately 50nm, as determined from the Scherer equation.

Microstructure analysis

Figure 3. shows the SEM micrograph of synthesised Y_2O_3 powder. The powder is agglomerated with the primary particle size of approximately 55 nm, which is in good accord with the X-ray diffraction data.

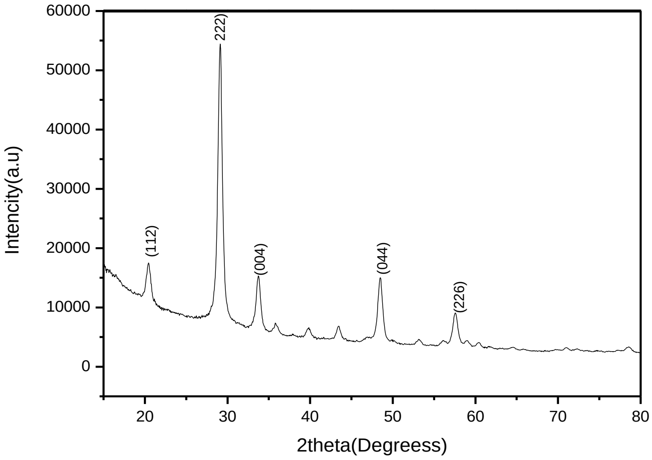

Fig 2. XRD pattern of prepared Y_2O_3 powder calcined at 700 °C

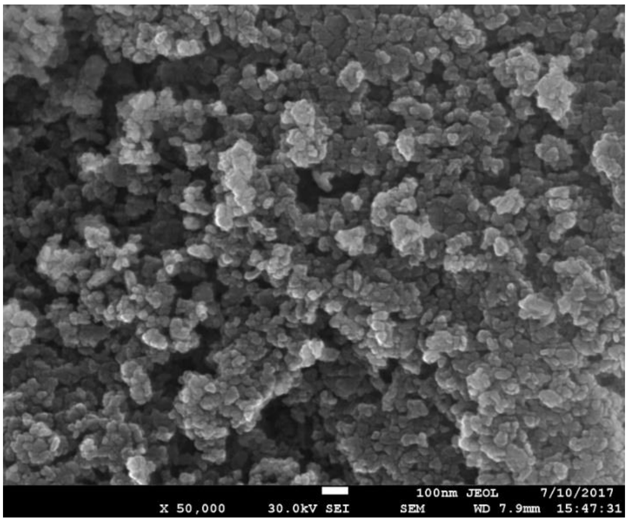

Fig 3. SEM micrograph of the prepared Y_2O_3 powder

Particle size distribution

Figure 4.summarizes the changes in particle size of yttria powder with the sonication time. Extension of the ultrasonication time results in significant reduction of both the mean size of powder particles, and the width of the particle size distribution, indicating de-agglomeration of the yttria powder. The error bar on graph represents the particle size distribution at different time interval. As can be seen particle size distribution narrows with the increasing of the sonication time. The best results were achieved after 32 minutes sonication time. However, the mean size of 200 nm clearly shows that the powder was not de-agglomerated down to primary particle size, and hard agglomerates with the diameter of about 200 nm are still present.

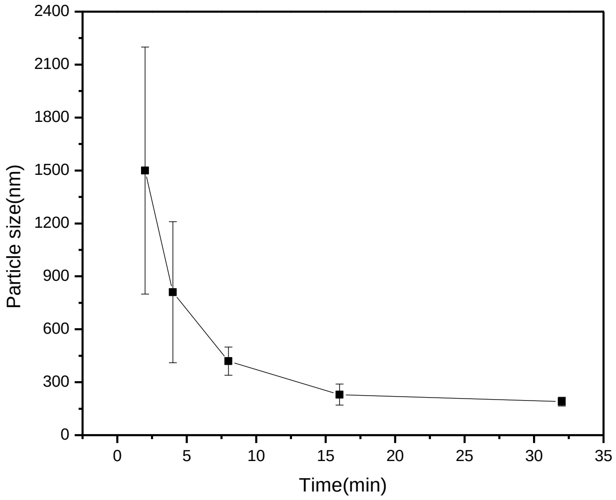

Fig 4.The change of particle size of the Y_2O_3 powder with the sonication time

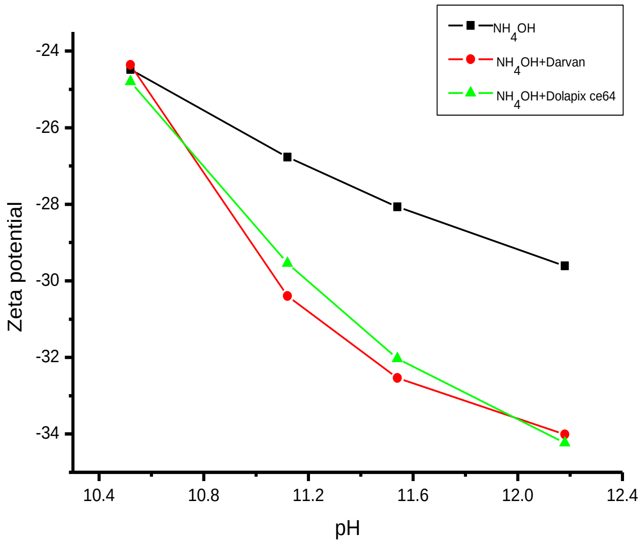

Fig.5.The results of Zeta potential measurements of yttria suspensions with different dispersants

Zeta potential and stability of suspension

The zeta potential of Y_2O_3 as function of pH is indicated in Fig. 5. Two different dispersants were used with the concentration of 2.0 wt. %: (Dolapix CE 64 and Darvan CN). Accocrding to literature the stability of the particles occurs zeta potential more than -30 mV [16]. The ammonia-water based Y_2O_3 suspension without dispersant shows zeta potential indicative values up to almost -30 mV. Yet, when the dispersant was used zeta-potential of the suspension reaches a maximum of ~35 mV. Both of the dispersant show similar values of zeta-potential in tested pH area; however, sedimentation rate of yttria suspension using Dolapix CE64 is lower when compared to Darvan CN [17], therefore Dolapix CE64 was selected for further experiments. Green compacts prepared by vacuum-pressure filtration out of yttria suspension stabilized with Dolapix CE64 reach relative density 43 %.

CONCLUSION

$Y_{1.99}Ce_{0.01}O_3$ nanopowder was synthesized via precipitation method. Partly agglomerated powders with the primary size of nanoparticles 55 nm and with cubic crystal structure were prepared. Ultra-sonication of yttria suspension de-agglomerated the particles to the mean size of 200 nm. Stabilization of the yttria suspension was reached in ammonia based water suspension with the addition of Dolapix CE64 as a dispersant. The green compact prepared by vacuum-pressure filtration method has the relative density about 43 %.

ACKNOWLEDGMENT

This paper is a part of dissemination activities of VEGA 2/0026/17, SAS-MOST 2015-06 and FunGlass. This project has received funding from the European Union´s Horizon 2020 research and innovation programme under grant agreement No 739566.

REFERENCES

[1] R.L. Coble. Transparent Alumina , US Patent 3,026,210. Mar. 20; (1962)

[2] R.L. Coble, J. Appl. Phys. 32 (1961) 787.

[3] G.C. Wei, J. Phys. D: Appl. Phys. 38 (2005) 3057.

[4] P.J. Patel, G.A. Gilde, P.G. Dehmer, J.W. McCauley, Proc. Soc. Photo-Opt. Instrum. Eng. 4102 (2000) 1.

[5] V. Lupei, A. Lupei, A. Ikesue, Opt. Mater. 30 (2008) 1781.

[6] J. Li, Y. Pan, Y. Zeng, W. Liu, B. Jiang, J. Guo, Journal Refract. Metals Hard Mater. 39 (2013) 44.

[7] C. Greskovich, S. Duclos, Annu. Rev. Mater. Sci. 27 (1997) 69.

[8] A.Ikesue,T.Kinoshita ,K.Kamata Journal American Ceramic Society, 78, 1033-1040 (1995).

[9] G.D .Miles, R.A.J. Sambell, J .Rutherfo, G.W. Stephens, Journal British Ceramic Society, 66,319 (1967)

[10] R.W.Rice, Journal of the American Ceramic Society, 54,205–207 (1971)

[11] C.Greskovich, M.J. Curran, C.R.Oclair. Journal American Ceramic Society ,55,324–325 (1972)

[12] H. Gong, T. Ding-Yuan, H. Hui, Z. Tian-Shu, M. Journal of Effect Mater. Chem. Phys, 112, 423426,(2008)

[13] M. Aghazadeh, A. Nozad, H. Adelkhani, and M. Ghaemi, Journal of the Electrochemical Society, vol. 157, no. 10, pp. D519–D522, (2010).

[14] R. Srinivasan, N. R. Yogamalar, J. Elanchezhiyan, R. J. Joseyphus, and A. C. Bose, Journal of Alloys and Compounds, vol. 496, no. 1-2, pp. 472–477,(2010).

[15] L. Muresan, E. J. Popovici, R. Grecu, and L. B. Tudoran, . Journal of Alloys and Compounds, vol. 471, no. 1-2, pp. 421–427,(2009)

[16] D.C.Grahame, *Chemical Review*, 41,441-451 **(**1987).

[17] Lingling Jin, Xiaojian Mao, Shiwei . Ceramics International 35 (2009) 925–927.

LUMINISCENCIA Er^{3+}/Yb^{3+} DOPOVANEJ ZIRKONIČITANOVEJ KERAMIKY INDUKOVANÁ UP-KONVERZIOU ŽIARENIA

UP-CONVERSION INDUCED LUMINESCENCE IN Er^{3+}/Yb^{3+} CO-DOPED ZIRCONATE CERAMICS

E. Trusova[1,2], R. Klement[3], Ľ. Bača[2], K. Podbolotov[4], P. Veteška[2], A.Gatial[2], Y. Halahovets[5], M. Janek[2,6]

[1]*Belarusian State Technological University, Minsk, Belarus*

[2]*Slovak University of Technology, Bratislava, Slovakia*

[3] *Centre for functional and surface functionalized glasses at the Alexander Dubček University of Trenčín, Trenčín, Slovakia*

[4]*The Physical-Technical Institute of the National Academy of Sciences of Belarus, Minsk*

[5]*Institute of Physics, Slovak Academy of Sciences, Bratislava, Slovakia*

[6]*Faculty of Natural Sciences, Comenius University, Bratislava, Slovakia*

ABSTRACT

Er^{3+}/Yb^{3+} co-doped lanthanum zirconate ceramics have been prepared using the solvo-chemical synthesis. The reflections on the XRD patterns indicate on the formation of cubic $La_2Zr_2O_7$ phase. Effects of Er^{3+}/Yb^{3+} ratio and temperature effect on up-conversion luminescent properties of the ceramic materials prepared were studied. It was found that the best up-conversion efficiency was achieved for the materials sintered at temperatures above 1400°C. RGB colour coordinates indicated that average emitted colour induced by up-conversion changed in the range of green to yellow emission, from ~550 nm towards 565 nm with increasing Er^{3+} content.

Keywords: zirconate ceramics, rare earths doping, up-conversion, luminescence.

INTRODUCTION

Up-converted luminescence (UCL) is well known as a nonlinear optical process involving the absorption of several excitation photons, usually in the IR spectral region resulting in resonant non-radiative energy transfer [1]. The emission is followed by a single photon with a shorter wavelength in the visible or ultraviolet spectral regions. This behaviour is a typical intrinsic property of trivalent rare-earth ions, such as erbium, thulium, holmium etc., that have a complex structure of electronic energy states and can produce visible green, red, blue etc. emissions under IR-excitation [2]. UCL in rare-earth doped systems has great interests due of its broad applications for phosphors, diode and visible lasers, display devises, solar cell, as labels of biomolecules etc. [3–7]. Among different host matrix like single crystals, nanoparticles, glass and glass ceramics [8–11] up-converting materials based on crystalline ceramics with pyrochlore/fluorite structure can be prospective matrix for efficient up-conversion. Among wide range of pyroclores, $La_2Zr_2O_7$ based materials are employed in a variety of different applications thanks their interesting thermal and catalytic properties [12–14]. However, according to best knowledge an up-conversion luminescence phosphors based $La_2Zr_2O_7$ matrix have not been reported yet. Therefore the current work is aimed on developing of optically active zirconate ceramics with expected compositions $(Er_xYb_y)La_2Zr_2O_7$ as perspective and efficient materials for diode lasers, display devices, detectors and other photonic applications with excitation in the near infrared region.

EXPERIMENTAL

For the synthesis of lantanium zirconate ceramics the solvo-chemical procedure was used. This involves gel formation using $Ln(NO_3)_3{\cdot}xH_2O$ (Ln = La, Er, Yb) and zirconyl nitrate from starting solutions. Prepared gel was dried, calcined in air at 800°C/4h, ground and pressed into discs of less than 1 mm thickness. The discs were fired in an electric furnace using heating ramp of 10 °C/min up to 1100–1500 °C with annealing time of 3 h. Depending on the erbium oxide concentration and the presence of ytterbium oxide, the samples have been labelled $(Er_xYb_{0.02})$LZ (x = 0.01; 0.02; 0.05; 0.10). X-ray diffraction (XRD) measurements were done using STOE Theta/Theta diffractometer equipped with CoKα radiation source. Diffraction angles were set in the range from 10 ° to 100 ° with a step width 0.020°. The density of samples was measured by the Archimedes's method using distilled water as liquid. The infrared-to-visible luminescence was studied under 980 nm laser excitation (adjustable DPSSL Laser MDL-W 4W) and UV-VIS spectrometer (Ocean Optics USB4000. The up-conversion emission was collected by the UV-VIS spectrometer in reflection mode, perpendicular to the sample and in angular direction of 30° to normal incident laser beam.

The CIE chromaticity coordinates (x, y) values for studied samples were calculated from corrected photo-luminescence emission spectra.

RESULTS

XRD patterns of $Er_{0.01}Yb_{0.02}$ ceramics obtained at 1100–1500 °C are present on Fig.1. It can be observed that all diffraction peaks are in good agreement with the formation of single phase of $La_2Zr_2O_7$. With the increase of the temperature, the intensity of the peaks becomes stronger, indicating a better crystallization that correlates well with density of ceramics (density of the ceramics slightly increased with temperature in the range of 4.5–5.5 g/cm^3) and the results of Raman spectroscopy. Fig. 2 presents the XRD patterns of $Er_xYb_{0.02}$LZ ceramics obtained at 1400 °C/3h. All diffraction peaks are similar and exhibit a single phase of $La_2Zr_2O_7$.

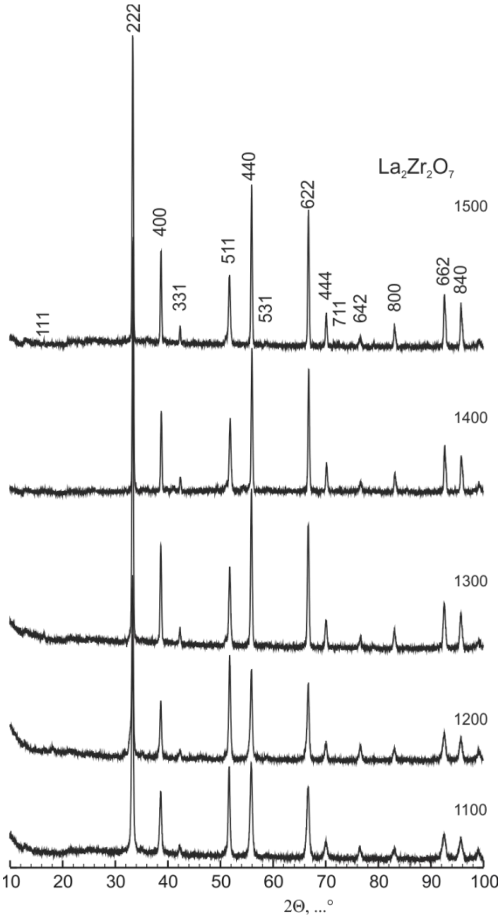

Fig. 1. XRD patterns for $Er_{0.01}Yb_{0.02}LZ$ ceramics obtained at different temperatures (indicated)

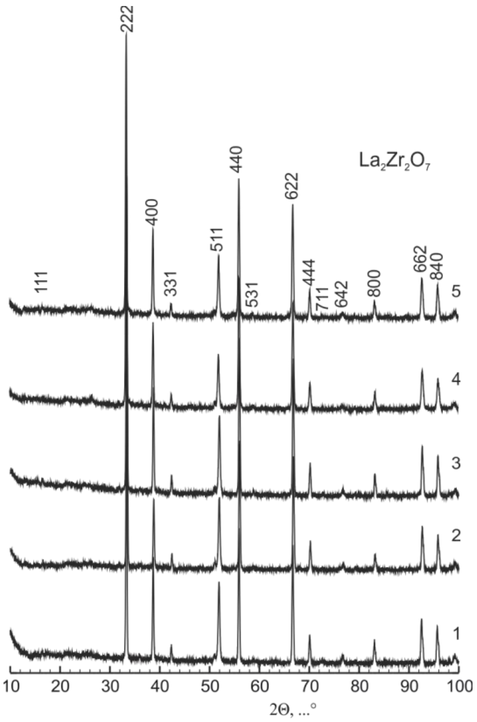

Fig. 2. XRD patterns for LZ (1); $Er_{0.01}Yb_{0.02}LZ$ (2); $Er_{0.02}Yb_{0.02}LZ$ (2); $Er_{0.05}Yb_{0.02}LZ$ (4) $Er_{0.1}Yb_{0.02}LZ$ (5)

The UCL spectra of lanthanum zirconate ceramics prepared at various temperatures are shown in Fig. 3 for samples with different Er^{3+}/Yb^{3+} ratios. For all samples, the emission in the green region at 525 nm and 545 nm is related to the $^{2}H_{11/2}\rightarrow{}^{4}I_{15/2}$ and $^{4}S_{3/2}\rightarrow{}^{4}I_{15/2}$ transition of Er^{3+} ions respectively [10, 15].

Red emission in the 655–680 nm range is related to the $^{4}F_{9/2}\rightarrow{}^{4}I_{15/2}$ transition of Er^{3+} [10, 15]. With the increase of temperature, UCL intensity increase for the green region and for the red region in the case $Er_{0.1}Yb_{0.02}LZ$. The heat-treatment of ceramics induces structuring of the UCL spectra, confirming the fact that Er^{3+} ions enter the crystalline phase. The UCL intensity $Er_{x}Yb_{0.02}LZ$ ceramics obtained at 1400 °C was integrated over the emission bands (green and red) and listed in table 1. To evaluate the ceramics performance on colour UCL emission, CIE chromaticity coordinates were evaluated (table 1).

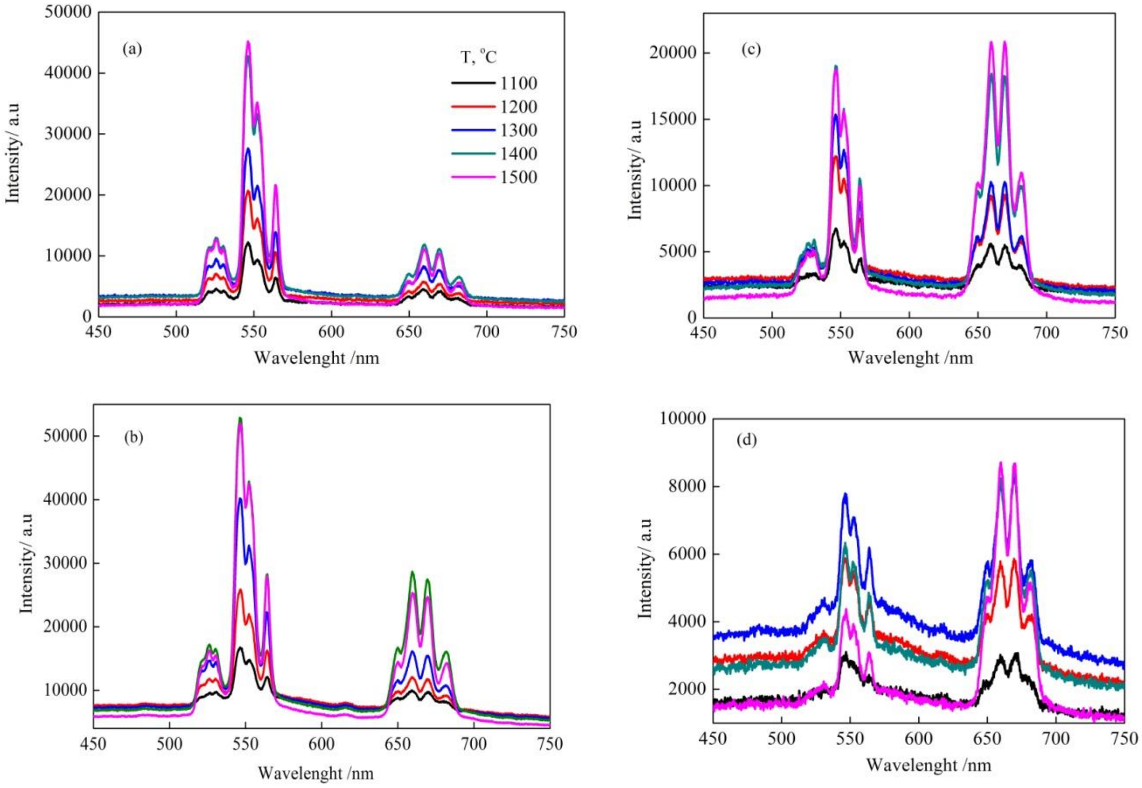

Fig. 3. Evolution UCL spectrum $Er_xYb_{0.02}LZ$ with the firing temperature: a) $Er_{0.01}Yb_{0.02}LZ$; b) $Er_{0.02}Yb_{0.02}LZ$; c) $Er_{0.05}Yb_{0.02}LZ$; d) $Er_{0.1}Yb_{0.02}LZ$

Table 1: Calculated G/R or R/G integrated intensity ratios and colour coordinates (CIE 1931)

Samples	G/R ratio	R/G ratio	Colour coordinates (x, y),	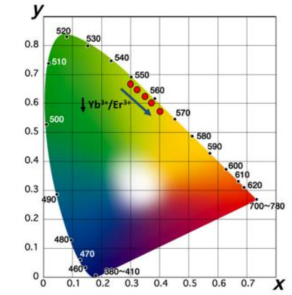
$Er_{0.01}Yb_{0.02}LZ$	2.983	0.335	(0.301, 0.685)	
$Er_{0.02}Yb_{0.02}LZ$	1.439	0.695	(0.324, 0.663)	
$Er_{0.05}Yb_{0.02}LZ$	0.646	1.548	(0.360, 0.629)	
$Er_{0.1}Yb_{0.02}LZ$	0.464	2.157	(0.382, 0.608)	

It can be observed that the increase of the Er^{3+} content in obtained ceramics results in the proportional increase of red emission. However, for all samples green emission are dominated.

CONCLUSION

Lantanium zirconate ceramics materials with varying Er^{3+}/Yb^{3+} rations and up-converting properties was successfully produced using solvo-chemical synthesis. The optimal ceramics sintering condition for best luminescence intensities observed were achieved for 1400°C/3h treatment. XRD patterns indicated the formation of pure $La_2Zr_2O_7$ phase. Simultaneous presence of the green and red emission bands in the luminescence spectra makes the lantanium zirconate structure attractive as up-converting phosphor materials.

ACKNOWLEDGMENT

The authors acknowledge financial support by the National Scholarship Programme of the Slovak Republic supporting the study stay of Assoc. prof. Dr. E. Trusova at the Department of Inorganic Materials, Faculty of Chemical and Food Technology, Slovak University of Technology (ID 20693). The financial support of the Slovak Grant Agency for Science VEGA No. 1/0906/17 is greatly appreciated. This work creation enabled also the project «Center for Applied Research of New Materials and Technology Transfer», ITMS 26240220088, supported by the Science and Research Operational Program by the European Regional Development Fund.

REFERENCES

[1] Azuel F.E. Materials and Devices with Using Double-Pumped Phosphon Energy Transfer. Proc. IEEE 61(6) (1973) 758–786.

[2] Chen Sh., Wang W., Wang K., Molokeev M.S., Mei L., Huang Zh. Crystal structure characterization and up-conversion luminescent properties of $BaIn_2O_4$ phosphor. Journal of Luminescence 192 (2017) 218–223.

[3] Jovanović D. J., Gavrilović T. V., Dolić S. D., Marinović-Cincović M., Smits K., Dramićanin M. D. Up-conversion luminescence of $GdVO_4$:Nd^{3+}/Er^{3+} and $GdVO_4$:Nd^{3+}/Ho^{3+} phosphors under 808 nm excitation. Optical Materials 82 (2018) 1–6.

[4] Heumann E., Bär S., Rademaker K., Huber G., Butterworth S., Diening A., Seelert W., Semiconductor-laser-pumped high-power upconversion laser. Appl. Phys. Lett. 88 (2006) 061108.

[5] Soni A. K., Rai V. K. Upconversion luminescence in $BaMoO_4$:Pr^{3+} phosphor for display devices AIP Conference Proceedings 1675 (2015) 030073.

[6] Qu B., Jiao Y., He Sh., Zhu Y., Liu P., Sun J., Lu J., Zhan X. Enhanced energy conversion of up-conversion solar cells by the integration of compound parabolic concentrating optics Solar Energy Materials & Solar Cells 140 (2015) 217–223.

[7] Pominova D.V., Ryabova A.V., Linkov K.G., Romanishkin I.D., Kuznetsov S.V., Rozhnova J.A., Konov V.I., Loschenov V.B. Pulsed periodic laser excitation of upconversion luminescence for deep biotissue visualization. Laser Physics 26 (2016) 084001.

[8] Zhao J., Jin D., Schartner E. P., Lu Y., Liu Y., Zvyagin A. V., Zhang L., Dawes J. M., Xi P. Piper J. A. Single-nanocrystal sensitivity achieved by enhanced upconversion luminescence. Nature nanotechnology 8 (2013) 729-734.

[9] Balabhadra S., Debasu M. L., Brites C. D.S., Ferreira R. A.S, Carlos L. D.Radiation-to-heat conversion efficiency in SrF2:Yb^{3+}/Er^{3+} upconverting nanoparticlesOptical Materials. 83 (2018) 1–6.

[10] Dymshits O.S., Loiko P.A., Skoptsov N.A., Malyarevich A.M., Yumashev K.V., Zhilin A.A., Alekseeva I.P., Tsenter M.Ya., Bogdanov K .Structure and upconversion luminescence of transparent glass-ceramics containing $(Er,Yb)_2(Ti,Zr)_2O_7$ nanocrystals. Journal of Non-Crystalline Solids 409 (2015) 54–62.

[11] Arzumanyan G., Vartic V., Kuklin A., Soloviov D., Rachkovskaya G., Zacharevich G., Trusova E., Skoptsov N., Yumashev K. Upconversion luminescence of Er^{3+} and co-doped

Er^{3+}/Yb^{3+} novel transparent oxyfluoride glasses and glass ceramics: spectral and structural properties. Journal of Physical Science and Application 4 (2014) 150–158.

[12] Lang M., Zhang F., Zhang J., Wang J., Lian J., Weber W. J., Schuster B., Trautmann C. Neumann R., Ewinga R. C. Review of $A_2B_2O_7$ pyrochlore response to irradiation and pressure Nuclear Instruments and Methods in Physics Research. B 268 (2010) 2951–2959.

[13] Wanga X., Zhu Y., Du L., Zhang W. The study on porosity and thermophysical properties of nanostructured $La_2Zr_2O_7$ coatings. Applied Surface Science 257 (2011) 8945–8949.

[14] Mohapatra M., Rajeswari B., Hon N.S., Kadam R.M., Natarajan V. Photoluminescence properties of 'red' emitting $La_2Zr_2O_7$:Eu pyrochlore ceramics for potential phosphor application. Journal of Luminescence 166 (2015) 1–7.

[15] Singh B. P., Parchur A. K., Singh R. K., Ansari A. A., Singh P., Rai S. B. Structural and up-conversion properties of Er^{3+} and Yb^{3+} co-doped $Y_2Ti_2O_7$ phosphors: Phys. Chem. Chem. Phys. 15 (2013) 3480–3489.

PREPARATION AND STUDY OF MICROSTRUCTURE OF YTTRIA AND CERIA STABILIZED TETRAGONAL ZIRCONIA POLYCRYSTALS FOR DENTAL APPLICATIONS

A. Nowicka [1], H. F. El-Maghraby [2], D. Galusková [1], D. Galusek [1]

[1] *FunGlass, Alexander Dubček University of Trenčín, Študentská 2, 911 50 Trenčín, Slovakia*

[2] *Dpt. VILA – Join Glass Centre of the IIC SAS, TnUAD, FChPT STU, Študentská 2, 911 50 Trenčín, Slovakia*

FunGlass, A. Dubček University of Trenčín, Študentská 2, 911 50 Trenčín, Slovakia

ABSTRACT

The overall aim of this work was the preparation of two different zirconia ceramics material stabilized in their tetragonal form by 3mol% of Yttria (3Y-TZP) and 12mol% of Cerria (12Ce-TZP), study the different sintering paramaters and their influence of the phase transformation, density and microstructure. 3Y-TZP and 12Ce-TZP powders after freeze granulation an freeze drying by 48h were subjected for unaxial pressing with pressure of 50MPa and then for Cold Isostatic pressing with pressure of 350MPa. Prepared materials were sintered in four different temperatures 1300°C, 1400°C, 1450°C and 1500°C with the dwell time 2h. After sintering the phase and microstructure analysis were carried out. The aim of the experiments is to select the best sintering method in order to obtain the finest microstructure of prepared Y-TZP and Ce-TZP ceramics and to evaluate their resistance for Low Temperature Degradation (LTD) and corrosion tests in acetic environment.

Keywords: Y-TZP, Ce-TZP, microstructure, sintering

INTRODUCTION

The excellent mechanical properties of zirconia-based materials combined with their superior aesthetics and biocompatibility characteristics have encouraged their application as bioceramics, particularly in the dental field. Yttria stabilized zirconia ceramics (Y-TZP) compared to other bio ceramics is characterized by its superior flexural strength and high fracture toughness, thus becoming very interesting materials for dental applications. In addition, it can be accurately processed to complex geometries using CAD-CAM Technologies or low pressure-injection moulding. However, this ceramic can undergo Low Temperature Degradation (LTD) which refers to a spontaneous zirconia phase transformation from the metastable tetragonal (t) phase to the stable monoclinic (m) [1] that can cause micro-cracking, loss of strength, roughness increase and the device destruction. [2]. For this reason, research focused on ceria-stabilized zirconia (Ce-TZP) is gaining a lot of interest. Our latest studies on two commercial Y-TZP dental ceramics and Ce-TZP ceramics prepared by MATEIS laboratory of Insa Lyon have shown that Ce-TZP is the most resistant for LTD. However, in the case of Y-TZP we have subjected two materials with similar composition but with different microstructure. Y-TZP ceramics with the finest grain-size was much less vulnerable for LTD. The presence of grain size bigger than 0.1 μm will make the zirconia microstructure more sensitive to LTD. It is very necessary to find out the rules controlling the grain size, phase content and sintered density. Low density, especially the presence of open porosity, offers to water molecules an easy access to the bulk of the material [3].

The aim of this our study is to select the best sintering method in order to obtain the finest microstructure of prepared 3Y-TZP and 12Ce-TZP ceramics. Our next step will be the evaluation of their resistance for Low Temperature Degradation (LTD) and corrosion tests in acidic environment.

EXPERIMENTAL

Powders using in this experiment, 3 mol% Yttria stabilized zirconia and 12 mol% Cerria stabilized zirconia were prepared using hydrothermal technique. The precursors were zirconium oxychloride ($ZrOCl2·8H2O$), 96% BDH Chemicals Ltd, England; Yttrium oxide ($Y2O3$), 99.9%, Fluka AG; Cerium (III) chloride hydrate ($CeCl3·8H2O$), Sigma Chemicals Co. 3Y-TZP and 12Ce-TZP powders after being freeze granulate and freeze dried were pressed unaxialy (p=50 MPa) into disc compacts and then Cold Isostatic Pressed with pressure of 350MPa, dwell time: 3min, drain time: 50s and the slow decompression. Such prepared materials were burning out in T1 = 400°C (heating rate: 10°C/h), after temperature were increased to T2= 800°C (heating rate: 120°C/h and dwell time: 30min). Sintering experiments were performed at four different temperatures 1300°C, 1400°C, 1450 °C, 1500 °C in air with 2 h soaking time. Scanning electron microscopy (JEOL JSM-7600

F/EDS/WDS/EBSD) was performed to observe the microstructures of the sintered samples, and the average grain size was estimated from the SEM micrographs by the intercept method. X-ray diffraction analysis was carried out using X-ray diffractometer, Panalytical Empyrean DY1098 to measure the phase content. The phase content were evaluated by Highscore HighScore Plus (v. 3.0.4.) with the COD crystallographic open database COD 2017.

RESULTS

The SEM micrographs of sintered in choosed temperatures, polished and thermally etched samples are shown below respectively for 3Y-TZP ceramics (fig 1.) and 12Ce-TZP ceramics (fig 2.). In the case of 3Y-TZP ceramics the high dense microstructure is obtained in 1450°C with the measured average grain sizes of 382 nm. 3Y-TZP ceramics sintered in 1450°C is characterized by fine-grained microstructure (fig. 1 c). The grains are isometric in shape. There is no visible porosity. However with the increasing of the sintering temperature to 1500°C the bigger grains with the average size of 487 nm were obtained.

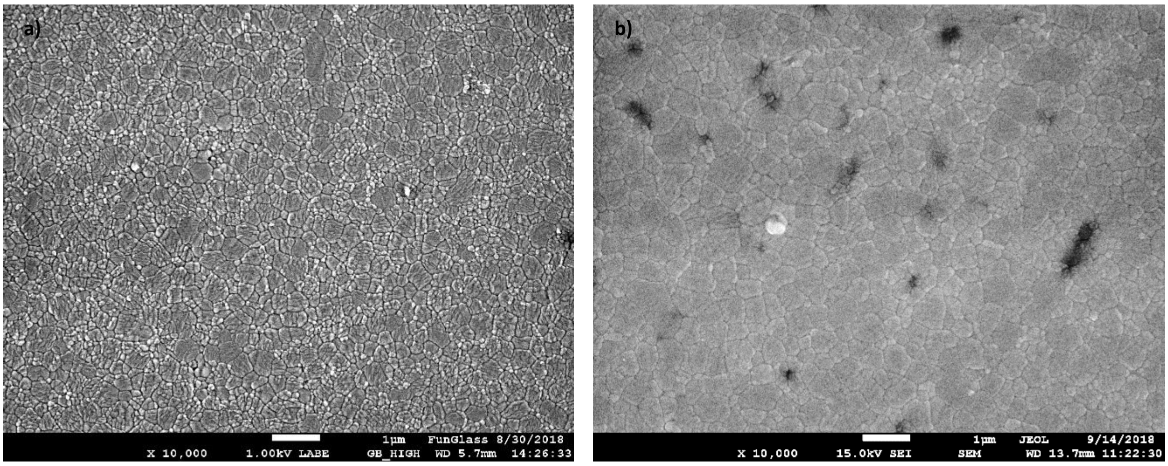

Fig 1. SEM micrographs - microstructure of a 3Y-TZP with different sintering temperatures: a) 1450°C b) 1500°C

In 12Ce-TZP ceramics, the grain boundaries were clearly visible in the highest sintering temperature (fig 2. d). However, the grain size was not uniform and was higher than 1000nm. X-ray diffraction analysis have shown that monoclinic phase occured only after polishing treatment in 3Y-TZP ceramic, sintered in T = 1450°C.

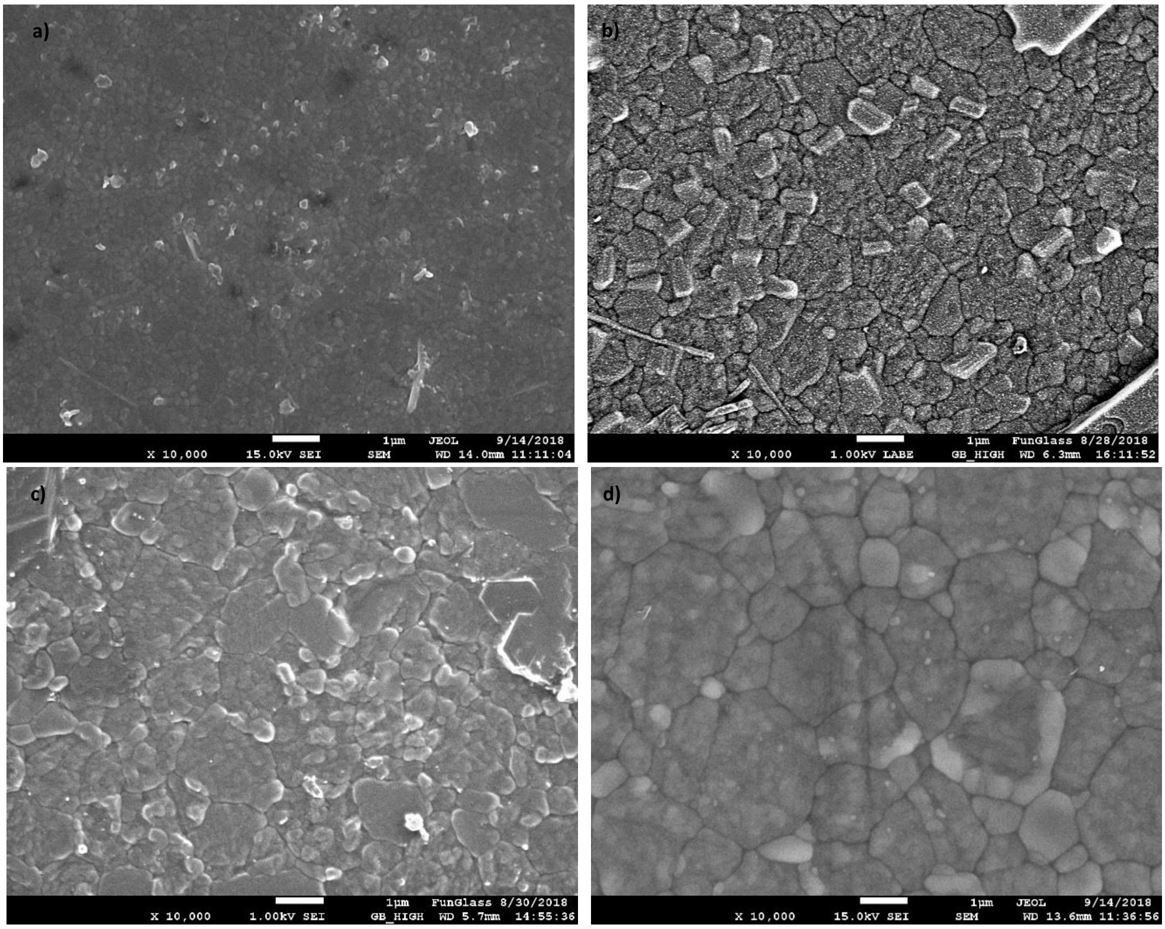

Fig 2. SEM micrographs - microstructure of a 12Ce-TZP with different sintering temperatures: a) 1300°C b) 1400°C c) 1450°C d) 1500°C,

CONCLUSIONS

In order to obtain the finest microstructure of prepared Y-TZP and Ce-TZP the sintering in 1450°C and 1500°C for both materials were selected. Y-TZP ceramics have much more fine-grained microstructure than Ce-TZP. It is thus very difficult to obtain a fine-grained, fully dense Ce-TZP. Chevalier et. al [4] reported that standard Ce-TZP achieve more extensive grain coarsening after sintering in comparison to Y-TZP. The mobility of grain boundaries is much higher in Ce-TZP than in Y-TZP. The experimental data will be expans for next evaluatenig resistance for Low Temperature Degradation (LTD) and corrosion tests in acetic environment the Y-TZP for both material sintered with selected method.

ACKNOWLEDGMENT

„This paper is a part of dissemination activities of the project FunGlass. This project has received funding from the European Union´s Horizon 2020 research and innovation programme under grant agreement No 739566“. Financial support of this work by the grant APVV SK-FR-2017-0008 0218-11 is gratefully acknowledged.

REFERENCES

[1] Lughi V, Sergo V. Low Temperature Degradation -aging- of Zirconia: A Critical Review of the Relevant Aspects in Dentistry. Dent Mater 2010;26:807-20 4.
[2] Chevalier J. What future for zirconia as a biomaterial? Biomaterials 2006;27:535-43.
[3] The effect of extended aging on the optical properties of diffrent zirconia materials. Aghazzawi, T. F. 2016, Journal of Prosthodontic Research.
[4] Ceramics for medical applications: A picture for the next 20 years. J. Chevalier, L. Gremillard. 2009, Journal of the European Ceramic Society 29 , pp. 1245-1255.

ADHESION AND IMPACT WEAR RESISTANCE OF TiC-BASED COATINGS PREPARED BY DCMS AND HIMIPS

J. Daniel[1], J. Grossman[1], T. Fořt[1], J. Sobota[1], L. Zábranský[2], P. Souček[2], K. Bernátová[2],
V. Buršíková[2], P. Vašina[2]

[1] *Institute of Scientific Instruments of the Czech Academy of Sciences, Královopolská 147, Brno 612 64, Czech Republic*

[2] *Masaryk University, Faculty of Science, Department of Physical Electronics, Kotlářská 2, Brno 611 37, Czech Republic*

ABSTRACT

This paper is focused on study of the adhesion and the dynamic impact wear of the nanocomposite nc-TiC/a-C:H coatings prepared by hybrid PVD-PECVD process. Two series of coatings with different amount of carbon were deposited on the cemented tungsten carbide substrates by the DC Magnetron Sputtering (DCMS) and the High Power Impulse Magnetron Sputtering (HiPIMS) processes. Series of the DCMS and HiPIMS prepared coatings behaved differently. The HiPIMS prepared coatings exhibited increase oh the adhesion with increasing carbon content. On the other hand, dependence of the adhesion on the total carbon content of the DCMS prepared coatings exhibited local maximum. Dynamic impact testing revealed different response of the DSMD and HiPIMS prepared coatings on dynamic impact load. The adhesion and the impact wear behaviour depended on mechanical properties of the coatings such as a H/E and H^3/E^2 ratio and on the coatings surface morphology.

Keywords: dynamic impact test, scratch test, titanium carbide, nanocomposite, HiPIMS

INTRODUCTION

Nanocomposite nc-TiC/a-C:H coatings consisting of nanocrystalline titanium carbide grains embedded in amorphous hydrogenated carbon matrix. This type of coating was widely studied due its advantageous combination of physical, chemical and mechanical properties such as high hardness, and low wear [1-3]. The nc-TiC/a-C:H coatings are usually prepared using a hybrid PVD-PECVD process of sputtering of titanium target in hydrocarbon containing plasma [4, 5]. In previous work was shown, that using high power impulse magnetron sputtering (HiPIMS) is possible to prepare the nc-TiC/a-C:H coatings with the same chemical composition as by direct current magnetron sputtering (DCMS) but with different microstructure and thus with different mechanical properties (higher E and higher E in the case of HiPIMS) [4, 6]. The chemical composition, microstructure and mechanical properties of the nc-TiC/a-C:H coatings are well described in literature. However, systematic analysis of the adhesion and the impact wear of the nc-TiC/a-C:H coatings has not yet been reported. The aim of this work is to systematically investigate the impact wear resistance and the adhesion of these coatings. Two series of the nc-TiC/a-C:H coatings with different carbon content were prepared by both the DCMS and HiPIMS. The scratch tests and the dynamic impact tests were carried out on all of the coatings. Differences in the dependencies of the adhesion and the dynamic wear behaviour on the coatings mechanical properties, microstructure and surface morphology were discussed.

EXPERIMENTAL

Nanocomposite nc-TiC/a-C:H coatings were deposited by hybrid PVD-PECVD process. Titanium target was driven by Hüttinger TruPlasma Bipolar 4010 generator operated in the DC mode or by Melec SIPP 2000 generator in the HiPIMS case. The cemented tungsten carbide was used as a substrate. Acetylene was used as a source of carbon; argon was used as a buffer gas. Due to lower deposition rates was used a longer deposition time in the HiPIMS mode. The bias of -100 V was used in the case of DCMS depositions, in the HiPIMS case was the substrate left on the floating potential. For detailed description of the deposition process see [4]. The adhesion of the coating to the substrate was analysed by scratch test. Scratch test was realized by scratch tester from Anton Paar. The tester was equipped with a 200 μm Rockwell indenter. A progressive scratch loading was applied to all samples (rate of 15 N/min in the range from 1 N up to 51 N on a 4 mm path). Behaviour of the coatings under dynamic impact load was investigated using impact tester developed at the ISI in Brno. A ball-shaped cemented tungsten carbide with diameter of 5 mm was used as an impact indenter. Frequency of impact testing was set to 8 Hz; impact testing was carried out with an impact load of 600 N. The thickness of coatings was determined using a calotester. Tescan MIRA SEM equipped with an EDX detector was used to determine the chemical composition. Fischerscope H100 depth sensing indenter with a Berkovich tip was used to measure hardness and effective elastic modulus. The indentation load of 40 mN was chosen in order to avoid the influence of the substrate. Depth and radius of the impact craters were measured by profilometer Talystep and confocal microscope Lext OLS 3100.

RESULTS

A set of the nc-TiC/a-C:H coatings with ~ 30 at. % - ~ 65 at. % of C was prepared by the DCMS process. Another set of the nc-TiC/a-C:H coatings with ~ 25 at. % - ~ 70 at. % of C was prepared by the HiPIMS process. Thickness of the DCMS prepared coatings was in the range of 3.1 – 3.8 μm, whereas in the HiPIMS case the thickness of coatings, even though deposited for twice as long time, was in the range of 2.4 – 2.8 μm. Scratch adhesion generally depends on the thickness of the tested coatings. The nc-TiC/a-C:H coatings prepared by DCMS exhibited different thickness than the HiPIMS prepared coatings. Therefore, dependencies of the adhesion will be discussed separately for the DCMS case and for the HiPIMS case.

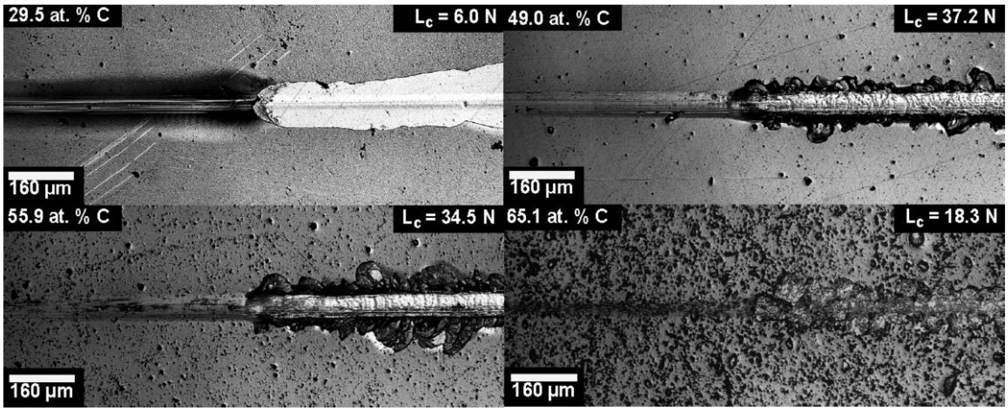

Fig. 1: Comparison of the failure modes of the DCMS prepared coatings under a scratch load

The DCMS prepared coatings with ~ 30 at. % and ~ 50 at. % of C exhibited smooth surface, surfaces of coatings with higher amount of C were more rough, as can be seen in Fig. 1. Dependence of the critical load L_C (the value of the scratch load when failure occurs) on the total carbon content in the DCMS case is shown on Fig. 2a. Critical load increased from ~ 6 N for the coating with ~ 30 at. % of C up to maximal value of ~ 37 N for the coating with 49 at. % of C. As the total carbon content increased further, the critical load decreased to ~ 18 N.

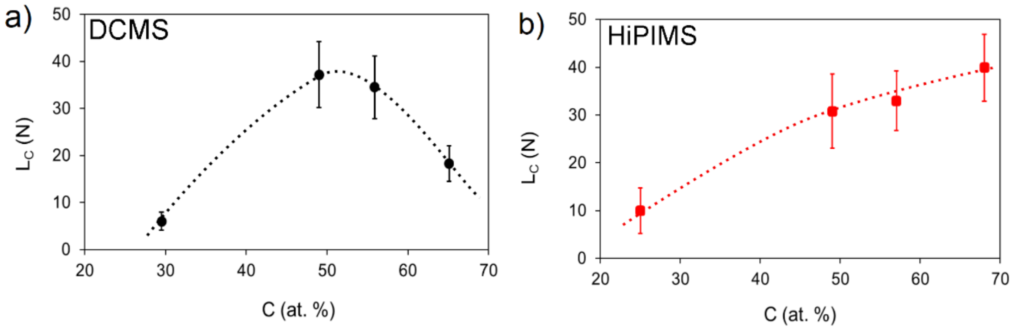

Fig. 2: Critical load L_C of the a) DCMS and b) HiPIMS prepared coatings

The HiPIMS prepared coating with the lowest amount of carbon (25.0 at. %) exhibited the highest surface roughness. All of the other HiPIMS prepared coatings exhibited smooth surfaces (see Fig. 3).

Evolution of dependence of L_C on the total carbon content of coatings prepared by HiPIMS is shown in Fig. 2b. HiPIMS coatings exhibited increase of the L_C from ~ 10 N for the coating with ~ 25 at. % of C up to ~ 40 N for the coating with ~ 68 at. % of carbon.

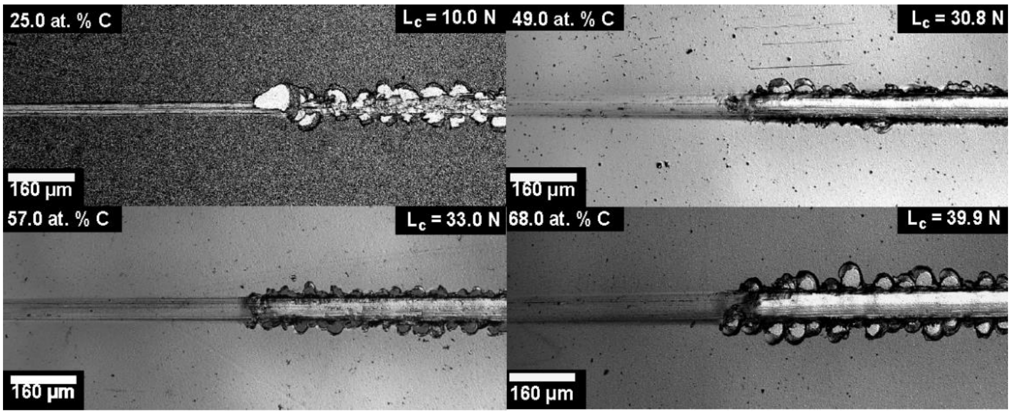

Fig. 3: Comparison of the failure modes of the HiPIMS prepared coatings under a scratch load

Volume of the impact craters was calculated using crater radius and average depth. Shape of the impact crater was approximated by a rotational paraboloid [7]. Typical result of dynamic impact analysis is a loading curve, a dependence of the crater volume on the number of impact cycles. Loading curves of the DCMS and the HiPIMS prepared coatings with the same carbon content of 49.0 at. % are compared in Fig. 4. In the DCMS case, the volumes of impact craters made by ≤ 10 000 impacts were lower than volumes of the impact craters in the HiPIMS case. Then, after reaching a critical number of impacts n_C (the highest number of impacts before coating failure) of 5 000, volume of the DCMS prepared coating rapidly increased. Loading curve of the HiPIMS prepared coating exhibited higher n_C between 5 000 and 20 000, accurate value of the n_C cannot be clearly seen from the loading curve. In some cases, determination of n_C from loading curve is ambiguous.

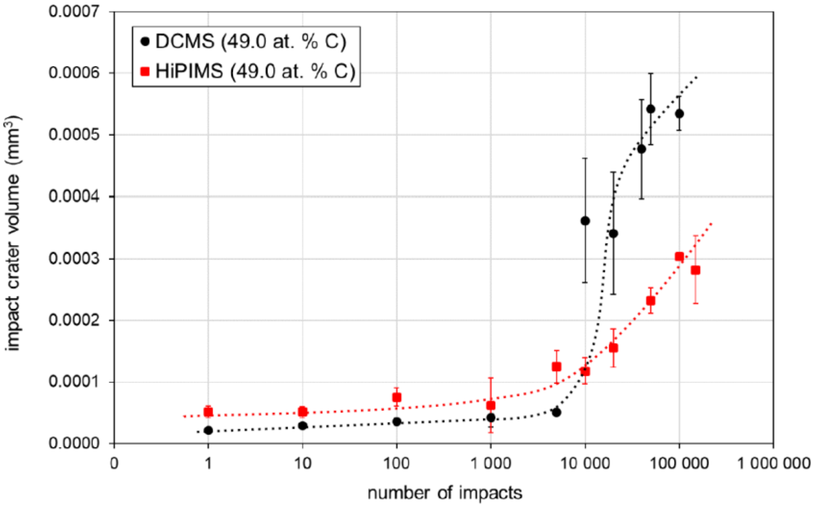

Fig. 4: Comparison of loading curves of the DCMS (black) and HiPIMS (red) prepared coatings. Both curves were prepared using the impact load of 600 N. Dot lines are added as a guides for the eye

Therefore, optical investigation of impact craters is often used for estimation of n_C. Such impact craters of the coatings with total carbon content of 49.0 at. % are shown in Fig. 5. In the DCMS case (Fig. 5a), the coating exhibited almost no impact crater after 1 impact cycle. After 1 000 cycles was the edge of the impact crater well visible. Finally, after 10 000 cycles and 100 000 cycles coating exhibited uncovered substrate on the crater bottom and sharp edges of the impact craters.

The HiPIMS prepared nc-TiC/a-C:H coating (Fig. 5b) also exhibited almost no impact crater after 1 impact cycle. The impact crater after 1 000 and 10 000 cycles exhibited less sharp edges. Uncovered substrate was observed on the bottom of the impact crater made by 100 000 cycles. From optical investigation was value of n_C for the HiPIMS prepared coating specified as 10 000 - 20 000.

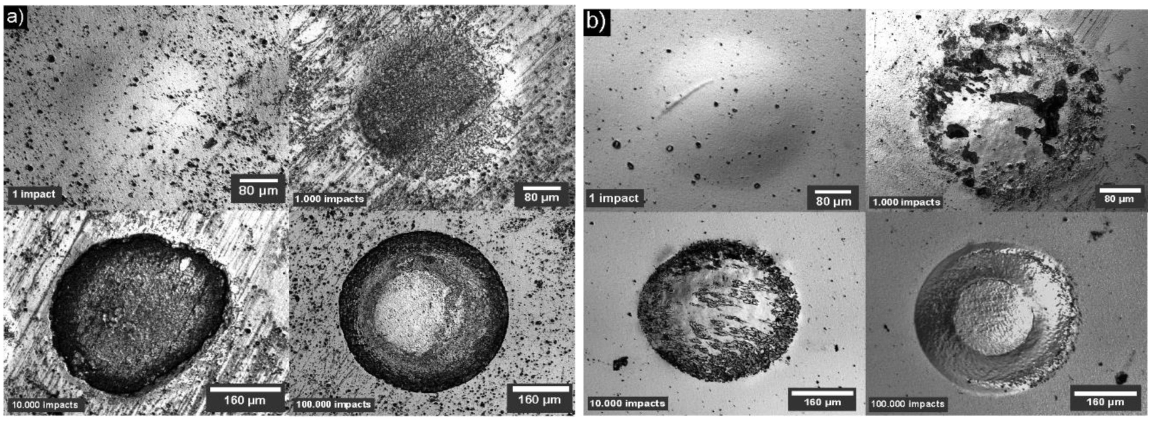

Fig. 5: Impact craters of the nc-TiC/a-C:H coating with 49.0 at. % of C prepared by a) DCMS and b) HiPIMS

Impact resistances of the DCMS and the HiPIMS prepared coatings are compared in Figure 6. In general, impact resistance was higher for low number of impact cycles due to the low crater volumes and low volume increase (see Fig. 4). As number of impact cycles increased, impact resistance decreased. After exceeding n_C, crater volume increased and impact resistance rapidly decreased. Both, the DCMS and the HiPIMS prepared coatings with the amount of carbon of ~ 30 at. % (Fig. 6a) exhibited lower impact resistance than coatings with 49 at. % of C (Fig. 6b) and coatings with the highest amount of C (Fig. 6c). All of the HiPIMS prepared coatings exhibited better impact resistance than the corresponding DCMS coatings. The n_C for all coatings were set using methods of loading curves, impact crater comparison and impact wear resistance dependencies. In cases, where value of n_C determined from stated methods were ambiguous, a final value was estimated as an average value of n_C. According to this approach, the n_C of the HiPIMS prepared coating with 49 at. % C was estimated as 15 000 ± 3 000.

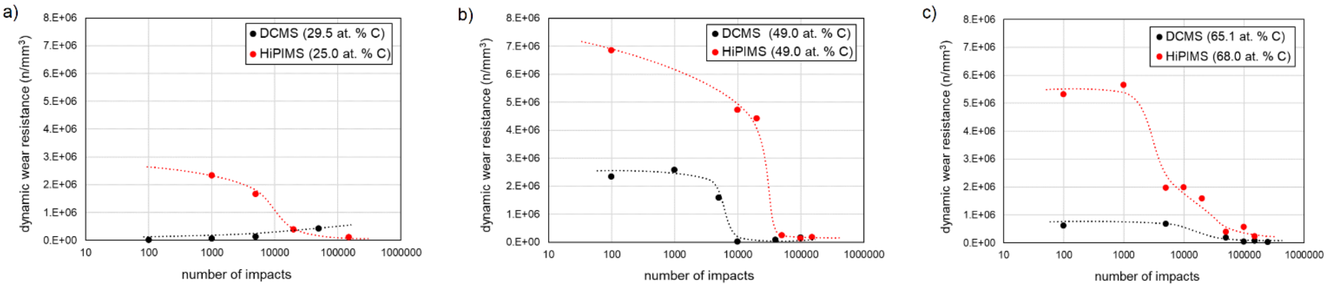

Fig. 6: Impact resistance of coatings prepared by the DCMS and the HiPIMS. Comparison of the coatings with a) the lowest, b) medium and c) the highest amount of C

The n_C of all of the tested coatings is depicted in Fig. 7. The n_C of the DCMS and HiPIMS coatings increased directly with total carbon content (Fig. 7a). The n_C of the DCMS and HiPIMS coatings also increased with the H/E ratio (Fig. 7b). All of the DCMS prepared coatings exhibited lower n_C than the corresponding HiPIMS prepared coatings, that they were even thinner.

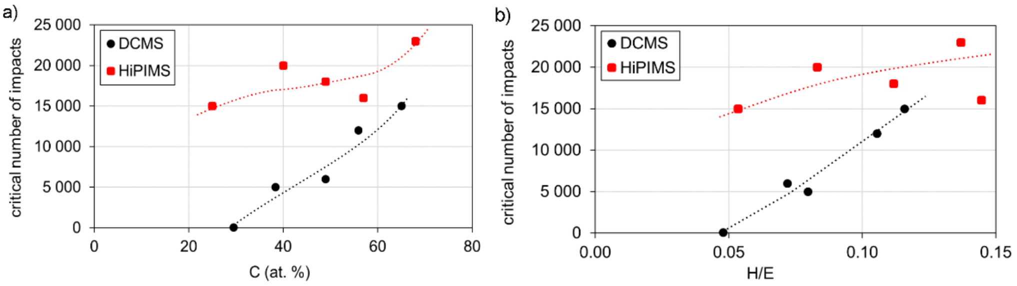

Fig. 7: Dependence of n_C of the DCMS and the HiPIMS coatings on a) total carbon content and b) H/E ratio

DISCUSSION

Value of critical load L_C decreases with increasing surface roughness as well as with increasing value of coffitient of friction (CoF) [3]. In case of the DCMS prepared coatings, adhesion represented by L_C increased with increasing total carbon content up to the value of ~ 50 at. % and then decreased. Thickness of all tested DCMS prepared coatings was approximately the same. The coatings with ~ 56 at. % of C and ~ 65 at. % of C exhibited higher surface roughness and CoF higher than coatings with lower amount of C. Higher surface roughness was reason of the observed decrease of the carbon-rich DCMS coatings adhesion. The L_C of the HiPIMS prepared coatings increased with total carbon content. Thickness of all tested coatings was similar. All of the coatings exhibited smooth surface with low roughness. Moreover, coatings with smooth surfaces exhibited decrease of CoF with carbon content [1]. Thus it can be excepted that CoF of the HiPIMS prepared coatings with high amount of C was lower than CoF of the coatings with lower amount of C. Therefore, smooth surface morphology and associated low CoF were the reasons of the observed high L_C of the HiPIMS prepared carbon-rich coating. Coatings prepared by the HiPIMS exhibited higher impact resistance than the corresponding coatings prepared by the DCMS. The H^3/E^2 ratio is related to the resistance of material against the plastic deformation [8]. Thus, better impact resistance, i.e. resistance against the plastic deformation caused by impact load, of the HiPIMS prepared coatings can be explained by the higher ratio of H^3/E^2 in comparison with the DCMS case. Critical number of impacts of both the DCMS prepared and the HiPIMS prepared coatings increased with increasing total carbon content and with increasing ratio of H/E. Ratio of H/E is related to the toughness and wear resistance of the coating and to the wear behaviour under dynamic impact [9]. Observed increase of the critical number of impacts is thus connected with increase of the H/E. Coatings prepared by HiPIMS exhibited higher wear resistance even with 30 % lower thickness than the DCMS coatings.

CONCLUSION

The nc-TiC/a-C:H coatings with different amount of carbon were prepared on the tungsten carbide substrates by the hybrid PVD-PECVD process by both the HiPIMS and the DCMS. Adhesion and dynamic impact wear were analysed and discussed. Results can be concluded in this points:

- DCMS prepared coatings with higher content of carbon exhibited higher surface roughness and thus lower critical load and lower adhesion, the HiPIMS prepared carbon-rich coatings exhibited smooth surface and thus good adhesion
- HiPIMS prepared coatings exhibited better impact resistance than corresponding DCMS coatings due to the higher value of H^3/E^2, related to the plastic deformation resistance
- critical number of impacts in both the HiPIMS and the DCMS prepared coatings increased with increasing value of the H/E ratio

ACKNOWLEDGMENT

This research has been supported by Ministry of Education, Youth and Sports of the Czech Republic (project LO1212). The research infrastructure was funded by Ministry of Education, Youth and Sports of the Czech Republic and European Commission (project CZ.1.05/2.1.00/01.0017) and by The Czech Academy of Sciences (project RVO:68081731) and by Project LO1411 (NPU I) funded by Ministry of Education, Youth and Sports of Czech Republic and the Czech Science Foundation (Project 15-17875S).

REFERENCES

[1] D. Martínez-Martínez, C. López-Cartes, A. Fernández, J.C. Sánchez-López: Influence of the microstructure on the mechanical and tribological behaviour of TiC/a-C nanocomposite coatings, Thin Solid Films 517 (2009) 1662-1671

[2] T. Zehnder, J. Patscheider: Nanocomposite TiC/a-C:H hard coatings deposited by reactive PVD, Surf. Coat. Technol. 133–134 (2000) 138-144

[3] D.M. Cao, B. Feng, W.J. Meng, L.E. Rehn, P.M. Baldo, M.M. Khonsari: Friction and wear characteristics of ceramic nanocomposite coatings: Titanium carbide/amorphous hydrocarbon, Appl. Phys. Lett. 3 (2001) 329-331

[4] P. Souček, J. Daniel, J. Hnilica, K. Bernátová, L. Zábranský, V. Buršíková, M. Stupavská, P. Vašina: Superhard nanocomposite nc-TiC/a-C:H coatings: the effect of HiPIMS on coating microstructure and mechanical properties, Surf. Coat. Technol. 311 (2017) 257–267

[5] J. Daniel, Souček, L. Zábranský, V. Buršíková, M. Stupavská, P. Vašina: On the effect of the substrate to target position on the properties of titanium carbide/carbon coatings, Surf. Coat. Technol. 328 (2017) 462- 468

[6] J. Daniel, P. Souček, K. Bernátová, L. Zábranský, M. Stupavská, V. Buršíková P. Vašina: Investigation of the influence of Ni doping on the structure and hardness of Ti-(Ni)-C coatings, Journal of Nanomaterials 2017 (2017)
[7] T. Fořt, T. Vítů, R. Novák, J. Grossman, J. Sobota, J. Vyskočil: Testing oh the impact load and tribological behavior of W-C:H hard composite coatings, Chem. Listy 105 (2011) 102-104
[8] Tsui T.Y., Pharr G.M., Oliver W.C., Bhatia C.S., White R.L., Anders S., Anders A., Brown I.G.: Nanoindentation and nanoscratching of hard carbon coatings for magnetic discs. MRS Proceedings, 383 (1995) 383-447.
[9] A. Leyland, A. Matthews: On the significance of the H/E ratio in wear control: a nanocomposite coating approach to optimised tribological behaviour, Wear 246 (2000) 1-11

TiO_2 – SiO_2 – Al_2O_3 FILMS FOR HUMIDITY SENSORS

VRSTVY TiO_2 – SiO_2 – Al_2O_3 PRE SENZORY VLHKOSTI

Katarína Faturíková [1], Alfonz Plško [1], Marek Liška [2]

[1] FunGlass – Centre for Functional and Surface Functionalized Glass, Alexander Dubček University of Trenčín, Študentská 2, Trenčín SK-911 50, Slovak Republic

[2] Fun Glass – Vitrum Laugaricio - Joint Glass Center of IIC SAS, TnU AD and RONA

Alexander Dubček University of Trenčín, Študentská 2, Trenčín SK-911 50, Slovak Republic

ABSTRACT

The influence of precursor sols composition on the properties of humidity sensors films prepared by sol – gel method was studied. The composition of prepared layers, expressed by SiO_2:TiO_2:Al_2O_3 molar ratio, was: 0:0.95:0.05; 0.32:0.63:0.05; 0.475:0.475:0.05; 0.63:0.32:0.05; 0.95:0:0.05. The suitability of studied layers for humidity sensors was investigated by impedance spetroscopy. Complex impedance spectra of thin film sensors for relative humidity ranging from 0.13 % to 97.7 % were measured with the frequency ranging from 1 kHz to 1 MHz. Equivalent circuits consisting from serial connection of different number of -(R/C)- , -(R/CPE)- and -R- were used to analyse obtained spectra. The compositional dependence of the humidity detection ability was evaluated on the basis of the dependecne of parameters of equivalent circuits on the relative humidity value.

Keywords: sol-gel, coatings, physisorption of water, impedance spectroscopy

INTRODUCTION

Humidity sensors based on metal oxides have wide range of application. Their main advantages are high lifetime and temperature stability. Materials based on metal oxides, used either as bulk or as films, are characterized by change of material properties induced by adsorption of air humidity [1]. This type of material surface adsorption is called physical adsorption and it is reversible [2]. The creation of adsorbed water layer on the material surface depends on the concentration of water vapour in the surroundings of sensor and surface concentration of –OH groups, which depends on the type of material used as the sensitive layer of sensor [3]. These –OH groups act as reaction centres on which water molecules are attached by hydrogen bonds. Sol-gel method is based on controlled hydrolysis of alkoxide precursors, $M(OR)_x$, where M–OH groups are created:

$$M(OR)_x + yH_2O \leftrightarrow M(OR)_{x-y}(OH)_y + yROH \qquad (1)$$

M–OH or M–OR groups are subsequently chained in condensation reactions:

$$M(OR)_{x-y}(OH)_y + M(OR)_{x-y}(OH)_y \leftrightarrow (OR)_{x-y}(OH)_{y-1}M\text{-}O\text{-}M(OR)_{x-y}(OH)_{y-1} + H_2O \qquad (2)$$

$$M(OR)_{x-y}(OH)_y + M(OR)_{x-y}(OH)_y \leftrightarrow (OR)_{x-y-1}(OH)_yM\text{-}O\text{-}M(OR)_{x-y}(OH)_{y-1} + ROH \qquad (3)$$

where M–O–M bond as well as H_2O or ROH molecule are created [4].

Properties of substrate and requirements for prepared film (porosity, concentration of residual M–OH groups and degree of water chemisorption during cooling of film from thermal treatment temperature to room temperature) are limiting factors. Films prepared by sol-gel method have wide range of applications in optics, protection of materials and humidity sensors [5]. Their dielectric properties are investigated by impedance spectroscopy. Measured impedance spectra can be studied by the method of equivalent circuits by serial and parallel connection of several substitute circuits. More advantageous are models that consist of serial connected resistance and -(R/C)- or -(R/CPE)- elements, where R is the resistance, C the capacitance, CPE is the Constant Phase Element, and "/" represents the parallel connection. For examined SiO_2-TiO_2-Al_2O_3 films we have studied the dependence of the amount and parameters of equivalent circuits, which depends on the process of adsorption and on the relative humidity values.

EXPERIMENTAL

SiO_2-TiO_2-Al_2O_3 films were prepared by sol-gel method using the dip-coating technique. Five different sol compositions (Table 1) were used. For synthesis of sols, titanium(IV) tetra-isopropoxide ($Ti(iPr)_4$), isopropyl alcohol (IPA), acetylacetone (AcAc), nitric acid (HNO_3) and distilled water (H_2O) were used. For the SiO_2-Al_2O_3 sol the molar ratios $HNO_3/SiO_2 = 1$ and $H_2O/SiO_2 = 2$ were used. For the TiO_2-Al_2O_3 sol the molar ratios $AcAc/TiO_2 = 0.6$, $HNO_3/TiO_2 = 0.5$, and $H_2O/TiO_2 = 1$ were used.

Table 1 Molar composition of solutions for preparation of sols.

Sample	$SiO_2 : TiO_2 : Al_2O_3$ / molar ratio	Component - molar amount / mol						
		SiO_2	TiO_2	Al_2O_3	AcAc	HNO_3	H_2O	IPA
S0T1A	0 : 0.95 : 0.05	0	0.0475	0.0025	0.0435	0.0238	0.0475	0.835
S1T2A	0.317 : 0.633 : 0.05	0.0159	0.0317	0.0025	0.0340	0.0317	0.0634	0.821
S1T1A	0.475 : 0.475 : 0.05	0.0238	0.0238	0.0025	0.0293	0.0356	0.0713	0.814
S2T1A	0.633 : 0.317 : 0.05	0.0317	0.0159	0.0025	0.0245	0.0396	0.0792	0.807
S1T0A	0.95 : 0 : 0.05	0.0475	0	0.0025	0.0150	0.0475	0.0950	0.793

The films were applied on the golden interdigital comb-like electrodes on Al_2O_3 substrate. Before the application, electrodes were cleaned in ammonia solution with hydrogen peroxide (1:3). Subsequently they were washed with distilled water, sonificated for 10 minutes and washed by isopropyl alcohol. Electrodes were coated with sol by the rate of 90 $mm.min^{-1}$. Then they were dried at 80 °C for 15 minutes and annealed at 500 °C for 50 minutes. Heating rate was 10 $°C.min^{-1}$. After heating process the electrodes were left in oven until the temperature decreased to 250 °C and then they were kept for 24 hours in place with relative humidity of 52.9 %.

Impedance spectra were measured at room temperature and relative humidity (RH) 0.13 %, 11.3%, 23.1%, 33.1%, 43.1%, 52.9%, 59.1%, 69.9%, 75.5%, 85.1 %, and 97.6 % in frequency interval from 1 kHz to 1 MHz, at voltage $U = 1.0$ V by the Fluke RCL Meter PM6306. Particular relative humidity were obtained in closed PE containers above saturated solution of salts, except the RH 0.13 % which was obtained above the silica. Measured dependences of complex impedance on frequency were evaluated by complex nonlinear least squares method. Serial connection with different counts of -R-, -(R/C)- and -(R/CPE)- equivalent circuits was used. The impedance was calculated by

$$Z^*(f)=\sum_{p=0}^{P}R_p+\sum_{l=0}^{L}\frac{R_l^{RC}}{1+jf/\left(f_{\max}^{RC}\right)_l}+\sum_{k=0}^{K}\frac{R_k^{RCPE}}{1+\left(jf/\left(f_{\max}^{RCPE}\right)_k\right)^n} \qquad (4)$$

where P, L, K is count of -R- , -(R/C)-, -(R/CPE)- equivalent circuits in model, f is frequency [Hz], f_{max}^{RC} is frequency of maximum Z´´ for equivalent circuit -(R/C)- [Hz], f_{max}^{RCPE} is frequency of maximum $Z´´$ for equivalent circuit -(R/CPE)- [Hz], R_P , R_l^{RC} , R_k^{RCPE} are values of ideal rezistances of corresponding equivalent circuits [Ω].

Then the least squares problem can be formulated

$$S=\sum_{i=1}^{m}\left\{w_i^{'}\left[\left(Z_i^{'}\right)^{exp}-\left(Z_i^{'}\right)^{clc}\right]^2+w_i^{''}\left[\left(Z_i^{''}\right)^{exp}-\left(Z_i^{''}\right)^{clc}\right]^2\right\}=\min \tag{5}$$

where $(Z_i^{'})^{exp}$, $(Z_i^{'})^{clc}$ stand for experimental and calculated real part of complex impedance, $(Z_i^{''})^{exp}$, $(Z_i^{''})^{clc}$ represent experimental and calculated imaginary part of complex impedance, $w_i^{'}=\left[(|Z_i^{'}|)^{exp}\right]^{-1}$, $w_i^{''}=\left[(|Z_i^{''}|)^{exp}\right]^{-1}$ are statistical weights of experimental data real and imaginary part of complex impedance and m is number of frequencies of digitized impedance spectrum.

RESULTS AND DISCUSION

Measured impedance spectra were analyzed by equivalent circuits. The optimal model was determined by testing a set of models with different numbers of components (P, L, K). The model with minimal value of objective function S was chosen. Within the set of measured spectra, we found out that model -R-(R/C)-(R/CPE)-, further marked as 3, was suitable for low RH values. At higher humidity values, the best results were observed with the model -R-(R_1/C_1)-(R_2/C_2)-(R/CPE)-, further marked as 4. In some cases, at the highest RH values, it was necessary to apply more complicated models, further marked as 5. At RH = 0.13 %, some of the prepared samples showed impedance values beyond the apparatus range, further marked as 0. According to data in the Tab. 2, measured dependence of the amount of circuit elements on the composition and on the air humidity values can be clarified in pursuance of these following assumptions. There are three cognizable stages of process of physical adsorption of water on the materials surfaces, in our case on the TiO_2-SiO_2-Al_2O_3 layers. In the first stage, at low RH values, adsorbed water creates islets which probably affect only the dielectric properties of layer. These islets are created on surface and they will not become evident within individual relaxation processes. The second stage is observed for higher RH values. In this stage, coherent layer of adsorbed water is formed. Water molecules in this layer are relatively tightly bounded with the layer surface by hydrogen bonds therefore their mobility is limited. The coherent layer of adsorbed water will become evident within individual relaxation process. In the third stage, at the high RH values, more layers of water molecules are adsorbed on the layer which was created in the second stage. Water molecules in these layers are bounded among them and therefore they have relatively high mobility. This leads to the creation of another polarization process. According these assumptions, it is possible to explain the fact, that it was necessary to use model 4 or 5 for evaluation of impedance spectra at higher RH values. Presence of second and third stage of water adsorption depends on the properties of layer surface. Using the assumption of previous facts, it is possible to assume that for examined compositions S0T1A, S1T2A, S2T1A and S1T0A (SiO_2 molar fraction 0, 0.317, 0.633 and 0.95), the transition between the second and the third stage of water adsorption (creation of coherent water layer) occurs at the RH value of 33.1 %. For the composition S1T1A (SiO_2 molar fraction 0.475), this transition occurs at the RH value of 43.2 %. Observed transition to the third stage can refer to known fact, that on the surface of

S1T0A layer (i.e. SiO_2-Al_2O_3 layer), there is relatively high concentration of –OH groups (compared to other layers) [3]. That creates good conditions for the adsorption on the surface.

Table 2 Dependence of the amount of circuit elements on the composition and on the air humidity values.

RH [%]	S0T1A	S1T2A	S1T1A	S2T1A	S1T0A
0.13	3	0	3	3	0
11.3	3	3	3	3	3
23.1	3	3	3	3	3
33.1	3	3	3	3	3
43.2	4	4	3	4	4
52.9	4	4	4	4	4
59.1	4	4	4	4	4
69.9	4	4	4	4	5
75.5	4	4	4	4	5
85.1	4	4	4	4	5
97.6	4	5	4	4	5

CONCLUSION

Using the impedance spectroscopy particular stages of physical adsorption of water and the transitions between them were identified for the examined compositions of SiO_2-TiO_2-Al_2O_3 films. In relation to S0T1A, S1T2A, S2T1A and S1T0A compositions (SiO_2 molar fractions 0, 0.317, 0.633 and 0.95) it was observed the transition between the first and the second stage, and the creation of compact water layer on surface occurs at the RH value of 43.2 %. This transition is at 52.9 % for the S1T1A (SiO_2 molar fraction 0.475). The significant difference in the course of physical adsorption onto the S1T0A layer (SiO_2:TiO_2:Al_2O_3 molar ratio 0.95:0:0.05) is clarified by higher concentration of –OH groups on the surface.

ACKNOWLEDGEMENT

This work was supported by the Grant Agency of Slovak Republic – VEGA 1/0431/18.

REFERENCES

1. G. Korotcekov: Metal oxides for solid-state gas sensors: What determines our choice? Materials Science and Engineering B 139 (2007) 1-23
2. Kan-Sen Chou, Tzy-Kuang Lee, Feng-Jiin Liu: Sensing mechanism of porous ceramic as humidity sensor, Sensors and Actuators B 56 (1999) 106-111

3. L.T. Zhuralev: The surface Chemistry of Silica – The Zhuralev Model. In: H.E. Berga, W.O. Roberts: Colloidal Silica Fundamentals and Applications, CRC Press Taylor & Francis Group, New York, 2006, ISBN 0-8247-0967-5, pp. 261-266
4. C.J. Brinker, G.W. Scherer: Sol-Gel Science: The Physics and Chemistry of Sol-Gel Processing, Academic Press, Boston, 1990, ISBN 0-12-134970-5
5. N. Carmona, E. Herrero, J. Llopis, M.A. Villegas: Chemical sol-gel-based sensors for evaluation of environmental humidity, Sensors and Actuators B 126 (2007) 455-460

PRÍPRAVA, CHARAKTERIZÁCIA A OXIDAČNÉ SPRÁVANIE KERAMICKÝCH POVLAKOV PRIPRAVENÝCH Z ORGANOKREMIČITÝCH PREKURZOROV S PASÍVNYMI PLNIVAMI

PREPARATION, CHARACTERIZATION AND OXIDATION BEHAVIOR OF POLYMER DERIVED CERAMIC COATINGS WITH PASSIVE FILLERS

Ivana Petríková[1], Milan Parchovianský[1], Peter Švančárek[1], Gunter Motz[2], Dagmar Galusková[1], Dušan Galusek[1]

[1]*FunGlass – Centre for Functional and Surface Functionalized Glass, Študentská 2, 911 50 Trenčín, Slovakia*

[2]*University of Bayreuth, Ceramic Materials Engineering, D-95440 Bayreuth, Germany*

ABSTRACT

The work is aimed at the development of an oxidation/corrosion resistant environmental barrier coating system on steel substrates. After stabilizing the coating slurries, double layers consisting of a bond coat applied by dip coating and a top coat with passive fillers deposited by spray coating were prepared on stainless steel substrates. After thermal treatment in air at 800 °C, uniform and crack-free composite coatings on stainless steel with a thickness up to 90 μm were prepared. The high temperature oxidation behavior of coated and uncoated samples in atmosphere of synthetic air was investigated at the temperatures up to 1000 °C. The tested layers provide effective protection from oxidation at 900 °C and 950 °C, while no significant corrosion damage was observed.

Keywords: polymer-derived ceramics, passive filler, high-temperature oxidation

INTRODUCTION

Recently polymer derived ceramics (PDC) have gained attention as promising candidates for preparation of an environmental barrier coatings (EBC). Advantages of preceramic polymers are based on the use of cost efficient manufacturing routes from polymer processing technologies such as dip-coating or spray coating, low conversion temperatures in a desired atmosphere, tailoring of the microstructure and resulting properties as a function of composition and thermal treatment parameters [1]. The major disadvantage of the used precursor, however, is a shrinkage of more than 50 vol. % occurring during transformation from polymer to an amorphous ceramic. To overcome this drawback passive fillers are applied to control the shrinkage and the porosity of the pyrolyzed ceramics by utilizing different filler combinations [2, 3]. Moreover, the addition of glasses has shown to be a suitable approach to obtain thick and dense coatings. The glass fillers should be responsible for densification and sealing of the system, increasing the efficiency as EBC [4]. In this work, a novel EBC system for steel consisting of a perhydropolysilazane (PHPS) bond coat and a polysilazane-based glass/ceramic composite top coat has been developed. The processing route, microstructure and high-temperature oxidation behavior of the coating are presented.

EXPERIMENTAL

The preparation of the coatings consists of the two main steps: the synthesis of the powder filler AYZ20 (Al_2O_3-Y_2O_3-ZrO_2) via Pechini sol-gel route and the processing of the coatings. The composition of the AYZ20 filler is derived from Y_2O_3-Al_2O_3 eutectic (76,8 mol. % Al_2O_3, 23,2 mol. % Y_2O_3) and modified by the addition of 20 mol. % ZrO_2. The PDC system consists of two layers that were consecutively applied to stainless steel (AISI 441) substrates. The bond-coat was prepared from pre-ceramic polymer PHPS by dip-coating of the ultrasonically cleaned metal sheets. The pyrolysis of the bond-coat was performed in air at the temperature of 500 °C for 1 h. The top-coat was prepared from the ceramic matrix forming polysilazane HTT 1800, filled with YSZ (yttria-stabilized zirconia) and AYZ20 powder as passive fillers, and the commercial barium silicate glass particles (G018-311, G018-385, Scott AG) as sealing agents. The resulting mixture was applied onto bond-coat by spray coating technique and the curing of the composite coatings was performed in air at the temperature of 800 °C with a holding time of 1 h. The composition of the top-coat is listed in Tab 1.

Tab. 1: The composition of the composite coating after pyrolysis

YSZ (vol. %.)	**AYZ20 (vol. %.)**	**G018-385 (vol. %.)**	**G018-311 (vol. %.)**	**HTT 1800 (vol. %.)**
30	21	16	14	19

High temperature oxidation tests were carried out in a high temperature horizontal electric tube furnace (Clasic 0213T, Clasic, Praha, Czech Republic) at the temperatures of 900 °C, 950 °C and 1000 °C and the exposure times in the range of 1 – 48 hours in flowing atmosphere of synthetic air (purity 99.5%, Linde, Slovakia). The SEM/EDS examination of the coatings before and after oxidation tests was conducted with the use of a FEG SEM JEOL

7600f. X-ray powder diffraction analysis (CuKα, 2θ range 10-80°, Empyrean DY1098, PANalytical B.V., Netherlands) was used to investigate the phase composition of the coatings.

RESULTS

In a Fig. 1a, a SEM micrograph of a HTT 1800/glass composite coating after pyrolysis in air is presented. Micrograph of the cross-section shows that the softening of glass additives leads to the formation of a homogeneous glass/ceramic matrix with evenly distributed filler particles. After thermal treatment in air at 800 °C, uniform, well adherent and crack-free composite coating on stainless steel were prepared. It can be concluded that the addition of powder filler AYZ20 was effective at preventing the formation of cracks and pores. The addition of the filler enable the formation of a rigid skeletal structure in the coating thus facilitating escape of gases during the pyrolytic conversion of the organosilicon precursor. XRD pattern of the coating is displayed in the Fig. 2. After pyrolysis in air the polysilazane-based coating contains three crystalline phases, namely monoclinic and tetragonal ZrO_2, and yttrium aluminum garnet, originating from the powder filler AYZ20.

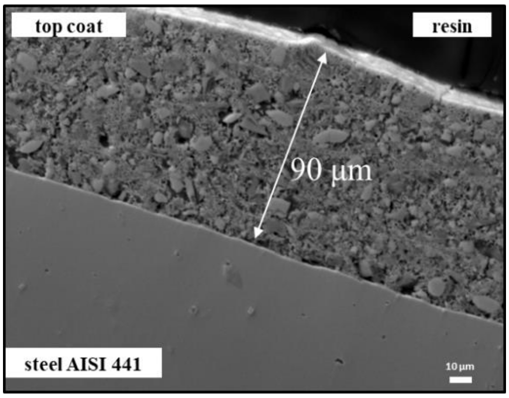

Fig. 1: Cross-sectional SEM image of the coating after pyrolysis in air at 800 °C

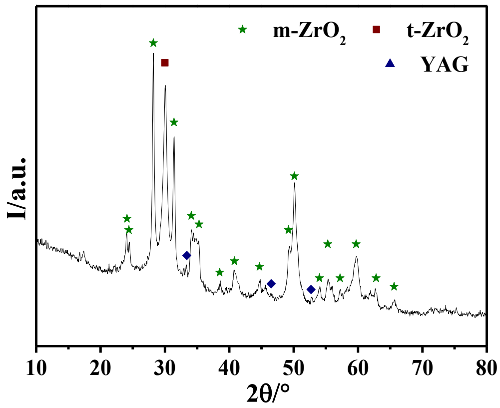

Fig. 2: X-Ray diffraction pattern of the coating after pyrolysis in air at 800°C

Fig. 3a shows the weight gains of the uncoated steel samples as a function of time during high-temperature oxidation. Uncoated steel substrates are subjected to significant oxidation due to the surface oxide scale growth. X-Ray diffraction along with SEM/EDS analysis (not shown) confirmed extensive corrosion of the uncoated steel accompanied by formation of oxide layer comprised Cr_2O_3 sub-layer and Mn-Cr spinel crystals top layer. On the contrary, Fig. 3b distinctly shows that the PDC coating system is able to efficiently reduce the weight gain due to oxidation at elevated temperatures. Compared to uncoated samples, only negligible mass loss was observed at all oxidation temperature. This can be associated with the release of residual hydrogen from cleavage of Si–H and C–H bonds [6]. Prior to long-term oxidation tests, coating systems were pyrolyzed for only 1 h, and this may not necessarily lead to fully transformed and stable ceramic products. However, at the temperature of 1000

°C and after 12 hours of oxidation, a significant weight loss was observed due to the gradual peeling off the protective layer.

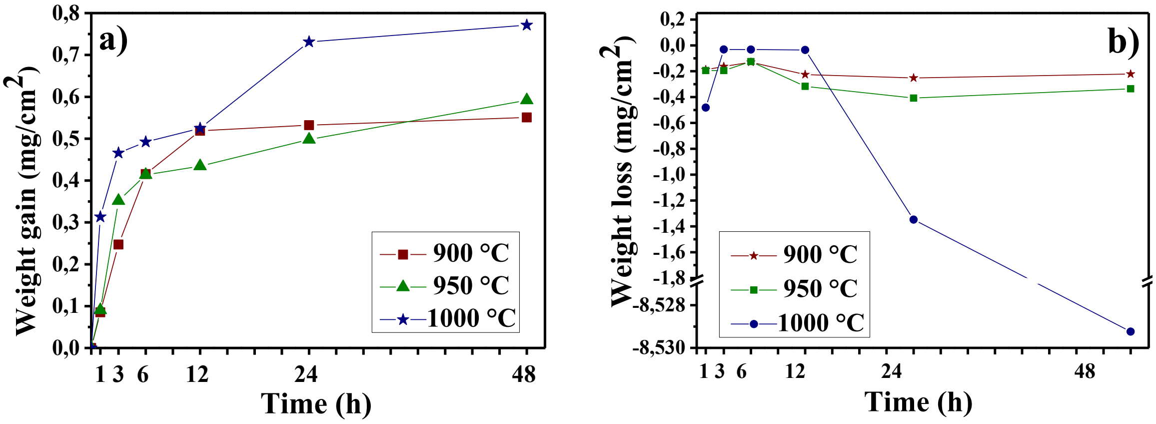

Fig. 3: Weight gain at various temperatures and different holding times: a) steel substrate, b) coated steel

From the weight gain measurements it is obvious that the tested layers provide effective protection from oxidation of stainless steel at 900 °C and 950 °C. No significant corrosion damage was observed by SEM analysis (Fig. 4a, b), coating appeared to be well adherent at these temperatures.

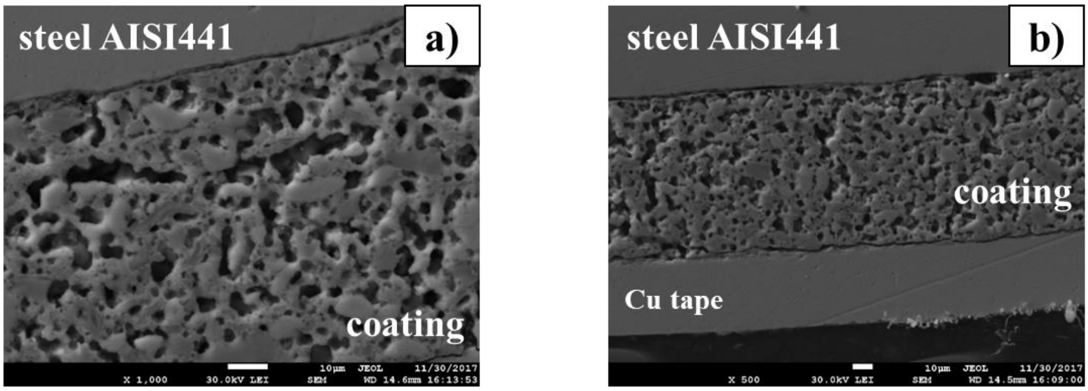

Fig. 4: SEM cross-sections of the coating after oxidation tests: a) 900°C/48h, b) 950°C/48h

Moreover, the cracks present on the surface of as-prepared coatings gradually healed due to the softening of the used glass additives. The surface of oxidized specimens was analyzed by XRD to identify new phases formed during oxidation. After longer period of oxidation, crystallization of the glass fillers lead to the formation of new crystalline phases ($Ba(AlSiO_4)_2$ – celsian, hexacelsian), but also to the formation of other phases ($ZrSiO_4$, YZr_8O_{14}) as a consequence of chemical reactions between the layer components. At higher oxidation temperature (1000 °C) and after 24 h of oxidation, the presence of oxidation products ($MnCrO_4$, Cr_2O_3) in XRD patterns (Fig. 5) was observed.

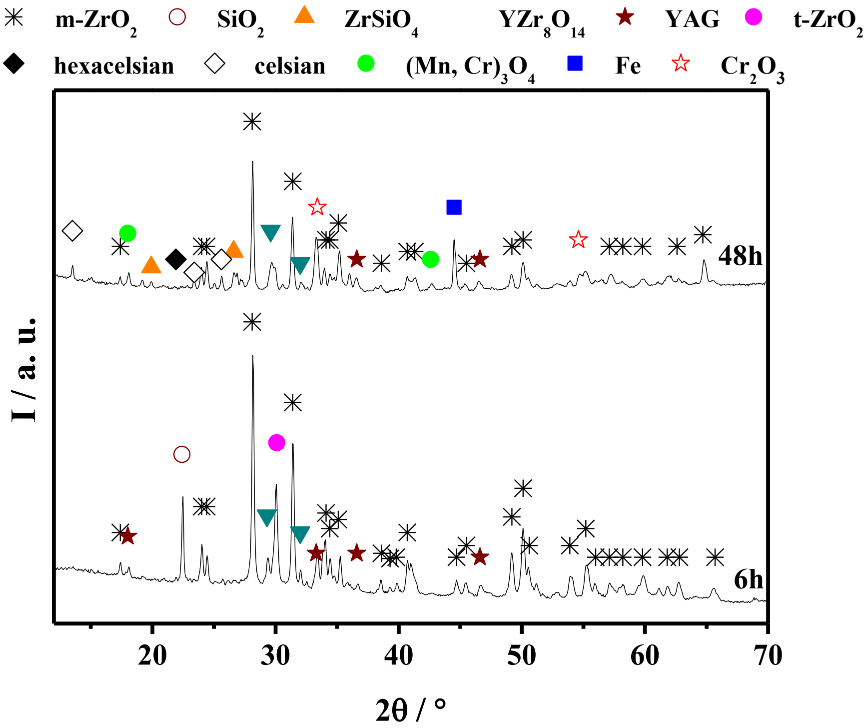

Fig. 5: XRD patterns of the coating after oxidation tests at 1000 °C

CONCLUSION

A novel polymer-derived ceramic coating system as an environmental barrier coating for stainless steel was developed, using a tailored combination of pre-ceramic precursor with passive fillers and glass frits used as sealants. The protective effect of the PDC coating system in oxidative atmosphere was observed at the temperatures up to 950 °C, while uncoated samples were strongly oxidized.

ACKNOWLEDGMENT

This paper is a part of dissemination activities of project FunGlass. This project has received funding from the grant APVV 0014-15 and European Union´s Horizon 2020 research and innovation programme under grant agreement No 739566.

REFERENCES

[1] Kappa M., Kebianyor, A., Scheffler, M. A two-component preceramic polymer system for structured coatings on metals, Thin Solid Films, vol. 519 (2010), 301–305.

[2] Greil, P. Active-Filler-Controlled Pyrolysis of Preceramic Polymers, Journal Of The American Ceramic Society, 78 (1995) 835-848.

[3] Colombo, P., et al, Polymer-Derived Ceramics: 40 Years of Research and Innovation in Advanced Ceramics, Journal Of The American Ceramic Society 93 (2010) 1805-1837.

[4] Günthner, M. et. al, High performance environmental barrier coatings, Part I: Passive filler loaded SiCN system for steel, Journal of the European Ceramic Society 31(2011) 3003–3010

[5] Kaindl, A., et al, Polymer-filler derived Mo2C ceramics, Materials Science and Engineering, 260 (1999) 101–107.

NOVEL ALKALI-ACTIVATION BASED PROCESS FOR THE MANUFACTURING OF SODA-LIME GLASS FOAMED PANELS AND GRANULES

A. Rincón[1], E. Bernardo[1].

[1]*Department of Industrial Engineering, University of Padova, Via Marzolo 9, 35131 Padova, Italy*

ABSTRACT

A new technique for the production of foamed glass foams and granules, was developed. The alkali activation of soda-lime waste glass allowed for the obtainment of well-dispersed concentrated suspensions, undergoing progressive hardening by treatment at low temperature (75 °C), owing to the formation of calcium-rich silicate hydrated compounds. The partially gelified suspensions can be foamed through mechanical stirring, also comprising a surfactant for the production of lightweight panels. The hardened suspensions could also be broken into fragments, and cast onto a rotating drum for the production of granules. Finally, a sintering treatment, at 700–800 °C, was applied, obtaining samples with high overall porosity and remarkable compressive strength.

Keywords: Gel casting; Alkali activation; Glass foams

INTRODUCTION

The recovery of glass in the urban waste collection, in order to manufacture new glass containers (‘closed-loop recycling’), has been successfully implemented in the last few years, reaching a rate of 73% of the overall volume of glass packaging in the European Union [1]. The recovery is beneficial, due to the significant savings in terms of raw materials and energy consumption upon melting (pre-formed glass acts as a flux for the reaction of mineral raw materials) [2], albeit with significant limitations. In fact, a complete reuse of glass cullet in the manufacturing of the original glass articles is far from being feasible. Glass foams are a valuable product used as thermal insulator in the building industry. The increasing demand for net-zero energy buildings along with their non-flammable properties make glass foams the perfect candidate to be used in the near future. However, their production is still expensive and quite difficult to control, and for this reason new and alternative fabrication techniques are needed to reduce production cost and increase environmental sustainability. A substantial change in the production approach of glass foams is offered by the separation of foaming and sintering steps, obtainable by gel casting technology [3], that may be applied to solutions (from sol-gel processing) [4], as well as to suspensions of glass powders [5,6]. In the present investigation, the gel provided by the alkali activation of soda-lime glass powders is used as an intermediate product for the foaming.

EXPERIMENTAL

Soda-lime glass (later referred to as ‘SLG’; chemical composition: SiO_2 = 71.9 wt%, Na_2O = 14.4%, K_2O = 0.4%, CaO = 7.5%, MgO = 4.0%, Fe_2O_3 = 0.4%, Al_2O_3 = 1.2%) from municipal waste collection of glass containers was used as starting material. It was provided by SASIL S.r.l. (Brusnengo, Biella, Italy) in the form of fine powders (75 μm). The initial fine powders were added to an aqueous solution containing 2.5 M KOH (Sigma– Aldrich, Gillingham, UK), for a solid loading of 65 wt%. The glass powders were subjected to alkaline attack for 3 hours, under low-speed mechanical stirring (500 rpm). After alkaline activation, the obtained suspension of partially dissolved glass powders was cast in closed moulds and cured at 75 °C for 0-4 h. The gels obtained at different curing times were first added with 4 wt% Triton X-100 then foamed by vigorous mechanical mixing (2000 rpm). Foamed gels were kept at 75 °C for 24 h, in order to complete the curing. Finally, hardened foamed gels were fired at 700 and 800 °C for 1 h with a heating rate of 1 °C/min or 10 °C/min. Alkali activated glass suspension was not subjected to mechanical foaming, at the early stage of gelification. After 3 hours of activation the suspension was poured into closed plastic moulds and let harden for 4 hours at 75°C. The hardened suspensions were shaped into green round aggregates through fragmentation and successive casting on a rotary drum, using dry glass to avoid amalgamation. Finally, hardened granules were fired at 800 °C for 10 minutes with a heating rate of 10 °C/min.

RESULTS

The suspensions, before foaming, due to the gelification process at low temperature, present a different rheological behaviour, which can be seen as a tuning parameter for the microstructure of the hardened foams as shown Figure 1.

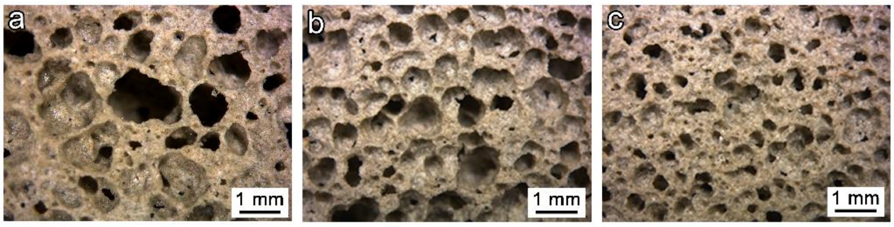

Figure 1. Hardened foamed gels after different gelification times

The hardened foams obtained after 2 hours exhibited a quite coarse microstructure, with many big interconnect pores surrounded by smaller ones, as an effect of a limited coalescence between adjacent bubbles (Fig. 1a). The higher viscosity of the suspension after a longer curing step, of 3 and 4 hours (Fig. 1b,c), progressively reduces the coalescence, and the hardened foams obtained present further spherical cells in a more homogeneous cell structure. In particular, a curing step of 4 h was found to enhance the uniformity of foams.

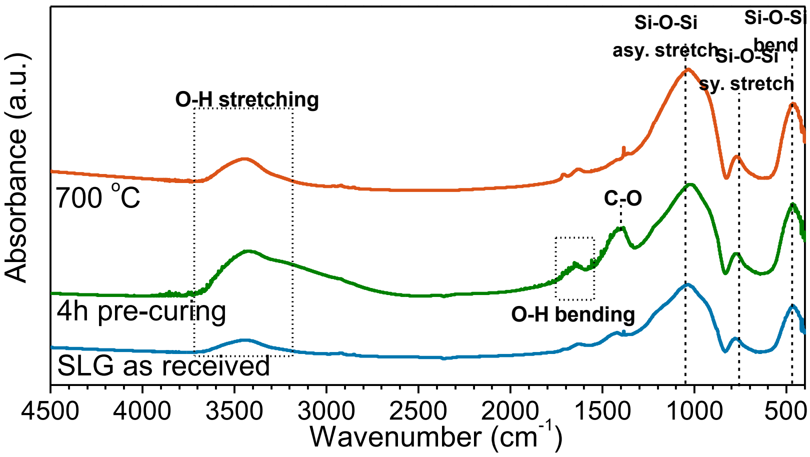

Figure 2. FTIR spectra of selected materials

Some indications relating to the nature of the compounds developed upon curing and the related transformations, upon firing, may come from the FTIR spectra of selected samples shown in Figure 2. The initial glass presents the characteristic symmetric and asymmetric stretch as well as the bending bands of Si-O groups centred at 1000, 700 and 450 cm^{-1} respectively. A broad band in the 3000-3500 cm^{-1} interval is detected in the hardened foams, and corresponds to the O-H symmetric stretch. The band at 1625 cm^{-1} generated by the bending vibrations of the OH groups. Both bands indicate the presence of hydrated compounds after alkali activation. A new band centred at 1450 cm^{-1} is produced by the stretching vibrations of O-C-O groups indicates the formation of carbonate compounds [7].

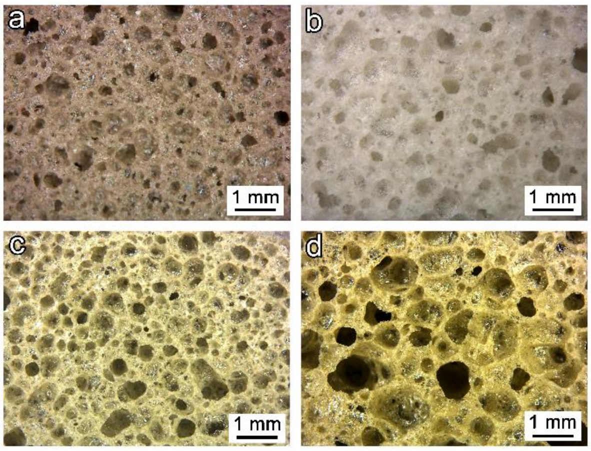

Figure 3. Microstructural details of heat treated glass foams

The pore structures of the samples produced after 4 hours of pre-gelation obtained after treatment at 700 and 800 °C, at 1 °C/min (Fig. 3a,b) and at 10 °C/min (Fig. 3c,d) are shown in Figure 3. In all samples an enlargement of the pores can be noticed, and the sample treated at 700 °C shows a more homogeneous structure presenting cells with spherical shape, meanwhile the distortion of the initial pore structure in the samples treated at 800 °C is much more evident, showing very large cells that lost their spherical form. The transformations of the cellular structure are likely due to the decomposition mentioned above of hydrated compounds, which determined a 'secondary foaming'. The secondary foaming process also determines the enlargement of the pore structure. The effect is more evident in the foams treated at a faster heating rate.

Table 1. Density, porosity and mechanical properties of the heat treated foams.

curing (hours)	Firing T^a (°C)	Density, ρ (g/cm³) geometric	apparent	true	Porosity (%) total	open	closed	σ_{comp} (MPa)
Slow heating rate (1 °C/min)								
4	700	0.30 ± 0.01	0.43 ± 0.06	2.50 ± 0.02	88 ± 1	31 ± 2	57 ± 1	4.8 ± 0.3
	800	0.28 ± 0.01	2.41 ± 0.05	2.66 ± 0.03	89 ± 1	88 ± 2	1 ± 1	2.9 ± 0.4
Fast heating rate (10 °C/min)								
4	700	0.34 ± 0.03	0.48 ± 0.08	2.48 ± 0.08	86 ± 1	29 ± 2	57 ± 3	3.3 ± 0.5
	800	0.17 ± 0.01	2.41 ± 0.06	2.66 ± 0.04	93 ± 2	84 ± 4	9 ± 2	0.4 ± 0.1

The density data in Table 1 confirm the microstructural changes that occur upon firing. After the thermal treatment, all the samples present an increment of the total porosity achieving values close to 90%, and this increase could be explained by the decomposition of the hydrates compounds with gas evolution, which promotes the foaming of the softening glass. The open porosity returned dominant at 800 °C, however, after the heat treatment at 700°C, some closed porosity is formed. It is evident that the more homogeneous samples, with 4h pre-foaming curing, fired at 700 °C in both heating modes, can be seen as the best, since they exhibited a crushing strength of more than 3 MPa with an overall porosity well above 85%.

Figure 4 shows the morphology of single granules of different sizes. The firing of green granules was accompanied by significant foaming, due to the decomposition of C-S-H compounds developed during alkali activation. It can be noticed a highly porous core surrounded by a relatively dense thin shell. The granules contain a significant volume of isolated pores of an approximately spherical shape. The formation of the outer layer plays crucial role in the final properties of the LWA as can be seen in Table 2, where the density and porosity of heat-treated LWA are reported. The produced granules present relative low densities, and can be noticed a continuous decrease of the geometrical density with increasing granule size. This fact suggests more effective foaming in the bigger granules. The granules present very high porosities, all above 70%. It can be noticed an increase of the porosity with the bigger granules size. However, the most significant changes can be detected between the incidence of open and closed porosity. Bigger granules present higher open porosity, which indicate a higher degree of coalescence between the bubbles during the fire treatment.

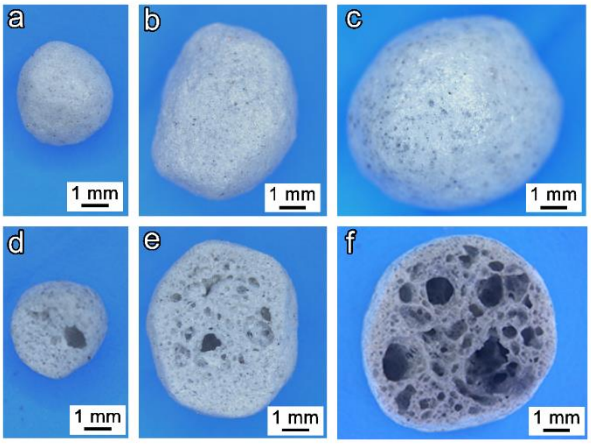

Figure 4. External aspect and cross section of waste glass derived granules

Table 2. Density, porosity and mechanical properties of heat-treated granules

Fraction (mm)	Density, ρ (g/cm^3)			Porosity (%)		
	geometric	apparent	True	total	open	closed
2 - 4	0.73 ± 0.05	0.98 ± 0.03	2.49 ± 0.02	70 ± 6	25 ± 5	45 ± 3
4 - 6.3	0.74 ± 0.06	0.98 ± 0.01	2.45 ± 0.01	70 ± 1	25 ± 1	45 ± 2
6.3 - 8	0.61 ± 0.04	0.98 ± 0.04	2.48 ± 0.01	75 ± 6	37 ± 9	37 ± 4
8 - 10	0.56 ± 0.02	1.12 ± 0.04	2.49 ± 0.01	77 ± 6	49 ± 4	27 ± 2
10 - 12.5	0.51 ± 0.02	0.98 ± 0.03	2.41 ± 0.01	76 ± 4	44 ± 7	35 ± 3
12.5 - 14	0.51 ± 0.02	0.98 ± 0.04	2.48 ± 0.01	79 ± 3	49 ± 6	30 ± 3

CONCLUSION

It can be concluded that a new generation of glass and glass-ceramic foams may be obtained by alkali activation of suspensions of the silica-rich materials and gel-casting, sintered later. The hardening of glass-based slurries is caused by the formation of calcium alumino-silicate hydrate (C-S-H)

ACKNOWLEDGMENT

This project has received funding from the European Union's Horizon 2020 research and innovation programme under the Marie Sklodowska-Curie Innovative Training Network ‘CoACH-ETN’ (‘Advanced glasses, Composites And Ceramics for High growth Industries European Training Network’, g.a. no. 642557, and the 8th European Framework programme for Research and Innovation Horizon 2020 programme (FunGlass – Centre for Functional and Surface Functionalized Glass) under grant agreement Nº739566

REFERENCES

[1] Press release European Container Glass industry welcomes long awaited circular economy package. Using waste as a secondary raw material in a closed loop is key Brussels, 02 December 2015.

[2] Beerkens, R., Kers, G., van Santen, E. Recycling of post-Consumer glass: energy savings, CO2 emission reduction, effects on glass quality and glass melting, Ceramic Engineering and Science Proceedings, 32 (2011) 167-194.
[3] Sepulveda, P., Jones J. R., Hench L. L. In vitro dissolution of melt-derived 45S5 and sol-gel derived 58S bioactive glasses. Journal of Biomedical Materials Research: An Official Journal of the Society for Biomaterials, 61 (2002) 301-311.
[4] Jones, J. R., Hench, L. L. Effect of surfactant concentration and composition on the structure and properties of sol-gel-derived bioactive glass foam scaffolds for tissue engineering, Journal of Materials Science, 38 (2003) 3783-3790.
[5] Wu, Zoe Y., et al. Melt-derived bioactive glass scaffolds produced by a gel-cast foaming technique, Acta Biomaterialia, 7 (2011) 1807-1816.
[6] Rincón, A., Giacomello, G., Pasetto, M., Bernardo, E. Novel 'inorganic gel casting'process for the manufacturing of glass foams, Journal of the European Ceramic Society, 37 (2017) 2227-2234.
[7] Vafaei, M., Allahverdi, A. High strength geopolymer binder based on waste-glass powder, Advanced Powder Technology, 28 (2017) 215-222.

NANOSTRUCTURED CATALYTIC THIN FILMS PREPARED BY SOLUTION COMBUSTION SYNTHESIS ON MULLITE-CORDIERITE CERAMICS

H. Shymanskaya[1], R. Papou[1], N. Sdobnyakov[2], D. Sokolov[2], V. Myasnichenko[2]

[1] Belarusian State Technological University, Belarus, Minsk, 220006, Sverdlova str.13a.

[2] Tver State University, Russia, Tver, 170100, Zhelyabova st. 33.

ABSTRACT

Solution combustion synthesis (SCS) is typically used to produce nanostructured oxides and bulk metallic materials for a variety of application including catalysis. Here, we report SCS of thin films catalysts supported on mullite-cordierite ceramics. The catalysts were characterized by XRD, SEM/EDX, and their catalytic activity has been determined in CO oxidation. Also, the effect of different types of fuels (urea, citric acid and hexamethylenetetramine) on the combustion process and characteristics of resultant solid products were investigated.

Keywords: nanopowders, solution combustion synthesis, catalyst, mullite-cordierite ceramics, metal-ceramic catalyst

INTRODUCTION

CO oxidation is a process widely used for neutralization of exhaust gases of internal combustion engines and in various industries such as metallurgical, petrochemical and et. [1, 2]. Many researchers note that the catalytic activity of the bimetallic catalyst is higher than the activity of the monometalic ones [3–5]. At the present time solution combustion synthesis is used for the preparation of oxide-based catalysts with a surface area higher than those obtained by co-precipitation methods. Recently, several metals (Ni, Cu, Fe, Co) have been synthesized by this method [6–7]. The aim of this work is to investigate the possibility of bimetallic catalysts synthesis by SCS in normal air atmosphere without additional post reduction and study of catalytic activity in CO oxidation. The effect of the different fuels on the combustion synthesis process and structure of metallic nanoparticles was also investigated. Mullite-cordierite ceramics were chosen as the catalyst carrier because of chemical inertness, mechanical strength and stability.

EXPERIMENTAL

Preparation of reactant solutions for SCS

The following materials were used in the experiments: copper nitrate – $Cu(NO_3)_2{\cdot}3H_2O$, "analytical grade" GOST 4163-78 (content of the main component is 99.6 wt.%), cobalt nitrate – $Co(NO_3)_2{\cdot}6H_2O$, "analytical grade" GOST 4528-78 (content of the main component is 99.6 wt.%), nickel nitrate – $Ni(NO_3)_2{\cdot}6H_2O$, "analytical grade" GOST 4055-78 (content of the main component is 99.6 wt.%), citric acid hydrate – $C_6H_8O_7{\cdot}H_2O$, "analytical grade" GOST 908-2004 (content of the main component is 99.8 wt.%), urea – CH_4N_2O, "analytical grade" GOST 6691-77 (content of the main component is 99.2 wt.%) and hexamethylenetetramine – $C_6H_{12}N_4$, "analytical grade" GOST 1381-73 (content of the main component is 99.5 wt.%). The quantities of used reactant are summarized in Table 1.

Table 1. Quantities of reactants used in preparation of reactive solutions

No. solution	Fuel / oxidizer ratios (φ)	Reactant (wt.%)					
		$Cu(NO_3)_2$	$Ni(NO_3)_2$	$Co(NO_3)_2$	CH_4N_2O	$C_6H_8O_7$	$C_6H_{12}N_4$
1	1.25	27.97	27.25	–	44.78	–	–
2	1.75	23.72	23.11	–	53.17	–	–
3	1.25	27.16	26.46	–	–	46.38	–
4	1.75	22.91	22.32	–	–	54.77	–
5	1.25	38.51	37.51	–	–	–	23.98
6	1.75	35.14	34.22	–	–	–	30.64
7	1.25	25.66	–	25.03	49.31	–	–
8	1.75	22.04	–	21.50	56.46	–	–
9	1.5	24.85	–	24.24	–	50.91	–
10	2.0	21.25	–	20.72	–	58.03	–
11	1.5	36.73	–	35.82	–	–	27.45
12	2.0	33.65	–	32.82	–	–	33.53
13	2.0	22.50	21.92	21.95	–	–	33.63
14	4.0	16.84	16.40	16.42	–	–	50.34

The reactive mixture (5 g) was dissolved in distilled water (5 ml). Ammonia was added to the resultant solution to adjust the pH value at about 7.

Process for producing metallic nanopowders

The obtained solutions were ignited and burned in thermal explosion mode in preheated to 500°C a muffle furnace in air atmosphere, leading to the formation of a fluffy powder, which was rapidly cooled in air in a quenching mode to prevent metal oxidation.

Synthesis of mullite-cordierite ceramics

The starting materials used to prepare mullite-cordierite ceramics were Vesko-Granitik refractory clay (TU U 14.2-00282049-003–2007, Ukraine), Onotsky talc (GOST 21235–75, Russia), GK-1 alumina (GOST 30559–98, Russia), aluminosilicate fireclay. The chemical composition of used raw materials summarized in Table 2.

Table 2. The chemical compositions of used raw materials (wt.%)

	SiO_2	Al_2O_3	TiO_2	Fe_2O_3	CaO	MgO	Na_2O+ K_2O	Calcination loss
Refractory clay	59.19	26.72	1.23	0.81	0.28	0.50	2.08	9.19
Talc	60.45	0.68	0.06	0.86	0.13	30.04	–	7.78
Alumina	0.30	99.30	–	0.03	0.06	–	0.18	0.13
Fireclay	32.56	64.09	0.40	0.67	0.14	0.06	2.08	–

The raw materials mixed in ratio, which corresponded to the stoichiometric composition of cordierite: $2MgO·2Al_2O_3·5SiO_2$. The slip was prepared by wet grinding of the components in a ball mill (Speedy, Italy) to 0.1–0.3 wt.% residue in a No. 0056 sieve with material : milling body : water ratio 1 : 1.5 : 0.5. Polyurethane reticulated foams were used as porous matrices, which were completely burnt out during sintering. The polyurethane matrices were substantially impregnated with obtained ceramic slip. The ceramic suspension settled on the matrix surface and repeated the matrix structure. The samples were dried at 100–120 °C during 3 h and sintered in a laboratory kiln Nabertherm (Netzsch) at 1250 °C for 1 h.

Fabrication of thin films on mullite-cordierite ceramics

The samples of mullite-cordierite ceramics were substantially impregnated with obtained solutions, then burned in thermal explosion mode in preheated to 500 °C a muffle furnace in air atmosphere and rapidly cooled in air. The photos of final materials are presented in Fig.1.

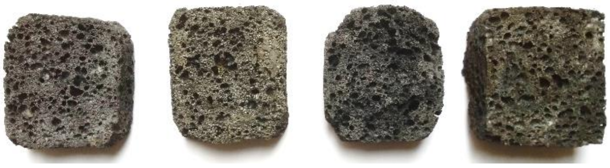

Fig.1. Photos of the synthesized metal-ceramic catalysts

Methods

The catalytic activity of SCS catalysts was studied on the installation shown in the research [1]. X-ray phase analysis was performed with a D8 ADVANCE (Bruker, Germany) setup. A JSM-5610 LV scanning electron microscope with an EXS JED-2201 JEOL chemical analysis system (Japan) was used to investigate the microstructure. To determine the size of crystalline blocks, we used the Scherrer equation.

RESULTS

Metal NPs were synthesized by SCS method during the first phase of the research. The results of X-ray diffraction analysis of the powders produced by SCS from the initial mixtures, at a different ratio of components, are shown in Table 3.

Table 3. Phase composition and average particle size of the synthesized powders.

No. catalyst	Phase composition	Average sizes of nanoparticles, nm
1	**CuO**, **NiO**	50–60
2	**NiO**, **$Cu_{0,63}Ni_{0,37}$** (a=3.5811(2) Å), NiO, Cu_2O	50–60
3	**$Cu_{0,67}Ni_{0,33}$** (a=3.5850(2) Å), NiO, CuO, Cu_2O	50–60
4	**$Cu_{0,86}Ni_{0,24}$** (a=3.5933(2) Å), NiO, CuO, Cu_2O	50–60
5	**$Cu_{0,48}Ni_{0,52}$** (a=3.5677(2) Å), **NiO**, **Cu,** CuO, Cu_2O	50–60
6	**$Cu_{0,51}Ni_{0,49}$** (a=3.5701(2) Å), **Cu**	50–60
7	**Cu**, **CuO**, **CoO**, Co_3O_4	50–60
8	**Cu**, **CuO**, **CoO**, Co, Co_3O_4	50–60
9	**Cu**, **CuO**, **CoO**, **Co_3O_4,** Co	50–60
10	**Cu**, **CuO**, **CoO**, Co, Co_3O_4	20–25
11	**Cu**, **CuO**, **CoO**, Co_3O_4	50–60
12	**Cu**, **CuO**, **CoO**, Co, Co_3O_4	50–60
13	**$Cu_{0,62}Ni_{0,38}$** (a=3.580 Å), **CoO**, **CuO**, **Cu–Ni–Co solid solution** (a=3.740 Å)	50–60
14	**Cu–Ni–Co solid solution** (a=3.740 Å), **Cu**	40–50

Diffraction peaks of metal oxide phases were also detected for this sample. It is evident, that the using of nonmodified SCS method does not yield pure metallic nanoparticles under normal air atmosphere without additional post reduction. All powders formed during the combustion had foam-like microstructure. SEM images of powders obtained in the systems $Cu(NO_3)_2 - Co(NO_3)_2 - Ni(NO_3)_2 - C_6H_{12}N_{14}$ (φ=4.0), sample of mullite-cordierite ceramics and synthesized mullite-cordierite catalysts, prepared using the solution 14, are shown in Fig. 2. As seen in Fig. 2 (c), the product formed during the combustion of the impregnated media had a highly porous nanoparticulate structure. Therefore, the extremely fine metallic particles formed in the combustion front oxidized evenduring the relatively short duration of the postcombustion zone [6]. The synthesized metal-ceramic catalyst had 45–50 % CO conversion at 100 °C.

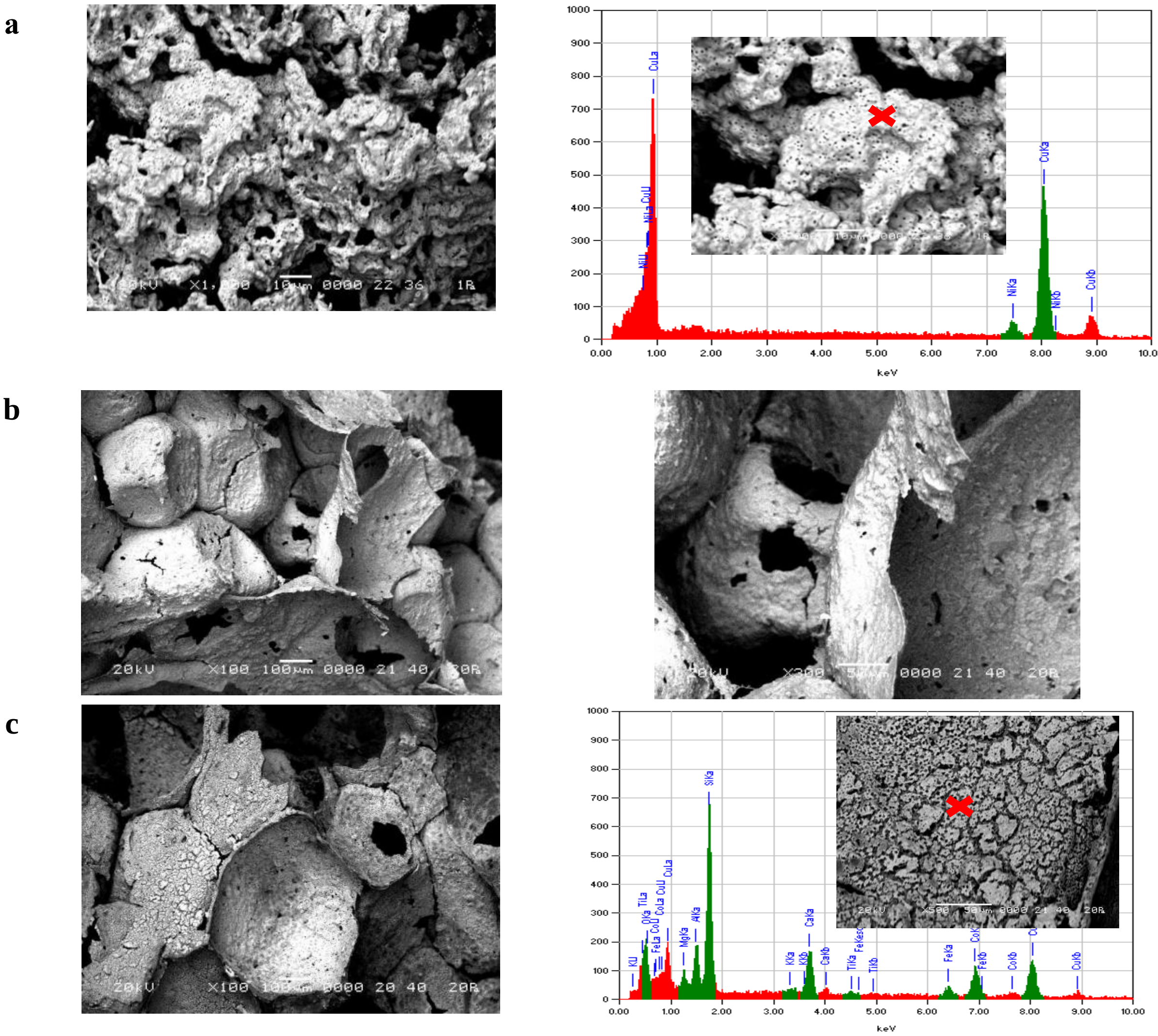

Fig. 2. SEM images and EDS spectrum of the: a) catalyst 14, b) mullite-cordierite ceramics, c) metal-ceramic catalyst.

CONCLUSION

For the first time, there has been shows the availability of the SCS technique for production of bimetallic Cu-Ni nanoparticles and Cu–Ni–Co solid solution by one-step synthesis in a normal air atmosphere without any post reduction processing. The fuel effects on the phase composition and grain size have been investigated. The formation of $Cu_{0,51}Ni_{0,49}$ solid solution and Cu was observed in the case of using of $C_6H_{12}N_4$ fuel (φ=1.75), Cu–Ni–Co solid solution and Cu – $C_6H_{12}N_4$ fuel (φ=4.0). It was found that the product formed during the combustion of the impregnated media were metal oxides due to rapid oxidation formed metallic particles.

ACKNOWLEDGMENT

The authors gratefully acknowledge the financial support of Belarusian Republican Foundation for Fundamental Research (research project X17PM-032), Russian Foundation for Basic Research (project 17-53-04010).

REFERENCES

[1] Novikov, V., Xanthopoulou, G., Knysh, Yu., Amosov, A.P. Solution Combustion Synthesis of nanoscale Cu-Cr-O spinels: Mechanism, properties and catalytic activity in CO oxidation, Ceramics International, 43 (2017) 11733–11742.

[2] Wang, L., Yang, L., Zhang, Y., Ding, W., Chen, S., Fang, W., Yang, Y. Promoting effect of an aluminum emulsion on catalytic performance of Cu-based catalysts for methanol synthesis from syngas, Fuel Processing Technology, 91 (2010) 723–728.

[3] Mirzaei, A. A., Beigbabaei, A., Galavy, M., Youssefi, A. A silica supported Fe–Co bimetallic catalyst prepared by the sol/gel technique: Operating conditions, catalytic properties and characterization, Fuel Processing Technology, 91 (2010) 335–347.

[4] Mirzaei, A. A., Habibpour, R., Faizi, M., Kash, E. Characterization of iron-cobalt oxide catalysts: Effect of different supports and promoters upon the structure and morphology of precursors and catalysts, Applied Catalysis A: General, 301 (2006) 272–283.

[5] De la Peña O'Shea, V., Alvarez-Galvan, M., Campos-Martin, J., Luis García Fierro, J. Fischer-Tropsch synthesis on mono- and bimetallic Co and Fe catalysts in fixed-bed and slurry reactors, Applied Catalysis A: General, 326 (2007) 65–73.

[6] Cross, A., Roslyakov, S., Manukyan, K., Rouvimov, S., Rogachev, A., Kovalev, D., Wolf, E., Mukasyan, A. In situ preparation of highly stable ni-based supported catalysts by solution combustion synthesis, The Journal of Physical Chemistry, 118 (2014) 26191–26198.

[7] Khort, A., Podbolotov, K., Serrano-García, R., Gun’ko, Yu One-step solution combustion synthesis of cobalt nanopowder in air atmosphere: The fuel effect, Inorganic Chemistry, 57 (2018) 1464−1473.

VPLYV PRÍDAVKU Al_2O_3 NA SPEKANIE A UPCONVERSION VLASTNOSTI $CaZrO_3$

INFLUENCE OF Al_2O_3 ADDITION ON SINTERING BEHAVIOUR AND UPCONVERSION OF $CaZrO_3$

P. Veteška[1], K. Tomanová[1], Z. Hajdúchová[1], Ľ. Bača[1], M. Janek[1]

[1]*Oddelenie anorganických materiálov, FCHPT STU v Bratislave*

ABSTRACT

This work is aimed at using ultrafine alumina as sintering agent for calcium zirconate material doped with Yb and Er for archieving upconversion properties using sintering temperatures below 1500°C. Several levels of alumina addition have been investigated (0,0.5,1.0,3.0 and

5.0 mol %). Correlation between alumina addition and changes in phase composition of samples have been observed. The positive effect of alumina addition to upconversion properties of prepared powders was confirmed for samples annealed at 1400°C where the addition of small amount of ultrafine Al_2O_3 leads to slight increase in upconversion intensities.

Keywords: upconversion, alumina, calcium zirconate, sintering, perovskite

INTRODUCTION

Calcium zirconate, $CaZrO_3$ is the most stable compound in the quasi-binary system ZrO_2 - CaO. Calcium zirconate has become a system of considerable interest due to its high melting point, good thermal shock resistance and its excellent chemical stability [1]. $CaZrO_3$-based doped oxides belong to the class of high-temperature perovskite-type proton conductors and are therefore applicable as electrolytes in solid oxide fuell cells [2]. Gas and humidity probes and up-conversion phosphors are another of the most frequently studied applications of calcium zirconate system [3]. Calcium zirconate ceramic as host for luminophores having of upconversion properties is often paired with Er^{3+} or Er^{3+}/Yb^{3+}. The Er^{3+} can replace the Ca^{2+} in the $CaZrO_3$ structure or preferably(if present - usually in systems with eutectic composition) calcia-stabilized zirconia(CaSZ) [4, 5]. Upconversion is a process where the absorption of two or more lower-energy photons leads to the emission of a higher energy photon. Most upconversion materials are based on the f-f transitions of rare-earth dopants e.g. Er^{3+}, Nd^{3+}, Pr^{3+}, Dy^{3+} and others [6]. Er^{3+} is one of the most frequently used doping agents as its absorption and emission spectra allow the use in various types of host materials to produce luminescence in the red and green spectral range. Due to low probability of f-f transitions in Er^{3+}, co-dopants are often employed to increase the efficiency of upconversion phosphors [5, 7].

EXPERIMENTAL

Calcium chloride dihydrate ($CaCl_2 . 2H_2O$, 99%, Sigma-Aldrich), Zirconium (IV) nitrate hydrate ($Zr(NO_3)_2 . xH_2O$, Sigma-Aldrich, 99%) Erbium (III) nitrate pentahydrate (Er(NO3)3 . $5H_2O$, 99.99%, Treibacher Industrie AG) and Ytterbium (III) nitrate pentahydrate ($Yb(NO_3)_3 . 5H_2O$, 99.99%, Treibacher Industrie AG) were used as the starting materials. For the synthesis of $CaZrO_3:Er_1Yb_2$ Pechini method was used, which include chelating of water dissolved salts by citric acid and esterification by ethylene glycol. Resulting gel was at first calcined at 600°C for 1h in air. After annealing, the samples were transferred to agate mortar, calculated amount of ultrafine alumina powder TM-DAR (Taimicron, Japan) ranging from 0,5mol.% to a maximum of 5mol.% was added and the powders were thoroughly homogenized. List of prepared powder samples is shown in Tab.1. Specimen were pressed to pellets using uniaxial press (pressure=5MPa) with the diameter of 10 mm and then sintered in supercantal furnace at 1400°C and 1500°C, respectively (heating/cooling rate 10°C/min, holding time 60 minutes). The density was calculated based on Archimedes law from mass values measured in mercury. The presence of crystalline phases in the samples was determined by XRD analysis (STOE Theta/Theta, Germany; CoKα radiation, λ = 0.179 nm, operating at 40 kV and 30 mA). The upconversion luminescence was studied under 980 nm laser excitation (adjustable DPSSL Laser MDL-W 4W) and UV-VIS spectrometer (Ocean Optics USB4000).

Tab.1. Overview of sample designation and their relative densities with respect to the pure orthorhombic $CaZrO_3$ *with the density of 4.63g.cm*$^{-3}$

Sample name	Al_2O_3 content (mol. %)	Relative Density	
		1400°C/1h	**1500°C/1h**
A0	0	67.2	73.6
A05	0.5	78.9	-
A10	1.0	85.6	94.6
A30	3.0	73.5	92.5
A50	5.0	61.9	61.8

RESULTS

The upconversion (UC) emission spectra of undoped and alumina doped $CaZrO_3:Er_1Yb_2$ samples sintered at 1400°C and 1500°C for 1h are shown in Fig.1. Samples were excited by laser diode operating at l=980nm with the power of 300mW. Due to absorption of laser energy, Yb^{3+} ions are excited from ground state $^2F_{7/2}$ to $^2F_{5/2}$ level. Large part of this energy is efficiently transfered to Er^{3+} ions due to the similarity between Yb^{3+} emission and Er^{3+} absorption. As a result of this transfer three main excited states of Er^{3+} ions are present: $^4F_{9/2}$, $^2H_{11/2}$ and $^4S_{3/2}$ showing green emissions due to $^2H_{11/2}(^4S_{3/2})\rightarrow{}^4I_{15/2}$ transition and the red emission from the $^4F_{9/2}\rightarrow{}^4I_{15/2}$ transition.

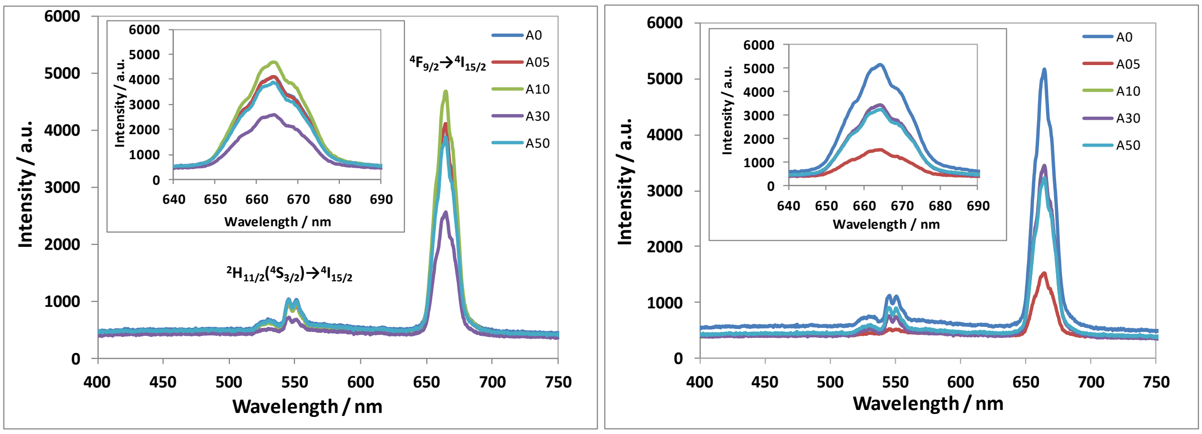

Fig. 1. Upconversion emission spectra of undoped and alumina doped $CaZrO_3:Er_1Yb_2$ *samples sintered at 1400°C (left) and 1500°C for 1h(right)*

The green emissions take place between 515 nm to 560 nm and red one in the range of 640 nm to 690 nm. The relative densities of samples sintered at 1400 °C show poor densification independently on the dopant concentration. At this temperature UC spectra show that the intensity of luminescence is the best for A10 sample followed by sample A05 and A0. An increase of sintering temperature to 1500°C caused the increase of relative UC intensity of undoped A0 sample, however drop in the samples A10 and A05 in spite of improvement of relative density to 94.6% for A10 sample. It is interesting to note that the relative density of samples doped with highest amount of alumina (A50) showed similar, poor densification as undoped one (A0). The phase analysis of the undoped and alumina doped $CaZrO_3:Er_1Yb_2$ samples sintered at 1400°C and 1500°C for 1h revealed the orthorhombic perovskite structure of $CaZrO_3$ (JCPDS 35-0790) in all samples (Fig. 2.). In addition to $CaZrO_3$ phases such as free CaO and carbon were identified as major impurities. These phases seem to be crucial during the densification process. The cubic CaO with unit cell volume of 111.64 Å^3 [10] can react with humidity to form trigonal $Ca(OH)_2$ with unit cell volume 54.82 Å^3 [9] and thus can considerably change not only the densification process, but also the luminescence properties. On the other side the luminescence of samples is also affected by presence of carbon impurities coming the most probably from incomplete combustions of organic rest.

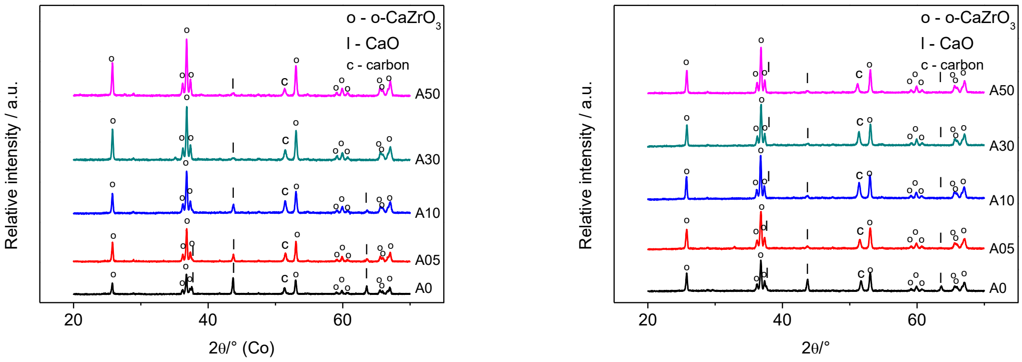

Fig. 2: XRD patterns and alumina doped $CaZrO_3:Er_1Yb_2$ samples at 1400°C (left) and 1500°C (right)

Presence of CaO is clearly visible in the diffraction patterns of A0 samples without alumina. As the amount of alumina increases, the intensity of CaO diffraction peaks decreases. Visible drop in CaO peak intensity is visible for samples A10 to A30 annealed at 1400°C. Then the CaO remains unreacted inspite of increasing amount of alumina. At 1500°C the diffraction intensities assigned to CaO also decline with the concentration of alumina and for samples A30 and A50 only very small peak of CaO can be found. The poor sintering behaviour of studied up-conversion material can be attributed to the high melting point of calcium zirconate, however also impurities found. Alumina with the max 3 mol.% addition seems to be good alternative for improving of sintering process. Higher amount of alumina didn´t show further progress in the densification of $CaZrO_3$ at studied temperatures.

CONCLUSION

A series of samples was prepared to examine the sintering behaviour of calcium zirconate ceramic when subjected to thermal processing at temperatures ranging from 1400°C to 1500°C. XRD analysis confirms that CaO content in the samples decreases with the addition of ultrafine alumina powder. Sintering process at 1500°C for 1h eliminates effectively the residual CaO even with only 0.5mol% addition of alumina, while for samples annealed at 1400°C higher amount of additive is required. With the addition of 1 mol.% of ultrafine alumina powder to $CaZrO_3:Er_1Yb_2$ the relative density reached almost 95% at 1500°C.

ACKNOWLEDGMENT

This work is based on the results of the project Center for Applied Research of New Materials and Technology Transfer, ITMS 26240220088, supported by the Science and Research Operational Program by the European Regional Development Fund. Financial support of projects VEGA 1/0906/17 and APVV-16-0341 is gratefully acknowledged.

REFERENCES

[1] DUDEK, M a G RÓG. Calcium zirconate as a solid electrolyte for electrochemical devices applied in metallurgy. Materials Science Poland [online]. 2006, roč. 24, č. 1, s. 253–260. ISSN 01371339. Dostupné z: http://yadda.icm.edu.pl/baztech/element/bwmeta1.element.baztech-article-BPW1-0021-0105

[2] YU, T., W. G. ZHU, C. H. CHEN, X. F. CHEN a R. Gopal KRISHNAN. Preparation and characterization of sol-gel derived CaZrO3dielectric thin films for high-k applications. Physica B: Condensed Matter [online]. 2004, roč. 348, č. 1–4, s. 440–445. ISSN 09214526. Dostupné z: doi:10.1016/j.physb.2004.01.147

[3] DU, Qingqing, Guangjun ZHOU, Juan ZHOU a Haifeng ZHOU. Combustion synthesis and photoluminescence properties of CaZrO3: Eu3+ with highly enhanced brightness by Li+ doping. Journal of Luminescence [online]. 2013, roč. 137, s. 83–87. ISSN 00222313. Dostupné z: doi:10.1016/j.jlumin.2012.12.046

[4] BALDA, R., S. GARCÍA-REVILLA, J. FERNÁNDEZ, R. I. MERINO, J. I. PEÑA a V. M. ORERA. Near infrared to visible upconversion of Er3+ in CaZrO3/CaSZ eutectic crystals with ordered lamellar microstructure. Journal of Luminescence [online]. 2009, roč. 129, č. 12, s. 1422–1427. ISSN 00222313. Dostupné z: doi:10.1016/j.jlumin.2009.01.024

[5] SINGH, Vijay, Vineet KUMAR RAI a Markus HAASE. Intense green and red upconversion emission of Er 3+ ,Yb 3+ co-doped CaZrO 3 obtained by a solution combustion reaction. Journal of Applied Physics [online]. 2012, roč. 112, č. 6, s. 063105. ISSN 0021-8979. Dostupné z: doi:10.1063/1.4751450

[6] FIGUEIREDO, Alberthmeiry T De, Cristiano M BARRADO, Raphael LUCAS, De SOUSA, D ALVARENGA, Fabiana V MOTTA, Carlos A PASKOCIMAS a Mauricio R D BOMIO. Luminescence Property of Perovskite Structure. International Journal of New Technology and Research. 2015, roč. 1, č. 7, s. 22–29.

[7] TIWARI, Neha a Vikas DUBEY. Luminescence studies and infrared emission of erbium-doped calcium zirconate phosphor. Luminescence [online]. 2016, roč. 31, č. 3, s. 837–842. ISSN 15227243. Dostupné z: doi:10.1002/bio.3039

[8] Shen, C.H., Liu, R.S., Lin, J.G., Huang, C.Y. Phase stability study of La1.2Ca1.8Mn2O7, Mater Res Bull, 36 (2001) 1139

[9] Busing, W.R. and Levy, H.A. Neutron Diffraction Study of Calcium Hydroxide, J. Chem. Phys, 26 (1957) 563

ODLIEVANIE A BEZTLAKOVÉ SPEKANIE Al_2O_3 KERAMIKY AKO MODELU PRE PRÍPRAVU 3D OBJEKTOV

CASTED ALUMINA CERAMICS AS A MODEL FOR SINTERING OF 3D PRINTED OBJECTS PREPARED BY FFF

M. Orlovská[1], K. Tomanová[1,2], V. Kovár[1], M. Kitzmantel[3], E. Neubauer[3], Ľ. Bača[1]

[1] Oddelenie anorganických materiálov, Ústav anorganickej chémie, technológie a materiálov FCHPT STU, Radlinského 9, 812 37 Bratislava

[2] Oddelenie spracovania polymérov, Ústav prírodných a syntetických polymérov, FCHPT STU, Radlinského 9, 812 37 Bratislava

[3] RHP-Technology GmbH, Forschungszentrum, 2444 Seibersdorf, Austria

ABSTRACT

For three commercial alumina powders grain size, density and porosity were investigated on samples prepared by casting. Relative densities higher than 95% of theoretical density (T.D.) and zero open porosities were obtained after conventional sintering at 1400°C for all three alumina powder types, but with significant changes in microstructure. Grain growth depending on sintering temperatures up to 1450°C is evaluated statistically by least square method. As a future outlook, the studied alumina powders could be used as a potential candidate for preparation of high purity alumina filaments suitable for 3D printing by fused filament fabrication (FFF).

Keywords: grain growth, alumina, microstructure, conventional sintering, casting

INTRODUCTION

Bulk density, porosity and grain sizes are major keys in investigation of sintering behaviour. In the literature, high purity alumina powder, called TM-DAR is used mostly for the experiments because of its small particle sizes (0.1 – 0.2 µm). Thanks to its properties and many types of sintering conditions, almost fully dense samples can be prepared at relative low temperatures [1 - 2]. Also, translucent alumina can be prepared if requirements as high relative density (99 % of T.D.) and grains of diameter below 0.5 µm are kept. In that case, conventional sintering in air, at high temperatures in vacuum or by hot isostatic pressing are used [3 - 4]. Corresponding to the literature where sintering of alumina is studied, it is assumed that a certain energetic barrier between the densification process and the grain growth can exist. Presence of the barrier could explain almost similar results achieved by using different sintering temperatures at two step sintering processes [5 - 7].

For commercial applications it is often a prerequisite to use different high purity alumina powders as a potential and cheaper replacement of TM-DAR powder. In this work, conventional sintering in air is used to achieve relative densities higher than 95 % and zero open porosity for three different powders described below. Grain sizes of the selected powders as a function of sintering temperature is presented besides scanning electron microscopy and statistical data evaluation.

EXPERIMENTAL

Green bodies were prepared by casting of water suspension containing of 74 wt.% of alumina powder (TM-DAR, AA-04 or PG4N25) and 0.8 wt.% of dispersant Dolapix CE64 [4]. Particle sizes of used alumina powders are in Table 1. Firstly, the suspension was homogenized on rollers for 8 hours and then poured into plastic moulds. Drying was done in vacuum for 12 hours at room temperature, at ambient conditions for 1 – 3 days (depending on the type of alumina powder) and in the drier at 40 °C for 3 hours. First, the temperature of 850°C was used for pre-sintering followed by sintering step in the temperature range of 1200 – 1450 °C (both regimes are given in Table 2, Table 3 shows the final sintering temperatures and corresponding open pore volume).

Table 1 Properties of alumina powders

	AA-04 powder	***TM-DAR powder***	***PG4N25 powder***
Particle size	0.4 – 0.7 µm	0.1 – 0.2 µm	0.5 – 0.8 µm
Purity	99.99 %	99.99 %	99.99 %

The basic properties, such as bulk density and open porosity were measured in mercury and according to ISO 5017:2013, respectively. The microstructure was characterized by scanning electron microscope JEOL 7500 equipped with SE and BSE detectors. Statistical analysis of grain diameters was done by least square method while ImageJ program helps with the diameter calculations.

Table 2 Presintering and sintering regime

	Final temperature	***Heating rate***	***Dwell time at final temperature***	***Atmosphere***
Presintering	850 °C	2 °C / min to 500 °C 5 °C / min to 850 °C	1h	air
Sintering	1200 – 1450 °C in steps of 50 °C	5 °C / min	1h	air

RESULTS

Open porosity and relative density as a function of the sintering temperature for 3 commercial alumina powders with different primary particle sizes are shown in Table 3 and Fig. 1, respectively.

Table 3 Results of volume of open pores (cm^3)

Temperature	*AA-04 powder*	*TM-DAR powder*	*PG4N25 powder*
850°C	0.0378	0.0417	0.0944
1200°C	0.0458	0.0086	0.0537
1250°C	0.0344	0.0003	0.0490
1300°C	0.0159	0.0003	0.0120
1350°C	0.0029	0.0000	0.0086
1400°C	0.0001	0.0000	0.0001
1450°C	0.0001	0.0000	0.0001

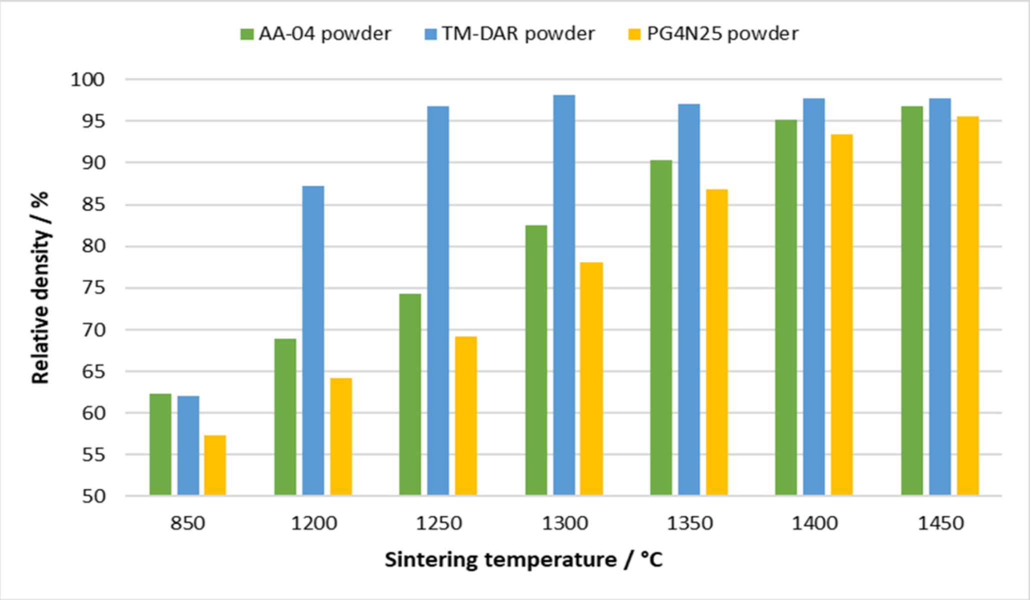

Fig. 1 Relative density as a function of sintering temperature

Absorptivity measurements revealed that the open porosity disappears after sintering at 1400 °C (1h) for AA-04 and PG4N25 powders, but for TM-DAR powder a lower sintering temperature of 1250 °C is sufficient. The same trend is observed in the results of bulk density measurements shown in Fig. 1. Relative density is calculated in relation to theoretical density of 3.99 g.cm^{-3}. It can be assumed that AA-04 or PG4N25 powders could replace TM-DAR in preparation of almost fully dense ceramics but the sintering temperatures need to be increased by 150 °C. This assumption is confirmed by results from SEM in Fig. 2, where the comparison of samples sintered at defined temperatures is shown: 1400°C for AA-04, 1250 °C for TM-DAR and 1450 °C for PG4N25 powders respectively.

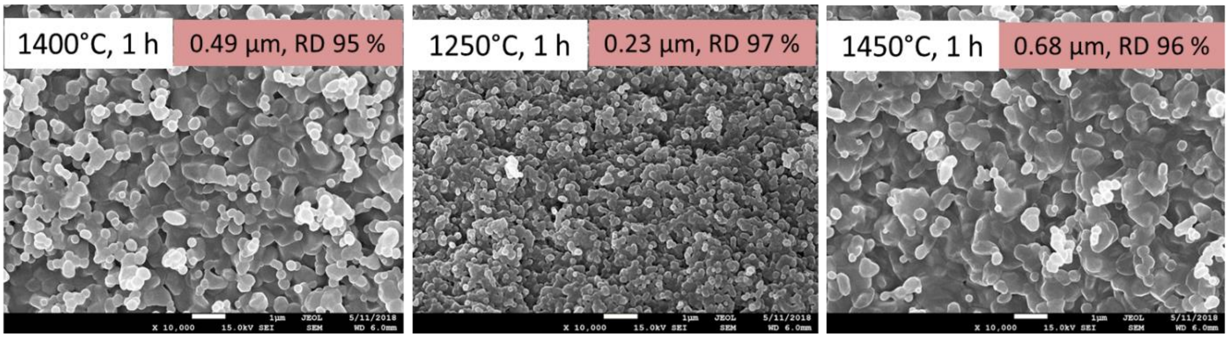

Fig. 2 SEM micrographs for AA-04, TM-DAR and PG4N25 powder sintered at desired temperatures, respectively. Relative density (RD) is kept between 95 and 97 % for all three powder types

Average grain sizes, given in Fig. 2, have only informative character about grain diameters in the samples but do not inform us correctly about the sintering process and a the process of grain growth. For this purpose, part of the Weibull statistical analysis with least square method as criteria was done on AA-04 powder samples. Over 500 grain diameters (*d*) for every sample have undergone mathematical operations to find an appropriate number of formula members and its parameters (*a*, *b*, *c*) which should fit experimental data. Basic form of the formula is given in Equation 1.

Equation 1

$$f(d) = \frac{b}{a^b}(d-c)^{b-1} exp\left[-\left(\frac{d-c}{a}\right)^b\right]$$

Results from the statistical analysis are illustrated in the Fig. 3 as a function of grain diameters. This diagram provides more information about grain size distribution compared to the average size only. It is seen, that alumina samples sintered at temperatures up to 1350 °C have narrow distribution of grains with the maximum at 0.25 µm and from this temperature upwards grain size distribution spreads to higher values. In the case of 1450 °C a polydispersion system is observed with its maximum at 0.6 µm.

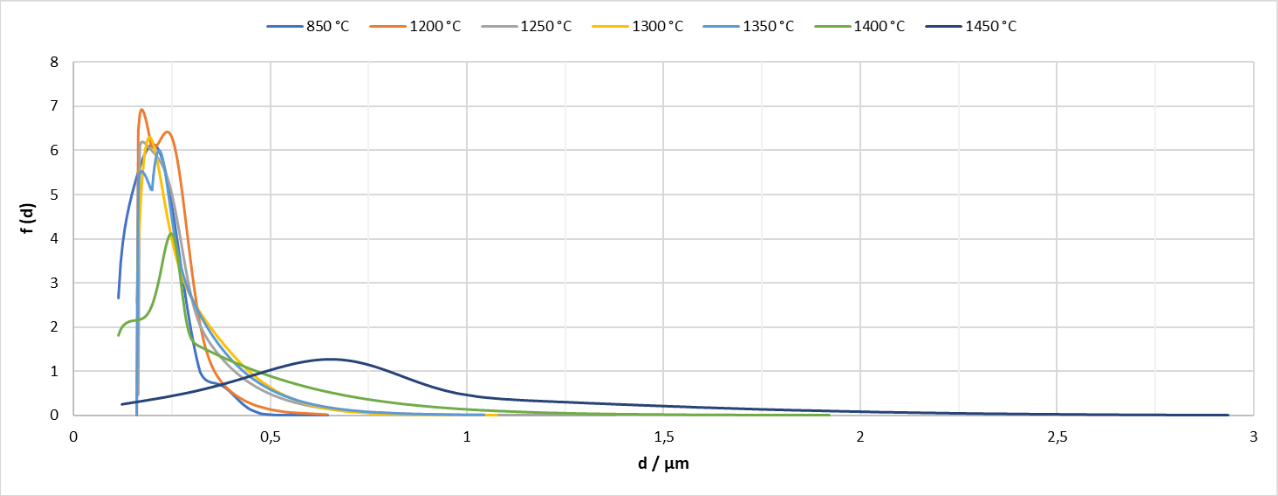

Fig. 3 Grain size distribution as a function of sintering temperature

CONCLUSION

In this work, three commercial alumina powders (AA-04, TM-DAR, PG4N25) with various particle sizes were used to compare their sintering behaviour. Following sintering temperatures were found to be necessary to reach relative density higher than 95% with zero open porosity – 1250 °C for TM-DAR powder and at least 1400 °C for AA-04 and PG4N25 powders. Weibull statistical analysis was used for determination of grain size distribution of sintered AA04 alumina samples. Statistical analysis of grain growth and its distribution was based on the SEM image analysis. Results revealed narrow distribution of grains in samples densified at temperatures up to 1350 °C with the maximum about 0.3 µm. At temperature of 1400°C grain size distribution was shifted to higher values. In the case of sintering temperature of 1450 °C a polydisperse distribution was observed with its maximum at 0.6 µm.

ACKNOWLEDGMENT

The financial support of this work by the project APVV-16-0341, project to support young researchers 1692 and FFG project "Flexible production of sintered metal and ceramic complex parts" under contract no. 860385 are gratefully acknowledged. This work is also based on the results of the project Center for Applied Research of New Materials and Technology Transfer, ITMS 26240220088, supported by the Science and Research Operational Program by the European Regional Development Fund.

REFERENCES

[1] Castro et al., Polycrystalline translucent alumina-based ceramic material, uses, and methods, Patent US006878456B2 (2005).

[2] X. Zhang et al., Mechanical and optical properties of transparent alumina obtained by rapid vacuum sintering, Ceramics International, 43 (2017) 420-426.

[3] X. Zhang et al., Fabrication of transparent alumina by rapid vacuum pressureless sintering technology, J. Am. Ceram. Soc., 95 [7] (2012) 2116–2119.

[4] A. Krell et al., Advanced spinel and sub-μm Al2O3 for transparent armour applications, Journal of the European Ceramic Society, 29 (2009) 275-281.
[5] A. Krell et al., Transparent sintered corundum with high hardness and strength, J. Am. Ceram. Soc., 86 [1] (2003) 12–18.
[6] K. Bodišová et al., Luminiscent rare-earth-doped transparent alumina ceramics, Journal of the European Ceramic Society, 36 (2016) 2975-2980.
[7] M. Trunec et al., Polycrystalline alumina ceramics doped with nanoparticles for increased transparency, Journal of the European Ceramic Society, 35 (2015) 1001 – 1009.

POVRCHOVÁ MODIFIKÁCIA Si_3N_4 KYSLÍK-ACETYLÉNOVÝM PLAMEŇOM – VPLYV ZLOŽENIA NA HRANICI ZŔN

SURFACE MODIFICATION OF Si_3N_4 BY OXYACETYLENE TORCH – INFLUENCE OF GRAIN BOUNDARY COMPOSITION

M. Hičák[1], M. Hnatko[1], M. Labudová[2], D. Galusková[3], J. Sedláček[1], P. Šajgalík[1]

[1]Institute of Inorganic Chemistry, Slovak Academy of Science, v.v.i., Dúbravská cesta 9, 842 36 Bratislava, Slovakia

[2] Biomedical Research Center of the Slovak Academy of Sciences, v.v.i., Dúbravská cesta 9, 845 05 Bratislava, Slovakia

[3] Centre for Functional and Surface Functionalized Glass, TnU AD, Študentská 2, 911 50 Trenčín, Slovakia

ABSTRACT

The formation of thin layer utilizing of high thermal treatment of dense silicon nitride with different grain boundary phase (SiO_2, SiO_2 + CaO or $Ca_3(PO_4)_2$) by oxyacetylene torch was studied. The structural and phase composition changes of surfaces of particular studied substrates after acetylene-oxygen flame thermal treatment (1475°C ± 25°C; O_2: C_2H_2= 1:1.1 ratio; dwell time up to 60s) and their bioactivity was discussed in this paper.

Keywords: Si_3N_4, oxyacetylene torch, surface layer, bioactivity

INTRODUCTION

Silicon nitride-based ceramics are characterized especially by high chemical resistance, superior combination of mechanical properties. Recently, silicon nitride also attracts interest for bio-applications in the human body as bioinert material. However, the biological applications often require additional properties, e.g. bioactivity, enabling stronger bonding to the host tissue. The possibilities how to enhanced bioactivity of bioinert materials like silicon nitride is surface engineering and different coating techniques [1]. The oxidation behaviour of Si_3N_4 ceramics is process (annealing at high temperatures from 1000 to 1600°C) witch markedly changed a surface. There are two mechanisms responsible for the phase change: i) oxidation, which changes the surface composition of specimens, ii) the crystallization of the grain boundary glassy phase. The literature shows some databases [2-4] about Si_3N_4 oxidation in different test conditions. Thick layer of glassy phase can be seen on the oxidized surface in the dependence on these different conditions. After the treatment the scale is brittle, large cracks are present and adhesion is low. Therefore is oxidation of Si_3N_4 surface by annealing at high temperature is not interesting for bioaplications for these reasons. However, exist the materials used in high temperature environment such as rocket engines and other thermal protection systems for space vehicles [5-7]. These materials (ultrahigh temperature ceramics UHTC) are tested by oxyacetylene torch test with a flame temperature about 3000°C.After relatively short time (120-300s) the thin protective oxide layers (a few microns) with high oxidation resistance are formed unlike traditional long-continuing annealing process (few hours or days). In this work, we would like to prove that by using the controlled thermal treatment it is possible to prepare on the surface of Si_3N_4 substrate an oxidic layer with certain thickness, porosity and phase/chemical composition, which can satisfied all conditions for surface bioactive ceramics.

EXPERIMENTAL

Preparation of dense Si_3N_4 substrates

Substrates were prepared using commercial Si_3N_4 powder (grade SN-E10, Ube Industries Ltd., Japan) and SiO_2 (Aerosil OX-50, Degusa, Germany, 50 m^2. g^{-1}) with using different bioactive phases that act also as sintering aid, i.e. CaO and $Ca_3(PO_4)_2$. Chemical compositions of the initial powder mixtures are summarized in Table 1.

Table 1 Chemical composition of the initial powder mixture

samples	Si_3N_4 wt%	SiO_2 wt%	CaO wt%	$Ca_3(PO_4)_2$ wt%	Sintering T °C	Δm wt %
SNSi	90	10	-	-	1750	5.24
SNSiCa	90	6.4	3.6	-	1600	3.8
SNCaP	90	-	-	10	1630	6.8

Samples with diameter of 20 mm and height of approx. 5 mm were prepared by hot pressing up to 1750°C (Table 1) at 30 MPa for 60 min dwell time under N_2 atmosphere. The densities of as prepared samples determined using Archimedes method were above 97 % of corresponding theoretical density (Table 2). The microstructures were observed by scanning electron microscopy (EVO 40HV, Karl Zeiss, Germany). For this purpose, the sintered samples were cut, polished and plasma etched (Diener Femto, O_2:CF_4 = 1:9). Prior a further treatment the samples were ground and polished to 1μm by diamond suspension using standard ceramographic method. Oxyacetylene torch was used for thermo-oxidative treatment of substrate surfaces using constant O_2: C_2H_2= 1:1.1 ratio and dwell time up to 60 sec. Temperature of surface in the range of 1475°C ± 25°C, measured with an optical pyrometer, was controlled by changing the distance between the nozzle tip of burner and treated surface. X-ray diffraction (Bruker AXS D8 Discover X-ray diffractometer) and scanning electron microscopy/energy dispersive spectroscopy (SEM/EDS) (JEOL JSM-7600 F/EDS/WDS/EBSD) were used to characterize respectively the phase composition and microstructure of the surface, chemical composition and cross section of the tested samples.

Bioactivity determination

The in vitro bioactivity of the samples was determined applying procedure described in detail in [8]. The samples were inserted into prepared SBF at pH 7.32 and left in incubator for four weeks at constant temperature (36.5 ± 0.1°C). After soaking, the specimens were removed from the fluid, washed with destilled water and the surfaces were studied by SEM (JEOL JSM-7600). Bioactivity should be proved by formation of HA on the surface of the samples and so by decrease of concentration of Ca^{2+} and PO_4^{3-} ions in SBF solution after soaking – concentration of Ca^{2+} and PO_4^{3-} ions were measured, using the optical emission spectroscopy with inductively coupled plasma ICP OES (5100 SVDV ICP-OES, Agilent).

RESULTS

The microstructure of all three prepared substrates consists mainly from elongated Si_3N_4 grains with hexagonal structure and minor grain boundary phase (Fig. 1). The results of X-ray powder diffraction analysis (XRD) of prepared samples are present in Table 2.

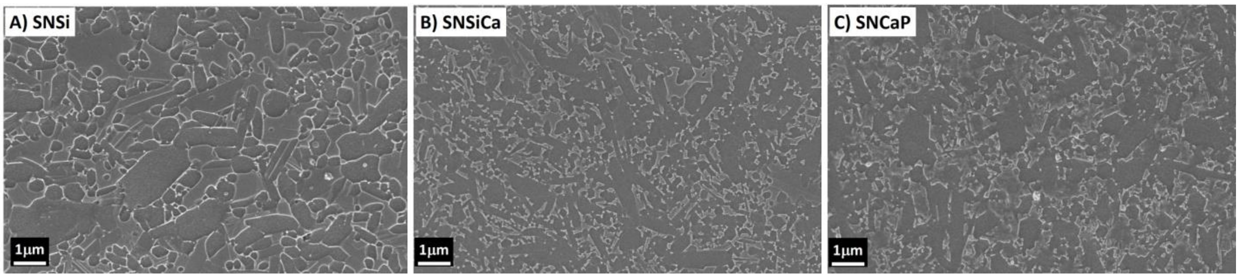

Fig.1 Microstructure of prepared substrates

Except of initial components, the presence of Si_2N_2O formed during the sintering, was also confirmed. Despite the fact that initial mixture of SNSiCa contains relatively higher amount of CaO (3.6 wt%) no phase containing Ca was confirmed by XRD in this substrate. Molar ratio of calcia to silica of 0.61 within the initial mixture was chosen in order to minimize the temperature of sintering (T_E = 1437°C) and to possible in situ formation of $CaSiO_3$ at the grains' boundaries during the sintering (this phase is considered to be highly bioactive) [9-11]. However, the amount of created $CaSiO_3$ is with the highest probability either under the detection limit of used method or it is a phase in amorphous state. This assumption is confirmed by EDX analysis of prepared samples; the results are shown in Table 3. The presence of calcium (1.87 wt%) in SNSiCa creates the assumption of presence of a certain amount of CaO (or $CaSiO_3$), which plays a key role in further processing of the substrate.

Table 2 Density and phase composition of prepared Si_3N_4 substrates

	SNSi	**SNSiCa**	**SNCaP**
Δm [%]	5.24	3.80	6.8
density [g.cm^{-3}]	3.05	3.07	3.11
TD [%]	97.13	97.15	97.49
Phase analysis by XRD	Si_3N_4, Si_2N_2O, SiO_2,	Si_3N_4, SiO_2	Si_3N_4, SiO_2, CaO

The substrate marked as SNCaP was prepared with the aim to gain the phase based on calcium phosphate at the grain boundaries of Si_3N_4. XRD analysis again did not confirmed the presence of such phase, but EDX analysis of grain boundary confirms the presence of Ca and P (Table 3). The presence of CaO (Table 2) indicates that the initial $Ca_3(PO_4)_2$ is dissociated during sintering. P_2O_5 with SiO_2 either becomes a part of glassy phase at the boundaries of Si_3N_4 grains, or leaves the system in the form of gas (Δm = 6.8 wt%).

Table 3 Chemical composition (EDX analyses) of substrate (wt%)

Substrate	N	O	Si	Ca	P
SNSi	36.99	15.98	47.02	0.00	0.00
SNSiCa	28.44	14.89	54.79	1.87	0.00
SNCaP	14.55	8.21	68.26	4.25	4.73

The structural changes of surfaces of studied substrates after acetylene-oxygen flame thermal treatment (1475°C ± 25°C; O_2: C_2H_2= 1:1.1 ratio; dwell time up to 60s) are shown in SEM micrographs (Figure 2A-C). The front faces of substrates were covered with a white layer adhered on the surface, indicating that the expected oxidation had occurred. Moreover, these surface layers were highly eroded and porous, Fig 2A-C. Based on the analysis of SEM results, the lowest effect of thermal treatment conditions, in terms of microstructural changes of surface, was observed in SNSi system where grain boundaries consist of SiO_2 (T_m = 1660°C) and/or Si_2N_2O (oxidative resistant phase up to 1600°C), (see Table 2).

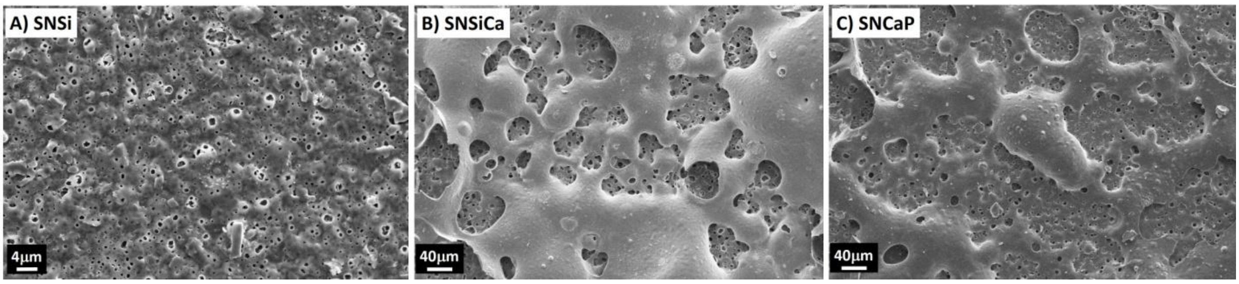

5 000x B) 500x C) 500x

Figure 2 Structure of substrate surfaces after flame thermal treatment (1475°C ± 25°C; O_2: C_2H_2= 1:1.1 ratio; dwell time up to 60s.)

Surface of the SNSiCa sample after the flame thermal treatment has evidently different nature of erosion compared to SNSi (in Fig. 2. the magnification of image is 10× higher than other two images). Due to the presence of CaO that significantly changes the grain boundary phase and its high temperature resistance resulted to different damaged of surface (Fig. 2B). The surface damage of sample SNCaP (Fig. 2C.) is after flame thermal treatment similar than SNSiCa surface (big interconnected droplets, broken/rough surface). Cross-sectional analysis of tested samples was performed to compare the thickness of formed layers and the chemical and phase compositions (Fig. 3 and Table 4).

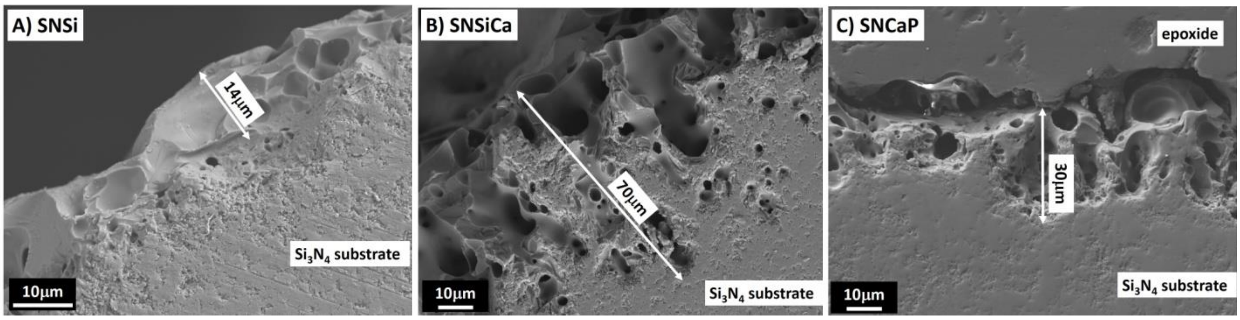

Figure 3 Cross section of the substrates after flame thermal treatment (1475°C ± 25°C; O_2: C_2H_2= 1:1.1 ratio; dwell time up to 60s.)

The different protective effect (passivation) of as formed melt on the sample's surfaces against oxidation/dissociation of Si_3N_4 is evidently present (Fig. 3.). Wide size distribution, interconnectivity as well as irregularity of pore shape results due to the rapid evolution of gaseous products related to the decomposition of nitride phase of substrate matrix. The thickness of as treated (eroded) surface layers are at the level from 2 to 100µm accordance grain boundary composition of substrates. In case of SNSi eroded sample clear interface between formed layer and original substrate is present contrary SNSiCa or SNCaP (Fig. 3B-C.). The phase composition of the layers was measured by the grazing incidence X-ray diffraction measurement (α=6°) with aim to catch mainly the diffractions from the surface of the samples, results are summarized in Table 4. In case of SNSi, the phase composition did not change compared to the reference state. The phase of $Ca_5Si_2N_6$ appears on the surface of sample SNSiCa. The presence of calcium silicate ($CaSiO_3$) was not confirmed in the surface layer, which is not suitable from the perspective of biological properties. Also in the third case, there was not achieved the initial intention to gain the surface layer rich in bioactive calcium phosphate ($Ca_3(PO_4)_2$). The surface layer of sample SNCaP compared to reference state except Si_3N_4, SiO_2 and CaO (Table 2) also $Si_{12}P_5$ and Si (Table 4). Based on such products it is obvious that used conditions were too extreme for this system and several dissociative reactions took place. The initial $Ca_3(PO_4)_2$ dissociates during the sintering process into crystalline CaO and probably P_2O_5 is present in amorphous state because was not confirmed by XRD method.

Table 4 Phase composition of substrate surface after thermal treatment testing measured by the grazing incidence X-ray diffraction measurement (α=6°)

	SNSi	**SNSiCa**	**SNCaP**
composition	Si_3N_4, Si_2N_2O, SiO_2	Si_3N_4, Si_2N_2O, SiO_2, $Ca_5Si_2N_6$	Si_3N_4, $Si_{12}P_5$, Si, SiO_2, CaO

This statement is confirmed also by the result of EDX analysis of the samples' surfaces after oxidation (Table 5). The surface of all three tested samples was proved to contain carbon in relatively high amount (6-8wt%). The combination of the gases and their ratio (O_2:C_2H_2) in the flame that was used results in formation of reducing environment.

Table 5 EDX analyses of substrate surface after thermal treatment (wt%)

Layer	**C**	**O**	**Si**	**Ca**	**P**
SNSi	7.9	51.2	40.9	x	x
SNSiCa	6.0	51.1	37.2	5.7	x
SNCaP	8.2	52.9	10.6	14.6	13.7

Given conditions at acetylene-oxygen flame treatment result in many chemical reactions and end with oxidation of Si_3N_4 (or Si_2N_2O phase in SNSi system): $2Si_3N_4(s) + 3O_2(g) = 6SiO\ (g) + 4N_2\ (g)$ and $Si_2N_2O(s) + 3/2O_2(g) = 2SiO_2\ (s) + N_2\ (g)$, or dissociation of Si_3N_4 $Si_3N_4(s) = 3Si\ (l) + 2N_2\ (g)$.

During the flame thermal treatment of surfaces, two processes occur parallel: i.) melting of oxide phases at the grain boundaries of Si_3N_4, its viscous flow or diffusion of cations (from the sintering aids or impurities) towards the surface and solidification on cooling, and ii.) oxidation/dissociation of Si_3N_4 that results in formation of gaseous phases and thus the pore formation. In all three cases there was due to these processes created a porous layer. All three systems were oxidized under the same conditions, which is not ideal in terms of creating the optimal structure of pores and their number. The conditions of oxidation (temperature of the flame and exposure time) needs to be adjusted based on the composition of the phase on the boundaries of Si_3N_4 grains. The cooling rate of 500 °C/min was sufficient for solidification of formed melts in amorphous state (without negligible crystallization) with preserved pore structure. The change of concentration of Ca^{2+} and PO_4^{3-} ions after 21 days in SBF solution is shown in Fig. 4. The concentration of both measured ions in SBF solution is almost the same as in the reference SBF solution (i.e. without presence of the same kind of sample). Also the SEM analysis has not confirmed any change of the surface of SNSi sample and the results confirm inert character of silicon nitride with addition of SiO_2.

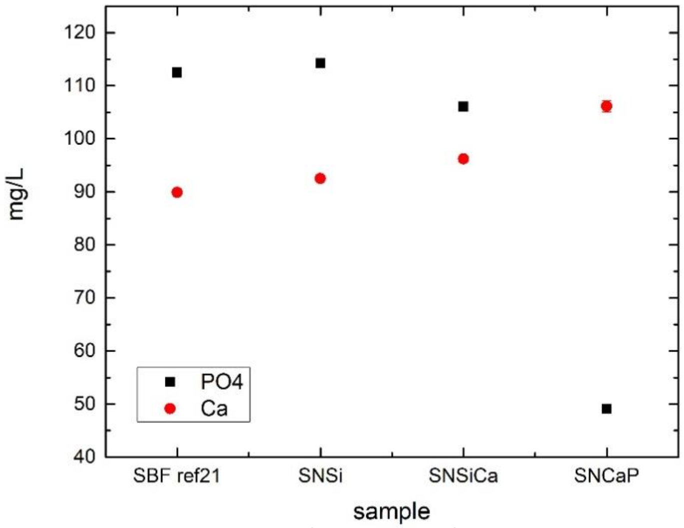

Fig.4 Change in concentration of Ca^{2+} *and* PO_4^{2-}*ions in SBF solutionafter21 days of sample immersion (test of bioactivity in SBF, 21 days, 36.5°C)*

In case of sample SNSiCa there is a more significant change. Much higher concentration of Ca^{2+} ions (in comparison with SBF_{ref}) suggests that calcium is released to the solution during the test (probably by dissolution of $Ca_5Si_2N_6$ phase, see Tab. 3). Detailed SEM analysis has shown the occurrence of small areas of precipitates (seeds) of phase on the surface, which were not present before the bioactivity test. From the results it is obvious that the conditions for formation of HA were not ideal - although there can be observed some nucleation of small rudiments, there are no noticeable higher units of CaP phase. In case of SNCaP sample there has been measured the highest concentration of Ca^{2+} ions in SBF solution. This is in accord with the results from EDX analysis of substrate surface after thermal treatment (14.6 wt%; Tab.5). On the contrary, the concentration of PO_4^{3-} in extract of this sample has rapidly decreased (in comparison with SBF_{ref} but also in the SNSiCa extract). In spite of the fact, that the surface of the sample already contains a certain amount of phosphorus (13.7 wt%; Tab.5), additional consumption of P ions from SBF solution arises during the incubation. The reason for such phenomenon is the formation of nanocrystals, whose structure is typical for calcium phosphate in the form of HA.

CONCLUSION

The dense silicon nitride materials with different grain boundary phase (SiO_2, SiO_2 + CaO or $Ca_3(PO_4)_2$) were prepared by hot pres method. The surfaces of substrates after acetylene-oxygen flame thermal treatment were highly eroded and porous. The different protective effect (passivation) of as formed melt on the sample's surfaces against oxidation/dissociation of Si_3N_4 is evidently present. The thickness of as treated (eroded) surface layers are at the level from 2 to 100mm accordance grain boundary composition of substrates. The results of bioactivity test in SBF confirm inert character of silicon nitride with addition of SiO_2 and SiO_2+CaO respectively. The surface of the SNCaP sample (with addition of $Ca_3(PO_4)_2$) is bioactive because considerable formation of HA nanocrystals was observed on the surface after bioactivity test in SBF.

ACKNOWLEDGMENT

This work was supported by the Slovak Grant Agency VEGA Project No. 2/0152/18, APVV-0540-15 and MVTS - CERANEA project (in frame of FLAG ERA II).

REFERENCES

[1] Koschwanez, H. E. Reichert, W. M. Textured and Porous Materials. In: Ratner, B. D., Hoffman, A. S., .Schoen, F. J., Lemons, J. E. Biomaterials Science, (2013) 321-331.

[2] Pan, X. Atomistic structure of silicon nitride/silicate glass interfaces. Journal of the American Ceramic Society, 79 (1996) 2975-2979.

[3] Echeberria, J., Castro, F. Oxidation of silicon nitride sintered with ceria and alumina. Materials Science and Technology, 6 (1990) 497-503.

[4] Biswas, S. K., Mukerji, J., Das, P.K. Oxidation of silicon nitride sintered with yttria and magnesia containing nitrogen rich liquid, Key Engineering Materials, 89–91 (1994) 271–274.

[5] Hou, X. H, Li, H.J., Chen, Y., Li, K.Z. Modeling of chemical vapor infiltration process for fabrication of carbon–carbon composites by finite difference methods. Carbon, 37 (1999) 669-677.

[6] Huang, J.F., Li, H.J., Zeng, X.R., Li, K.Z. Yttrium silicate oxidation protective coating for SiC coated carbon/carbon composites. Ceramics International, 32 (2006) 417-421.

[7] Vix-Guterl, C., Grotzinger, C., Dentzer, J., Bacosb, M.P., Ehrburger, P. Reactivity of a C/SiC composite in water vapour. Journal of the European Ceramic Society, 21 (2001) 315-323.

[8] Kokubo, T., Takadama, H. How useful is SBF in predicting in vivo bone bioactivity? Biomaterials, 15 (2006) 2907-2915.

[9] Liu, X.,Morra, M., Carpi, A., Li, B. Bioactive calcium silicate ceramics and coatings. Biomedicine & Pharmacotherapy, 62 (2008) 526-529.

[10] Yao Dai, Hairong Liu, Binbin Liu, Zhenxing Wang, Yongsheng Li, Guangdong Zhou, Porous β-Ca_2SiO_4 ceramic scaffolds for bone tissue engineering : In vitro and in vivo characterization. Ceramics International, 41 (2015) 5894–5902.

[11] Nana Wang, Zheng Zhou, Leilei Xia, Yao Dai, Hairong Liu. Fabrication and characterization of bioactive β-Ca_2SiO_4/PHBV composite scaffolds. Materials Science and Engineering C, 33 (2013) 2294-2301.

ÚLOHA FYZISORBOVANÝCH ČASTÍC PRI ELEKTROFORETICKEJ DEPOZÍCII PRÁŠKOV Al_2O_3 A YSZ

THE ROLE OF PHYSISORBED SPECIES ON ELECTROPHORETIC DEPOSITION OF Al_2O_3 AND YSZ POWDERS

J. Ráheľ[1], M. Ilčíková[1], J. Dugáček[1], D. Pavliňák[1], D. Drdlík[2]

[1]*Masaryk university, Faculty of Science, Department of physical electronics, Kotlářská 2, 611 37 Brno, Czech Republic*

[2] *Institute of Materials Science and Engineering, Brno University of Technology, Technicka 2, 616 00 Brno, Czech Republic*

ABSTRACT

Electrophoretically deposited (EPD) layers prepared from plasma activated powders of Al_2O_3 or ZrO_2 exhibit a substantially smaller surface roughness than EPD layers prepared from pristine powders. Performed analysis of plasma induced changes on powder surface pointed out a possible importance of physisorbed species generated within the plasma itself. In the presented work, the amount plasma introduced physisorbed species was gradually reduced by partial thermal desorption at successively increased temperatures. Above 300°C the positive effect of plasma activation was lost completely. This particular temperature was in excellent agreement with the activation temperature for desorption of plasma introduced adsorbed species, found by thermal desorption spectroscopy in our previous work.

Keywords: electrophoretic deposition, plasma treatment, DCSBD, Al_2O_3, ZrO_2

INTRODUCTION

Electrophoretic deposition (EPD) is a versatile shaping method used for fabrication of ceramic films. During the EPD charged ceramic particles dispersed in a liquid medium (typically a non-aqueous organic solvent) are attracted and deposited onto a conductive substrate of opposite charge due to an applied electric field. In our most recent paper [1] we have reported the discovery of positive changes in EPD process when non-thermal plasma activated Al_2O_3 powder is used. Plasma powder activation resulted in a substantially smoother EPD layer (Fig. 1-right), smaller mean grain size and slightly higher relative density. The effect of plasma activation was fully comparable, or even better, than the known use of monochloroacetic acid additive [2]. The dynamics of EPD was affected significantly too, as the process had switched to the opposite polarity electrode. In our follow-up work we were able to show, that EPD from plasma pre-treated ZrO_2 powders exhibits the same positive effect too ([3, 4], Fig.1-left). Thorough analysis of plasma treated surfaces (FTIR, XPS, thermoluminescence, TGA and TDS) pointed out the importance of plasma originated molecular gases being adsorbed on the powders surface [1].

The main arguments supporting this hypothesis are as follows: (1) the effect is not material specific, as it manifested itself on both Al_2O_3 and ZrO_2 powders; (2) more than 200 fold increase of specific conductivity of EPD dispersion from plasma treated powders suggests an release of powders surface adsorbed species into the solution; (3) TDS (thermal desorption spectroscopy) analysis of powders revealed an ample amount of low-molecular weight species present on the plasma activated powders, which were desorbed at temperatures above 300°C (Fig. 2). The aim of presented work is to prove the causality relationship between the plasma introduced adsorbed species and the positive EPD effect we have carried out series of thermal desorption experiments.

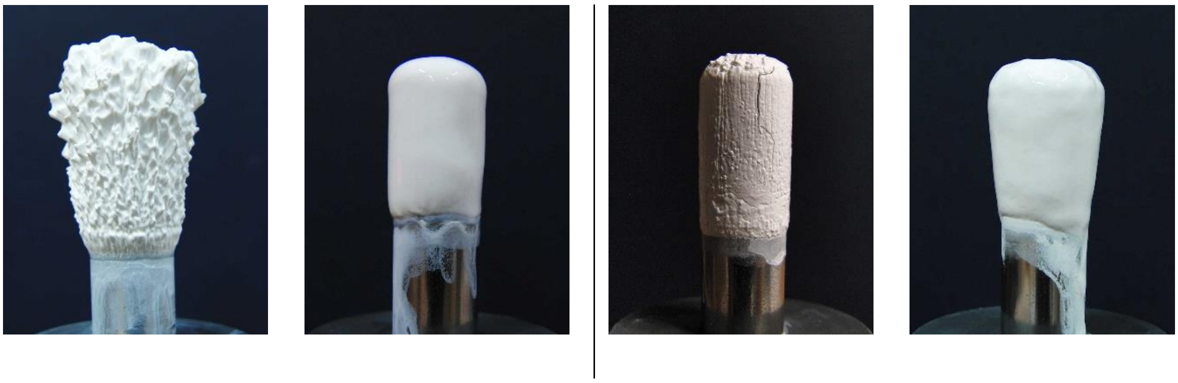

Al_2O_3 **ZrO_2 (YSZ)**

Fig.1. Improvement in the surface roughness of EPD deposit. Left – Al_2O_3 reference vs. plasma treated. Right – YSZ reference vs. plasma treated

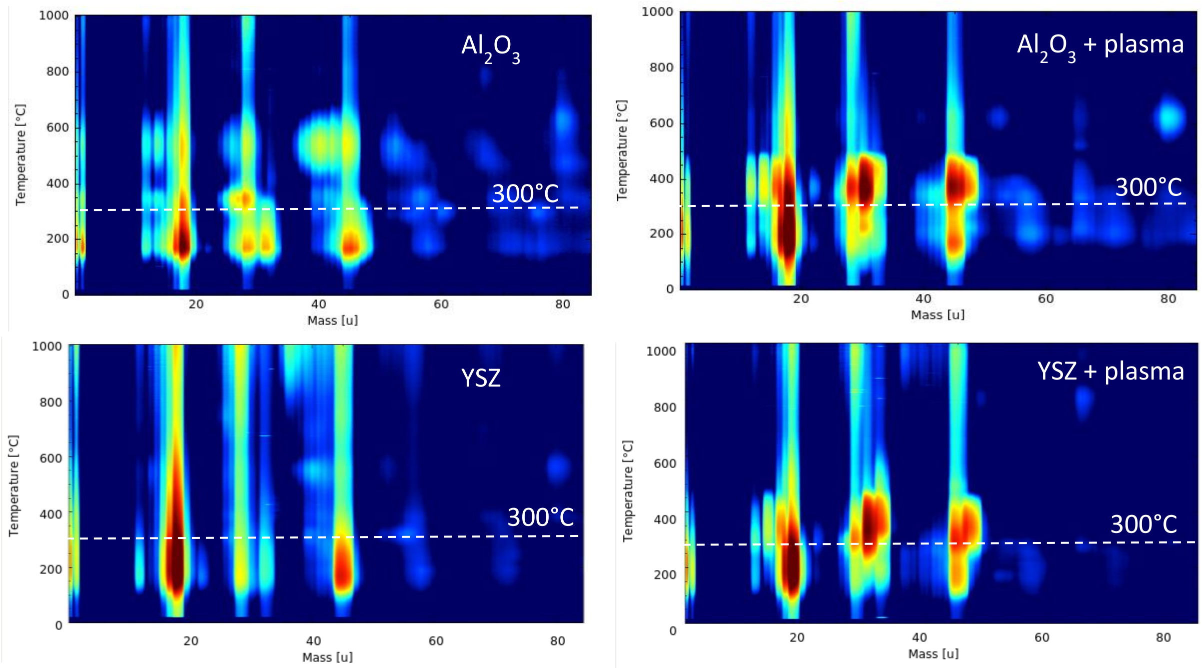

Fig.2. Pair comparison of 2D TDS maps of untreated and plasma-treated Al_2O_3 powders (top) and untreated and plasma-treated yttrium stabilized ZrO_2 powders (bottom)

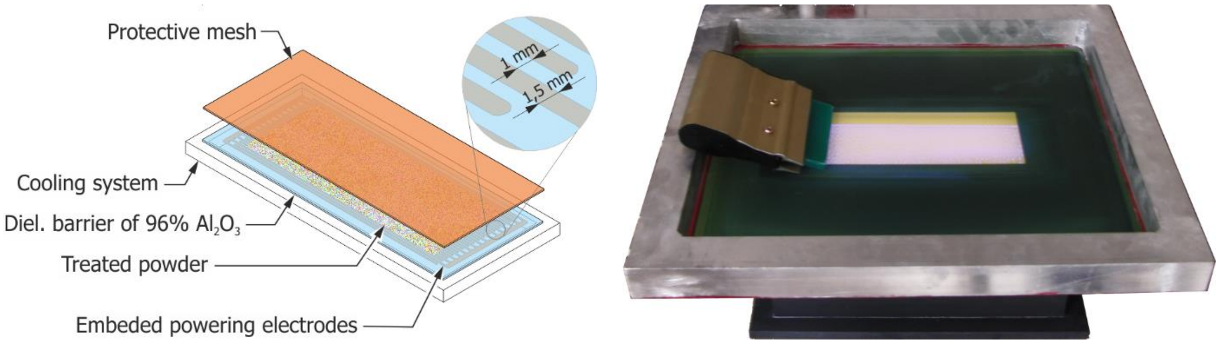

Fig. 3. Schematics (left) and actual appearance (right) of DCSBD system with protective screen printing mesh

Plasma treated Al_2O_3 and ZrO_2 powders were gradually heated to facilitate a partial desorption of gases from powder surface. The impact of adsorbed gases removal on EPD deposition rate was then investigated.

EXPERIMENTAL

Sub-micron alumina powder (TM-DAR, Taimei Chemicals, Japan) and yttrium stabilized zirkonia powder (TZ-3YS-E, Tosoh, Japan) was plasma treated by the Diffuse Coplanar Surface Barrier Discharge (DCSBD). The DCSBD generated a thin (< 0.3 mm) layer of non-thermal plasma above the flat dielectric panel made of 96% Al_2O_3. The system was energized by a pair of embedded comb-like high voltage electrodes Fig. 3 [1]. The width of electrode strips was 1.5 mm, their mutual distance was 1 mm. The system was powered by sinusoidal HV of 30 kHz, at 20 kV peak-to-peak and 500 W input power, supplied by in-house build power generator. Discharge was operated in still (no flow) atmospheric pressure air of absolute humidity within the range of 3–8 g/m^3. Active area of generated plasma of used DCSBD unit was 8 × 20 cm. Maximum temperature of DCSBD dielectric panel was less than 70 °C. The treatment was done in a discontinuous regime. A small amount (approximately 0.4 g) of alumina powder was sifted through the screen printing mesh (SEFAR PET 1500, 48/123-70W) on the surface of DCSBD panel, to form a thin powder layer. After the set treatment time of 30 sec, the treated powder was scraped away, collected for further processing, and the whole process was repeated again. Treated powder exhibited no static charge on its surface. Partial thermal desorption was done by exposing treated powders to the set temperature (140°C, 200°C and 300°C) for 4 hours. The furnace was operated in ambient air. EPD solutions were prepared from 15 wt% of powder dispersed in 2-propanol (p.a., Lachner, Czech Republic). The dispersions were mechanically stirred in an ultrasonic bath for 30 min. The deposition took place on the central stainless steel cylindrical electrode (D=12 mm, l=20 mm) of a co-axial deposition cell. The deposition was made at constant current of 5 mA (current density 0.66 mA/cm^2). The total time of deposition was 30 min. The deposition was interrupted at 5 min intervals to weigh the layer deposited on the electrode.

RESULTS

Resulting deposition rates are shown in Fig. 4. To take into account the loss of powder which stayed adhered to the walls of mixing beaker (sediment), the deposition rate was expressed as a relative reduction of fraction of dispersed powder, using the formula:

$$\Delta m = \frac{M_{dep}}{M_{in} - M_{sed}} \cdot 100\%$$

where M_{dep} states for the mass of deposited powder, M_{in} is total mass of initially dispersed powder and M_{sed} is mass of powder lost to the walls of mixing beaker.

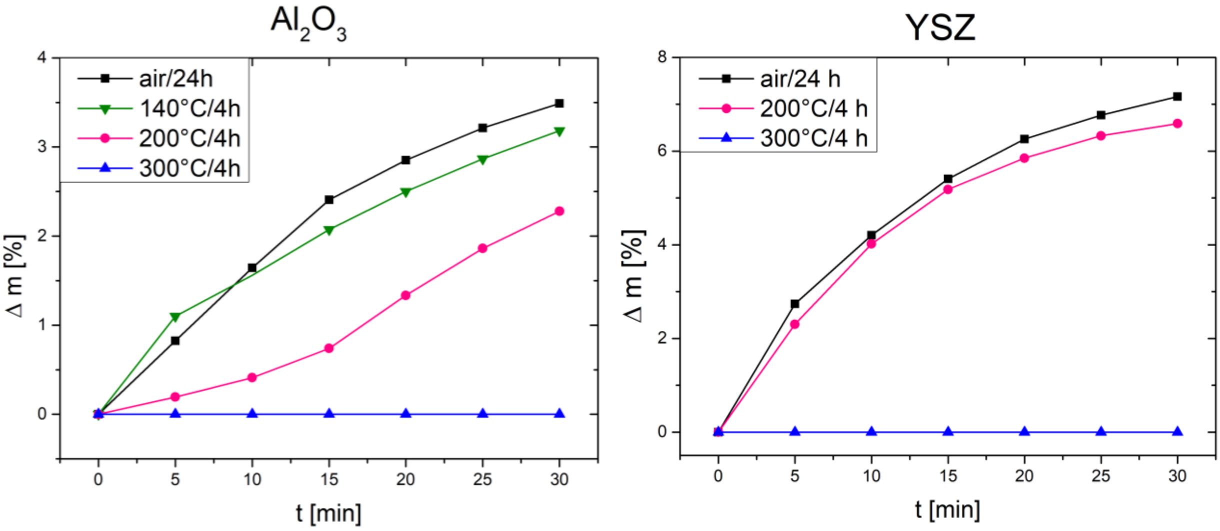

Fig. 3. The effect of gradual heating on the EPD deposition rate

Thermally desorbed samples were compared with the reference samples, which were left exposed for 24 hours to room temperature ambient air. Such reference was adopted to address the aging effect of plasma treatment. For both types of powders, 4 hours lasting thermal exposure of 300°C removed the positive EPD effect completely. The removal of effect was gradual for Al_2O_3 powders, and steep for YSZ powders. The temperature threshold of 300°C is in excellent agreement with the onset temperature of adsorbed species identified by TDS (Fig. 2).

CONCLUSION

Exposing plasma treated powders to the temperature above 300°C will completely remove the positive EPD effect brought by the previous plasma treatment. Almost identical value of onset temperature for plasma introduced species observed by TDS provides a strong supportive evidence for the hypothesis of critical role played by physisorbed (plasma introduced) species during the EPD.

ACKNOWLEDGMENT

The work was financially supported by the Czech Science Foundation, contract No. GA17-05620S, project TE02000011, project CZ.1.05/2.1.00/03.0086 funded by European Regional Development Fund and project LO1411 (NPU I) funded by Ministry of Education, Youth and Sports of Czech Republic.

REFERENCES

[1] Drdlík, D., Morávek, T., Ráheľ, J. *et al.* "Electrophoretic deposition of plasma activated sub-micron alumina powder", *Ceramics International*, **44** (8), 2018, pp. 9787-9793.

[2] Maca, K., Hadraba H., Cihlář, J „Electrophoretic deposition of alumina and zirconia: I. Single-component systems", *Ceramics International,* **30** (6), 2004, pp. 843-851.

[3] Ilčíková, M. "The influence of plasma activated ceramic powders on electrophoretic deposition of fine-grained oxide ceramics", *Master thesis*, Masaryk university, 2018.

[4] Dugáček, J., Prokeš, L., Sťahel P. *et al.* "Investigation of atmospheric pressure plasma surface modified zirconium dioxide nanopowder by thermal desorption spectroscopy" Proc. of 16th HAKONE, Beijing, China, Sept 2-7, 2018.

CHARAKTERISTIKY THz ODOZVY Er^{3+}/Yb^{3+} DOPOVANEJ $La_2Zr_2O_7$ KERAMIKY

CHARACTERSTICS OF THz RESPONSE FOR Er^{3+}/Yb^{3+} DOPED $La_2Zr_2O_7$ CERAMICS

M. Janek[1, 2], E. Trusova[3], Ľ. Bača[1], P. Veteška[1], R. Klement[4], M. Naftaly[5]

[1] *Slovak University of Technology, Faculty of Chemical and Food Technology, Radlinského 9, 812 37 Bratislava, Slovakia*

[2] *Comenius University, Faculty of Natural Sciences, Department of Physical and Theoretical Chemistry, Mlynská dolina Ch1, 842 15 Bratislava, Slovakia*

[3] *Belarusian State Technological University, 13a, Sverdlova str., Minsk, 220006, Belarus*

[4] *Alexander Dubček University of Trenčín, FunGlass Centre, Department of Functional Materials, Študentská 2, 911 50 Trenčín, Slovakia*

[5] *National Physical Laboratory, Hampton Rd, Teddington, Middlesex, TW11 0LW, United Kingdom*

ABSTRACT

Terahertz-time domain spectroscopy (THz-TDS) is a novel spectroscopic experimental technique covering far infrared region with low frequency and phonon lattice vibrations response. However, it is not quite frequently applied for characterisation of ceramic and glass materials. THz-TDS offers systematic study of solid phase with increased sensitivity towards dielectric and spectral changes in far infrared region. For the first time we have characterised absorption coefficient and refractive index frequency dependence of Er^{3+}/Yb^{3+} co-doped $La_2Zr_2O_7$ ceramics. Such type of ceramic has distinct up-converting properties and can be used for detector materials. Clear dependence of low frequency band detected as function of Er^{3+} doping element concentration was found at about 0.9 THz.

Keywords: Terahertz-time domain spectroscopy, Far-infrared, Dielectric properties, Rare earths doping, Lanthanum-zirconates

INTRODUCTION

The ceramic materials are frequently used as insulators and dielectrics not only in the conventional household/industrial electro-technical applications, but are utilised in car or air transportation industry, as special and functional devices. As such functional devices can be considered the temperature sensors and IR detectors for specific military applications. The Terahertz-time domain spectroscopy (THz-TDS) has found applications in fields such as material quality checks and tomography imaging including chemical sensing, which can be applicable successfully in the studies of ceramic materials [1–3]. Thanks to the coherent detection of THz radiation, it is able to extract from one sample measurement, including the determination of a background spectrum, the frequency dependence of the complex refractive index ($\tilde{n}_s = n_s - i\kappa_s$) of the investigated material. Here, n_s is the real part of the refractive index, and κ_s the absorption index as the imaginary part. Under specific conditions the thickness, *l*, of the absorbing medium can be determined from one sample measurement too, if multiple Fabry-Pérot oscillations are detected. THz-TDS is the only experimental technique, which allows direct determination of material absorption coefficient $\square_s$. From the known frequency dependent refractive index and absorption index can be found the material complex dielectric permittivity $\tilde{\varepsilon}_s = \varepsilon'_s - i\varepsilon''_s$, while $\varepsilon'_s = n_s^2 - \kappa_s^2$, and $\varepsilon''_s = 2n_s\kappa_s$. The real part of dielectric permittivity ε'_s characterise material polarisability and propagation of the radiation through material. The imaginary part corresponding to loss factor ε''_s, represents the material ability to absorb electromagnetic radiation at given frequency. Rare earths (Re) doped ceramics draw much attention due to their practical applications in the fields of optical phosphors in modern energy saving light bulbs and interesting optical, electrical, magnetic and catalytic properties. Lanthanum zirconate ceramics with the pyrochlore structure co-doped with Er^{3+}/Yb^{3+} are efficient mediators for radiation up-conversion [4–5]. Therefore, the main objective for our study was the determination of the dielectric and frequency response of lanthanum-zirconate materials with up-converting properties after their doping with Er^{3+}/Yb^{3+} cations.

EXPERIMENTAL

Synthesis of lanthanum zirconate (LZ) ceramics was done using the solvo-chemical synthesis from Re nitrates $Re(NO_3)_3{\cdot}xH_2O$ (Re = La, Er, Yb) and zirconyl nitrate. The nitrate salts were dissolved in aqueous solution along with nitric acid to suppress hydrolysis at pH ~ 2. Homogeneous precipitation of respective hydroxides was induced using ammonia solution after adjusting the pH ~ 8. The Er^{3+}/Yb^{3+} co-doping was recalculated to final composition $Er_xYb_{0.02}LZ$ where x = 0.005; 0.010; 0.020; 0.050. Additional compositions were prepared using lithium nitrate salt by the same procedure to induce excess of Lithium as structural atoms at the level of y = 0.050; 0.100; 0.200 to verify its effect on optical properties in the UV-VIS region. Prepared gel was dried, calcined in air at 600°C, ground and pressed into discs of about 1 mm thickness. The discs were fired at 1400°C for 3h and sample numbering is shown in the Table 1.

Table 1. Composition of lanthanum zirconate samples prepared by solvo-chemical synthesis

Sample number	**Chemical composition**
1	$La_2Zr_2O_7$
2	$Er_{0.01}Yb_{0.02}La_2Zr_2O_7$
3	$Er_{0.02}Yb_{0.02}La_2Zr_2O_7$
4	$Er_{0.05}Yb_{0.02}La_2Zr_2O_7$
5	$Er_{0.10}Yb_{0.02}La_2Zr_2O_7$
6	$Er_{0.01}Yb_{0.02}La_2Zr_2O_7{:}Li_{0.05}$
7	$Er_{0.01}Yb_{0.02}La_2Zr_2O_7{:}Li_{0.10}$
8	$Er_{0.01}Yb_{0.02}La_2Zr_2O_7{:}Li_{0.20}$

The X-ray powder diffraction (XRPD) of all Er^{3+}/Yb^{3+} co-doped calcined lanthanum zirconate materials was determined using Stadi Stoe P diffractometer equipped with theta-theta goniometer and linear position sensitive detector using Co(Kα1) radiation (λ = 0.1788965 nm). Patterns were collected using 0.2° theta step in 25 – 100 2 theta range. The pyrochlor structure had matched to XRPD card no. 96-200-2249. The structure represents face-centred cubic (fcc) conventional unit cell, corresponding to the space group $Fd\bar{3}m$ and crystal structure shown in the Figure 1.

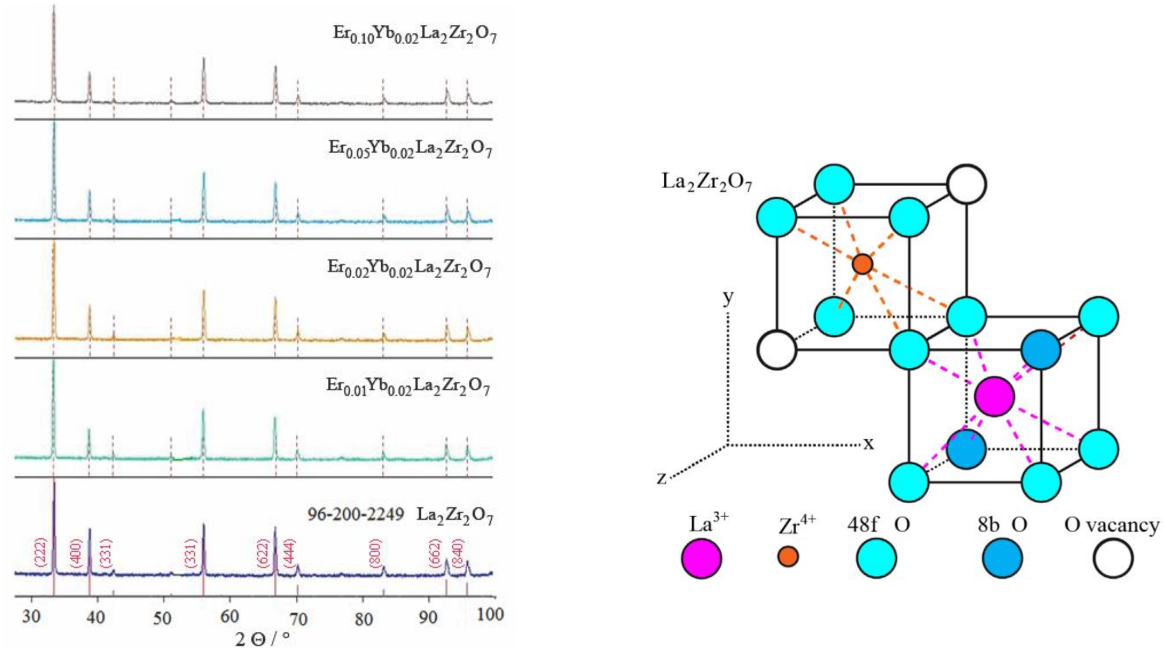

Figure 1. Typical XRPD patterns of $La_2Zr_2O_7$ (left) and structure projection (right)

The THz-TDS measurements were obtained on laboratory built equipment based on femtosecond-laser driven photoconductive emitter and electro-optical detection, with typical components shown in Figure 2: **bs**, beam splitter; **lp**, linear polarizer; **dl**, optical delay line; **l**, lens; **te**, terahertz emitter; **pm**, parabolic mirror; **s**, sample position; **eoc**, electro-optic crystal; **λ/4**, quarter wave plate; **wp**, Wollaston prism, **pdd**, photoconductive detection) [6–8].

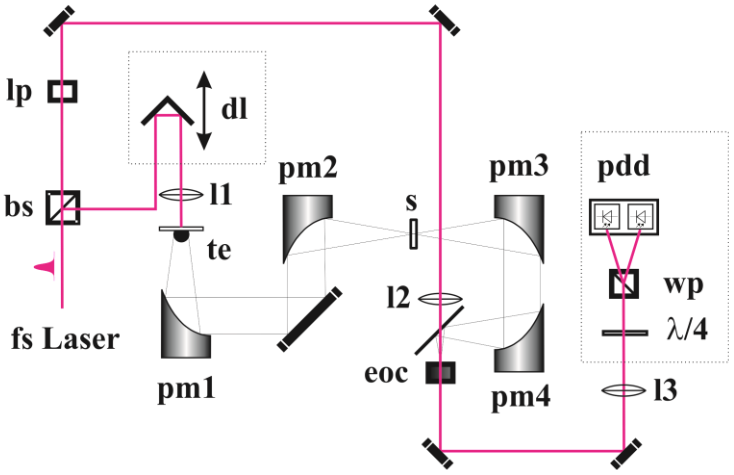

Fig. 2. Schematic representation of terahertz-time domain spectrometer

Frequency dependences of refractive index and absorption coefficient of all studied materials listed in Table 1 are shown in the Figure 3. The refractive indexes can be observed in the range of 3.1 – 3.9, absorption coefficient shows broad absorption bands with increasing intensity growth for the samples 1 – 5.

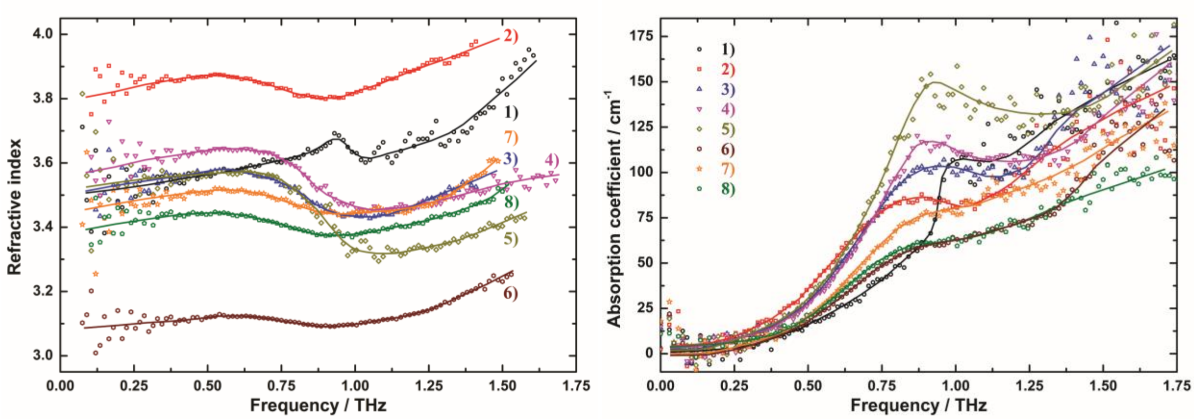

Fig. 3. Frequency dependences of refractive index (left) and absorption coefficient (right) of $La_2Zr_2O_7$ samples (solid lines represents just the estimates to guide the eye for the dependences observed)

RESULTS

There is well accepted mechanism of energy transfer of up-converting processes which may occur without charge transport. One can distinguish between radiative and nonradiative resonant energy transfers, while the transfer is radiative when the photons emitted by the “sensitizer” ions are absorbed by any “activator” ion so that transfer depends upon the local arrangements of emitter and receiver in the crystal structure [9]. As it was found by the XRPD analysis, all materials prepared had face-centred cubic structure shown in the Figure 1. The location of the structural cations and the dopants in the structure has essential effect on final up-converting and luminescence properties. Depending on the concentrations of Er^{3+}/Yb^{3+} in the pyrochlor lattice structure, these trivalent cations can substitute most probably the occupancy sites for lanthanum cations, but at higher concentrations zirconium replacements and self interstitial positions cannot be excluded. The XRPD did not found changes in diffraction intensities of observed peaks, however, small changes in their positions can be detected with changes of Er^{3+}/Yb^{3+} concentrations. The face-centred cubic crystal structure indicate an isotropic material properties which can be preferred for electron energy transfer by any mechanism considered, such as Förster resonant nonradiative energy transfer (FR-NET), phonon-assisted nonradiative energy transfer (PA-NET) or cooperative luminescence sensitization (CLS) and the cooperative energy transfer plus photon absorption (CET-PA). From these mechanisms, the contribution from PA-NET mechanism could be investigated using phonon sensitive technique detecting vibrations of elastic structures of structural atoms of investigated material. From this reason the investigation of low frequency vibrations of prepared Er^{3+}/Yb^{3+} co-doped lanthanum zirconate using THz-TDS was performed for the first time. The experimental investigation was done on laboratory build THz-TDS spectrometer schematically shown in the Figure 2. The results achieved represent frequency dependence of refractive index and absorption coefficient of investigated material in far-infrared region (Figure 3). The values of refractive index were observed in the range of 3.1-3.8, with distinct inflection point indicating the presence of absorption band in the frequency range investigated. The THz-TDS is the only spectroscopic technique able directly determine the frequency dependent absorption coefficient for known thickness of the material, thanks to its coherent detection scheme. Indeed, there can be seen broad low frequency bands observable for the absorption coefficient in all $La_2Zr_2O_7$ doped materials investigated (Figure 3 - right). The most striking feature found is the shift of the absorption band of parent $La_2Zr_2O_7$ observed at ~1.00 THz towards lower frequencies after Er^{3+}/Yb^{3+} structure co-doping in the range of ~ 0.85 – 0.95 THz. Such frequency shift is in good agreement with theoretical change of the molecular vibration oscillator, if mass of one of the atoms is increased. Hence, if Er^{3+} is replacing either La^{3+} or Zr^{4+}, observed shift of low frequency bands can be good indicator for the replacing process and/or Er^{3+} incorporation into the $La_2Zr_2O_7$ structure. In addition, the fact that peak position change is associated with the Er^{3+} doping is supported by the observation of gradual peak intensity increase, according to Er^{3+} growing concentration used for the doping (Table 1). The addition of Li^+ cations into the material structure, decreased the peak intensity for the given level of Er^{3+} and indicate that presence of small cation e.g. in the interstitial positions affects the neighbouring molecular vibration oscillations (Figure 3 - right).

CONCLUSIONS

The Terahertz-time domain spectroscopy was used for the first time for the investigation of low frequency vibrations of prepared Er^{3+}/Yb^{3+} co-doped lanthanum zirconate material with face-centred cubic structure. It was found that co-doping of the $La_2Zr_2O_7$ using Er^{3+}/Yb^{3+} cations result in the shift of the absorption band of parent material towards lower frequencies. At the same time the peak intensity can be used for the monitoring of the Er^{3+} incorporation into the structure. The addition of accessory Li^+ cations to the material structure, decrease the peak intensity at the given level of Er^{3+}. This indicates that presence of small cation in the interstitial positions affects the neighbouring vibration of structural cations in the investigated pyrochlor structure.

ACKNOWLEDGMENT

The financial support of the Slovak Grant Agency for Science VEGA grants No. 1/0278/16, 1/0906/17 and 1/0527/18 are greatly appreciated.

REFERENCES

[1] Ferguson, B. and Zhang, X.C. Materials for terahertz science and technology. Nature Materials, 1 (2002) 26–33.

[2] Reimann K. Table-top sources of ultrashort THz pulses. Rep. Prog. Phys. 70 (2007) 1597–1632.

[3] Hoffmann M.C., Fülöp J.A. Intense ultrashort terahertz pulses: generation and applications. Journal of Physics D: Applied Physics, IOP Publishing, 44 (8), (2011) pp.83001.

[4] Ibrahim, I.A.M., Lenčéš, Z., Šajgalík, P., Benco, Ľ. J. Lumin. 164 (2015) 131–137. DOI: 10.1016/j.jlumin.2015.03.035.

[5] Zhang, Y.Y., Ding, B.F., Yin, L.Q., Xin, J.D., Zhao, R., Zheng, S.K., Yan, X.B. Inorg. Chem. 57 (2018) 507-518. DOI: 10.1021/acs.inorgchem.7b02787.
[6] Dexheimer S.L., Terahertz Spectroscopy – Principles and Applications, CRC Press Taylor & Francis Group, Boca Raton, FL, 2008.
[7] Kröll J., Darmo J., Unterrainer K. Electron. Lett. 40 (763) (2004) 763–764.
[8] Zhao G., Schouten R.N., van der Valk N., Wenckebach W.Th., Planken P.C.M., Rev. Sci. Instrum. 73 (2002) 1715–1720.
[9] Auzel F.E., IEEE, 61(6), (1973) 758–786.

MIKROŠTRUKTÚRA A VLASTNOSTI TI-B_4C KOMPOZITOV PRIPRAVENÝCH PROCESOM ADITÍVNEJ VÝROBY

MICROSTRUCTURE AND PROPERTIES OF Ti-B_4C COMPOSITES PREPARED BY ADDITIVE MANUFACTURING

Ľ. Bača [1], N. Stelzer [1], L. Vály [2], D. Grech [2], E. Neubauer [2], M. Kitzmantel [2]

[1] *Aerospace & Advanced Composites GmbH, Viktor-Kaplan-Str. 2, building F, 2700 Wiener Neustadt, Austria*

[2] *RHP-Technology GmbH, Forschungs- und Technologiezentrum, 2444 Seibersdorf, Austria*

ABSTRACT

Titanium – boron carbide composites have been manufactured by additive manufacturing using plasma transfer arc (PTA) process. In this process plasma transfer arc (PTA) is used as a heat source for in-situ reaction between Ti and B_4C, which allows a formation of TiB and TiC phases during the deposition. Additive layer manufacturing using Machine for Multi-Material-Manufacturing (“4M-System”) developed by RHP-Technology GmbH offers a production of large and complex 3D components on one side and a gradient structures or multi-material concepts on the other side. Fully dense and crack free Ti specimens with 10 vol. % of B_4C were obtained by additive manufacturing with the optimized deposition parameters. In comparison to the pure titanium Grade 1.0 the Ti with 10 vol.% B_4C test samples show higher Young`s Modulus (155 GPa against 103 GPa of the pure Ti) as well as higher hardness values (374 ± 28 HV) and tensile strength (572 ± 49 MPa). The total strain at break however, is very low showing ceramic like behaviour.

Keywords: Titanium, Boron Carbide, Composite, Plasma Transfer Arc (PTA), Additive Manufacturing

INTRODUCTION

Within the past years a strong trend towards the use of additive layer manufacturing processes has been observed. Especially space industry and aeronautic industry are the markets and application areas where this technology is of significant interest due to possibilities for weight saving, integration of functionalities in components, reduction of processing steps and of course the availability of components at more competitive costs especially when it comes to the manufacturing of prototypes and small series.

Multi-material manufacturing has been demonstrated at R&D level where blown powder or wire-feed systems have been used in combination with PTA welding [1, 2], Tungsten Inert Gas (TIG) Welding [3], Gas Metal Arc Welding (GMAW) [4, 5], Plasma Arc Wire (PAW) Welding and Electron Beam (EB) Welding [6, 7]. Titanium matrix composites have several beneficial properties over the unreinforced metals, such as corrosion resistance, heat resistance, high specific modulus and high specific strength [8, 9]. B_4C reinforced Titanium matrix composites exhibit significantly enhanced properties, such as higher hardness, improved corrosion and wear resistance since it serves as precursor for TiB, TiB_2 and TiC phases [10, 11]. For producing 3D particle reinforced composites, the most commonly used techniques are sintering, hot pressing, hot isostatic pressing and casting [12].

EXPERIMENTAL

The 4M system with the PTA as a heat source was used for deposition of blown Ti-B_4C powder mixture to create a layer of Ti- B_4C composite on the substrate. At the subsequent layers the heat source creates again a welding pool with the blown mixture of powders, which then solidifies on the previously deposited layer. In this way, layer by layer are built up to a complete 3D structure of a required material with selected parameters (Tab. 1.).

Calculated amount of boron carbide powder (10 vol.%) with the grain size of 45-75 μm and Titanium Grade1 powder with the grain size of 75-180 μm were dry-mixed as 500g batch for one hour in a Turbular Powder Mixer (Sintris 43TM). Ti Grade2 plates with dimensions of 200x200x10 mm^3 were used as substrates. Samples were then cut by Wire Electric Discharge Machining (W-EDM) for microstructure analysis and determination of mechanical properties. The microstructural characterization was carried out using a light microscope Leica DM and scanning electron microscope coupled with EDAX analysis (FESEM, Carl Zeiss SUPRATM 40VP). The hardness was measured using a Vickers indenter of a Qness 10 M hardness test machine. Tensile test specimens were tested according to EN 2561 using a universal testing machine type Shimadzu AGC-10/TC with a maximum load of 100 kN.

Tab. 1. Welding parameters of the test seams with Ti+10vol% B_4C powder.

Seam Nr.	Pilot arc [A]	Welding current [A]	End current [A]	Powder feed [g/min]	Travel speed [mm/min]	Seam length [mm]	Layer number
S274	30	120	110	10	120	50	5
S275	30	120	110	10	140	50	5
S276	30	120	110	10	160	50	5
S277	30	120	110	10	180	50	5
S279	30	120	110	10	220	50	5
S283	30	120	110	10	260	50	5
S284	30	120	110	10	260	120	47

RESULTS

For the deposition of Ti- B_4C composite on the Ti substrate a travel speed as one of processing parameters was regularly modified to obtain dense, pore and crack free material. Following the calibration of the powder feed rate, 50 mm long, single layered seams were deposited as the first optimization step. After optimization of the deposition parameters multilayers up to 5 layers were manufactured. Table 1 summarizes processing parameters used during the deposition of 5 layers with the length of 50 mm. In case of multilayers, additional requirements had to be optimized, such as the built-up test structure has to keep the required geometry without losing the original dimensions through partial (run-off) or complete melting (loss of layered structure). From first test campaign the best parameters for the manufacturing of Ti- B_4C composite (Fig.1a) which consisted of 47 layers with the length of 120 mm were selected. Out of this wall, 8 pieces of tensile samples (Fig. 1b) were cut by EDM taking into account the deposition history.

Fig.1. Layered structure of a) Ti-B_4C composite prepared by additive manufacturing and b) cutting plan for preparation of tensile samples.

Young's modulus, ultimate tensile strength (UTS) and Vickers hardness (Hv) were measured and evaluated. Testing of tensile samples of Ti- B_4C composite revealed enhancement of Young's modulus (1.4 times), UTS (2.8 times) and hardness (3.1 times) in comparison to the minimum required properties of Titanium Grade1. On the other hand the improvement of these properties by addition of 10 vol.% of B_4C caused loss of elongation.

Tab. 2 Summary of properties of Ti-B_4C composite.

Sample	Density	Young's modulus [GPa]	Ultimate tensile strength [MPa]	Total strain at break [%]	Vickers hardness
S284	4.48 ± 0.02	155.9 ± 8.9	572.0 ± 48.8	0.36 ± 0.04	374 ± 28 HV
Ti Gd1 minimum	4.51	105	240	24	122

The cross-section analysis of microstructure revealed that unreacted boron carbide particles were layer wise distributed in the matrix. It seems that they followed layer by layer manufacturing steps. The detailed insight showed that the matrix is composed of titanium with new phases such as TiB and TiC. These phases appear due to the in-situ reaction as follows: $5Ti + B_4C \rightarrow 4TiB + TiC$. [14, 15] In the Fig.2b can be seen the unreacted B_4C particle surrounded with the reacted phase in the forms of thin, thick laths and/or prisms.

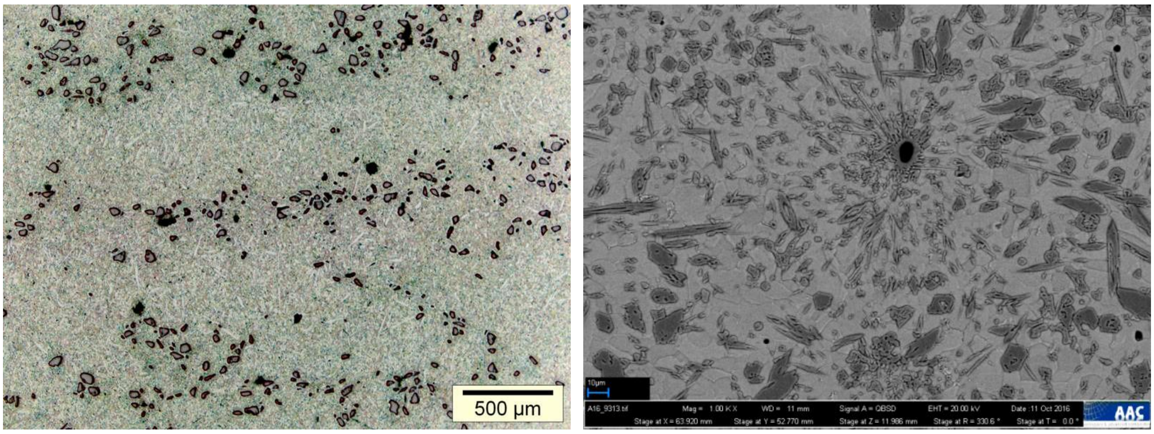

Fig. 2. Microstructure of Ti-B_4C composite a) layered ordering of unreacted B_4C and b) phases formed during reaction of Ti with B_4C.

According to binary Ti-B phase diagram the eutectic composition occurs at B content of 1.6 wt.% at temperature 1540°C. On the other hand the eutectic composition in the Ti-C combination is produced at approximately 100 °C higher temperature (1646°C) as for Ti-B. Considering the boron to carbon ratio in the B_4C and reaction mentioned above the primary TiB phase is formed.

CONCLUSION

Titanium - 10 vol.% B_4C composites were manufactured layer by layer by the 4M-System. Results revealed that the specific stiffness consisting of the elastic modulus per mass density of Ti-B_4C composites was considerably enhanced to 34.8 10^6 m^2s^{-2} in comparison to 23.3 10^6 m^2s^{-2} for pure titanium. The microstructure showed partially unreacted B_4C particles distributed in layers vertically aligned copying the deposition strategy. Boron carbide particles formed by reaction with Ti matrix mostly TiB particles in the form of laths and prisms.

ACKNOWLEDGMENT

This project has received funding from the European Union's Horizon 2020 research and innovation program under grant agreement No [673817].

REFERENCES

[1] Xiong, X., Zhang, H., Wang, G. "Metal direct prototyping by using hybrid plasma deposition and milling," J Mater Process Technol, 209 (2009) 124.

[2] Zhang, H., Xu, J., Wang, G., "Fundamental study on plasma deposition manufacturing," Surf Coat Technol, 171 (2002) 112.

[3] Katou, M., Oh, J., Miyamoto, Y., Matsuura, K., Kudoh, M., "Freeform fabrication of titanium metal and intermetallic alloys by three-dimensional micro welding," J. Mater. Design, 28 (2007) 2093.

[4] Clark, D., Bache, M., Whittaker, M. "Shaped metal deposition of a nickel alloy for aero engine applications," J Mater Process Technol, 203 (2008) 439.

[5] Song, Y.-A., Park, S., Choi, D., Jee, H. "3D welding and milling: Part I direct approach for freeform fabrication of metallic prototypes," Int J Mach Tool Manu, 45 (2005) 1057.

[6] Wanjara, P., Brochu, M., Jahazi, M., "Electron beam freeforming of stainless steel using solid wire feed," Materials and Design, 28 (2007) 2278.

[7] Gibbons, G. J., Hansell, R. G. "Direct tool steel injection mould inserts through the arcam EBM free-form fabrication process," Assembly Autom, 25 (2005) 300.

[8] Jimoh, A., Sigalas, I., Hermann M., In Situ Synthesis of Titanium Matrix Composite (Ti-TiB-TiC) through Sintering of TiH_2-B_4C, Mater Sci Appl, 3 (2012) 30

[9] Yang, Z. F., Lu, W. J., Xu, D., Qin, J. N., Zhang, D. "In Situ Synthesis of Hybrid and Multiple-Dimensioned Tita-nium Matrix Composites," J. Alloys Compd., 419 (2006) 76.

[10] Dariel, M. P., Frage, N., Levin, L., "A Novel Approach for the Preparation of B_4C-Based Cermets," Int. J. Refract. Met. Hard Mater., 18 (2002) 131.

[11] Prasad, V. V. B., Subramanyam, J., Bhat, B. V. R. "Preparation of Ti-TiB-TiC & Ti-TiB Composites by in-Situ Reaction Hot Pressing," J Mater Sci Eng A, 325 (2002) 126.

[12] Ni, D. R., Geng, L., Zhang, J., Zheng, Z. Z. "Effect of B_4C on Microstructure of in Situ Titanium Matrix Composites Prepared by Reactive Processing of Ti-B_4C System," Scripta Mater, 55 (2006) 429.

[13] http://asm.matweb.com/search/SpecificMaterial.asp?bassnum=mtu010

[14] Zhang, Y., Sun, J., Vilar, R., Characterization of (TiB+TiC)/TC4 in-situ titanium matrix composites by laser direct deposition, J.Mater.Process.Technol., 211 (2011)597–603.

[15] Tian, Y.S., Chen, C.Z., et al., Wear properties of alloyed layers produced by laser surface alloying of pure titanium with B_4C and Ti mixed powders, J.Mater.Sci. 40 (2005)4387.

SYNTÉZA, SPEKANIE A OPTICKÉ VLASTNOSTI SPINELOV MgAlON A $MgAl_2O_4$

SYNTHESIS, SINTERING AND OPTICAL PROPERTIES OF MgAlON AND $MgAl_2O_4$ SPINEL CERAMICS

M. Radwan, Z. Lenčéš, P. Šajgalík

Institute of Inorganic Chemistry, Slovak Academy of Science, Dúbravská cesta 9,

84536 Bratislava, Slovakia

ABSTRACT

The paper focuses on the examination of the morphology of spinel MgAlON powders formed by solid-state reaction and understanding of the influence of composition on crystal growth. MgAlON powders with seven different compositions were prepared from MgO, Al_2O_3 and AlN mixtures by heat treatment at 1800 °C for 3 h in nitrogen atmosphere. The SEM analyses of the as-synthesized powders showed a reduction in the particle size of the MgAlON powder with increasing the concentration of AlN and demonstrated that the MgAlON particles grow in principal by a layer-by-layer stacking mechanism. The sintering of translucent MgAlON and transparent $MgAl_2O_4$ has been also investigated. Translucent MgAlON spinels were prepared from one of synthesized composition by two-step sintering: pressureless field-assisted pre-sintering (1800°C/3h) and hot-isostatic pressing (18000°C/5h/200 MPa Ar). Highly transparent $MgAl_2O_4$ spinel ceramic were prepared from a commercial nano powder by a powder metallurgy approach including formulation of stable aqueous spinel slurry, freeze granulation and drying, CIP-ing of powders to green pellets and subsequent two-step sintering: pressureless pre-sintering in air (1550°C/2h) and hot-isostatic pressing (1550°C/5h/200 MPa Ar). The real in-line optical transmission (RIT) at $\lambda = 632.8$ nm of the polished dense $MgAl_2O_4$ spinel samples reached 87% of the theoretical transmittance.

Keywords: MgAlON; spinel; solid-state reaction; morphology; transparent

INTRODUCTION

MgAlON ceramics have a wide range of solid-solution compositions in the MgO-Al_2O_3-AlN system with cubic spinel structure [1]. It possesses good mechanical [3-5], thermal [3,5], optical [5-11] and dielectric [5, 12] properties, and except of already established optical applications can be used also in other fields of industry.

MgAlON is usually prepared by reactive solid-state sintering of MgO, Al_2O_3 and AlN mixtures in the temperature range of 1400°C - 2000°C in nitrogen atmosphere using pressureless sintering [13-15], hot pressing [1, 2, 16], and spark plasma sintering [3]. During these four decades, only two reports were published in the early of 1990s about the optical properties of MgAlON by Mathers et al. [6] and Granon et al. [7] and the reported in-line transmittances were low (~60%) in the visible range of the spectrum. Growing interest on the optical properties of MgAlON emerged since 2014, when Liu et al. succeeded to fabricate transparent MgAlON with high in-line transmittance (~80%) in the visible wavelengths using two-steps processing approach: i) synthesis of fine MgAlON powder and ii) densification of MgAlON by application of an appropriate sintering method [5]. However, there is no prior literature about the morphology of the powder, the crystal growth mechanism, and the effect of composition on the morphology. To understand this, MgAlON powders with seven different compositions were prepared by solid-state reaction followed by SEM examination of the morphology of prepared powders. In addition, sintering studies of lab-made MgAlON and commercial nano $MgAl_2O_4$ powders was performed. Optical transmissions of sintered spinel ceramics were also determined.

EXPERIMENTAL

MgAlON powders with seven different compositions (Fig. 1) were prepared from pure MgO (EMSURE, Merck), Al_2O_3 (TM-DAR, Taimicron), and AlN (grade C, H.C. Starck) powders.

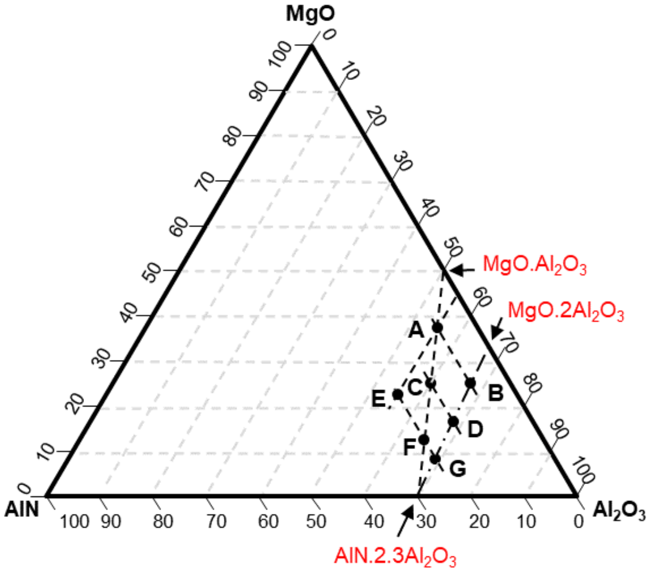

Fig. 1.Studied compositions in the $MgO–Al_2O_3–AlN$ system (in mol%)

The powder mixtures were wet mixed in HDPE bottles using isopropanol and Al_2O_3 balls (Ø 4 mm) as media. The dry mixtures were annealed in BN crucible at 1800°C for 3 h in N_2 atmosphere. The phase composition of prepared powders was determined by XRD analysis.

The morphologies of the as-synthesized powders were analyzed by SEM. The average particle size was determined by using the ImageJ software.

A commercial nano $MgAl_2O_4$ powder (S30CR, Baikowski) was used as the starting material for the preparation of transparent $MgAl_2O_4$. The initial spinel powder was dispersed in an aqueous medium with the aid of an organic surfactant Darvan to form stable spinel suspensions which were used for making soft spinel granules by freeze granulation and drying. Different sintering techniques were used for the densification of MgAlON and $MgAl_2O_4$ samples like direct hot-pressing (DHP), pressureless sintering (PLS) in vacuum, air or nitrogen, hot isostatic pressing (HIP) under 200 MPa Ar pressure. The real inline transmittance (RIT) was determined using a red He-Ne laser light (λ = 632.8 nm) with a distance between the sample and the detector of 1 m.

RESULTS

Influence of starting composition on the particle size of MgAlON

The XRD results showed the formation of single-phase MgAlON spinels. Table 2 gives the measured lattice parameters from the XRD data (a_{exp}) of the MgAlON compositions compared to the calculated lattice parameters (a_{cal}) according to the equation proposed by X. Wang et al. [2]. The small difference between (a_{exp}) and (a_{cal}) indicates that the compositions of the synthesized MgAlON powders were very close to the starting formulations.

Table 2. Experimental (a_{exp}) and calculated (a_{cal}) lattice parameters of studied compositions

	MgAlON compositions (see Fig. 1)						
Lattice parameters [nm]	A	B	C	D	E	F	G
Experimental, (a_{exp})	0.8046	0.7995	0.8012	0.7979	0.8020	0.7981	0.7966
Calculated, a_{cal}	0.8006	0.7975	0.7987	0.7966	0.7967	0.7967	0.7957
Difference, (a_{exp}) - (a_{cal})	0.0040	0.0020	0.0026	0.0013	0.0028	0.0014	0.0009

The morphologies of prepared MgAlON powders are shown in Fig. 2. It can be noticed that the size and shape of the particles varied with the composition. The oxide-rich MgAlON powders had strong agglomeration of coarse MgAlON particles >10 μm with polyhedral morphology, while the nitrogen-rich MgAlON compositions had softer agglomeration of finer MgAlON particles ≤ 1μm with weak crystalline morphology. The relationship between the particle size and the content of AlN in MgAlON powders is shown in Fig. 3. With increasing AlN content in the MgAlON composition the particle size decreases, i.e. the dissolved AlN hinders the growth of MgAlON crzstals. From the surface details of the particles it can infer that the reactive solid-state synthesis of MgAlON involved surface crystal growth steps.

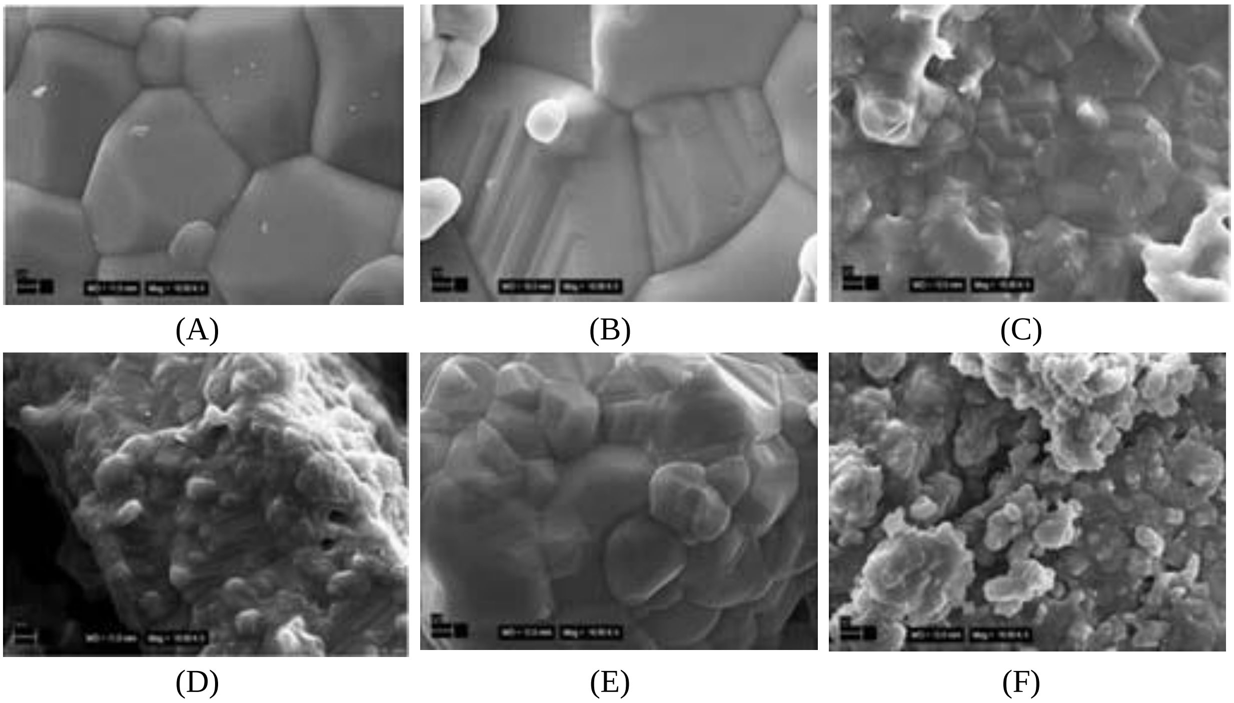

Fig. 2. SEM micrographs of MgAlON powders (bar 1 μm, magnif. 10000×)

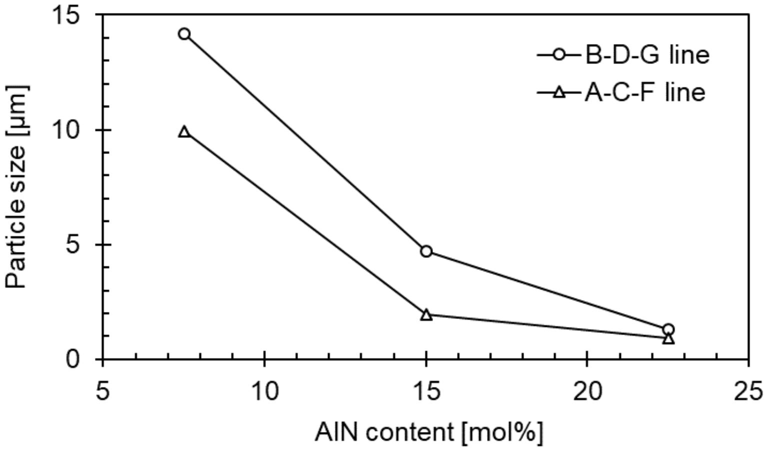

Fig. 3. Effect of AlN content on the particle size of MgAlON powders

Dense MgAlON and transparent MgAl$_2$O$_4$ spinel samples

The images of dense MgAlON samples (t.d. > 99%) are shown in Fig. 4. The highest RIT ~30% was achieved for the samples prepared by two-step sintering, i.e. pressureless sintering (PLS) in vacuum followed by hot isostatic pressing (HIP) in 200 MPa Ar. A little bit higher RIT was obtained for the samples sintered in alumina crucible (bottom right in Fig. 4) compared to the samples sintered in BN crucible (bottom left in Fig. 4)

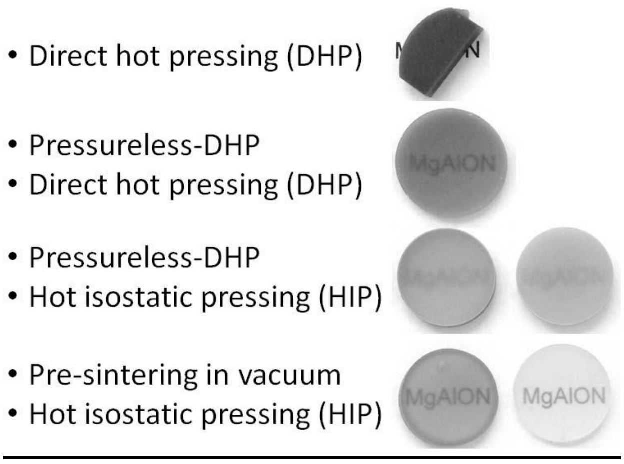

Fig. 4. Optical micrographs of MgAlON samples densified with different sintering techniques

The dependence of zeta potential and agglomerate size on pH of $MgAl_2O_4$ slurries is shown in Fig. 5. Due to the smaller agglomerate size on Darvan was used (in an amount from 0.5 wt% to 5.0 wt%) for the preparation of transparent samples. The images of transparent $MgAl_2O_4$ samples with different Darvan content are shown in Fig. 6. The highest RIT 87.2 % was obtained for the sample containing 2 wt% Darvan surfactant in the starting powder mixture.

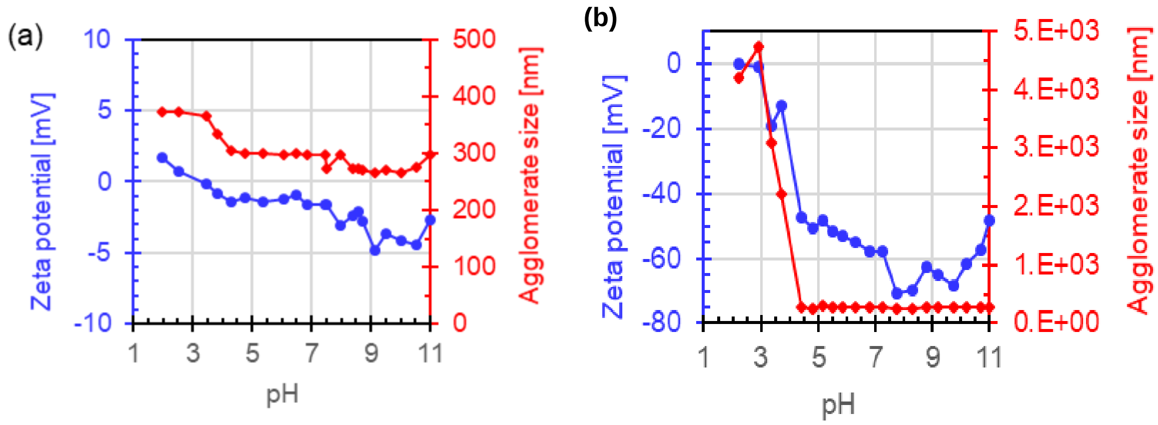

Fig. 5. Zeta potential and agglomerate size versus pH of $MgAl_2O_4$ slurries with (a) 0.5 wt% Dolapix and (b) 0.5 wt% Darvan

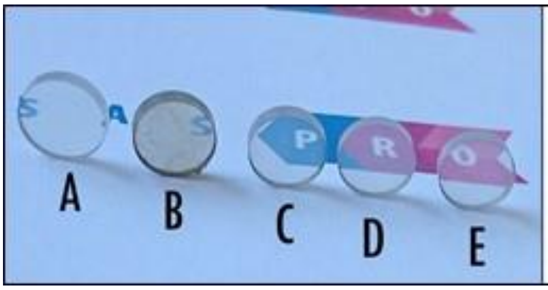

		RIT (%)
A	as-received powder	78.7
B	freeze granulated (0.5% Darvan)	62.9
C	freeze granulated (2.0% Darvan)	87.2
D	freeze granulated (3.0% Darvan)	83.7
E	freeze granulated (4.0% Darvan)	85.3

Fig. 6. Transparent $MgAl_2O_4$ samples (~2 mm thick) and their RIT

ACKNOWLEDGEMENTS

This work was part of the SASPRO project (contract number 1329/03/02) co-funded by the FP7-Marie Curie Action (Project ID number 609427) and the Slovak Academy of Sciences. The financial support from APVV-14-0385 and VEGA 2/0164/18 is also appreciated.

REFERENCES

[1] J. Weiss, P. Greil, The system Al-Mg-O-N, *J. Am. Ceram. Soc.*, 65 (1982) C68-C69.

[2] X. Wang, W. Li, S. Seetharaman, Kinetic studies of oxidation of MgAlON and a comparison of the oxidation behaviour of AlON, MgAlON, O'SiAlON-ZrO_2, and BN-ZCM ceramics, *Z. Metallkd.*, 93 (2002) 545-553.

[3] W. Dai, A. Yamaguchi, W. Lin, J. Ommyoji, J. Yu, Z. Zou, Preparation and properties of spark plasma sintered magnesium aluminum oxynitride, *J. Ceram. Soc. Jpn.*, 115 (2007) 525-529.

[4] J.-F. Roy, P. Goeuriot, F. Thevenot, Reactive hot-pressing study of the Al_2O_3-AlN-MgO system, *J. Mater. Sci. Lett.*, 13 (1994) 530-532.

[5] X. Liu, H. Wang, B. Tu, W. Wang, Z. Fu, Highly transparent $Mg_{0.27}Al_{2.58}O_{3.73}N_{0.27}$ ceramic prepared by pressureless sintering, *J. Am. Ceram. Soc.*, 97 (2014) 63-66.

[6] J.P. Mathers, R. G. Frey, Transparent ceramic composite article comprising aluminum oxide and aluminum magnesium oxynitride, US Patent No. 5096862, 1992.

[7] A. Granon, P. Goeuriot, F. Thevenot, Aluminum magnesium oxynitride: a new transparent spinel ceramic, *J. Eur. Ceram. Soc.*, 15 (1995) 249-254.

[8] X. Liu, H. Wang, B. Tu, W. Wang, Z. Fu, Novel divalent europium doped MgAlON transparent ceramic for shortwave ultraviolet erasable windows, *Scripta Mater.*, 105 (2015) 30-33.

[9] X. Liu, B. Chen, B. Tu, H. Wang, W. Wang, Z. Fu, Characterization in activators' distribution and photoluminescence properties of Ce^{3+} doped MgAlON transparent fluorescent ceramic, *J. Eur. Ceram. Soc.*, 36 (2016) 2801-2805.

[10] K. Li, H. Wang, X. Liu, W. Wang, Z. Fu, Mn^{2+} activated MgAlON transparent ceramic: a new green-emitting transparent ceramic phosphor for high-power white LED, *J. Eur. Ceram. Soc.*, 37 (2017) 4229-33.

[11] X. Liu, B. Chen, B. Tu, H. Wang, W. Wang, Z. Fu, Variation of structure and photoluminescence properties of Ce^{3+} doped MgAlON transparent ceramics with different doping content, *Materials*, 10 (2017) 792.

[12] O. Morey, P. Goeuriot, D. Juve, D. Treheux, Dielectric investigations on 'MgAlON' compounds: role of nitrogen content, *J. Eur. Ceram. Soc.*, 23 (2003) 345-355.

[13] H.X. Willems, G. de With, R. Metselaar, Thermodynamics of Alon III: stabilization of Alon with MgO, *J. Eur. Ceram. Soc.*, 12 (1993) 43-49.

[14] A.Granon, P. Goeuriot, F. Thevenot, J. Guyader, P. L'Haridon, Y. Laurent, Reactivity in the Al_2O_3-AlN-MgO system. The MgAlON spinel phase, *J. Eur. Ceram. Soc.*, 13 (1994) 365-370.

[15] S. Bandyopadhyay, G. Rixecker, F. Aldinger, H. Maiti, Effect of controlling parameters on the reaction sequences of formation of nitrogen-containing magnesium aluminate spinel from MgO, Al_2O_3, and AlN, *J. Am. Ceram. Soc.*, 87 (3) (2004), pp. 480-482
[16] X. Wang, W. Li, S. Seetharaman, Synthesis and characterisation of MgAlON, *Z. Metallkd.* 93 (2002) 540-544.

PREPARATION OF YB_4 CERAMICS BY REACTION SINTERING FROM ELEMENTS

Z. Kováčová[1,2], L. Bača[1], E. Neubauer[2]

[1]*Institute of Inorganic Chemistry, Technology and Materials, Faculty of Chemical and Food Technology, Slovak University of Technology, Radlinského 9, 812 37 Bratislava*

[2] *RHP-Technology GmbH, Forschungs- und Technologiezentrum, A-2444 Seibersdorf, Austria*

ABSTRACT

Yttrium tetraboride (YB_4) was prepared using direct synthesis from elements by reaction sintering. Influence of temperature and boron content on densification and phase evolution of samples was studied. Reactions were performed at temperatures from 1100°C to 1800°C for 1 hour with 30MPa pressure in vacuum. Boron amount varied from stoichiometric content to 5 and 10wt% excess in terms of considering reaction from elements. Stoichiometric reaction led primarily to the formation of YB_2 and YB_4 and several secondary phases such as Y_2O_3, YBO_3 and $Y_{16.86}B_8O_{38}$. YB_4 as a main phase was formed only at elevated temperatures (1700°C and 1800°C) but certain content of impurities was still present. Excess of B amount resulted in formation of YB_4 as a primary phase in all prepared samples.

Keywords: YB_4, reaction sintering

INTRODUCTION

Borides of rare earth metals are interesting high-temperature materials with curious chemical and structural properties. In spite of this, detailed studies of RE-B systems are rare and there has been very little research into the potential of rare earth metal borides for use as materials for ultra-high temperature applications. Many fundamental and potentially useful properties have not been widely explored. However, some of them are also suitable as candidates for application in extreme environments [1-3]. One of these candidates seems to be also yttrium tetraboride (YB_4), which can act as a source of yttrium for the stabilization of oxide scale formed due to oxidation of ZrB_2 based UHTCs. In contrast to the other borides of yttrium, the YB_4 possesses the highest melting point and chemical stability. Moreover, YB_4 exhibits high hardness, strength, good electrical and thermal properties [1]. YB_4 has been the subject of a few previous studies, mainly related to crystal structure [4] and investigation of physical and chemical properties [5-7]. Recent data on physical properties are rare or still not available. Furthermore, YB_4 powder is not commercially available and the synthesis method has not been widely explored. In general, several methods are available for the synthesis of borides. High-purity single crystals of YB_4 were successfully prepared by the floating zone technique [5,8-10]. Most of the studies dealt with the preparation of YB_4 powder by reduction of yttria by boron [7,11-13], boron carbide [2,3] and combined boron carbide/carbothermal reduction [1] was also reported. The result of these methods is powder which has to be further processed by sintering or hot-pressing. Reaction sintering from elements [5,14,15] allows us to prepare bulk YB_4 ceramic in one step.

The present study is focused on preparation of fully dense YB_4 ceramics by reaction sintering from elements. The effect of temperature and boron content on reaction products was investigated.

EXPERIMENTAL

Commercially available Y (<75 µm, 99,9%, CRM China Rare Metal Material Co.) and B (1-2µm, 99,9%, CRM China Rare Metal Material Co.) were used as starting materials.

The YB_4 reaction synthesis was performed from elements according to following reaction:

$$Y(s) + 4\,B(s) = YB_4(s) \qquad (1)$$

The amount of starting powders was mixed regarding to reaction (1) in stoichiometric proportion and with 5 and 10wt% excess of boron calculated. Powder mixtures were homogenized on rolls in cyclohexane using zirconia balls and dried in evaporator. Powder was filled into graphite mould coated with BN. Reaction sintering was performed in hot-press (experimental inductive hot-press (IHP), PTC AIT, 2009) in vacuum for 1 hour with 30 MPa pressure at temperatures from 1200°C to 1800°C. After synthesis, samples were grinded in order to remove surface layer and analysed by XRD (Stoe Theta-Theta Cokα radiation). The bulk densities were measured using the Archimedes method. When the samples were porous, approximated density was calculated from dimensions and weight.

RESULTS

According to the Y-B phase diagram (Fig. 1) five following compounds: YB_2, YB_4, YB_6, YB_{12} and YB_{66} can rise by the reaction of yttrium and boron. Recent studies showed the existence of new phases of yttrium boride. An YB_3 phase was reported by Binder [5] and a higher boride, YB_{50}, was investigated by Tanaka [16]. For the ultra-high temperature application the most stable yttrium borides such as YB_2, YB_4 and YB_6 are of the interest, especially YB_4 with the highest melting point and stability. Higher borides, such as YB_{12}, YB_{50} and YB_{66} were not considered for high temperature application due to the high boron content in compound. Formation of higher amount of liquid B_2O_3 phase during oxidation turning into volatile B_2O_2 at elevated temperatures during oxidation would lead to marked mass loss and subsequent material degradation. In-situ reaction hot-pressing was used for preparation of yttrium boride samples in the temperature range of 1300 °C up to 1800 °C.

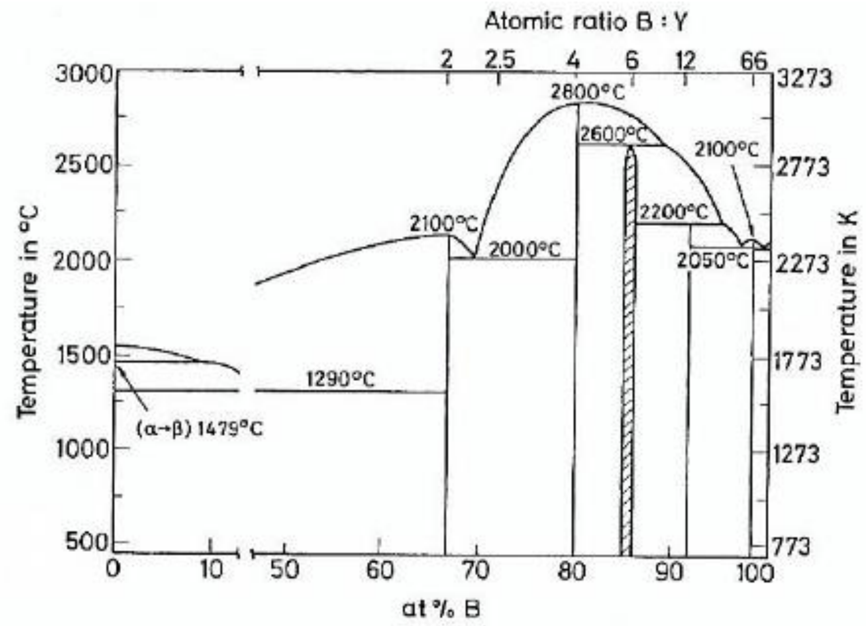

Fig. 1. The Y-B phase diagram given by Lundin (1961), later reviewed by Oliver and Brower (1971) [5,15]

Table 1 summarizes results of densification and phase composition in relation to the reaction temperature and the boron content in starting powder.

Tab. 1. Summary

Reaction temp.	**Y-B stoichiometric**		**Y-B + 5wt% excess of B calculated**		**Y-B + 10wt% excess of B calculated**	
°C	**densification**	**phases identified by XRD**	**densification**	**phases identified by XRD**	**densification**	**phases identified by XRD**
1200	72.2%*; porous	**YB_2**, YB_4, Y_2O_3, YBO_3, $Y_{16.86}B_8O_{38}$				
1300	>100%	**YB_2, YB_4**, Y_2O_3, YBO_3, $Y_{16.86}B_8O_{38}$	67.2%*; porous	**YB_4**, YBO_3 $Y_{16.86}B_8O_{38}$	63.1%*; porous	**YB_4**, YBO_3
1400	>100%	**YB_2, YB_4**, Y_2O_3, YBO_3, $Y_{16.86}B_8O_{38}$				
1500	>100%	**YB_4, YB_2**, Y_2O_3, YBO_3, $Y_{16.86}B_8O_{38}$	86.9%*	**YB_4**, YBO_3 $Y_{16.86}B_8O_{38}$	76.3%*; porous	**YB_4**, YBO_3
1600	>100%	**YB_4**, YB_2, Y_2O_3, YBO_3, $Y_{16.86}B_8O_{38}$	99.0%	**YB_4**, YBO_3 $Y_{16.86}B_8O_{38}$	95.9%	**YB_4**, YBO_3
1700	>100%	**YB_4**, Y_2O_3, YBO_3, $Y_{16.86}B_8O_{38}$	99.2%	**YB_4**, YBO_3 $Y_{16.86}B_8O_{38}$	97.6%	**YB_4**
1800	>100%	**YB_4**, Y_2O_3, $Y_{16.86}B_8O_{38}$	98.9%	**YB_4**, YBO_3 $Y_{16.86}B_8O_{38}$		

* dimensional density

Stoichiometric reaction led primarily to the formation of YB_2 and YB_4 and several secondary phases such as Y_2O_3, YBO_3 and $Y_{16.86}B_8O_{38}$. As the reaction temperature rose, the proportion of YB_4 to YB_2 intensities was also enhanced. At temperatures of 1700°C and 1800°C almost pure YB_4 phase was detected. However, certain content of impurities was still present as indicated also by the density measurement. The density of these samples was above 100% as a result of presence of the products with higher density (YB_4 – 4.32 g.cm^3, YB_2 – 5.05 g.cm^3, Y_2O_3 – 5.01 g.cm^3, YBO_3 – 4.46 g.cm^3). Increased excess of boron resulted in a reduction of densification after reaction sintering of elements, especially after sintering at 1500°C and 1600°C. On the other hand, XRD analysis showed formation of YB_4 as a main phase. In case of 5wt% excess of boron, small content of secondary phases such as YBO_3 and $Y_{16.86}B_8O_{38}$ still remained. If the 10wt% excess of boron was used, $Y_{16.86}B_8O_{38}$ phase disappeared. After reaction sintering performed at 1700°C, only YB_4 was identified by XRD (Fig. 2). Almost fully dense YB_4 ceramic material with the density of 97.6% was prepared from mixture of powders with the 10 wt.% excess of boron. On the other hand, 5 wt. % of boron powder in reaction mixture didn´t yield the pure YB_4 phase though the density reached 99.2%. Similar high density (above 100 % of relative density of YB_4) was observed in the sample prepared from stoichiometric amount of powders. However, it must be emphasized that the relative density was calculated with respect to the pure YB_4 and without consideration of any impurities.

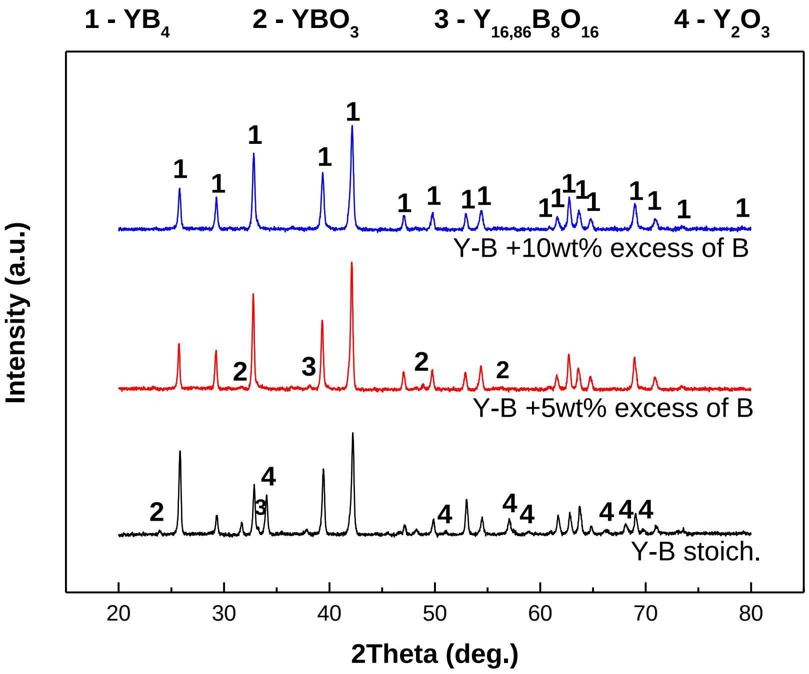

Fig. 2. XRD analysis of the surface of samples prepared at 1700°C/1h/30MPa in vacuum from powders with various boron content

CONCLUSION

Stoichiometric reaction resulted especially in the formation of YB_2 and YB_4 and several secondary phases such as Y_2O_3, YBO_3 and $Y_{16.86}B_8O_{38}$. The proportional abundance of detected phases changed with increasing temperature. YB_4 as a main phase was formed only at elevated temperatures (1700°C and 1800°C) but certain content of impurities was still present. If the excess of calculated amount of boron was only 5wt%, borates were still detected even if the reaction was performed at 1800°C. Using 10wt% excess of calculated amount of boron the pure YB_4 was identified at 1700°C with 97.6% of densification. Below this temperature small content of YBO_3 was identified.

REFERENCES

[1] Zaykoski, J. A., Opeka, M. M., Smith, L. H., Talmy, I. G. Synthesis and characterization of YB_4 Ceramics, Journal of the American Ceramic Society, 2011, p. 4059-4065.5.

[2] Li, J., Peng, A., He, Y., Yuan, H., Guo, Q., She, Q., Zhang, L. Synthesis of Pure YB_4 Powder via the Reaction of Y_2O_3 with B_4C, Journal of the American Ceramic Society, 2012, p. 2127-2129.

[3] Guo, Q., Xiang, H., Sun, X., Wang, X., YHOU, Y. Preparation of porous YB_4 ceramics using a combination of in-situ borothermal reaction and high temperature partial sintering. Journal of European Ceramic Society, 2015, vol. 35, p. 3411-3418.

[4] Giesse, R. F., Matkovich, V. I., Economy, J. The crystal structure of YB_4, ZeitschriftfürKristalographie, 1965, p. 423-432

[5] Gmelin Handbook of Inorganic and Organometallic Chemistry, 8th Edition, Springer – Verlag, ISBN 0-387-93604-1.

[6] Fu, Y.-Y., LI, Y.-W., Huang, H.-M. Elastic and Dynamical Properties of YB4: First-Principles Study, Chin. Phys. Lett., 2010, p. 116201-1 – 4.Second edition. A Wiley-Interscience Publication, 1976. ISBN 0-471-47860-1.

[7] Waskowska, A., Gerward, L., Staun Olsen, J., Ramesh Babu, K., Vaitheeswaran, G., Kanchana, V., Svane, A., Filipov, V.B., Levchenko, G., Layschenko, A. Thermoelastic properties of ScB_2, TiB_2, YB_4 and HoB_4: Experimental and theoretical studies. ActaMaterialia, vol. 59, 2011, p. 4886-4894.

[8] Otani, S.,Korsukova, M.M.,Mitsuhashi, T.,Kieda, N. Floating zone growth and high-temperature hardness of YB_4 and YB_6 single crystals. Journal of Crystal Growth, 2000, vol. 217, p. 378-382.

[9] Otani, S., Xuan, Y., Yajima, Y., Mori, T. Flux growth of YB_4 crystals and their magnetic properties, Journal of Alloys and Compounds, vol. 361, 2003, p. L1-L2.

[10] Günster, J., Tanaka, T., Souda, R. Surface reorganization observed on YB_4(001). Physical review B, vol. 56, 1997, p. 15962-66

[11] Kudintseva, G.A., Kuznetsova, G.M., Bondarenko, V.P., Selivanova, N.F., Shlyuko, V.Ya. Preparation and emissive properties of some yttrium and gadolinium borides. PoroshkovayaMetallurgiya, vol. 2, 1968, p. 45-53.

[12] Menelis, R.M., Meerson, G.A., Zhuravlev, N.N., Telyukova, T.M., Stepanova, A.A., Gramm, N.V. Vacuum.-thermal preparation of yttrium and gadolinium borides, and some of their properties. PoroshkovayaMetallurgiya, vol. 11, 1966, p. 77-84.

[13] Jäger, B., Paluch, S., Wolf, W., Herzig, P., Zogal, O.J., Shitsevalova, N., Paderno, Y. Characterization of the electronic properties of YB_4 and YB_6 using ^{11}B NMR and first-principles calculations. Journal of Alloys and Compounds, vol. 385, 2004, p. 232-238.

[14] Greenwood, N. N., Earnshaw, A. Chemistry of the Elements, Second edition, Elsevier, ISBN 0-7506-3365-4.
[15] Matkovich, V. I. Boron and Refractory Borides, Second edition, Springer - Verlag, 1977, ISBN 978-3-642-66622-3.
[16] Tanaka, T., Okada, S., Ishizawa, Y. A new yttrium higher boride: YB50. Journal of Alloys and Compounds, 1994, vol. 205, p. 281-284.

PRÍPRAVA A CHARAKTERIZÁCIA VYSOKOTEPLOTNEJ KERAMIKY NA BÁZE ZrB_2-SiC

PREPARATION AND CHARACTERIZATION OF ZrB_2-SiC BASED ULTRA HIGH TEMPERATURE CERAMICS

Z. Fürdősová[1], I. Dlouhý [2], P. Tatarko[1]

[1]Institute of Inorganic Chemistry, Slovak Academy of Sciences, Dúbravska cesta 9, 845 36, Bratislava, Slovak Republic

[2] Institute of Physics of Materials, Academy of Sciences of the Czech Republic, Žižkova 22, 61662 Brno, Czech Republic

ABSTRACT

The influence of powder processing (2 different planetary milling conditions: 150rpm/7h; 250rpm/4h), and different content of Lu_2O_3 (2wt.% and 5wt.%) on the sintering, microstructure evolution, phase composition, and mechanical properties of ZrB_2-SiC ceramics was investigated. All the samples achieved a relative density above 98% when sintered at 2050°C/90MPa/7min in Ar using field assisted sintering technology. A finer particle size and a higher amount of WC contamination in the powder did not lead to the better sinterability of the materials. Despite having slightly lower both the density and the hardness when compared to the ZrB_2-SiC without Lu_2O_3, the materials with 5 wt.% Lu_2O_3 showed the highest bending strength, Young's modulus and fracture toughness among all of the investigated materials.

Keywords: zirconium diboride, ultra-high temperature ceramics, mechanical properties

INTRODUCTION

Zirconium diboride (ZrB_2), similar to other so-called Ultra High Temperature Ceramics (UHTCs), has high melting temperature (above 3000°C), good thermal and electric conductivity, good oxidation resistance and strength at elevated temperatures [1]. Such materials are used for applications performing at high temperatures, such as rocket propulsion, or thermal protection system for sharp leading edges of hypersonic vehicles [1, 2].

Although ZrB_2 has extremely high melting temperature (3246°C), monolithic material has limited oxidation resistance [3,4], as during oxidation in air above 1000°C, B_2O_3 starts evaporating, and the porous ZrO_2 layer is the only phase remaining after the oxidation at 1500°C [5]. The phase transformation of ZrO_2 (1000-1200°C) has also a negative effect leading to the volume change and the increase of ZrO_2 layer porosity, which accelerate the oxidation rate [6]. Silicon carbide (SiC) is one of the most commonly used additives to improve the oxidation resistance of monolithic ZrB_2 ceramics. During oxidation it forms a borosilicate glass on the surface of ZrB_2-SiC, which reduces the oxygen permeation [1]. For this reason, a ZrB_2-25vol.% SiC system has been considered as the most promising material system for ultra-high temperature environments [7]. However, new materials for hypersonic applications need to meet strict requirements of aerospace industry to survive temperatures above 2000°C. The aim of the work is to develop a new diboride material for extreme applications by introducing the Lu_2O_3 additive into the commonly used ZrB_2 – 25vol.%SiC material system. The work is focused on the study of the effect of different particle size of raw materials, contamination, and different content of Lu_2O_3 on the sintering, microstructure evolution, phase composition, and mechanical properties of ZrB_2-SiC ceramics.

EXPERIMENTAL PROCEDURE

Commercially available powders of ZrB_2 (d50 ~1.5-3.0 μm, grade B, H.C. Starck, Germany), β-SiC (d50 ~0.6 μm Superior Graphite, USA, β-SiC) and Lu_2O_3 (d50 ~3.0-15.0 μm, Treibacher, Austria) were used as raw materials. Three different compositions of powder mixtures were prepared: ZrB_2-25vol.%SiC – "*ZS*"; ZrB_2-25vol%SiC-2wt.%Lu_2O_3 – "*ZS2Lu*"; ZrB_2-25vol.%SiC-5wt.%Lu_2O_3 – "*ZS*$_5$*Lu*". In order to investigate the effect of particle size and contamination, two different planetary milling conditions (Retsch PM 100) were used: 150 rpm for 7 hours (h) and 250 rpm for 4h. The powders were milled in isopropylalcohol, in a tungsten carbide (WC) jar, with WC balls having a diameter of 3mm. The particle size distribution of the powders was determined using a laser particle sizer (Fritsch Analysette 22, Germany) by wet method in deionized water. The stability of water-based suspension of the as-received ZrB_2, as well as milled ZrB_2 powders was investigated by the sedimentation test. The dried milled powders were uniaxialy pressed in a graphite die with a diameter of 20 mm at a pressure of 30 MPa. The sintering was performed using a direct hot press (DHP) apparatus (DSP 507, Dr. Fritsch GmbH., Germany) at the temperatures of 2000°C, or 2050°C, and pressure of 70, or 90 MPa, in Argon atmosphere. Both the heating and cooling rates were 100°C/min, while the dwell time was 7 minutes. The density was measured by the Archimedes method. Theoretical density was calculated by the rule of mixture basis, considering the weight percentages and densities of ZrB_2, SiC, Lu_2O_3, and WC (determined by Rietveld analysis). The microstructure was investigated using an optical microscopy (VHX-1000 KEYENCE). Both the three-point bending strength (INSTRON 8862; a span of 16 mm, a cross-head speed of 0.5 mm/min) and the Young´s modulus (IMCE HT1600; resonance technique) were measured on the bars with dimensions of 1.5 x 2.2 x 18 mm. The hardness and the indentation fracture toughness were evaluated using a Vickers indentation (ZWICK ROELL Z2,5), at the loads of 9.81 N and 98.1 N. The crystalline phases were identified using X-ray diffraction (Panalytical Empyrean, Cu Kα radiation), followed up by Rietveld analysis.

RESULTS

The two milling conditions of 150rpm/7h and 250rpm/4h were selected based on the study of various milling conditions for the pure ZrB_2 powder with the aim to obtain the final particle size below 1 μm and an acceptable level of WC contamination (not shown here). Table 1. and Table 2. show the average particle size of all three compositions after milling at two different conditions. The milling at 250rpm/7h was more effective (d50 ~ 0.22-0.51μm) than the milling at 150rpm (d50 ~ 0.41-0.62μm), while in both cases there was the significant refinement of the particles (D90 ≤ 1.07μm) from the initial particle size of the powders. Such remarkable refinement of the particle size had positive effect on the stability of water-based suspension. Fig.1a and Fig.1b show the results of sedimentation test for the as-received and milled powders after one and 14 days, respectively. The XRD and Rietveld analysis revealed that the milling at 250rpm/4h resulted in a more significant WC contamination (2.30 - 2.70 wt.%) when compared to the milling at 150rpm/7h (0.60 – 0.80 wt.%), Table 3.

Tab. 1 The particle size analysis after the planetary ball milling at 150rpm / 7h

150 rpm	ZS-150	ZS2Lu-150	ZS5Lu-150
d10 [μm]	0.25	0.32	0.34
d50 [μm]	0.41	0.57	0.62
d90 [μm]	0.69	1.00	1.07

Tab. 2 The particle size analysis after the planetary ball milling at 250rpm / 4h

250 rpm	ZS-250	ZS2Lu-250	ZS5Lu-250
d10 [μm]	0.12	0.23	0.30
d50 [μm]	0.22	0.40	0.51
d90 [μm]	0.40	0.69	0.87

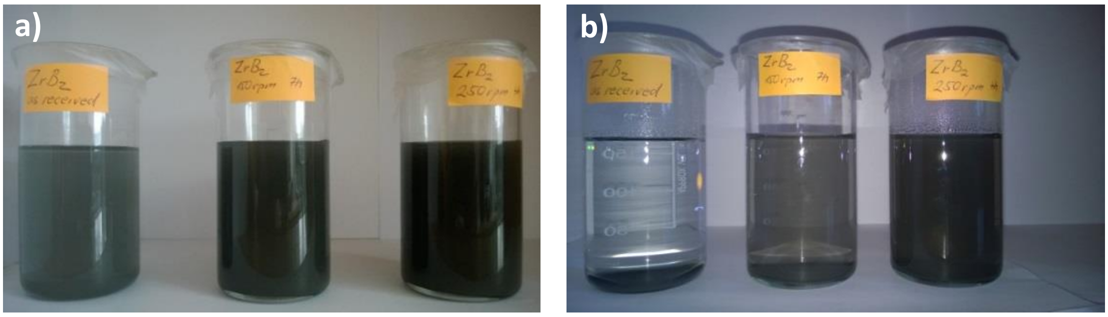

Fig. 1. Sedimentation test a) during 1 day and b) after 14 days

The effect different sintering conditions on the final material density was investigated for the ZrB_2-25vol.%SiC composition without Lu_2O_3. In these experiments, the dwell time was kept to 7 minutes and Argon atmosphere was used. As shown in Fig. 2, when the pressure of 70 MPa was applied in the temperature range of 1800-2000°C, the spontaneous sintering started at 1448°C (sample No.1). The relative density of the sample was 97.03%. To ensure that the maximum pressure was applied when the spontaneous sintering would have started, the pressure of 70 MPa was applied in the temperature range of 1200-1500°C (sample No. 2). The densification started shortly after applying the pressure, at 1225°C, while from 1700°C there was no further densification of the sample, leading to RD 96.85%. Therefore, the pressure of 70 MPa was then applied in the temperature range of 1500-2000°C (sample No. 3). Similar to the first case, the simultaneous compaction started at 1458°C and was significant to 1730°C. A further improvement in the density was not achieved (RD: 96.29%). The densification of the material when the pressure was applied in a wide temperature range of 400 to 2000°C started at 730°C and was significant between 1400-1643°C (sample No. 4), leading to the final RD 97.07%. To further improve the density, the temperature and the pressure were increased to 2050°C and 90 MPa, respectively (sample No. 5). The material with the highest relative density, 99.82%, was obtained.

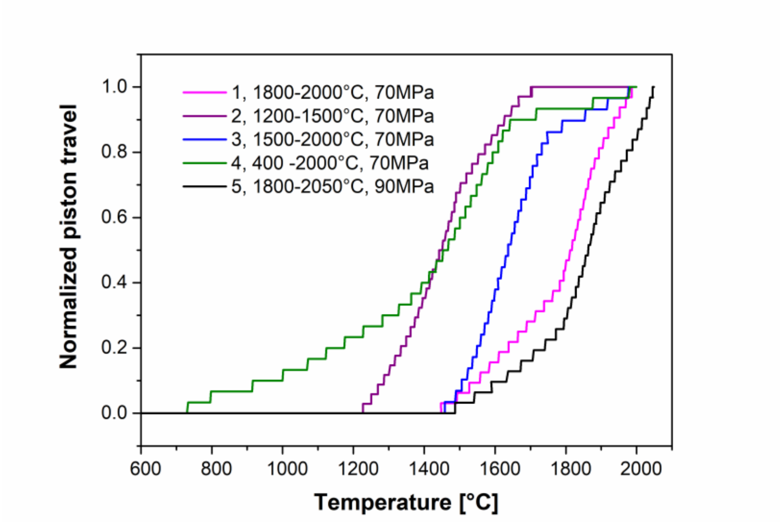

Fig. 2. The sintering curves for the reference ZrB_2-SiC material sintered at different conditions

Therefore, the sintering regime of 2050°C/90MPa/7 min/Ar was used for further study. All the final 6 samples (3 different compositions prepared using two milling conditions) achieved a relative density above 98 % (Table 3). Fig. 3 shows the microstructures of all the final 6 samples (3 different compositions prepared using two different milling conditions). It is obvious that the microstructures of the samples prepared after milling at 250rpm/4h were more porous than the samples after milling at 150rpm/7h. More importantly, the materials sintered after milling at 150rpm/7h showed finer microstructures when compared to the materials sintered after milling at 250 rpm/4h.

Tab. 3 Density of the investigated materials after sintering at 2050°C / 90 MPa / 7 min / Ar

density/no		ZS-150	ZS2Lu-150	ZS5Lu-150	ZS-250	ZS2Lu-250	ZS5Lu-250
WC contam. [wt.%]		0.7	0.6	0.8	2.7	2.7	2.3
ρ real	[g/cm^{-3}]	5.38	5.39	5.49	5.36	5.44	5.48
ρ theor.	[g/cm^{-3}]	5.39	5.43	5.50	5.44	5.50	5.56
RD	**[%]**	**99,82**	**99.26**	**99.82**	**98.53**	**98.91**	**98.56**

Mechanical properties of the materials are in good accordance with the density results, as the better properties were observed for the denser materials after milling at 150rpm/7h (Table 4). When the effect of different amount of Lu_2O_3 is compared, the material with 5 wt.% Lu_2O_3 showed the highest bending strength, Young’s modulus and fracture toughness among all of the investigated materials.

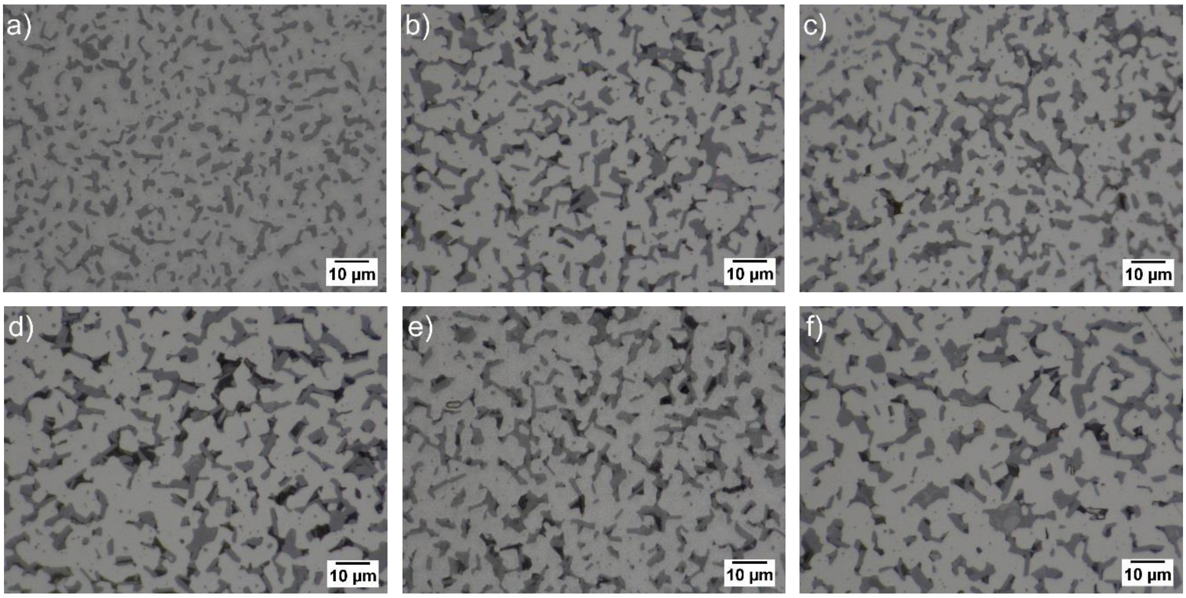

Fig. 3 Microstructure of a) ZS150, b) ZS2Lu150, c) ZS5Lu150, d) ZS250, e) ZS2Lu250, f) ZS5Lu250

Tab. 4 The bending strength, Young´s modulus, Vickers hardness and indentation fracture toughness of the investigated materials

property\material		ZS-150	ZS2Lu-150	ZS5Lu-150	ZS-250	ZS2Lu-250	ZS5Lu-250
Flexural strength		732.3 ± 39.3	715.7 ± 18.4	775.5 ± 18.0	546.1 ± 13.1	678.7 ± 27.7	644.2 ± 14.4
Young´s modulus		435.5 ± 0.1	442.3 ± 0.1	468.1 ± 0.5	427.9 ± 1.4	423.9 ± 0.1	465.7 ± 0.1
HV	**HV 1**	17.6 ± 0.5	15.3 ± 1.1	16.4 ± 0.7	14.1 ± 0.5	15.2 ± 0.7	15.0 ± 0.9
	HV 10	16.2 ± 0.2	14.5 ± 0.8	15.9 ±0.3	13.8 ± 0.4	15.3 ± 0.2	14.6 ± 0.2
Fracture toughness K_{ic}	**9.81N**	2.17 ± 0.2	2.8 ± 0.3	2.93 ± 0.3	2.60 ± 0.6	2.81 ± 0.39	2.72 ± 0.2
	98.1N	2.69 ± 0.3	3.22 ± 0.2	3.15 ± 0.1	3.00 ± 0.1	2.85 ± 0.07	3.02 ± 0.1

CONCLUSION

The work was focused on the study of the effect of different powder processing (milling 150rpm/7h and 250rpm/4h) and different content of Lu_2O_3 (2wt.% and 5wt.%) on the sintering, microstructure, phase composition, and mechanical properties of ZrB_2-SiC ceramics. Although the milling at 250rpm resulted in a finer particle size and a higher amount of WC from milling (which is considered as sintering additives for ZrB_2), the final density of the materials after sintering was lower when compared to the materials milled at 150 rpm. Accordingly, the final mechanical properties (hardness, strength, Young's modulus and indentation fracture toughness) were always higher for the materials milled using 150 rpm/7h. When the materials after milling at 150rpm/7h are compared, the highest density was measured for the reference ZrB_2-SiC material without Lu_2O_3 additive, making it the hardest material. On the contrary, the material with 5 wt.% Lu_2O_3 showed the highest bending strength, Young's modulus and fracture toughness among all of the investigated materials.

ACKNOWLEDGMENT

This work was supported by the Slovak Research and Development Agency under the contract no. APVV-SK-CN-2017-0040 and APVV-17-0328. The support of the Joint Mobility Project within Czech-Slovak scheme for the period 2018–2020 under the ASCR-SAS agreement is also acknowledged. The work was also supported by the MVTS project of SAS "UltraCom" within the scheme of "Support of the Seal of Excellence projects".

REFERENCES

[1] W.G. Fahrenholtz, E.J. Wuchina, W.E. Lee, Y. Zhou: Ultra-high temperature ceramics – Materials for extreme environment applications, John Wiley & Sons, Inc., Hoboken, New Jersey (2014), ISBN 978-1-118-70078-5

[2] B. Berton, M. Bacos, D. Demange and J. Lahaye, "High-temperature oxidation of silicon carbide in simulated atmospheric re-entry conditions", J. Mater. Sci. vol. 27, pp. 3206-3210, 1992.

[3] M.A. Levinstein, in Proceedings of Metallurgical Society Conference on Refractory Metals and Alloys, Chicago, edited by M. Semchysen and I. Perlmutter (Interscience Publishers, New York, London, 1963).

[4] A.K. Kuriakose, J.L. Margrave, "The oxidation kinetics of zirconium diboride and zirconium carbide at high temperatures," J. Electrochem. Soc., vol.111, no.7, pp.827-831, 1964

[5] L. Kaufman, E. V. Clougherty and J. B. Berkowitz-Mattuck, "Oxidation Characteristics of Hafnium and Zirconium Diboride" Trans. Metall. Soc. AIME, vol.239, no.4, pp.458–66, 1967

[6] T.A. Parthasarathy, R.A. Rapp and M. Opeka, "Effects of phase change and oxygen permeability in oxide scale on oxidation kinetics of ZrB_2 and HfB_2" J. Am. Ceram. Soc.,vol.92, no.5, pp.1079-1086, 2009

[7] D.D. Jayaseelan, E. Zapata-Solvas, P. Brown, W.E. Lee: In situ formation of oxidation resistant refractory coatings on SiC-reinforced ZrB_2 ultra high temperature ceramics, J. Am. Ceram. Soc. 95[4] (2012)

VPLYV MORFOLÓGIE PRÁŠKOV NA BEZTLAKOVÉ SPEKANIE KERAMIKY Z B_4C: POTENCIÁL PRE APLIKÁCIU V 3D-TLAČI

EFFECT OF POWDERS MORPHOLOGY ON THE PRESSURELESS SINTERING OF B_4C CERAMICS: POTENTIAL FOR 3D-PRINTING APPLICATION

M. Vozárová[1], Zuzana Kováčová[1,2], E. Neubauer [2], M. Kitzmantel [2], L. Bača [1], Ľ. Orovčík [3], Veronika Trembošová [3], M. Janek [1,4]

[1] *Department of Inorganic Materials, Institute of Inorganic Chemistry, Technology and Materials FCHFT STU, Radlinského 9, 812 37 Bratislava*

[2] *RHP-Technology GmbH, Forschungs- und Technologiezentrum, A-2444 Seibersdorf, Austria*

[3] *Institute of Materials and Machine Mechanics SAV v. v. i., Dúbravská cesta 9/6319, 84513 Bratislava*

[4] *Comenius University, Faculty of Natural Sciences, Department of Physical and Theoretical Chemistry, Mlynská dolina Ch1, 842 15 Bratislava*

ABSTRACT

Boron carbide is an important technical material known for its hardness, wear resistance and low density. The influence of particle size on sintering behavior and its effect on microstructure of boron carbide ceramics sintered by pressureless sintering was investigated. Four different boron carbide powders with particle size ranging from ~ 1µm to ~ 42µm were used to examine the effect of particle size on the sintering behaviour. Samples were sintered at a temperature of 2200°C in vacuum. As important technical parameters, microstructure and density of prepared samples were studied. The main conclusions found from this research indicates various opportunities to use the behaviour of various types of B_4C powders in pressureless sintering having the potential processing to be applied for 3D-printed objects.

Keywords: B_4C, powder morphology, pressureless sintering, densification

INTRODUCTION

Boron carbide has attracted considerable attention due to its excellent physicochemical properties such as high hardness (the third hardest material after diamond and cubic boron nitride), low density and high elastic modulus [1]. B_4C has been used for various applications such as ballistic armor, abrasive materials and wear-resistant components. It has also been widely used in the nuclear industry for neutron absorbing parts in nuclear power plants [2]. Sintering of pure boron carbide in to fully dense parts is a challenging process because of many factors working against the densification for example strong covalent bonding causes low self-diffusion and high resistance to grain boundary sliding. One of the major limits is a surface oxidation. The presence of B_2O_3 film on the powders prevents direct contact between particles. The film facilitates B_4C particles coarsening through providing rapid diffusion path at large particle surfaces when it‘s melted and evaporated during sintering process [3]. Up to 95% of the theoretical density could be obtained by hot pressing over 2200°C, however grain coarsening occurs during the process causing a decrease in mechanical properties [4]. Furthermore, hot pressing is applicable only to rather simple shapes. Pressureless sintering (PS) is often preferable to avoid expensive diamond machining required to form complex shapes. However, pure boron carbide powder with average grain size of 2 μm sintered at 2375°C reaches only 85% relative density using (PS). Therefore, many attempts have been reported to obtain dense B_4C parts, such as the usage of super-fine powders, nevertheless it didn’t reached satisfactory values [5, 6]. Various additives were also used to promote densification of B_4C without pressure for example carbon (in various forms), TiB_2, Si and its compounds, Al and Al_2O_3, ZrO_2, etc. [7-13]. The aim of our research was densification process of four different commerially available boron carbide powders by pressureless sintering.

EXPERIMENTAL

Four types of commercially available high-purity B_4C powders from different companies were used as the starting material. These powders are labelled as A, B, C and D. The morphology, phase composition, particle size distribution and impurity level of the powders are shown in Tab. 1. The data are reported from suppliers‘ certificates of own analysis. The images of boron carbide powders are shown in the Fig. 1. The boron carbide powders were uniaxially pressed using pressure of 100 MPa and 150 MPa to form cylindrical pellets with diameter 20 mm. The density of pellets as green bodies (GB) was calculated from their dimension and corresponding weights. The density of sintered samples was determined using Archimedes method. The pellets were sintered in a gas pressure sintering furnace under vacuum for 4 hours at a temperature of 2200°C and analysed by optical and scanning microscopy (SEM).

Tab. 1: Characterisation of boron carbide powders

Powder	**A**	**B**	**C**	**D**
Surface Area	22 – 25 m^2/g	6-9 m^2/g	3-4 m^2/g	1 m^2/g
Particle size	0.9 µm (90 vol.%)	3.7 µm (90 vol.%)	7µm	42µm
	0.5 µm (50 vol.%)	1.5 µm (50 vol.%)		
	0.2 µm (10 vol.%)	0.3 µm (10 vol.%)		
Impurity level	0.2-0.7% N	0.2-0.7% N	0.25% B_2O_3	3625 ppm W
	2.3-2.6% O	0.7-1.2% O	0.19% Fe_2O_3	120ppm Fe
	0.0-0.1% Fe	0.0-0.1% Fe	0.39% free B	110ppm S
	0.13-0.15% Si	0.14-0.15% Si	2.29% free C	300ppm Al
	0,03-0,05%Al	0,01-0,05%Al		500ppm Ca
Total carbon	21.9%	21.8-22.1%	20.68%	n.l.
B/C atomic ratio	3.7-3.9	3.8-4.0	n.l.	n.l.

n.l.=not listed

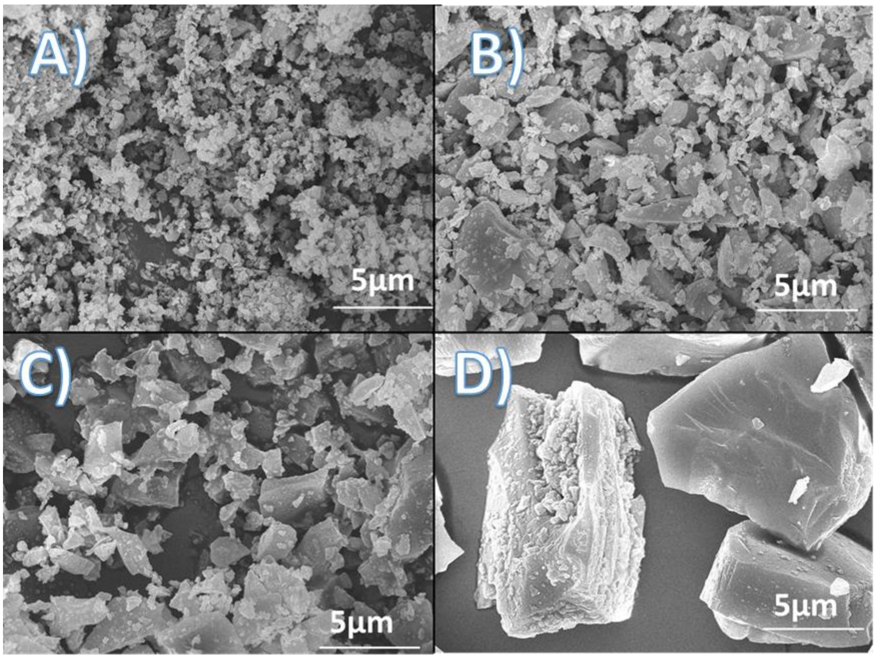

Fig. 1: SEM images of boron carbide particles sizes.

RESULTS

First differences among the used powders were already identified during cold pressing. The powder A was very well compressible unlike powders B, C and D. The densities of green bodies (GB) are summarised in Tab.2. The green density of powders A and B were similar and had values of 59% (100 MPa and 150 MPa) for powder A and 56% (100 MPa) or 57% (150 MPa) for powder B. The lowest green density values were found at the level of 51% (150 MPa) and 52% (100 MPa) when using the coarsest powder D. The higher pressure led obviously to an over-pressing of the sample which resulted in a delamination of the pellet during the sintering process. The grain size of powders is closely related to their oxidative contamination influencing the densification of samples during sintering. An impurities present in these commercial powders are summarized in the Tab.1. This oxide layer on the surface of B_4C particles creates a barrier which hinders B_4C to reach full density as mentioned above [3]. Another effect connected to coarsening of sintered powders and low sintered density is the grain interparticle coordination (GIC). The GIC depends on the number of touching neighbours. The grain shape and grain growth are related, because the low coordinated grains, with fewer sides, tend to shrink during coarsening. In the samples, the porosity disappears more efficiently if as many grains as possible are as close as possible to each other [4]. Based on this assumption, fine-grain samples should meet this conditions better. Unfortunately, this process is inhibited at the same time by the formation of bubbles from B_2O_3 impurity, which evaporates in the gaseous phase at the point at which the sintering begins. This leads to the formation of new pores, which are combined with the original porosity. The coarse-grain samples with lower surface area can accommodate less oxides and thus the problem with gaseous B_2O_3 is less manifested. Nevertheless, the compaction is inhibited here by a small number of touching grains and therefore fewer necks at which the material may diffuse is formed. In contrary, the grains of finer powders existing in closer contacts and more coordinated with each other, so the diffusion at the grain boundaries can be facilitated more intensively. Therefore finer powders after sintering should result in better density than in case of usage of coarse-grain powders. As the Tab.2 shows, this assumption is not entirely correct. The sample A, made from the finest powder didn't achieve the best relative density (RD).

Tab. 2: Material properties of pressureless sintered boron carbide samples

Pressure [MPa]	**Sample**	**Binder [g]**	**GB density [%]**	**GB density [g/cm^3]**	**Density [g/cm^3]**	**Relative density [%]**	**Shrinkage [%]**
100	A1	-	59	1,49	2,19	87	39
150	A2	-	59	1,47	2,19	87	39
100	B1	-	56	1,42	2,35	93	44
150	B2	-	57	1,43	2,35	93	43
100	C1	0,5	71	1,79	2,18	87	38
150	C2	0,5	69	1,75	2,26	89	46
100	D1	0,5	52	1,31	-	-	-
150	D2	0,5	51	1,29	-	-	-

The best RD achieved the value 93% which was obtained by samples made from powder B. However, powders C and D behaved according to the hypothesis stated above and achieved a lower RD value which is linked to their morphology. The deviation in the trend of expected densities can be explained by the presence of a higher content of B_2O_3 as an impurity in fine-grained powders with a larger surface area. At the same time, the samples D1 and D2 were also delaminated after sintering that it was not possible to measure their sintered densities or dimensions. The particle size of the powders affected the resulting pores shape of sintered samples as shown in Fig.2. The sample A2 prepared from the finest powder is having the best compressing properties of this powder, more porous than sample B2. The pores of both samples are superficial and their shape is asymmetric. The microstructure of sample D2 revealed extensive porous structure. Samples C2 and D2 were cracked and the compact areas showed large and deep interconnected pores.

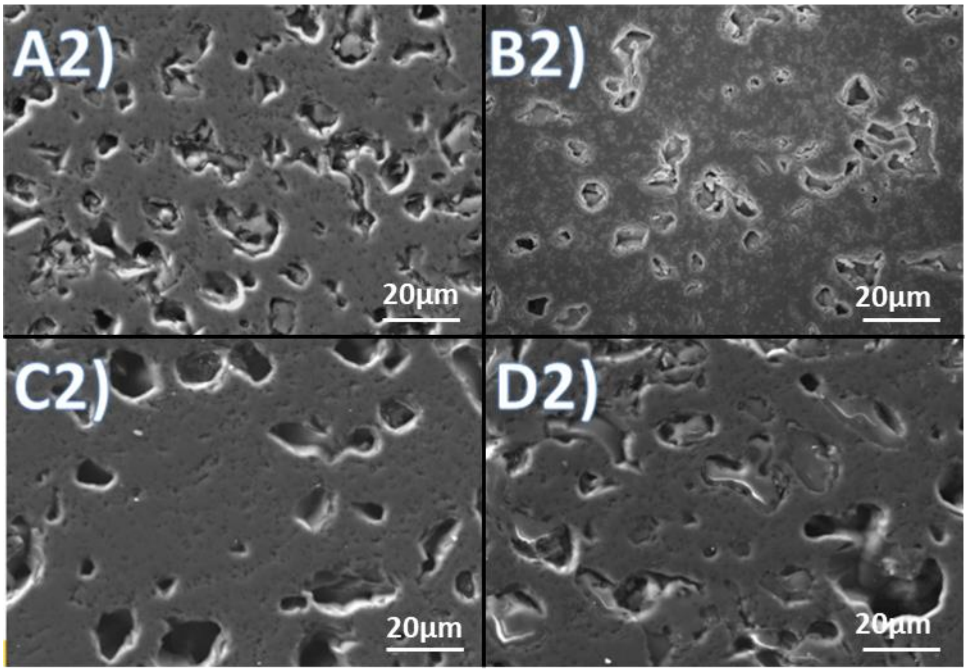

Fig. 2: SEM images of boron carbide samples after sintering at 2200°C in vacuum

CONCLUSION

The experimental observations confirmed the relation between particle size distribution of powders grains and density of sintered boron carbide materials. The use of very fine powders leads to microstructural coarsening and pore evolution due to the presence of a greater amount of volatile B_2O_3 impurities e.g. 2,3% for powder A in comparison to the powder B with 0.7%. The use of very coarse powders resulted in low green as well as relative density and delamination of samples. This was in very good agreement with the high interfacial energy and low material diffusion at the grain boundaries. The most promising results were achieved for powder B, containing lower amount of oxygen impurities together with good packing density. Further extensive analysis of powder particle size effects and presence of additives during sintering can be helpful in 3D-printing application of B_4C materials.

ACKNOWLEDGMENT

I would like to express my appreciation to Dipl. Ing. Kladler (RHP Seibersdorf, Austria) for his valuable advice and technical support during experimental work. The financial support of the Slovak Grant Agency for Science VEGA grant No. 1/0906/17 and Slovak Research and Development Agency APVV-16-0341 are greatly appreciated.

REFERENCES

[1] F. Thevenot, “Boron carbide - a comprehensive review,” Journal of the European Ceramic Society, vol. 6, 1990, pp. 205-225.

[2] D. Emin and T. L. Aselage, “A proposed boron-carbide-based solid-state neutron detector,” Journal of Applied Physics, vol. 97, no. 1, 2005, p. 013529.

[3] M. Asadikiya and et al., “Thermodynamic modeling and investigation of the oxygen effect on the sintering of B4C,” Journal of Alloys and Compounds, vol. 699, 2017, pp. 1022-1029.

[4] B. Yavas and et al., “Effect of particle size, heating rate and CNT addition on densification, microstructure and mechanical properties of B4C ceramics,” Ceramics International, vol. 41, no. 7, 2015, pp. 8936-8944.

[5] X. Du and et al., “Hot-pressing kinetics and densification mechanisms of boron carbide,” Journal of American Ceramic Society, vol. 98, 2015, pp. 1400-1406.

[6] H. Lee and R. F. Speyer, “Pressureless sintering of boron carbide,” Journal of American Ceramic Society, vol. 86, 2003, pp. 1468-1473.

[7] R. M. da Rocha and F. C. Lourenço de Melo, “Effect of TiO2 and TiB2 on pressureless sintering of B4C,” Materials Science Forum, Vols. 727-728, 2012, pp. 1022-1027.

[8] Z. Zhang and et al., “Microstructure and mechanical protperties of B4C-SiC intergranular/intragranular nanocomposite ceramics fabricated from B4C, Si and graphite powders,” Journal of European Ceramics Society, vol. 34, 2014, pp. 2135-2161.

[9] S. Hayun, A. Weizmann, M. P. Dariel and N. Frage, “Microstructural evolution during the infiltration of boron carbide with molten silicon,” Journal of the European Ceramic Society, vol. 30, 2010, pp. 1007-1014.

[10] M. Mashhadi, E. Taheri-Nassaj, V. M. Sglavo, H. Sarpoolaky and N. Ehsani, “Effect of Al addition on pressureless sintering of B4C,” Ceramics International, vol. 35, 2009, pp. 831-837.

[11] H.-W. Kim, “Densification and mechanical properties of B4C with Al2O3 as sintering aid,” Journal of AMiercan Ceramics Society, vol. 83, no. 11, 2000, pp. 2863-2865.

[12] H.-W. Kim, “Reaction sintering and mechanical properties of B4C with addition of ZrO2,” Journal of Material Research, vol. 15, no. 11, 2000, pp. 2431-2436.

[13] X. Shi, “Effect of the addition of carbon on the sintering properties of boron carbide ceramics prepared by presusreless sintering,” Proceeding of the 3rd International Conference on Material, Mechanical and Manufacturing Engineering (IC3ME 2015), 2015, pp. 27-28.

3D TLAČ OXIDOVEJ KERAMIKY Z POLYMÉRNYCH KOMPOZITOV POUŽITÍM FDM TECHNOLÓGIE

3D PRINTING OF OXIDE CERAMICS FROM POLYMER COMPOSITES USING FDM TECHNOLOGY

K. Randová[1], P. Veteška[1], Z. Hajdúchová[1], J. Feranc[2], K. Tomanová[1,2], R. Plavec[2], Ľ. Bača[1], M. Janek[1,3]

[1] *Slovak University of Technology, Faculty of Chemical and Food Technology, Department of Inorganic Materials, Radlinského 9, SK-812 37 Bratislava, Slovakia*

[2] *Slovak University of Technology, Faculty of Chemical and Food Technology, Department of Plastics, Rubber and Fibbers, Radlinského 9, SK-8ň12 37 Bratislava, Slovakia*

[3] *Comenius University, Faculty of Natural Sciences, Department of Physical and Theoretical Chemistry, Mlynská dolina, SK-842 15 Bratislava, Slovakia*

ABSTRACT

Model ceramic objects were produced using Fused Deposition of Ceramics (FDC) by 3D printing technology. For this purpose it was developed composite filament containing components such as Al_2O_3, SiO_2, Na_2O, K_2O and thermoplastic polymer, aiming for production of mullite based ceramics after sintering. The composition of filament and rheological behaviour was optimised for the green body manufacturing process using FDC. During green body debinding and sintering, the linear dimensional shrinkage is an important parameter to receive well defined size and well maintained object shape of final ceramic objects.

Keywords: 3D-printing, additive manufacturing, oxide ceramics, fused deposition of ceramic

INTRODUCTION

In recent years, was noticed the focus of industries towards product development using rapid prototyping (RP) methodologies to shorten the product development cycle time. Application of RP technology, with absence of tooling allows forming of complex geometries in least time possible. The additive manufacturing (AM) technique allows RP to produce final object from computer aided design (CAD) models, by successively deposited material layers.[1] Fused deposition ceramics (FDC) technology is an AM process that builds ceramic 3D shapes by using composite filaments of thermoplastic polymer and desired ceramic powder. Formable material is than extruded at elevated temperatures through a small nozzle diameter onto a building platform.[2] FDC belongs therefore to a clean, simple-to-use, office-friendly 3D printing process. This technology may build the parts of any shape desired with required accuracy allowing their further testing in application.[3] FDC is a modified FDM process where ceramic powder loaded with thermoplastic polymer is extruded using commercial FDM systems.[4] Traditionally the FDM systems were able to fabricate parts only from thermoplastics and waxes, while current FDM systems can process parts in a range of engineering plastics such as acrylonitrile butadiene styrene (ABS), polycarbonate (PC) or different blends of ABS and PC.[5] For FDC process binder properties must be specially tailored, based on the behaviour of the filler phase during the FDC process. Therefore, a detailed understanding of the various polymer ingredients and their role in the final composite formulation must be understood. The degree of dispersion of the powder in the molten thermoplastic binder has a dramatic effect on the rheological properties of resulting FDC filament.[6] For cases where shaping of complex ceramic structures cannot be cast or machined easily, three-dimensional printing enables a big jump in ceramics geometrical flexibility.[7] Suitable thermoplastic polymers filled with ceramic powder in desired operation solid contents enables to print green body objects that can be debinded to brown body and sintered to dense ceramic parts.[8,9] From these reasons the main objective of our study was to investigate the shrinkage of green body model objects produced from the filament prototype suitable for FDC process.

EXPERIMENTAL

The extrusion of inorganic-polymer composite material prepared as filament with diameter 1.75 mm was done using single screw extruder with polymer part in the range 35, 60 weight %. The green bodies were printed on FDM 3D printer Leapfrog Creatr™ with temperature set to 215°C. The parts with circular shape and rectilinear infill were debinded and sintered in a laboratory oven Classic™. The microstructure of the samples after their debinding and sintering was monitored by the field emission gun scanning electron microscope JEOL 7500F, using an acceleration voltage of 15 kV and a working distance of 6 – 10 mm. An aluminium target with diameter of 2.5 cm and a carbon both-sided adhesive tape were used to mount samples onto target used to transfer the specimen into the microscope. The samples were coated with gold/platinum plasma for 60s using the Balzers coater.

RESULTS

The 3D printed test green body objects with open structure with 60 mass % of thermoplastic polymer binder after FDC process and after sintering are shown in the Figure 1. The structure was printed on the board of Leapfrog Creatr™ printer with temperature of 55°C similar to conventional printing parameters. After printing, the green body is subjected to debinding process and the polymeric part must be removed without the shape deformation of the structure formed in the FDC process. Well attained testing object shape after debinding at temperature 850°C during 1 hour was achieved. The polymeric part was completely eliminated during debinding process. The debinding was carried out at 850°C that was determined from preliminary TG experiments of material used. Depending on the heating ramp required for sintering, remains of the binder could lead to surface bloating deformations with surface cracking and object defects. However, no significant disorders were observed in 3D printed open structures prepared from green parts after sintering at temperatures 1200°C, 1300°C and 1400°C (Figure 1,2).

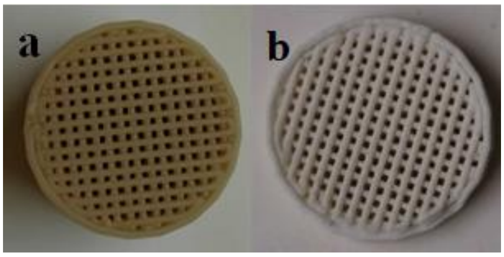

Fig. 1. 3D printed open structures with 60 mass % of polymeric part a) after 3D printing, b) after debinding at temperature 850°C

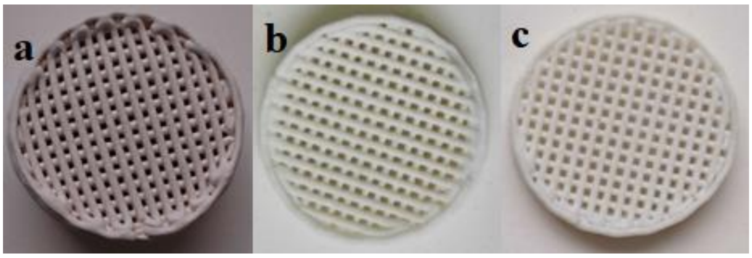

Fig. 2. 3D printed open structures after sintering of debinded parts at temperatures a) 1200°C, b) 1300°C, c)1400°C

The dimension shrinkage of printed test object as a function of temperature is shown in the Figure 3. The shrinkage was observed as two parameter i) shrinkage of the sample body diameter shown in Figures 1,2 and ii) shrinkage of material line supports, forming the rectilinear infill. Both of these parameters show comparable shrinkage values at specified temperatures except the highest sintering temperature 1400°C. The shrinkage of sample body diameter was lower than shrinkage of material line supports observed.

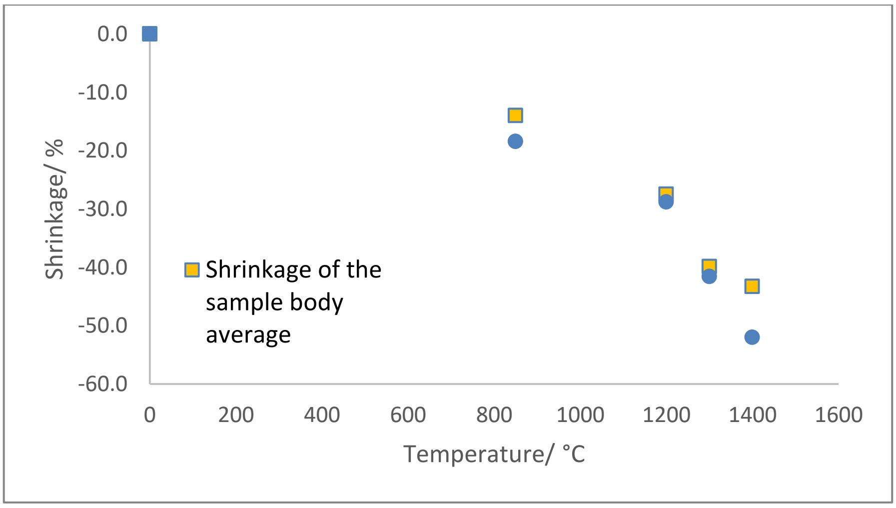

Fig. 3. Shrinkage of the sample body diameter and infill lines as a function of temperature

After the debinding process, the shrinkage values found were at the level of ~15%. However, significant increase in shrinkage values occurred after the debinded brown bodies were heated to sintering temperatures. Additional shrinkage of brown bodies at the levels of ~25, ~40 and ~45 % was observed after the heating to sintering temperatures 1200, 1300 and 1400 °C, respectively.The microstructure of materials observed on SEM images after debinding and sintering at 1200°C b), 1300°C c), 1400°C d) are shown in the Figure 4. The SEM analysis confirmed individual particles in the structure after debinding process at 850°C (Figure 4a). Similar microstructure was observed for sample sintered at 1200°C, indicating insufficient sintering of the material at this temperature. As can be seen for the SEM images, at lower sintering temperatures, the microstructure exhibits greater porosity and the porous ceramic parts with brittle nature were prepared. Increase of the sintering temperature resulted in grains bonding and increasing the compactness of the material. Improved grain bonding can be observed for sample sintered at 1300°C. For samples sintered at 1400 ° C well sintered material with glass-like phase of sample was achieved.

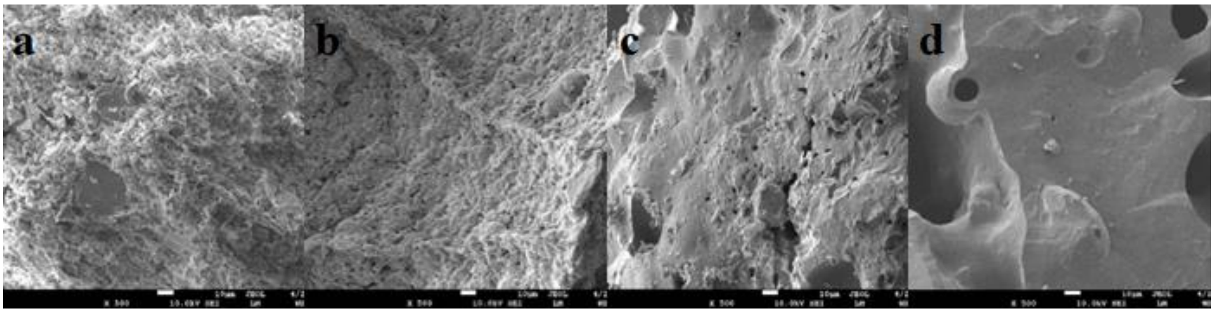

Fig. 4. Microstructure of materials on SEM images at temperatures a) 850°C b) 1200°C, c) 1300°C, d) 1400°C

CONCLUSION

The prototype filament containing components such as Al_2O_3, SiO_2, Na_2O, K_2O was proved to be viable for practical uses in FDC technology. The composition of filament and experimental conditions during printing was optimised to be used for the green body forming process. The filament consisted of 60% of the polymer part and the rest was an inorganic part which was altering. The optimization of 3D printing parameters to create structures which were suitable for study of sintering behaviour was performed. Shrinkage of model objects in the form of their diameter changes was studied to characterize the shrinkage of filament materials. The shrinkage of the sample body diameter and shrinkage of material line supports show comparable values. The SEM microscopy showed significant sintering of material tested at temperatures above 1300°C. The impact of individual components on the resulting processing of ceramic requires further investigation and optimization to achieve user friendly debinding and sintering process parameters.

ACKNOWLEDGMENT

The financial support of the Slovak Grant Agency for Science VEGA grant No. 1/0906/17 and Slovak Research and Development Agency APVV-16-0341 are greatly appreciated. The creation of the work enabled also the project "Center for Applied Research of New Materials and Technology Transfer", ITMS 26240220088, supported by the Science and Research Operational Program by the European Regional Development Fund.

REFERENCES

[1] Narang, R., Chhabra, D. Analysis of Process Parameters of Fused Deposition Modeling (FDM) Technique. Intern. J. Future Revol. Comp. Sci. & Comm. Eng. 3(1), 2017, 41–48.
[2] Mireles, J., Espalin, D., Roberson, D., Zinniel, B., Medina, F., & Wicker, R. Fused deposition modeling of metals. Proceedings of the Solid Freeform Fabrication Symposium, Austin, TX, USA. 2012, 6-8.
[3] Kruth, J. Material incress manufacturing by rapid prototyping techniques. CIRP Annals-Manufacturing Technology, 40(2), 1991, 603-614.
[4] Seyi, O., Susmita, B., Amit, B. Fused deposition of ceramics (FDC) and composites. Proceeding of SFF symposium held in Austin, Texas. 2001, 224-232.
[5] Nikzad, M., Masood, S. H., Sbarski, I. Thermo-mechanical properties of a highly filled polymeric composites for fused deposition modeling. Materials & Design, 32(6), 2011, 3448-3456.
[6] McNulty, T. F., Mohammadi, F., Bandyopadhyay, A., Shanefield, D. J., Danforth, S. C., & Safari, A. Development of a binder formulation for fused deposition of ceramics. Rapid Prototyping Journal, 4(4), 1998, 144-150.
[7] Eckel, Z. C., Zhou, C., Martin, J. H., Jacobsen, A. J., Carter, W. B., & Schaedler, T. A. Additive manufacturing of polymer-derived ceramics. Science, 351(6268), 2016, 58-62.
[8] Nötzel, D., Eickhoff, R., Hanemann, T. Fused Filament Fabrication of Small Ceramic Components. Materials, 11(8), 2018, 1463.
[9] Salea, A., Prathumwan, R., Junpha, J., & Subannajui, K. Metal oxide semiconductor 3D printing: Preparation of copper (II) oxide by fused deposition modelling for multi-functional semiconducting applications. Journal of Materials Chemistry C, 5(19), 2017, 4614-4620.

PRÍPRAVA FEROSILICIDOV SPRACOVANÍM DRUHOTNÝCH SUROVÍN Z PRIEMYSLU

PREPARATION OF FERROSILICIDES BY UTILIZATION OF WASTE MATERIAL OF INDUSTRY

R. Bystrický, M. Hnatko, J. Sedláček

[1]*Ústav anorganickej chémie, Slovenskej akadémie vied, Dúbravská cesta 9, 84104 Bratislava*

ABSTRACT

Two types of waste produced in industry with high amount of Fe and Si were investigated as a source of iron and silica to produce ferrosilicon. At first laboratory experiments at 1550 °C were carried out on the mixture of waste with high amount of iron, silica and carbon with the aim to determine the possibility of ferrosilicon formation. Subsequently, waste with high amount of iron and silica were mixed together with carbon and ferrosilicon was prepared after 5 minutes of holding time. During heating separated slag and alloy was formed. XRD pattern showed that the alloy is composed from Fe_5Si_3 and FeSi. Slag is composed form Fe_5Si_3, FeSi, SiC and Ca_2SiO_4.

Keywords: waste, silicides, ferrosilicon, melting

INTRODUCTION

The production of steel is important part of Slovak industry. During the processing of iron ore 200 kg of slag is generated when 1 ton of steel is produced. Another waste is generated during cleaning the air from impurities as well as during cleaning of waste water. This waste is generated in amount of tens of thousands of tons per year and pose a huge burden on the environment. In recent years, some papers are focused to recycling of industrial waste into the construction materials (cement, concrete, bricks, ceramics and fire prevention materials). [1, 2, 3, 4, 5, 6]

Waste with high ratio of iron can be used to ferrosilicon production when it is mixed with another waste with high ratio of silicon. Ferrosilicon is mostly used in steelmaking and foundries as a source of silicon in the production of carbon steels, stainless steels, cast iron and other ferrous alloys. Ferrosilicon reduces the oxidation of valuable elements like Cr in stainless steel production. [7] Farzana et al. concerned to processing of industrial waste where they prepared ferrosilicon from automotive glasses (as silicon source), bakelite and Fe_2O_3. [8]

The aim of this work was to prepare of ferrosilicon from industrial waste applying a technology which is usable in industry during processing of industrial waste at a scale of tons.

EXPERIMENTAL

In this study, waste with high amount of Fe produced in steel industry (USS10), SiO_2 (Aerosil OX-50, Degusa, Germany), waste with high amount of Si produced in ferroalloys industry (CaSi), carbon black (pigment grade, 1000 $m^2.g^{-1}$) were used as starting materials. The composition of wastes is shown in Table 1.

Tab.1 Major oxides in industrial waste

Waste	Fe_2O_3	Al_2O_3	SiO_2	MnO	CaO	K_2O	MgO
USS10	71.02	1.36	4.98	–	6.56	2.21	2.82
CaSi	–	1.03	75.33	1.52	17.5	0.58	1.52

Pellets were prepared with the weight ratio of USS10, SiO_2 and carbon black (C) 1.4:1:0.62. When CaSi waste was used instead of SiO_2, the ratio was changed to 1.4:1.33:0.62 because of presence of impurities in CaSi waste. A stoichiometric amount of carbon was used to produce ferrosilicon with equal amounts of silica and iron oxide by using a mole ratio based on reactions 1 and 2.

$$SiO_2\ (s) + 2C\ (s) \rightarrow Si\ (s, l) + 2CO\ (g) \tag{1}$$

$$Fe_2O_3 + 3C\ (s) \rightarrow 2Fe\ (s, l) + 3CO\ (g) \tag{2}$$

The powder mixtures were homogenized by hand in agate bowl by wet route using ethanol. The mixtures were subsequently dried on air by IR lamp. Green pellets were placed into the graphite crucible and heat treated in direct hot-press (DSP 507, Dr. Fritsch, Germany) at 1550 °C for 3, 5 and 10 min, respectively. 15 MPa mechanical pressure was used only for achieving the contact between the crucible and the electrodes. Heating and cooling rate was 100 °C/min. The crystalline phases present in the heat treated samples were identified using X-ray diffraction (XRD) (Panalytical Empyrean, Netherlands, Cu Kα radiation). The microstructures were observed by optical microscope (VHX-1000, Keyence). For this purpose the sintered samples were cut and polished. Photos were made by camera (Canon PowerShot SX520 HS).

RESULTS

The experiments in USS10-SiO2-C system were carried out because of testing the possibility of ferrosilicon formation during heating process. For this reason three experiments were done where different holding time (3, 5, 10 minutes) at 1550 °C were used. The holding time where the highest yield of ferrosilicon was achieved, was used in the USS10-CaSi-C system.
The photos of cooled USS10_SiO2_C pellets captured by camera are shown in Figure 1.

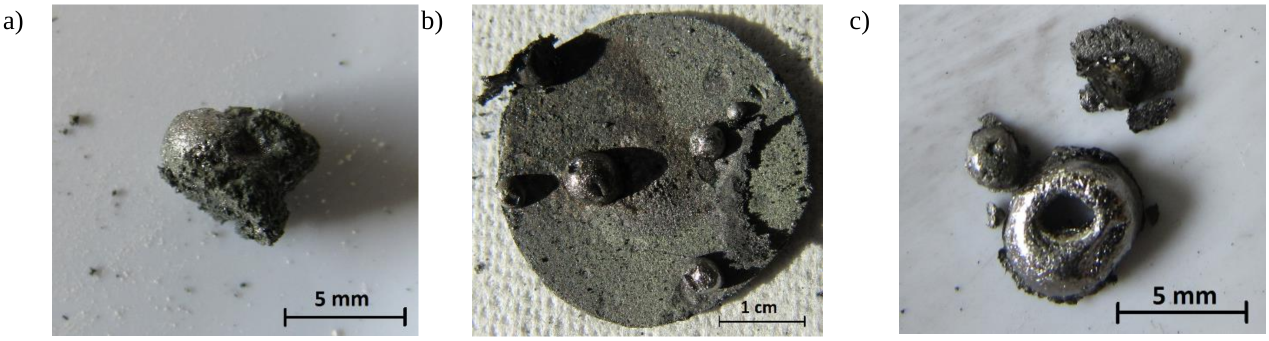

Fig. 1 Photos of heat treated samples a) USS10_SiO2_C-3min ,
b) USS10_SiO2_C-5min, c) USS10_SiO2_C-10min

All samples were melted during heating process. After 3 minutes at 1550 °C the slag and metal alloy were segregated from each other (Figure 1a). After 5 min of holding time only metal alloy was present in the crucible (Figure 1b). After 10 minutes at 1550 °C there was no visible change on metal alloy (Figure 1c).

XRD patterns of reduced pellets (Figure 2) showed that the FeSi and SiC was the main product for all samples. SiC formation is concurrent reaction during ferrosilicon formation. After 5 minutes of holding time ferrosilicon of Fe_5Si_3 composition is formed. In the sample USS10_SiO2_C (5 min) carbon phase is detected. This phase come from carbon paper which is placed into the crucible as protection from infiltration of melt.

Tab. 2 Phase composition of samples in the system USS10-SiO2-C made by X-ray powder diffraction analysis

Sample	**Phase composition**
USS10_SiO2_C (3 min)	FeSi, SiC
USS10_SiO2_C (5 min)	Fe_5Si_3, SiC, FeSi, C
USS10_SiO2_C (10 min)	FeSi, Fe_5Si_3, SiC

From the previous results in USS10-SiO2-C system 5 minutes of holding time was selected for the USS10_CaSi_C heating process. The photo of cooled sample is shown in Figure 2. From the photo it is clear that in contrast with the sample USS10_SiO2_C (5 min) also slag is present in this case after heating up to 1550 °C. The slag is created mainly from the higher amount of other oxides in both USS10 and CaSi, respectively.

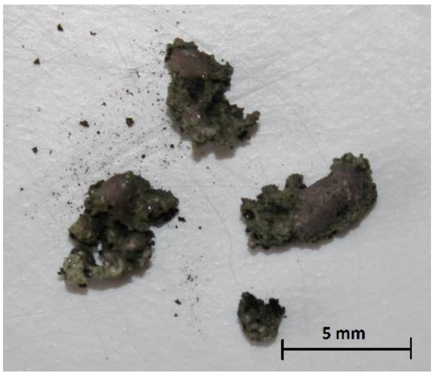

Fig. 2 Photo of heat treated sample USS10_CaSi_C (5min)

XRD pattern of the USS10_CaSi_C shows that the alloy consists of ferrosilicon. In the slag SiC and Ca_2SiO_4 is present.

Tab. 3 Phase composition of sample in the system USS10-CaSi-C identified by X-ray powder diffraction analysis

Sample	**Phase composition**
USS10_CaSi_C	alloy melt: Fe_5Si_3, FeSi, slag: SiC, Fe_5Si_3, FeSi, Ca_2SiO_4

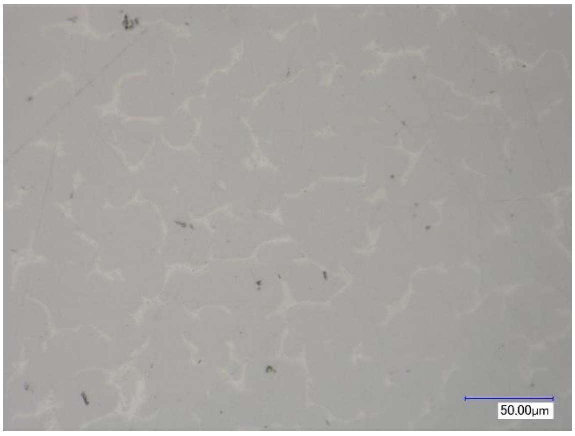

Fig. 3 Image of microstructure of USS10_CaSi_C from optical microscope

Image from optical microscope was taken on USS10_CaSi_C to observe the morphology of the synthesized ferrosilicon alloys (Figure 3). The microstructure consists of two phases which are distinguishable by different colour. The brighter phase represents the presence of higher iron concentration and lower Si concentration.

CONCLUSION

Ferrosilicon alloys were synthesized from industrial waste. XRD analysis showed that the alloy contains two types of ferrosilicon - Fe_5Si_3 and FeSi. In the USS10_CaSi_C there is also slag which contains SiC. Formation of SiC decreases the yield of Si from waste. Next experiments will be focused on the decreasing of the amount of SiC in the sample.

This approach provides a new opportunity to transform industrial waste into a value added material for the production of ferrosilicon alloys and will reduce amount of industrial waste in landfill.

ACKNOWLEDGMENT

This work is the result of the project Competence center for new materials, advanced technologies and energy ITMS 26240220073, supported by the Research and Development Operational Program funded by the European Regional Development Fund. This work was financially supported by the Slovak Grant Agency VEGA Project No. 2/0152/18, APVV-15-0540 and CERANEA (Multifunctional Ceramic/Graphene Coatings for New Emerging Applications).

REFERENCES

[1] Su, L., Wang, L., Zhang, F.-S. A novel process for preparing fireproofing materials from various industrial wastes J Environ. Manag, 219 (2018) 332-339

[2] Jayaranjan, M.L.D., van Hullebusch, E.D., Annachhatre, A.P. Reuse options for coal fired power plant bottom ash and fly ash. Rev. Environ. Sci. Bio-Technol. 13 (2014), 467–486

[3] Siqueira, F.B., Holanda, J.N.F. Reuse of grits waste for the production of soil cement bricks. J. Environ. Manag. 131 (2013), 1–6.

[4] Gonzalez-Corrochano, B., Alonso-Azcarate, J., Rodas, M. Production of lightweight aggregates from mining and industrial wastes. J. Environ. Manag. 90 (2009), 2801–2812

[5] El-Amir, A.A.M., Ewais, E.M.M., Abdel-Aziem, A.R., Ahmed, A., El-Anadouli, B.E.H., 2016. Nano-alumina powders/ceramics derived from aluminum foil waste at low temperature for various industrial applications. J. Environ. Manag. 183, 121–125
[6] Qin, B.T., Jia, Y.W., Lu, Y., Li, Y., Wang, D.M., Chen, C.X., 2015. Micro fly-ash particles stabilized Pickering foams and its combustion-retardant characteristics. Fuel 154, 174–180.
[7] Tangstad, M. Ferrosilicon and silicon technology in Handbook of ferroalloys: Theory and technology, edited by Michael Gasik, Elsevier, 2013
[8] Farzana, R., Rajarao, R., Sahajwalla, V. Synthesis of ferrosilicon alloy using waste glass and plastic, Materials Letters, 116 (2014) 101-103

ELEKTROSTATICKÉ ZVLÁKŇOVANIE – JEDINEČNÁ TECHNOLÓGIA PRÍPRAVY MIKROVLÁKIEN NA BÁZE TITÁNU

ELECTROSPINNING - A UNIQUE TECHNOLOGY FOR PRODUCTION Ti - BASED MICROFIBERS

I. Shepa[1,2], E. Mudra[1], A. Kovalcikova[1,2], J. Dusza[1]

[1] *Institute of Materials Research, Slovak Academy of Sciences, Watsonova 47, 040 01 Kosice, Slovakia*

[2]*Faculty of Materials, Metallurgy and Recycling, Technical University, Letná 9, 040 01 Kosice, Slovakia*

ABSTRACT

The aim of the paper is to present the influence of the post-spinning heat treatments of precursor fibers on the structural properties and morphology of final ceramic microfibers. The post-spinning treatment conditions were: calcination in air at 450°C, 600°C and pyrolysis in argon at 1000, 1500°C. Conventional calcination in air at 450°C resulted in a production of anatase-rich fibers but increasing the temperature up to 600°C created pure rutile phase fibers. In a result of the same precursor pyrolysis at 1000°C the Carbon/TiO_2 composite fibers were obtained. Further rising of the treatment temperature in inert atmosphere led to the crystallization of pure titanium carbide fibers. All the obtained products on the each formation step were well characterized by scanning electron microscopy (SEM) and X-ray diffraction (XRD).

Keywords: fiber, electrospinning, precursor, carbon fiber, oxide ceramic fibers

INTRODUCTION

One-dimensional nanostructures have received considerable attention due to their tunable physical and electroactive properties, such as mechanical strength, toughness, ferromagnetism, ferroelectricity, etc. One of the most perspective, cost-effective and versatile technique for the preparation fiber nanostructures in the large scale is electrospinning. The preparation of nanostructured materials became available with the expansion of electrospinning from polymers to composites and to ceramics or carbon-based fibers. The typical property of the prepared fibrous materials is a high surface-to-volume ratio which makes them useful for variety of applications. Titanium dioxide (TiO_2) is a well-known multifunctional ceramic material that due to its outstanding physical-chemical properties, excellent stability and relatively low cost, during the last decades has been used in a wide variety of applications, like water treatment [1], photocatalytic applications [2], solar cells [3], Li/Na-ion batteries [4], sensors [5], white pigment in paints and pharmacy, self-cleaning, high refractive index materials and sunscreens [6]. One of the most promising and efficient forms of TiO_2 usage is nano or microfibers, because of its simultaneous relatively high mechanical strength, porosity, surface area and photocatalytic properties [1,2]. Titanium carbide belongs to the group of ultrahigh temperature ceramics due its high melting point. It is often used due to its high strength, chemical stability, corrosion and wear resistance, electrical, heat conductivity and mechanical properties along with its low cost. It can be used for a production not only of cutting and machining tools, or cermets, but also for electronic applications, electrocatalysis, low-temperature fuel cells, ceramic filters for aggressive chemicals and for special composites development [7]. Nanocomposites with metal or ceramic matrices reinforced with refractory metal carbides, such as TiC, possess superior hardness, wear and crack resistance. These properties are highly dependent on the size and dimensionality of the reinforcement material. Particles and unaligned fibers will provide isotropic properties of the composites. The present work reports a successful synthesis of a wide scale of different types of titanium-based fibers from the same precursor system using the combination of needle-less electrospinning and post-spinning treatment processes. This work describes a production of oxide and non-oxide ceramics from the same precursor material in a form of microfibers, which are suitable for variety of applications.

EXPERIMENTAL

Production process of titanium-based micro/nanofibers consist of two basic steps: preparation of electrospun precursor fibers and a post-spinning treatment. Polyvinylpyrrolidone (PVP, Acros Organics, M_w=50,000g.mol^{-1}), ethanol (MICROCHEM, absolute), titanium (IV) isopropoxide - ($Ti(IPO)_4$, Acros Organics, 98+%) and acetic acid (Acros Organics, 99.7+%) were used without further purification for the preparation of solution for needle-less electrospinning. The basic solution for electrospinning was prepared as follows: an appropriate amount of PVP was dissolved in absolute ethanol and mixed at 40°C by a magnetic stirrer for 4 hours. Then, $Ti(IPO)_4$ were added to the polymer solution and left mixing in a sealed bottle. For a enhancing the conductivity and catalysis of sol-gel transition process, 3.2 wt.% of acetic acid was added to each precursor solution and further mixed for 1 hour. The as-prepared solution was electrospun from a wire electrode of Nanospider^{TM} NS Lab machine from ELMARCO using a needle-less electrospinning technology. The applied voltage was 75kV, and a distance from electrode to collector – was 150 mm. The process was performed at ambient temperature with a relative humidity of 50%. Electrospun fiber mats were left for 24 hours in a lab ambient air to complete the hydrolysis of $Ti(IPO)_4$. The final ceramic fibers were prepared using the conventional heat treatment processes in alumina crucibles in a lab chamber furnace at 450°C and 600°C in air, and at 1000°C, 1500°C in the inert atmosphere. The phase composition and thermal decomposition of the samples were analysed using X-ray diffraction analysis (XRD, PhilipsX' PertPro, CuKα radiation). The morphology and substructure of fiber samples were observed by the scanning electron microscopy (SEM/FIB ZEISS AURIGA Compact, accelerating voltage: 5 kV).

RESULTS

The phase composition and crystallinity of the final fibers were evaluated by XRD analysis. As-spun composite precursor fibers were made of the amorphous particles of TiO_2 and PVP (not showed on the patterns). Fig.1 shows the XRD patterns of the heat threated samples. After the calcination of amorphous electrospun precursors at 450°C two-phase TiO_2 system was formed, consisting of anatase (2Θ = 25.4°,37.8°, 48°,62.8°, ICOD 96-901-5930) and rutile (2Θ = 27.4°,36°, 39.2°, 41.2°, 44°, 54.3°, 56.6°, 62.8°, 64.1°, 69°, 69.7°, 82.4°, 84°, 89.3°, ICOD 96-900-4143). Character of the products, the presence of rutile and anatase to rutile ratio depends not only on the calcination temperature. After the increase in the calcination temperature up to 600°C pure rutile phase was obtained due to the full phase transformation. Observed transformation was also accompanied with increase of grain size. Pyrolysis at 1000°C in argon led to the polymer carbonization and amorphous carbon fibers formation with the embedded nanocrystals of anatase (Fig.1). However, the temperature increase to 1500°C resulted in a single crystalline stable phase product - titanium carbide (TiC, ICOD 96-591-0092) and some amorphous carbon residues.

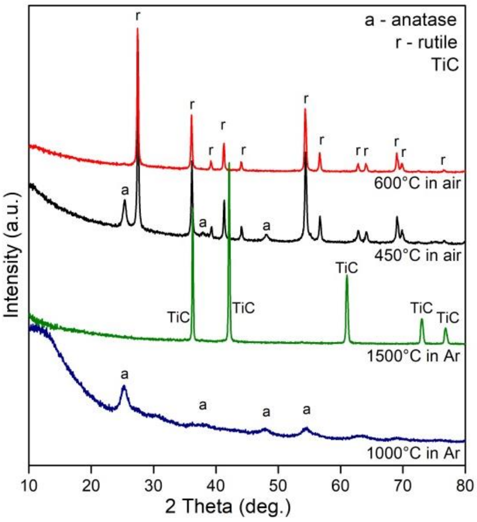

Fig.1 XRD patterns of the final fibers

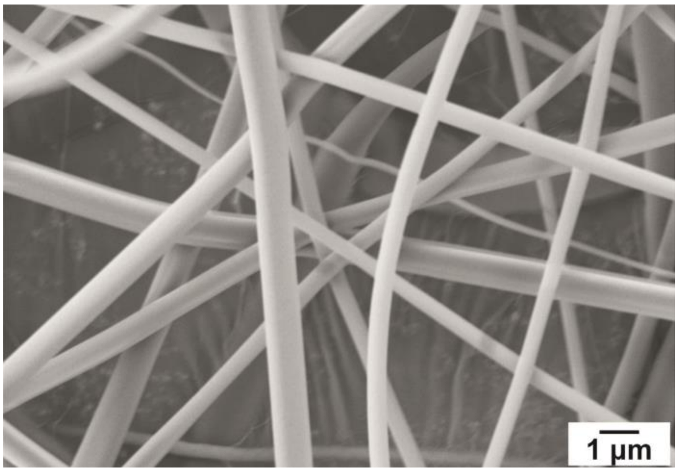

Fig.2 SEM image of the precursor fibers

The SEM images of the precursor fibers and the fibers morphology and topology after the heat treatments at different temperatures and environments are shown in Fig.2. The continuous electrospun precursors were homogenous, had a smooth surface and round shape with average the diameter of ~0.67 μm (Fig.2). The oval-shape polycrystalline ceramic fibers were obtained after calcination at 450 °C, which consisted of the small crystallites of anatase and rutile (Fig.3a). As the temperature increased to 600°C, these crystallites grew and transformed fully to rutile fibers with the average diameter of 0.49 μm (Fig.3b). Fig.3c, shows the circular-shaped carbon fibers produced at 1000°C in argon. The average diameter of the amorphous carbon fibers is about 0.75 μm. The specific single-grain cross section structure of the final titanium carbide based fibers obtained after pyrolysis and carbothermal reduction at 1500°C is depicted in Fig.3d). It is clearly seen that the nanocrystals with a specific cubic structure forms an interconnected 3-dimensional fibrous network with a high surface area. In the present work, the single one composite precursor microfibers were heat treated in two atmospheres - in air and in argon, what resulted in different types of products with different phase composition, depending on the selected heat treatment temperature. It is well-known, that $Ti(IPO)_4$ is very sensitive to presence of water. It can rapidly hydrolyse even by the air moisture. In our case continuous networks (gels) of TiO_2 were formed *in situ* in the nanofibers once they had been ejected from the spinning electrode [8]. As a result the composite precursor fibers were obtained which consisted of amorphous TiO_2 nanoparticles in PVP matrix [8]. After the heat treatment in oxidative atmosphere the precursor samples were transformed to continuous titania nanofibers, but with reduced average diameter. This size reduction is caused by the loss of PVP and the crystallization of TiO_2 [8].

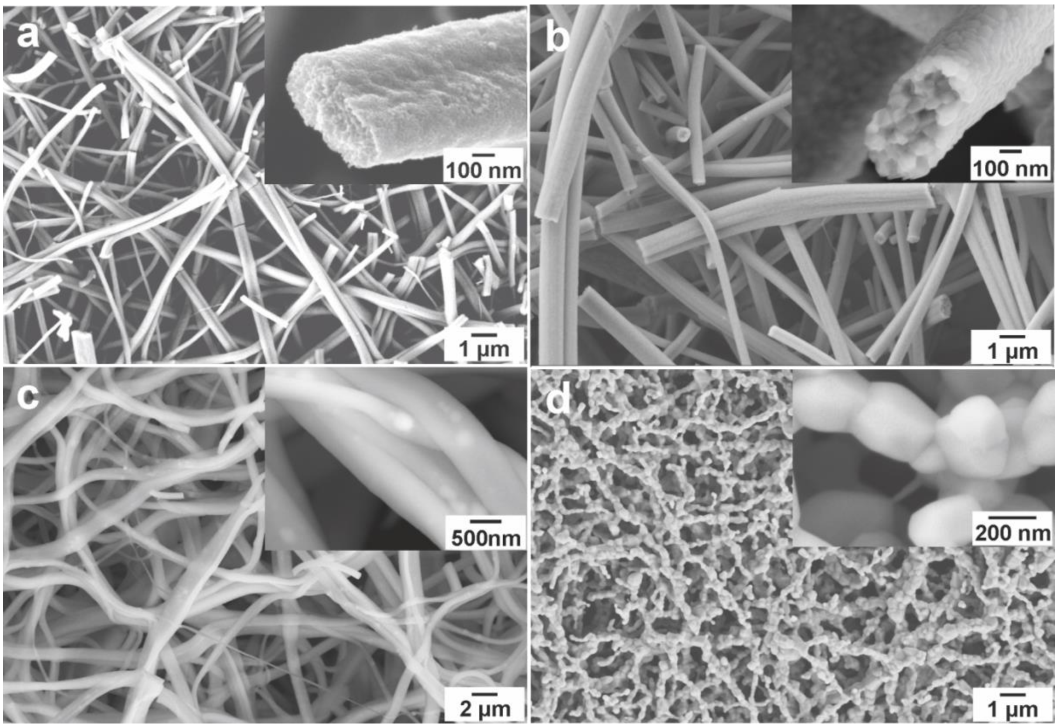

Fig.3 SEM images and detail of the surface: a) fibers calcinated at 450°C and b) at 600°C in air; c) fibers pyrolyzed at 1000°C and d) 1500°C in Ar

In oxidative atmosphere TiO_2 crystallized in 2 phases: anatase at low temperature and rutile phase at higher temperature [9]. Adjusting the calcination process temperature and conditions – phase composition can be easily tailored. In the case of inert atmosphere polymer decomposed and was pyrolyzed with the formation of volatile gaseous products (carbon oxides and nitrogen) and carbon, which reduced TiO_2 to some intermediate phases and titanium carbide at elevated temperatures. These processes are schematically shown in Fig.4.

At 1000°C only carbon fibers with some anatase-phase TiO_2 nanoparticles embedded in carbon matrix were formed. Further temperature elevation to 1500°C provided the full oxides reduction and the formation of titanium carbide three-dimensional highly interconnected network formed by single grain in a cross-section of the fibers. This kind of morphology was caused by the growth of the carbide crystallites formed inside the fibers and interconnected by the ones formed outside already at the lower temperature.

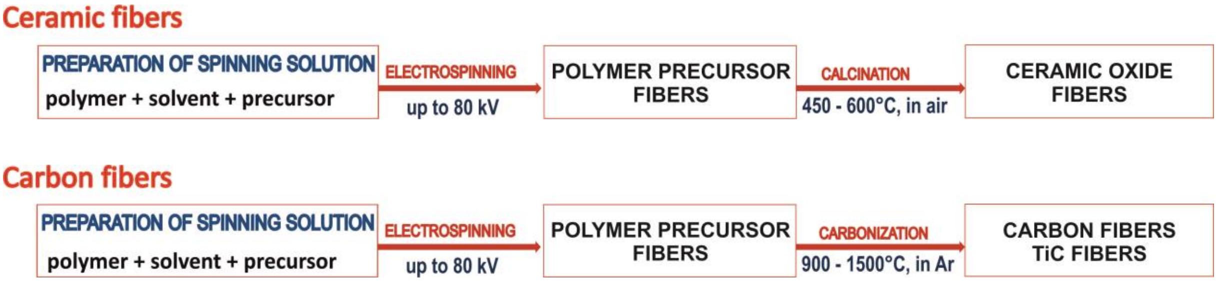

Fig.4. Scheme of formation of oxide and carbon- and/or TiC -based fibers

CONCLUSION

The wide scale of ceramic fibers were successfully prepared from single TiO_2/PVP precursor fibers using needle-less electrospinning technique, followed by different heat treatment strategies. This new route allows preparation both oxide and non-oxide ceramics from the same oxygen-containing metal-organic precursors in a form of microfibers by simply changing the post-spinning treatment conditions.

ACKNOWLEDGMENT

This work was supported by the Scientific Grant Agency of the Ministry of Education, Science, Research and Sport of the Slovak Republic and the Slovak Academy of Sciences, projects No. VEGA 2/0099/18, 2/0163/16, Slovak Research and Development Agency under the contract No. APVV-15-0469, the project „Centre of Excellence for Ceramics, Glass and Silicate Materials „CeKSiM", ITMS 26220120056 and the project „Research Centre of Advanced Materials and Technologies for Recent and Future Applications „PROMATECH", ITMS 26220220186, supported by the Operational Program "Research and Development" financed through European Regional Development Fund.

REFERENCES

[1] Fu, P., Luan, Y., Dai, X. Preparation of activated carbon fibers supported TiO_2 photocatalyst and evaluation of its photocatalytic reactivity, J. Mol. Catal. A Chem. 221 (2004) 81-88.

[2] Mishra, S., Ahrenkiel, S.P. Synthesis and characterization of electrospun nanocomposite TiO_2 nanofibers with Ag nanoparticles for photocatalysis applications, J. Nanomater. 2012 (2012).
[3] Grätzel, M. Dye-sensitized solar cells, J. Photochem. Photobiol. C Photochem. Rev. 4 (2003) 145-153.
[4] Zhang, Y., Tang, Y., Li, W., Chen, X. Nanostructured TiO_2 -Based Anode Materials for High-Performance Rechargeable Lithium-Ion Batteries, ChemNanoMat. 2 (2016) 764-775.
[5] Li, F., Gao, X., Wang, R., Zhang, T., Lu, G. Study on TiO_2-SnO_2 core-shell heterostructure nanofibers with different work function and its application in gas sensor, Sensors Actuators, B Chem. 248 (2017) 812-819.
[6] Tu, R., Huo, G., Kimura, T., Goto, T. Preparation of Magnéli phases of $Ti_{27}O_{52}$ and Ti_6O_{11} films by laser chemical vapor deposition, Thin Solid Films. 518 (2010) 6927-6932.
[7] Williams, W.S. Transition metal carbides, nitrides, and borides for electronic applications, J. Miner. Met. Mater. Soc. 49 (1997) 38-42.
[8] Li, D., Xia, Y. Fabrication of titania nanofibers by electrospinning, Nano Lett. 3 (2003) 555-560.
[9] Hanaor, D.A.H., Sorrell, C.C. Review of the anatase to rutile phase transformation, J. Mater. Sci. 46 (2011) 855-874.

PRÍPRAVA KOMPAKTNÝCH A NANORÚRKOVÝCH TiO_2 VRSTIEV NA FLEXIBILNEJ KAPTONOVEJ FÓLIÍ A ŠTUDOVANIE ICH FOTOKATALYTICKÝCH VLASTNOSTÍ

PREPARATION OF COMPACT AND NANOTUBE TiO_2 LAYERS ON FLEXIBLE KAPTON TAPE AND STUDY OF THEIR PHOTOCATALYTIC PERFORMANCE

P.Petrisková[1,2], M. Motola[3], O. Monfort[4], G.Plesch[1]

[1]Comenius University in Bratislava, Faculty of Natural Sciences, Department of Inorganic Chemistry, Ilkovičová 6, Mlynská Dolina, 842 15 Bratislava, Slovakia;
patricia.petriskova@gmail.com

[2]Institute of Inorganic Chemistry, Slovak Academy of Sciences, Dúbravská cesta 9, 84536 Bratislava, Slovakia

[3]Center of Mater. and Nanotechnologies CEMNAT, University of Pardubice,Čs. legií 565 530 02 Pardubice,Czech Republic

[4]Univ Rennes, Ecole Nationale Supérieure de Chimie de Rennes, CNRS, ISCR–UMR 6226, F-35000 Rennes, France

ABSTRACT

Titania (TiO_2) photocatalytic layers are already used for the decontamination of air and water, but the enhancement of their performance for various applications (environmental, medical, etc.) is still the matter of intense research. This work is devoted to the preparation of thin TiO_2 layers in the form of compact film and nantubes.The compact and nanotube TiO_2 layers were prepared by sol-gel method and electrochemical anodization of titanium layer, respectively, on flexible Kapton® polyimide tape. Their photocatalytic performance in the removal of an organic dye (Rhodamine B) has been also investigatedand showed that the photocatalytic properties of closely packed aligned TiO_2 nanotubes (TiNTs) were better compared to TiO_2 layers deposited by sol-gel method. TiNTs exhibit much higher surface area while thin sol-gel layers are relatively dense. Therefore, TiO_2 nanotubes exhibits better photocatalytic efficiency than compact layer in the removal of organic dye.

Keywords: TiO_2; photocatalysis; nanotubes; sol-gel; Kapton®

INTRODUCTION

Titania (TiO_2) is the most popular photocatalyst which is still the subject of intense research, although many studies have been published [1]. TiO_2 has numerous advantages such as high photocatalytic activity under UVA irradiation, low cost, non-toxicity and stability against corrosion, thus making TiO_2 an ideal candidate for photocatalytic application compared to any other materials [1,2]. The significant efficiency of TiO_2 in the photocatalytic degradation of organic pollutants is due to its ability, in aerated media, to form reactive oxygen species (ROS) such as $O_2^{\bullet-}$, H_2O_2 and $HO^{\bullet}$. These oxidative radicals are formed during the photoactivation process of TiO_2 under appropriate irradiation [2]. The photooxidative degradation of pollutants has gained much attention in the purification of air and water because it provides an attractive alternative to the more conventional methods such as adsorption, incineration, and conventional catalysis [2]. Moreover the main advantage of photocatalysis over other treatments is the use of light as activation energy, which allows degradation of the pollutants at ambient temperature and pressure without the use of external energy [2]. Therefore, TiO_2-based photocatalysis can be considered as green process. However, for the engineering of solar energy devices e.g. photocatalytic reactors and solar cells, the morphology of TiO_2 is a crucial parameter [3]. Indeed the porosity of the photocatalyst governs the surface area which is related to the number of photocatalytic sites in contact with the polluted medium. Therefore, porous nanomaterials and especially self-organized nanotube arrays are ideal candidates for the design of solar devices for environmental applications (e.g. conversion of CO_2, water splitting and dye-sensitized solar cells) and medical applications [3,4]. Cheaper way is the preparation/deposition of titania layer on various substrates such as silicon, glass, alumina, metals and polymers [1]. Polymeric substrates such as Kapton® are interesting since they are innoxious materials being mechanically stable with high durability [1]. Their hydrophobic nature gives them an added advantage to pre-concentrate the organic pollutants on the surface and this increases the efficiency of adsorption and subsequent photooxidation in the presence of photocatalyst, because the photodegradation mechanism is based on the surface-adsorbed reactants. In addition such organic flexible substrates are inexpensive and readily available compared to similar inorganic substrates such as Pt and Ti foils. The deposition of TiO_2 nanotube arrays on flexible Kapton® was only studied for dye-sensitized solar cells and sensors [3-5]. In the present work nanoporous TiNTs and dense sol-gel layers were deposited on Kapton® tape and their performance in the photocatalytic degradation of organic pollutants was evaluated.

EXPERIMENTAL

Prior to deposition of TiO_2 materials, Kapton® substrates were cleaned using an ultrasonic bath in acetone, ethanol and deionized water. Titanium dioxide nanotubes were obtained via anodization of a titanium layer deposited by DC-magnetron sputtering on Kapton® HN. Self-organized TiNT arrays were subsequently grown in ethylene glycol-based electrolyte containing NH_4F and distilled water at 40 V. For a comparison, in the second batch of samples the TiO_2 sol-gel layers were deposited by spin-coating. The sol-gel precursor was prepared by mixing titanium(IV) isopropoxide in ethanol. For increasing adherence of the sol-gel onto the flexible organic substrate, the surface of Kapton® was modified by treatment in KOH or by plasma. The dimension of TiNT and TiO_2 sol-gel layers was approximately 2 cm^2. After deposition, the layers were annealed at 450°C for 1h in order to crystallize the amorphous TiO_2.

The prepared samples were characterized by SEM (TescanLyra III) to study the morphology of TiO_2 layers. The crystalline phase composition was determined using and XRD analysis (PANalytical X-Pert Pro MRD Diffractometer). Photocatalytic measurements were performed by monitoring the decolorization of a Rhodamine B solution (20 mL of 10^{-5} M) under UVA irradiation (Philips – HPA 400W; $\lambda_{max} = 365$ nm) using a UV-Vis spectrophotometer (Jasco V-530). The photocatalytic measurements encompassed 2 steps: (1) 30 min in the dark to reach adsorption-desorption equilibrium and (2) 5 hours irradiation under constant air bubbling. The photocatalytic performance of each material was evaluated by plotting the relative concentration of RhB against time *t*.

RESULTS AND DISCUSSION

The morphology of the prepared TiO_2 layers investigated by SEM is presented in Fig. 1. The TiNT layer is composed of self-organized nanotubes array (Fig. 1a). In addition it was shown that the average diameter of nanotubes was 42 nm while the average length was about 2.6 µm (data not shown here). On the other hand, the sol-gel layer (Fig. 1b) exhibited a dense and compact structure. The comparison of the morphology of the two types of TiO_2 layers showed that the surface area of TiNTs would be much higher than that of sol-gel layer (since it has a tubular morphology i.e. it is more porous). The XRD measurements confirmed the presence of crystalline TiO_2 anatase phase, the most photoactive phase of titania, in all the annealed samples.

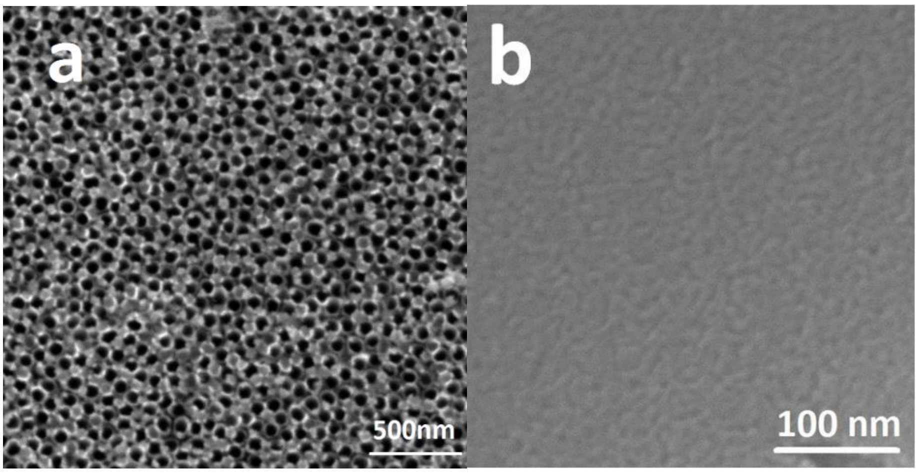

Fig. 1. SEM image of the surface of (a) TiNT arrays and (b) sol-gel layer.

The tests of the photocatalytic performance of the photocatalysts in the removal of Rhodamine B showed that TiNTs layer was more efficient than sol-gel layer under UVA irradiation (Fig. 2). Indeed, after 5 hour irradiation, 70% of RhB was degraded using TiNTs, while less than 50% efficiency was obtained for sol-gel layer under the same conditions. This observation can be explained by the surface area of the photocatalysts. Since TiNTs have a porous morphology, their active surface area would be much higher surface area than that of the sol-gel layers.

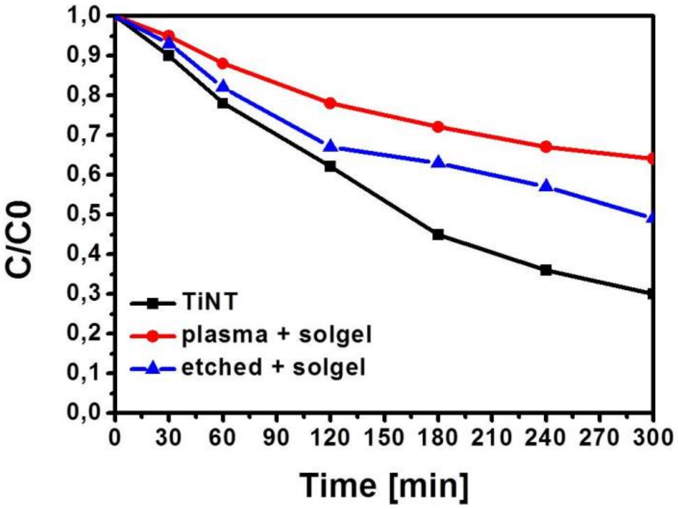

Fig. 2. Photocatalytic degradation of RhB using different TiO_2 photocatalysts (C/C_0 vs. t).

It is worth noting that without surface treatment of Kapton® prior to sol-gel deposition, no adherence of the prepared TiO_2 layer was observed, because the unmodified organic substrate is hydrophobic. In the case of plasma treatment, thin film of TiO_2 can be deposited on Kapton® and showed a degradation efficiency of RhB about 35%. In the case of surface etching using KOH, the deposited TiO_2 layers were delaminated during the photocatalytic measurements, thus changing the “state” of the material from supported to suspended photocatalyst. This is a potential explanation of its better efficiency compared to supported sol-gel layer (with plasma treatment). Even the suspension exhibited better photocatalytic results, the deposition in the form of films is more practical, e.g. for post-separation of photocatalyst, environmental and medical applications such as filter and antibiofilm, etc.

CONCLUSION

The preparation of TiO_2 photocatalysts in a form of nanotubes or compact sol-gel-prepared layer on organic flexible substrate is feasible and leads to highly photoactive materials in the degradation of organic pollutants, especially organic dyes. The TiO_2 nanotube layers are more efficient than compact film deposited by sol-gel method. Such an organic substrate is, due to its advantageous flexibility, promising for photocatalytic applications e.g. construction of photoreactors for environmental remediation and disinfection of medical implants.

ACKNOWLEDGMENT

Authors appreciated the financial support through the scientific project VEGA 1/0276/15. Authors highly acknowledge Dr. Leonid Satrapinskyy and Assoc. Prof. Tomas Roch for SEM and XRD measurements, respectively. This work is also the results of the project implementation ITMS 26210120010 and 26240220027 supported by the Research & Development Operational Program funded by the ERDF.

REFERENCES

[1] Singh S., Mahalingam H., Singh P. K., *Appl. Catal. A*, 462-463 (2013) 178.

[2] Kalousek V., Tschirch J., Bahnemann D., et al., *Superlat. Microstruc.*, 44 (2008) 506.

[3] Galstyan V., Vomiero A., Concina I., et al. *Small*, 7 (2011) 2437.

[4] Farsinezhad S., Mohammadpour A., Dalrymple A. N., et al., *J. Nanosci. Nanotech.*, 13 (2013) 2885.

[5] Vomiero A., Galstyan V., Braga A., et al., *Energ. Environ. Sci.*, 4 (2011) 3408.

SYNTÉZA A VLASTNOSTI BÓROM DOPOVANÝCH NANOČASTÍC ZnO V THz OBLASTI

SYNTHESIS AND PROPERTIES OF BORON DOPED ZnO NANOPARTICLES IN THz REGION

D. Furka[1], S. Furka [1], M. Naftaly [2], A. Czímerová[3] M. Čaplovičová[4], M. Janek [1,5]

[1]*Univerzita Komenského, Prírodovedecká fakulta, Katedra fyzikálnej a teoretickej chémie,*
Mlynská dolina Ch1, 842 15 Bratislava

[2] *National Physical Laboratory, Hampton Rd, Teddington, Middlesex, TW11 0LW,*
United Kingdom

[3] *Ústav Anorganickej Chémie Slovenksej Akadémie Vied, Dúbravská cesta 9,*
845 36 Bratislava

[4] *Slovenská Technická Univerzita v Bratislave, Centrum Nanodiagnostiky, Vazovova 5,*
812 43 Bratislava

[5] *Slovenská Technická Univerzita v Bratislave, Fakulta Chemickej a Potravinárskej*
Technológie, Oddelenie anorganických materiálov, Radlinského 9, 812 37 Bratislava

ABSTRACT

Increased demand for semiconductors intended for the production of precision sensors, and solar cells, require the preparation of new materials with low cost and appropriate parameters. As reasonable alternative were investigated pure and boron doped Zinc oxide (ZnO) nanoparticles prepared by co-precipitation hydrothermal synthesis. This way of preparation offer simple-controllable conditions to achieve good homogeneity in specific shape and size during growth of ZnO nanoparticles. ZnO is a semiconductor with a wide band gap (3.1 eV - 3.3 eV) and suitable optical transparency in the UV-VIS spectrum. The dielectric response of ZnO can be affected by synthesis conditions or doping. The dopant integration into the lattice structure of the semiconductor crystal leads to the defined modification of material conductivity. For the first time, the boron oxide was used for doping ZnO during co-precipitation hydrothermal synthesis of ZnO nanoparticles. THz time domain spectroscopy was utilised to investigate the dielectric response of prepared ZnO nanoparticles. The aim of our work was to verify the co-precipitation hydrothermal synthesis for B_2O_3 doping of ZnO nanoparticles and to characterize the frequency dependent dielectric properties of ZnO nanoparticles.

Keywords: Boron oxide doped ZnO, THz-TDS, semiconductor, doping, band gap.

INTRODUCTION

ZnO is a substance with interesting semiconducting properties having valence band width in the range 3.1 eV - 3.3 eV [1, 2]. Sufficient electromechanical response along with the absence of the center of symmetry in the Wurtzite-like structure of ZnO leads to its piezoelectric and pyroelectric properties. Improved electron conductivity due to the presence of oxygen vacancies and zinc atom deposition disorders includes ZnO into a grup of N-type semiconductors. The large exciton coupling energy (60 meV) allows the utilization of ZnO in the production of optoelectronic components such as LED diodes, lasers and biosensors. Absorption of electromagnetic radiation allows the use of ZnO nanoparticles as a photocatalyst for the photo-electrochemical conversion of selected organic compounds or for the reduction of carbon dioxide to hydrogenated species such as alcohols. Optical and dielectric properties are important properties of ZnO that can be affected by doping. However, extend of size and morphology of parent synthesized nanoparticles which may affect the properties of final solid phase is not known. The nanoparticle morphology can be influenced easily by presence of additives during their synthesis. Additives cause preferential crystal growth in a certain crystallographic plane, but they are not incorporated into the nanoparticle structure. Morphology of the nanoparticles may be also influenced by extend of doping. During doping, the addition of a small number of atoms from the adjacent group of periodic system of elements causes structural disturbances, resulting in a change in electron conductivity along with subsequent change in optical and dielectric properties. Well-defined and doped ZnO nanoparticles of different morphology combined with other supporting components such as clay nanolayers and/or organic dyes, can find utilization in a gas sensing, photocatalytic or electronic applications. From these reasons, the study of boron oxide as dopant on the resulting optical and dielectric properties of ZnO was investigated as a possible electron donor component in the solid phase structure.

EXPERIMENTAL

For the production of pure and doped nanoparticles, hydrothermal synthesis was used, applying zinc acetate dihydrate ($Zn(Ac)_2 \cdot 2H_2O$) as starting ZnO precursor. Hydrothermal synthesis allows affecting the size of prepared nanoparticles by the rate of precursor addition, by adjusting the concentrations of the components of the synthesis mixture, by affecting the temperature and synthesis time. The basic building block of ZnO crystals is the complex anion $[Zn(OH)_4]^{2-}$. The amount of this anion in the reaction mixture depends on the concentration of OH^- ions during the ligands exchange and the degree of hydrolysis of the organic precursor in solution. To modify the morphology of synthesized particles, triethylene tetamine (TETA) was used in the reaction mixture. TETA changes the coordination of Zn^{2+} cations, which leads to a slowing of growth along the crystallographic axis a and b. The crystals grow preferably in the direction of the crystallographic axis c resulting in spindle particle morphology [3]. In the case of doping nanoparticles with boron oxide (B_2O_3), the trihydrogen borate acid was used as precursor substance. During the synthesis 2 types of particle morphologies i) pseudohexagonal and ii) elongated-spindles we prepared. The boron concentrations varied in reaction mixture and included pure un-doped nanoparticles used as reference materials. The mol fraction of boron was increasing toward zinc at levels of 0.5, 1.0, 5.0, 10.0, 15.0 and 20.0 molar %. Separated, washed and dried ZnO nanoparticle powders were then cold pressed using isostatic pressure of 10 MPa. The compressed pellets were sintered at 900° C for 2 hours using a temperature ramp of 5° C. min $^{-1}$ for heating and cooling regime. Prepared pellets were used to determine their band-gaps using diffuse reflection spectroscopy in the UV-VIS region of electromagnetic radiation. The calculated energies of band-gaps as function of boron concentration and different particle morphology are shown in the Figures 1 and 2. The energy values of the band-gaps for pure ZnO synthesized as reference material (3.1815 eV) are in good agreement to the data published [2]. An interesting finding was that the energy of the ZnO material synthesized from the elongated-spindle particles revealed higher band-gap energy values (3.2196 eV), than the material prepared from the pseudohexagonal particles.

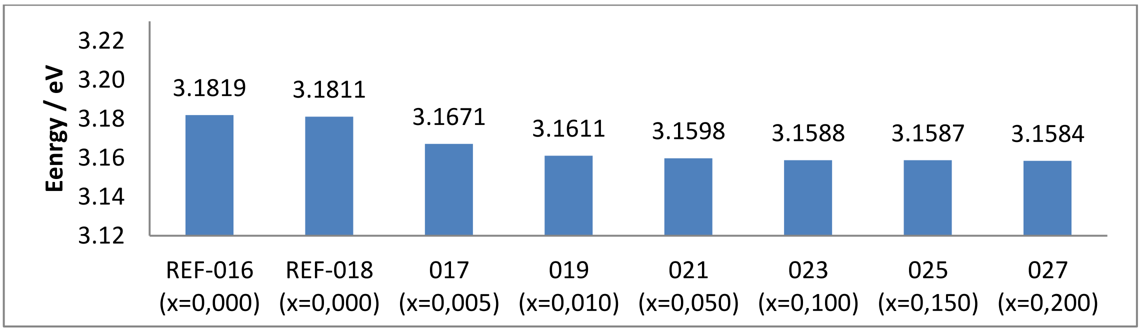

Fig. 1. Determined energy band-gaps of both pure and doped ZnO nanoparticles with pseudohexagonal particle morphology.

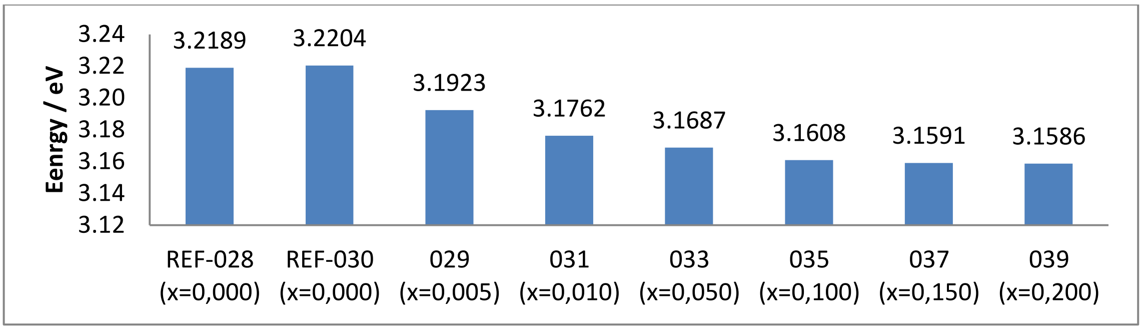

Fig. 2. Determined energy band-gaps of both pure and doped ZnO nanoparticles with elongated-spindle like particle morphology.

The dielectric properties of pure and doped ZnO pellets determined by THz time-domain spectroscopy in the far IR region are summarised in the Tables 2 and 3.

Tab. 2. Dielectric properties of ZnO with different mol fraction of boron in the far IR region at 1 THz.

Hexagonal nanoparticles	**0,00%**	**0,50%**	**1,00%**	**5,00%**	**10%**	**15%**	**20%**
Refractive index – n	2,342	2,441	2,218	2,429	2,215	2,223	2,342
Absorption coefficient - α	2,508	8,152	10,555	14,017	4,801	4,923	7,016
Absorption index – κ	0,168	0,193	0,253	0,325	0,100	0,110	0,167
Relative permittivity - ε' real part	2,278	2,445	2,225	2,411	2,225	2,217	2,049
Relative permittivity - ε'' imaginary part	0,776	0,924	1,105	1,618	0,446	0,446	0,781

Tab. 3. Dielectric properties of ZnO with different mol fraction of boron in the far IR region at 1 THz.

Elongated-spindle nanoparticles	**0,00%**	**0,50%**	**1,00%**	**5,00%**	**10%**	**15%**	**20%**
Refractive index – n	2,150	2,051	2,096	2,198	2,150	1,962	2,0499
Absorption coefficient - α	4,403	4,221	4,223	4, 800	4,503	4,505	4,795
Absorption index – κ	0,104	0,100	0,101	0,115	0,107	0,106	0,115
Relative permittivity - ε' real part	2,098	2,079	2,096	2,197	2,154	1,904	2,050
Relative permittivity - ε'' imaginary part	0,398	0,459	0,432	0,497	0,428	0,456	0,465

RESULTS

The structure of pure ZnO nanoparticles was confirmed by RTG powder diffraction analysis with typical diffractions at 2θ° corresponding to (hkl) for 31.80° (100), 34.52° (002), 36.33° (101), 47, 63° (102), 56.70° (110), 62.96° (103), 68.10° (112). Diffraction data confirmed the expected Wurtzit-like structure of ZnO in all prepared samples. Infrared spectra of pure ZnO nanoparticles and nanoparticles synthesized in the presence of the additive exhibited a characteristic absorption band of zinc oxide at a wavelength range from 450 cm^{-1} to 490 cm^{-1}, corresponding to the valence vibration of Zn–O bomd. In the case of boron doped nanoparticles, we observe the absorption band between 1429 cm^{-1} and 1564 cm^{-1} , corresponding to the valence vibration of B–O bond with coordination number 3 [4]. At the same time, the presence of valence vibrations of B–O bonds was confirmed without the presence of significant valence vibrations of O–H groups that are typical for H_3BO_3 in the region from 2030 cm^{-1} to 2260 cm^{-1}. Based on results of the IR spectra obtained, it can be assumed the incorporation of B_2O_3 into the crystalline phase of ZnO. Images from the scanning and transmission electron microscopy confirm the morphology of the prepared nanoparticles and support information about the nanoparticles size distribution. ZnO nanoparticles used for preparation of the pellets were sintered and measured by THz time-domain spectrometry. Obtained transfer function allowed the calculation of frequency dependent refractive index $n(\omega)$ and absorption coefficient $\alpha(\omega)$. Pure and boron doped samples of ZnO showed a transparent behaviour in the THz region of electromagnetic radiation. The refractive index of material sintered from pseudohexagonal particles was 2.316 with a standard deviation of 0.0998 at 1THz. This value is about 13% higher than value observed for monocrystalline zinc oxide [5]. The real component of relative permittivity reached an average of 2.264 with a standard deviation of 0.1329. This value is significantly lower than value of monocrystalline ZnO with a value of 7.8 [6]. The data found are summarized in the the Table 1.The refractive index values of the pellets sintered from the elongated-spindle particles reached a value of 2.0938 with a standard deviation of 0.0799, which is close to the refractive index of the monocrystalline ZnO measured at a wavelength of 500 nm [3]. This value differs significantly from material prepared from hexagonal nanoparticles. The real component of the relative permittivity of the elongated-spindle particles revealed the value 2.146 with a standard deviation of 0.1806. This value is significantly lower than the dielectric constant of monocrystalline ZnO found in the literature (7.8 [6]) and is at the same time lower than the dielectric constant of material sintered from hexagonal nanoparticles. These results indicate that the morphology and size of nanoparticles used for sintering of bulk ZnO can influence their sintering behaviour resulting in optical and dielectric differences of the studied material. The main factors affecting the observed changes in optical and dielectric properties are the amount of boron oxide incorporated into the ZnO nanoparticles along with the porosity of the material after sintering of the bulk ZnO material (Table 2).

CONCLUSION

Application of co-precipitational hydrothermal synthesis for preparation of boron doped ZnO nanoparticles was investigated. Verification of the boron oxide doping into the nanoparticles by the hydrothermal synthesis was not yet published, despite the fact that boric oxide is a well-known glass-forming additive. Obtained ZnO material with a defined pore size distribution and suitably adjusted optical and dielectric properties can be utilized in optical sensors and windows for detection of near and far infrared electromagnetic radiation, in optoelectronic components, as green chemistry photocatalyst for the reduction of carbon dioxide from the atmosphere.

ACKNOWLEDGEMENT

The financial support of Grant for PhD students and young UK researchers (UK/163/2017 and UK/403/2018) and financial support of the Slovak Grant Agency for Science VEGA grants No. 1/0278/16 and 1/0906/17 are greatly appreciated.

REFERENCES

[1] Han, J., Zhang, W., et al. Terahertz Dielectric Properties and Low-Frequency Phonon Resonances of ZnO Nanostructures, J. Phys. Chem. Vol 111 (2007) 371-392.

[2] V. Srikant and D. R. Clarke,. On the optical band gap of zinc oxide 1998 Journal of Applied Physics 83, 5447

[3] Furka, D. Hydrotermálna syntéza nanočastíc ZnO a jeho dielektrické vlastnosti v THz oblasti (Diplomová práca), Univerzita Komenského v Bratislave (2016).

[4] Jun, L., Shuping, X., Shiyang, G. FT-IR and Raman Spectroscopic Study of Hydrated Borates, Spectrochimica Acta, Vol. 51A (1995) 519-532.

[5] Bond, W., Measurement of the refractive indices of several crystals, J. Appl. Phys, Vol. 36 (1965) 1674-1677.

[6] Madelung, O., et al. Zinc oxide (ZnO) dielectric constants - II-VI and I-VII Compounds, Semimagnetic Compounds, Vol 17B-22A (2001).

KIMS Korea-SAS Slovakia Workshop on Advanced Ceramics

HIPIMS VS. DC SPUTTERED HYDROGENATED W-C:H COATINGS: STRUCTURE AND MECHANICAL PROPERTIES

F. Lofaj[1], M. Kabátová[1], A. Kovalčíková[1], V. Girman[1,2], J. Dobrovodský[3], D. Vaňa[3], M. Beňo[3]

[1] *Institute of Materials Research of the Slovak Academy of Sciences, Watsonova 47, 04001 Košice, Slovakia*
[2] *Pavol Jozef Šafárik University in Košice, Faculty of Science, Institute of Physics, Department of Condensed Matter Physics, Park Angelinum 9, Košice, 040 01, Slovakia*
[3] *Advanced Technologies Research Institute, Faculty of Materials Science and Technology in Trnava, Slovak University of Technology in Bratislava, J. Bottu 25, 91724 Trnava, Slovakia*

ABSTRACT

The investigation the effects of the level of hydrogenation on hardness and elastic modulus of W-C:H coatings deposited by hybrid sputtering using DC magnetron sputtering and High Power Impulse Magnetron Sputtering (HiPIMS). The levels of hydrogenation and hybridization were measured as a function of acetylene and hydrogen additions into sputtering atmosphere by Rutherford Backscattering (RBS)/Elastic Recoil Detection Analysis (ERDA) methods. Hardness was measured by nanoindentation. It was found out that the addition of acetylene results in the increase of hydrogen concentration in the carbon matrix more effectively than the addition of hydrogen. Subsequent increase of the contents of free carbon and hydrogen caused strong decrease of hardness of DCMS W-C:H coatings whereas it was significantly rather small in HiPIMS coatings. The advantages of HiPIMS technology compared to DCMS in terms of hardness were emphasized.

ACKNOWLEDGEMENTS

The financial support provided by the projects APVV-15-0168 and APVV 17-0320 is acknowledged. The equipment used in the work was acquired from the project "Research Centre of Advanced Materials and Technologies for Recent and Future Applications" PROMATECH, ITMS: 26220220186 and "University Scientific Park Campus MTF STU – CAMBO" ITMS: 26220220179.

FACILE SURFACE MODIFICATION TECHNIQUES OF CERAMIC MEMBRANES FOR THE APPLICATION TOWARDS WATER PURIFICATION

Jongman Lee, Jang-Hoon Ha, In-Hyuck Song

Powder and Ceramics Division, Korea Institute of Materials Science (KIMS), Republic of Korea

ABSTRACT

The pristine alumina membranes are usually susceptible to membrane fouling during water purification process. It is attributed mostly to the positively charged surface properties, which resulted from relatively high isoelectric point (IEP) of 9.4. For improving the fouling resistance of alumina membranes, we endeavored to control the surface properties using two different methods: organic and inorganic surface modifications. For the organic modification, three representative organosilanes presenting neutral ($-CH_3$), positive ($-NH_2$), and negative ($-SO_3$) charges were allowed to graft onto alumina membranes. In the membrane filtration test using humic acid, the neutral and negatively charged membranes maintained higher flux patterns. Notably, the negatively charged membranes achieved the most remarkable flux behavior during entire fouling procedure. This result is primarily ascribed to the electrostatic repulsion force between the organosilane-grafted membranes and negatively charged humic acid (IEP: 4.7).For the inorganic modification, the alumina membranes were modified using a SiO_2 sol-gel process to mitigate membrane fouling. Due to low isoelectric points, SiO_2-coated membranes have a strong negative surface charge (-130 mV at pH 6.5), which results in the electrostatic repulsion forces against humic acid. The membranes with higher TEOS concentrations exhibited higher flux levels during membrane fouling procedures. Thus, the respective surface modifications with organosilane and amorphous SiO_2 could successfully produce the negatively charged membranes. These surface-modified membranes would prevent the serious humic acid adsorption via electrostatic repulsion and enhance the fouling resistance of alumina membranes.

HIGH ENTROPY CARBIDES: NOVEL MATERIALS FOR EXTREME ENVIRONMENTS

Tamás Csanádi[1], Elinor Castle[2], Mike Reece[2], Ján Dusza[1,3]

[1]*Institute of Materials Research, Slovak Academy of Sciences, Watsonova 47, 04353 Košice, Slovak Republic*
[2]*Queen Mary, University of London, Mile End Road, London, E1 4NS, UK*
[3]*Donát Bánki Faculty of Mechanical and Safety Engineering, Óbuda University, Népszínház utca 8, 1081 Budapest, Hungary*

ABSTRACT

Bulk equiatomic (Hf-Ta-Zr-Ti)C and (Hf-Ta-Zr-Nb)C high entropy Ultra-High Temperature Ceramic (UHTC) carbide compositions were fabricated by ball milling and Spark Plasma Sintering (SPS). It was found that the lattice parameter mismatch of the component monocarbides is a key factor for predicting single phase solid solution formation, revealing a vast new compositional space for the exploration of new UHTCs. The microstructure characteristics were investigated using X-ray diffraction (XRD), scanning electron microscopy (SEM) in combination with electron back scattered diffraction (EBSD) and transmission electron microscopy (TEM). Atomic structure and local chemical disorder was determined by means of scanning transmission electron microscopy (STEM) in conjunction with energy dispersive X-ray spectroscopy (EDS). The (Hf-Ta-Zr-Ti)C sample was observed to chemically decompose; indicating the presence of a miscibility gap. While this suggests the system is not thermodynamically stable to room temperature, it does reveal further potential for the development of new in situ formed UHTC nanocomposites. Further optimisation of processing route revealed high purity, dense (99%), single phase and homogeneous high entropy carbide with Fm-3m crystal structure for (Hf-Ta-Zr-Nb)C. The grain size ranged from approximately 5 µm to 25 µm with average grain size of 12 µm. Chemical analyses proved that all grains had the same chemical composition at the micro as well as on the nano/atomic level without any detectable segregation. This optimised material was subjected to nanoindentation testing and directly compared to the constituent mono/binary carbides, revealing a significantly enhanced hardness (36.1±1.6 GPa,) compared to the hardest monocarbide (HfC, 31.5±1.3 GPa) and the binary (Hf-Ta)C (32.9±1.8 GPa).

ACKNOWLEDGMENT

This work was realized within the frame of the project „Centre of Excellence for Ceramics, Glass and Silicate Materials „CeKSiM“, ITMS 26220120056 and the project „Research Centre of Advanced Materials and Technologies for Recent and Future Applications “PROMATECH” ITMS 26220220186, supported by the Operational Program “Research and Development” financed through European Regional Development Fund.

IMPROVED THERMAL CONDUCTIVITY OF SILICON NITRIDE BY INTENTIONAL OXYGEN REMOVAL

Ha-Neul Kim, Yinsheng Li, Young-Jo Park, Jae-Woong Ko, Hai-Doo Kim

Powder and Ceramics Division, Korea Institute of Materials Science (KIMS), Republic of Korea

ABSTRACT

Silicon nitride (Si_3N_4) is a promising substrate material for high-power electronic devices, owing to its excellent thermal and mechanical properties. Oxygen is widely recognized as one of the most detrimental impurities to the thermal conductivity of Si_3N_4 ceramics. In order to fabricate Si_3N_4 with enhanced thermal conductivity, the ceramic processing was adjusted to allow intentional oxygen removal. Firstly, a BN/graphite powder bed was used for reaction bonded Si_3N_4(RBSN) and its post-sintering processes. Owing to the strong reducing ability of graphite, the BN/10 wt% C powder bed could significantly facilitate the removal of SiO_2 from Si compacts during nitridation, resulting in altered chemistry of secondary phase, larger rod-like β-Si_3N_4 grains, and lower lattice oxygen content in the RBSN product. Benefiting from the decreased lattice oxygen content and the optimized microstructure, the sintered RBSN sample obtained great improvement in thermal conductivity from 86 to 121 W·m-1·K-1. Secondly, novel sintering additive, $Y_2Si_4N_6C$, is applied to sinter the Si_3N_4 ceramic. Commercial Si_3N_4 powder was compacted and densified at 1900°C for 12 h under 1 MPa nitrogen pressure, using MgO and self-synthesized $Y_2Si_4N_6C$ as sintering aids. The microstructures and thermal conductivity of as-sintered bulk were systematically investigated, in comparison to the counterpart doped with Y_2O_3-MgO additives. $Y_2Si_4N_6C$ addition induced a higher nitrogen/oxygen atomic ratio in the secondary phase by introducing nitrogen and promoting the elimination of SiO_2, resulting in enlarged grains, reduced lattice oxygen content, increased Si_3N_4-Si_3N_4 contiguity and more crystallized intergranular phase in the densified Si_3N_4 specimen. Consequently, the substitution of Y_2O_3 by $Y_2Si_4N_6C$ led to a great increase of ~30.4% in thermal conductivity from 92 $W{\cdot}m^{-1}{\cdot}K^{-1}$ to 120 $W{\cdot}m^{-1}{\cdot}K^{-1}$ for Si_3N_4 ceramic.

A STUDY ON POROUS CERAMIC MEMBRANES PREPARED BY LOW-COST RAW MATERIALS FOR POTENTIAL MICROFILTRATION APPLICATIONS

Jang-Hoon Ha, Jongman Lee, In-Hyuck Song

Powder and Ceramics Division, Korea Institute of Materials Science (KIMS), Republic of Korea

ABSTRACT

Recently porous ceramic membranes have become a subject of special interest due to their outstanding thermal and chemical stability. To alleviate the manufacturing cost issues of porous ceramic membranes, recent research is focused on the utilization of low cost raw materials. In this study, we introduced porous ceramic membranes prepared from low cost raw materials such as diatomite, kaolin, pyrophyllite, and silicon carbide. And we report the results of our efforts to determine whether we could prepare a low-cost ceramic support layer that could control the average pore size, the largest pore size, the flexural strength and the air/water permeability effectively. The pore characteristics of the specimens were studied by scanning electron micrography, mercury porosimetry, capillary flow porosimetry, and a dead-end microfiltration system with particle counters.

ELECTRIC FIELD ASSISTED JOINING OF ADVANCED SiC-BASED CERAMICS

Peter Tatarko[1], Xiaobing Zhou[2], Salvatore Grasso[3], Ivo Dlouhý[4], Monica Ferraris[5]

[1]*Institute of Inorganic Chemistry, Slovak Academy of Sciences, Dubravska cesta 9, 845 36, Bratislava, Slovakia*
[2]*Engineering Laboratory of Specialty Fibers and Nuclear Energy Materials, Ningbo Institute of Materials Technology and Engineering, Chinese Academy of Sciences, Zhejiang, 315201, Ningbo, China*
[3]*Key Laboratory of Advanced Technologies of Materials, Ministry of Education, School of Materials Science and Engineering, Southwest Jiaotong University, Chengdu, 610031, China*
[4]*Institute of Physics of Materials, Academy of Sciences of the Czech Republic, Zizkova 22, 616 62, Brno, Czech republic*
[5]*Politecnico di Torino, Applied Science and Technology Department, Corso Duca degli Abruzzi 24, 10129 Torino, Italy*

ABSTRACT

SiC-based ceramic matrix composites (CMCs), such as carbon fibres reinforced silicon carbide (C/SiC) or silicon carbide fibres reinforced silicon carbide (SiC/SiC), are the primary candidates for the components for aerospace and industrial applications performing at extreme conditions (e.g. nuclear applications). A critical issue for the wider utilisation of these materials is the development of inexpensive and reliable joining methods to assemble large components into complex structures. In this work, Spark Plasma Sintering (SPS) and Flash-SPS were employed to join monolithic CVD-SiC and CMCs via indirect and direct heating of the joined component, respectively. A temperature as low as 1300°C was sufficient to achieve a defect-free joining interface when the MAX phase Ti_3SiC_2 was applied as the joining interlayer. The initial bending strength of the CVD-SiC joints (~ 220 MPa) did not deteriorate at 1000°C in vacuum, and the joints retained 70% of their initial strength at 1200°C. Some plastic deformation of the large Ti_3SiC_2 grains was found in the form of micro-lamellae sliding and bending. Conformal behaviour of the Ti_3SiC_2 foil and its infiltration into the surface cracks in the CVD-SiC coating of CMCs resulted in the apparent shear strength of the CMCs up to ~ 32 MPa. When a Ti foil was used as the interlayer, the temperature of 1700°C had to be used to obtain sound joints. A significant reduction of both the joining temperature (to ~ 1250°C) and the process time (to 8 seconds) was observed when a direct Flash-SPS joining process of CMCs with the Ti foil was employed (the maximum heating power of 2.2 kW). The apparent shear strength of the joints matched the interlaminar shear strength of the composites. A sound joint was obtained by forming a metallic kind of joint (Ti-based) at the joining temperature, in which the absence of any reaction phases (titanium silicides, carbides or ternary phases) significantly shortened the time necessary for the solid-state diffusion bonding. The Ti interlayer also partially filled up the surface cracks in the CVD coating on the CMCs due to plastic flow. This is believed to strengthen the joint. This constitutes a significant reduction in a processing time and the maximum temperature required, which in turn leads to energy savings and potentially higher industrial interest in the process.

ACKNOWLEDGMENT

This work was supported by the Slovak Research and Development Agency under the contract no. APVV-SK-CN-2017-0040 and APVV-17-0328. The support of the Joint Mobility Project within Czech-Slovak scheme for the period 2018–2020 under the ASCR-SAS agreement is also acknowledged. The work was also supported by the MVTS project of SAS “UltraCom” within the scheme of “Support of the Seal of Excellence projects”.

POROUS THERMAL INSULATION COATINGS FOR INTERNAL COMBUSTION AUTOMOBILE ENGINES

Jong-Jin Choi, Sae-Jung Yoon, Cheol-Woo Ahn, Byung-Dong Hahn

Powder and Ceramics Division, Korea Institute of Materials Science (KIMS), Republic of Korea

ABSTRACT

Under the Paris Agreement on Climate Change, all countries are strongly responsible for reducing greenhouse gas emissions, which results in putting pressure on the auto industry to drastically increase the average fuel economy of each company's fleet. Many researchers have carried out a large number of studies on in-cylinder thermal insulation ceramic coating to improve engine thermal efficiency and fuel economy. High-density ceramic materials, which have low thermal conductivity, have been commonly coated on metals such as an aluminium or iron alloy, succeeding in reducing heat loss by decreasing the temperature difference between the in-cylinder gas and the combustion chamber wall. However, these coatings caused constantly high temperature on combustion wall surface during the whole stroke, and therefore lead to engine knocking problem and deterioration of the engine's lifespan. To overcome these problems, novel porous ceramic coatings, which have low thermal conduction and low heat capacity, have been recently developed. In comparison with conventional dense insulation coating, the porous coating can reduce surface temperature of insulation coat on combustion chamber wall rapidly, according with the fluctuating temperature of in-cylinder gas. Therefore, insulation coating with both low thermal conductivity and low volumetric specific heat is useful for heat loss reduction of engine combustion chamber without any sacrifice in other engine performances. For low volumetric specific heat, the coating should be porous. Also, the porous film should have high enough durability – adhesion strength, hardness, and chemical inertness in real operating condition. In this work, we fabricated porous and reliable ceramic insulation coatings on Al alloy substrate by room-temperature operating powder spray coating process. The film showed low thermal conductivity (< 0.5 W/mK), low volumetric heat capacity (< 2000 kJ/m^{3}K), and high adhesion strength (>20 MPa). Characterization of the resultant coating materials was also performed.

EFFECT OF DIFFERENT PROCESSING TECHNOLOGIES ON DEVELOPMENT OF BORON CARBIDE/GRAPHENE PLATELETS CERAMICS

Richard Sedlák, [1]Alexandra Kovalčíková, Paweł Rutkowski,[2] Aleksandra Dubiel,[3] Salvatore Grasso[4], Harshit Porwal[4], Vladimír Girman[5], Martin Fides[1], Erika Múdra[1], Ján Balko[1], Michael J Reece[4], Ján Dusza[1]

[1] Institute of Materials Research, Slovak Academy of Sciences, Division of Ceramic and Non-Metallic Systems, Watsonova 47, 040 01 Košice, Slovak Republic
[2] AGH University of Science and Technology in Krakow, Faculty of Materials Science and Ceramics, al. A. Mickiewicza 30, 30-059 Krakow, Poland
[3] The Institute of Advanced Manufacturing Technology, Wroclawska 37a, 30-011 Krakow, Poland
[4] School of Engineering & Materials Science and Nanoforce Technology Ltd., Queen Mary University of London, Mile End Road, London E1 4NS, United Kingdom
[5] Pavol Jozef Šafárik University in Košice, Faculty of Science, Institute of Physics, Department of Condensed Matter Physics, Park Angelinum 9, 040 01 Košice, Slovak Republic

ABSTRACT

Boron carbide/graphene platelet (B_4C/GPLs) composites have been prepared with the addition of different weight percent and various types of GPLs by hot-press processing technology (HP), conventional Spark Plasma Sintering (SPS) and application of the novel and superfast processing method Flash Sintering (FS), which reduces sintering time only to 24 seconds. The effect of processing technology and influence of the GPLs addition on microstructure development, fracture toughness, electrical conductivity and tribological properties was investigated. The microstructure was studied by SEM, TEM, HRTEM, XRD and Raman spectroscopy. SEVNB method was used for fracture toughness and four-point Van der Pauw method for electrical conductivity measurement. Almost fully dense B_4C/GPLs composites have been prepared with lower wt.% of GPLs additives with relatively homogeneously distributed platelets in the matrix. With increasing amount of GPLs additives, the fracture toughness increased due to the activated toughening mechanisms in the form of crack deflection, crack bridging, crack branching and graphene sheet pull-out. The highest fracture toughness of 4.48 MPa.m$^{1/2}$ was achieved at 10 wt.% of GPLs addition, which was ~50 % higher than the K_{IC} value of reference material. A significant improvement of electrical conductivity around two orders of magnitude was noticed. The friction and wear behaviour of B_4C/GPLs composites have been investigated using the ball-on-flat technique with SiC ball under dry sliding conditions at room temperature. The coefficient of friction for composites was similar, however, the wear rate significantly decreased ~77 % in the case of B_4C+10 wt.% GPLs when compared to reference material at a load of 5 N, and ~60 % at a load of 50

N. For revealing and observation of the wear damages under the worn surfaces, focused ion beam (FIB) technique was used for the preparation of the cross-section of wear tracks.

ACKNOWLEDGEMENTS

The authors gratefully acknowledge the financial support from Journal of ECerS Trust (Contract 2016116, Contract 2016124-19) and from projects: APVV-15-0469, VEGA 2/0163/16, and VEGA 2/0130/17.

RESEARCH ACTIVITIES ON THE TRANSPARENT POLYCRYSTALLINE CERAMICS AT KIMS

Young-Jo Park, Ha-Neul Kim, Jae-Woong Ko, Hai-Doo Kim

Powder and Ceramics Division, Korea Institute of Materials Science (KIMS), Republic of Korea

ABSTRACT

Since Dr. Coble at GE opened up the new era of a translucent polycrystalline alumina at early 1960’s, lots of polycrystalline ceramics have been demonstrated to be transparent by careful pretreatment of powders and elaborated seeking of sintering technique. At year 2013 researchers at KIMS (Korea Institute of Materials Science) have launched the 5-year project on transparent ceramics for the application in the military defense system, in which both transmittance and mechanical reliability is strongly required. Two ceramic materials have been tackled; one is spinel ($MgAl_2O_4$) for bullet-proof and the other is yttria (Y_2O_3) for mid-IR window. A pressureless sintering for spinel and hot press sintering for yttria were mainly employed, respectively. In this talk, process routine and earned material properties developed at KIMS will be disclosed.

SiC-GRAPHENE COMPOSITES WITH HIGH ELECTRICAL AND THERMAL CONDUCTIVITY

Ondrej Hanzel[1], Zoltán Lenčéš[1], Young-Wook Kim[2], Pavol Šajgalík[1]

[1] Institute of Inorganic Chemistry, Slovak Academy of Sciences, Dúbravska cesta 9, 845 36 Bratislava, Slovak Republic
[2] Functional Ceramics Laboratory, Department of Materials Science and Engineering, University of Seoul, Seoul 02504, Republic of Korea

ABSTRACT

Dense SiC/graphene nanoplatelets (GNPs) and SiC/graphene oxide (GO) with yttrium oxide and scandium oxide as a sintering additives were prepared by rapid hot pressing (RHP). The content of GNPs or GO was in the range 1 – 10 wt. %. Sintering of composites was performed in nitrogen atmosphere at 2000°C for 30 min under uniaxial pressure of 50 MPa. The sintered samples were annealed in gas pressure sintering (GPS) furnace at 1800°C for 6 h under 3 MPa nitrogen pressure. Significant anisotropy of thermal diffusivity and electrical conductivity was confirmed as a result of preferential orientation of graphene layers during sintering (RHP). Also the post-sintering thermal treatment significantly influenced the functional properties of SiC-graphene composites. The thermal diffusivity of sample with 5 wt.% of GNPs in parallel direction to graphene layers remarkably increased after annealing to 104,4 mm^2/s from value 72,3 mm^2/s measured for the reference sample (without addition of graphene and annealing). At the same time the electrical conductivity increased from 1400 S/m (for reference sample) to 9402 S/m for composite with 5 wt. % of GNPs.

ACKNOWLEDGEMENTS

The work was supported by CERANEA FLAG ERA II project.

PROMATECH

Research Centre for Advanced Materials and Technologies

RESEARCH CENTRE PROMATECH
Pavilón materiálových vied
Watsonova 47
0401 Košice
gps: 48°44'02''N 21°14'19''E
promatech@promatech.sk

MISSION

Research Centre „PROMATECH“ has an ambition to become a top, national, integrated, interdisciplinary and sustainable center, producing excellent frontier and applied research, performing excellent international co-operation, expertise activities and consulting service for industrial partners, technological and knowledge of industry and dissemination of results together with popularization of the Centre.

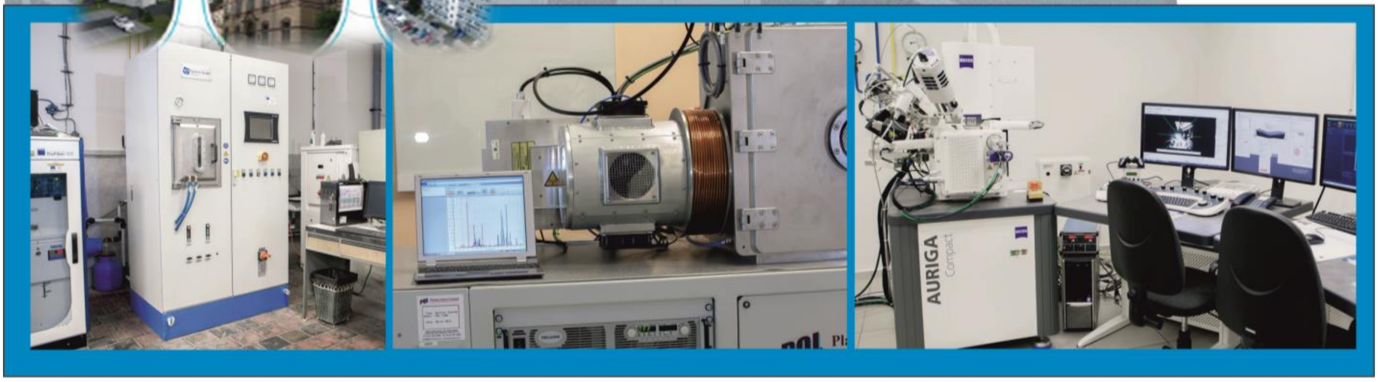

The Main Areas of Research are:

- Research and development of advanced steels, alloys, ceramics, powder metallurgy materials and products and hard coatings.
- Research and development of materials and technologies for biomedical and environmental applications.
- Materials for ICT technologies and cryotechnologies.
- Research and development of new magnetic materials.

V rámci výskumného programu SAV pre spoločenské využitie s názvom Otvorená akadémia bola financovaná aj zábavno-vzdelávacia akcia pre talentované deti, ktoré sa nielen oboznámili so zaujímavou prácou vedcov na ÚMV SAV v Košiciach, ale zároveň samé prispeli svojimi predstavami k dotvoreniu nanosveta materiálov.

Otvorená akadémia

- platforma na napĺňanie spoločenského poslania vedy.

Veda očami malých umelcov.

ZUŠ Košických mučeníkov
Čordákova 50, Košice

Deti vidia nanosvet trochu inak.

Takto dokreslili fotografie mikroštruktúr keramických materiálov zobrazených pomocou rastrovacieho elektrónového mikroskopu.